



ScuDo

Scuola di Dottorato ~ Doctoral School
WHAT YOU ARE, TAKES YOU FAR



Doctoral Dissertation
Doctoral Program in Aerospace Engineering (33rd Cycle)

COMPREHENSIVE APPROACH TO ELECTRIC PROPULSION FOR INNOVATIVE SPACE PLATFORMS

Christopher Andrea Paissoni

* * * * *

Supervisors

Prof. Nicole Viola, Supervisor

Prof. Fabrizio Paganucci, Co-Supervisor

Doctoral Examination Committee:

Dr Guillermo Ortega, Head Guidance, Navigation & Control Section, ESA-ESTEC

Dr. Marco Di Clemente, Italian Space Agency

Dr Ilaria Roma, Head of the Systems and Concurrent Engineering Section, ESA-ESTEC

Prof. Stéphanie Lizy-Destrez, Institut Supérieur de l'Aéronautique et de l'Espace

Prof. Richard Ambrosi, University of Leicester

Politecnico di Torino

June 30th, 2021

This thesis is licensed under a Creative Commons License, Attribution-Noncommercial - NoDerivative Works 4.0 International: see www.creativecommons.org. The text may be reproduced for non-commercial purposes, provided that credit is given to the original author.

I hereby declare that the contents and organisation of this dissertation constitute my original work and does not compromise in any way the rights of third parties, including those relating to the security of personal data.

.....
Christopher Andrea Paissoni
Turin, June 30, 2021

Summary

This dissertation investigates the new mission opportunities and methods enabled by innovative propulsion space systems based on electric propulsion devices. In recent years, the international community has advanced new technological development roadmaps targeting expanding the utilisation activities in space toward future challenges. Among the identified roadmap building blocks, the electric propulsion field has been recognised as one of the most impacting sectors where several innovations could represent true cornerstones. In particular, the consolidation of the adoption of Hall Thruster devices has nowadays enabled the possibility of adopting innovative architecture alternatives to extend the benefits of these technologies further. Embracing these benefits and considering the new space market needs, space system concepts already presented in the past can be renewed for a feasibility assessment.

This is the case of the space tug proposed to provide On-Orbit Servicing for the Geostationary market. This reusable system should transfer telecommunication satellites from their deployment orbit up to their final GEO positions. In addition, it can be exploited for relocated the telecom satellites to a new GEO position to capitalise on free-market shares. To obtain the preliminary design at the component level of the space tug, including the capability of analysing the alternative propulsion subsystem architectures, a multi-input/output software tool has been developed. This user-friendly virtual environment allows the derivation of the main mission and system budgets sizing of the space tug subsystems pat the component level in an iterative process with a trajectory propagator necessary to simulate the predefined mission profile.

Then, the optimal space tug configurations are evaluated by mean of a trade-off analysis among the considered alternative design solutions considering figures of merit which guarantees the pros and cons of the alternative propulsion subsystem architecture impacts.

The capabilities developed tool has been further extended by introducing both analysis and design blocks necessary for the feasibility assessment of a Very Low Earth Orbit mission. In particular, the strong interaction of the spacecraft surrounding environment characterised by the high level of drag generated by the exposed surfaces forces to introduce unconventional design methods to embrace all possible cross effects that impact the design and operation of the spacecraft itself. In this analysis, this problem was challenged through the introduction of an MDO process for the definition of a Pareto front of optimal solutions. According to the selection criteria defined by the user as a result of a stakeholder needs evaluation, the optimal solution is selected and further analysed in terms of operative altitude ranges, alternative solar array configuration, and trajectory evolution with a preestablish in-orbit demonstration scenario.

As a part of the evaluation of the innovative spacecraft architectures introduced in this work, a fundamental aspect has been identified in the reliability of the architectures usually included in the trade-off process. The evaluation of this system feature is often a critical process due to the intrinsic complexities of the system and the lack of knowledge of the different mode of failures.

Therefore, in the current technology taxonomy, the development of methodologies aimed to evaluate the health status of the involved component is clearly highlighted to extend the understanding of modes of failure and improve the information necessary for the evaluation of the component reliability.

This key aspect has been investigated in the dissertation to develop an Engine Health Monitoring (EHM) method for Hall thruster-based system exploiting the Gas Path Approach (GPA), which is a health monitoring methodology already largely used in the aeronautic field.

The GPA consists of the identification of the deviations of a set of unmeasured parameters, representing the health status of the components from their nominal values. This is accomplished by investigating the variations of a set of measured parameters set from their nominal values correlated to the set of unmeasured parameters through a coefficient matrix called Influence Coefficient Matrix (ICM). The followed approach was divided into two steps. First, a phenomenological model of the Hall thruster has been introduced and exploited to derive the theoretical ICM coefficients between the two parameters sets. Second, relying on experimental data, the ICM has been derived through a numerical method, and its coefficients have been consequently compared with those related to the theoretical matrix. Finally, to demonstrate the effectiveness in the failure detection capability of this method, a set of experimental data collected during a test campaign on

SITAEL's HT20k DM, where a failure on the feeding system of the thruster occurred, were exploited.

To my parents

Contents

1. Introduction.....	18
2. CASE STUDY: the SPACE TUG	25
2.1 Space Tug concept & Mission Opportunities.....	25
2.2 Mission definition.....	27
2.3 Space tug: mission architecture and spacecraft definition.....	30
2.4 Space tug OOS scenario	36
2.4.1 Mission phases	36
2.4.2 Modes of operation	40
2.4.3 OOS traffic plan.....	44
2.5 MAGNETO – MultidisciplinAry design Electric Tug Tool	47
2.5.1 Scenario definition: the input module.....	48
2.5.2 Scenario analysis: design module of the Space Tug.....	51
2.5.2.1 Electric propulsion subsystem design module	51
2.5.2.2 Direct Drive configuration	60
2.5.2.3 Alternative propellant selection	67
2.5.3 S/C subsystems design module.....	68
2.5.3.1 Electric Power and Management Subsystem (POW).....	69
2.5.3.2 Thermal Control Subsystem (TCS).....	69
2.5.3.3 Chemical Propulsion Subsystem (cPROP)	70
2.5.4 Scenario optimization: Trajectory Propagation Module.....	72
2.5.5 Output and result analysis module.....	77
2.6 Main case study results.....	80
2.6.1 EPS architecture comparison	80
2.6.2 Scenario comparisons	88
3. CASE STUDY: VLEO missions	105
3.1 The ramEP concept & VLEO environment.....	106

3.2	Literature review: in between of thruster concept and new mission scenarios	109
3.3	RAMEP future market opportunities.....	125
3.3.1	VLEO market: general description	125
3.3.2	Application identification	129
3.3.3	Current application market subdivision	132
3.4	VLEO scenario mission definition	137
3.4.1	VLEO IoD mission objectives	137
3.4.2	Mission architecture.....	139
3.5	ramEP spacecraft concept.....	141
3.5.1	ramEP Platform Functional Definition	141
3.5.2	ramEP ConOps: Design Reference Mission and mission phases .	145
3.5.2.1	Reference orbits.....	146
3.5.2.2	Mission Phases	148
3.5.3	Modes of Operation	150
3.6	Platform Definition.....	153
3.6.1	MAGNETO: software modifications.....	156
3.6.1.1	Input module	156
3.6.1.2	PLATFORM DESIGN: Multidisciplinary design approach.	157
3.6.1.3	SCENARIO PROPAGATION – Manoeuvres and altitude control logic	175
3.7	MDO and trajectory propagation results	189
4.	Engine Health Monitoring applied to Hall Thrusters	206
4.1	Engine Health Monitoring concept.....	206
4.2	GPA/EHM state of the Art	210
4.4	EHM application process	216
4.5	HT Performance Model	219
4.6	Overview of the experimental apparatus	227
4.6.1.	IV10 Vacuum facility	227
4.6.2	Laboratory power supply	228
4.6.3	Xenon Feeding System	229
4.6.4	Diagnostics.....	230
4.7	HT20k Test points	231

4.8 Results	235
5. Conclusion and way forward	243
6. References.....	249
7. Appendix A - Functional Analysis and Function/Product Matrices for space tug OOS mission	264
8. Appendix B – Results of Space Tug architecture analysis	268

List of Tables

Table 1: Modes of transition.....	43
Table 2: subsystem status for the different modes of operation.	44
Table 3: safety margin on S/C budgets.....	49
Table 4: thruster parameters collected in the database.	50
Table 5: Ht5k and HC20 main specification [40].....	55
Table 6: HT20k and HC60 specifications.....	56
Table 7: EPS component sizing features.	57
Table 8: Anodic module assumed design parameters.....	62
Table 9: SA design parameters.	64
Table 10: battery design parameters.	65
Table 11: relative dry mass fraction for each space tug subsystem.....	71
Table 12: in-plane and out-of-plane angles for each controlled orbital parameter.	75
Table 13: trade-off FoM, weights direction and results' source.....	78
Table 14: alternative design options under analysis.	81
Table 15: SET#1 of operative points for HT5k and HT20k.....	81
Table 16: SET#2 of operative points for HT5k and HT20k.....	82
Table 17: Monolithic vs Cluster architecture, SET#1 operative points, comparison results. The bolded value results in the optimal trade-off solution.	83
Table 18: PPU cs DDU, SET-1 operative points, comparison results.....	84
Table 19: Xe vs Kr, SET#1 operative points.	84
Table 20: Monolithic vs Cluster, SET-2 operative points, comparison results.	86
Table 21: PPU vs DDU, SET-2 operative points, comparison results.	86
Table 22: Xe vs Kr, SET#2 operative points, comparison results.....	87
Table 23: comparison of all the cases under analysis.....	88
Table 24: HT20k selected operative points.	90
Table 25: HT5k selected operative points.	91

Table 26: space tug configurations simulated for MS.2.	94
Table 27: Requirements for thruster operative points	94
Table 28: operative points.....	95
Table 29: Angles combinations	98
Table 30: Total mission time data.....	99
Table 31: angle combinations for direct comparison of delta-V, phase durations, eclipse durations.	103
Table 32: results for HT5k configuration.	103
Table 33: results for HT20k configuration.	103
Table 34: Small/medium launch vehicle list.....	108
Table 35: conventional thrusters operated with oxygen-nitrogen mixtures.	120
Table 36: ramEP function/product matrix.	142
Table 37: mission phases description.	148
Table 38: mission phases characterization.....	150
Table 39: ramEP S/C mode transition characterization.....	152
Table 40: mission and configuration trade-off.	155
Table 41: MDO design variables.	159
Table 42: MDO output variables.,	160
Table 43: selected solar period.	169
Table 44: summary of the heat fluxes formulation.....	174
Table 45: D1 level, decision options.	180
Table 46: D2 level, decision options.	185
Table 47: D5 level, decision options.	186
Table 48: D6 and D7 levels, decision options.	186
Table 49: D9 and D10 levels, decision options.	187
Table 50: D4, D11, D12, D13 and D14 levels, decision options.....	188
Table 51: main output of the selected MDO results.	191
Table 52: optimal operative altitude ranges for the selected configuration.....	197
Table 53: alternative spacecraft wing configurations.	199
Table 54: additional available surfaces for the alternative wing configurations.	199
Table 55: T/D ranges and acceleration voltage ranges reported for each solar activity period.....	203
Table 56: Independent variable list.....	219
Table 57: Dependent variable list	219
Table 58: ICM coefficient derivation.	226
Table 59: main technical characteristics of IV10 vacuum facility.	228
Table 60: Main characteristics of the Xenon feeding system.	229
Table 61: Thrust balance specifications.....	230

Table 62: main characteristics of the employed oscilloscope.....	231
Table 63: HT20k DM2 characterization matrix.	232
Table 64: HT20k DM2 characterization matrix used during failure investigation.	233
Table 65: derived ICM matrix values.	238
Table 66-ANNEX-A: Function/Product matrix for POW subsystem.	265
Table 67-ANNEX-A: Function/Product matrix for EPS subsystem.	265
Table 68-ANNEX-A: Function/Product matrix for TCS subsystem.....	265
Table 69-ANNEX-A: Function/Product matrix for POW subsystem.	266
Table 70-ANNEX-A: Function/Product matrix for STRUCT subsystem.....	266
Table 71-ANNEX-A: Function/Product matrix for COMM subsystem.	267
Table 72-ANNEX-A: Function/Product matrix for CDH subsystem.....	267
Table 73 - APPENDIX-B: Mission total duration, HT20k configurations.	268
Table 74 - APPENDIX-B: Mission total duration, HT5k configurations.	269
Table 75 - APPENDIX-B: Mass dry HT20k configurations.....	269
Table 76 - APPENDIX-B: Mass dry HT5k configurations.....	270
Table 77 - APPENDIX-B: Mass wet HT20k configurations.	271
Table 78 - APPENDIX-B: Mass wet HT5k configurations.	271
Table 79 - APPENDIX-B: Mass wet + mass serviced satellite, HT20k configurations.....	272
Table 80 - APPENDIX-B: Mass wet + mass serviced satellite, HT5k configurations.	273

List of Figures

Figure 1: (Left) Artistic rendering of the Mission Extension Vehicle-2 (MEV-2) to the Intelsat 10-02 (IS-10-02) commercial communications satellite occurred in February 2020 (credits: Northrop Grumman). (Right) NASA’s BIG Idea Challenge space tug concept (credits: NASA).....	20
Figure 2: General overview of the past mission at very low altitudes with some reference mission as ISS, GRACE/FCO and Hubble.	22
Figure 3: possible application range for the space tug concept.	26
Figure 4: space tug for OOS Functional Tree.....	28
Figure 5: Functions/Products matrix at Segment level.	29
Figure 6: Functions/products Matrix at System level.....	29
Figure 7: OOS space tug Interconnection Block Diagram at segment level.	30
Figure 8: SpaceX’s refuelling concept for Starship operation (credits: SpaceX)..	32
Figure 9: GEO satellite mass trend with respect to the year of launch.....	33
Figure 10: GEO satellite angular distribution.....	34
Figure 11: MS1 Design Reference Mission.....	39
Figure 12: MS2 Design Reference Mission.....	39
Figure 13: activation of the modes of operation with respect to the foreseen operation in both scenarios. The coloured boxes refer to the modes of operation that can be triggered during the related mission phase. The dashed boxes highlight the modes of operation that could be eventually triggered in case of necessity.....	41
Figure 14: Space tug modes of operation.	42
Figure 15: MS1 operational timeline- The TBD phase durations are related to the low thrust transfer (phase 3 and 6) and waiting phase (phase 9)	46

Figure 16: MS2 operational timeline. The TBD phase durations are related to the low thrust transfer (phase 3, 6, 8 and 10) and waiting phase (phase 13).	46
Figure 17: functional structure of MAGNETO.	48
Figure 18: MATLAB user interface, user folder selection.	51
Figure 19: simplified scheme of a monolithic propulsion subsystem based on Hall thruster technology.	52
Figure 20: (a) HT5k during integration on thrust stand; (b) HT5k during characterization campaign.	54
Figure 21: (a) HT20k DM2-L; (b) HT20k DM2-L during the first characterization campaign [42].	55
Figure 22: Simplified block diagram of an EPS based on cluster architecture.	58
Figure 23: Conceptual functional block diagram of a conventional PPU.	62
Figure 24: (a) Chopper Switching Frequency (SF) vs component power; (b) Inverter transformer Switching Frequency (SF) vs component power [53].	63
Figure 25: Anodic module block diagram power conditioning steps.	63
Figure 26: block diagram with the components considered in the DD approach.	66
Figure 27: projection of the PPU mass vs DDU mass with respect to the input power of the EP string.	67
Figure 28: phasing phases.	76
Figure 29: graphical comparisons with the related percentage for (i) dry and propellant mass budget (top-left), (ii) transfer time (top-right), (iii) propellant cost (bottom-left), (iv) total power (bottom-right).	85
Figure 30 graphical comparisons with related percentage for (i) dry and propellant mass budget (top-left), (ii) transfer time (top-right), (iii) propellant cost (bottom-left), (iv) total power (bottom-right).	87
Figure 31: alternative tree of the simulations performed with MAGNETO on both scenarios.	89
Figure 32: (left) propellant mass ($M_{propellant}$) and (right) transfer time ($t_{transfer TOT}$) w.r.t. the space tug dry mass (M_{dry}) derived for MS.1 for the operative points of both HT5k and HT20k.	92
Figure 33: (left) propellant mass ($M_{propellant}$) and (right) transfer time ($t_{transfer TOT}$) w.r.t. the space tug wet mass (M_{wet}) derived for MS.1 for the operative points of both HT5k and HT20k.	92
Figure 34: (left) transfer time ($t_{transfer TOT}$) vs number of thrusters in the cluster ($\#thr$) vs propellant mass ($M_{propellant}$) and (right) transfer time ($t_{transfer TOT}$) vs wet mass (M_{wet}) vs total space tug power budget ($PS/C TOT$) derived for MS.1 for the operative points of both HT5k and HT20k.	93

Figure 35: (left) transfer time ($t_{transfer TOT}$) vs total generated thrust ($TEPS$) (right) transfer time ($t_{transfer TOT}$) vs total space tug power budget ($PS/C TOT$) derived for MS.1 for the operative points of both HT5k and HT20k.	93
Figure 36. (a) The total power is compared with the total wet mass of the spacecraft [HT5k vs HT20k]. (b) The total power is compared with respect to wet mass and total mission time [HT5k vs HT20k]	95
Figure 37. (a) Wet mass vs Total thrust. (b) Total thrust compared with mission time and wet mass	96
Figure 38. (a) Wet mass vs Dry mass. (b) Wet mass vs Dry mass vs number of thrusters.....	96
Figure 39. (a) Wet mass vs propellant mass. (b) Wet mass vs propellant mass vs number of thrusters	97
Figure 40. (a) Dry mass vs prop mass. (b) Dry mass vs prop mass vs Number of thrusters.....	97
Figure 41. Total mission time vs second phasing manoeuvre angles [HT20k vs HT5k all n. thrusters configuration].....	98
Figure 42. (a) Mission time [HT20k:1 thr vs HT5k:4 thr]; (b) Mission time for HT20k configurations.	99
Figure 43. Dry mass vs second phasing manoeuvre angles [HT20k vs HT5k all n. thrusters configuration]	99
Figure 44.(a) Dry mass [HT20k:1 thr vs HT5k:4 thr]; (b) Dry mass for HT20k configuration	100
Figure 45. Wet mass vs second phasing maneuver angles [HT20k vs HT5k all n. thrusters configuration]	100
Figure 46:(a) Wet mass [HT20k:1 thr vs HT5k:4 thr]; (b) Wet mass for HT20k configuration.	101
Figure 47. Wet mass with serviced satellite mass vs second phasing manoeuvre angles [HT20k vs HT5k all n. thrusters configuration]	101
Figure 48:(a) Wet mass with serviced satellite mass [HT20k:1 thr vs HT5k:4 thr]; (b) Wet mass with serviced satellite mass for HT20k configuration.....	102
Figure 49. Propellant mass vs second phasing manoeuvre angles [HT20k vs HT5k all n. thrusters configuration]	102
Figure 50: ramEP S/C concept.....	106
Figure 51: ABIE intake concept [99].....	112
Figure 52: Schematic diagram of the ESA RAMEP intake concept [100].....	113
Figure 53:MAHBET spacecraft concept (credits: [101]).	114
Figure 54: spacecraft concept (credit: [103]).....	115

Figure 55: internal RF thruster main concept location (credit: [104]).	116
Figure 56: artistic impression of GOCE during thruster firing (credits: ESA).	117
Figure 57: GOCE mission altitude variation (credit: ESA).	118
Figure 58: DISCOVERER spacecraft concept [124].	122
Figure 59: (top) prototype of the SITAEL's ramEP concept (bottom) SITAEL's ramEP prototype during the first firing test (credit: SITAEL) [132].	123
Figure 60: main objectives of the SITAEL projects about ramEP technology.	124
Figure 61: Space market revenues in 2020 (a) Source: [139–141] (b) Source: [137], (c) Source [142], (d) Source [143].	126
Figure 62: ramEP foreseen value chain.	127
Figure 63: Space market economic segmentation for: (i) application (internal graph) and (ii) exploited orbits (external graphs).	133
Figure 64: number of satellites in LEO w.r.t. their application.	135
Figure 65 number of satellites in MEO w.r.t. their application.	136
Figure 66: number of satellites in GEO w.r.t. their application.	136
Figure 67: number of satellites on elliptical orbits w.r.t. their application.	136
Figure 68: Notional system architecture block diagram.	139
Figure 69: RAMEP Platform Functional Tree.	141
Figure 70: ramEP platform functional block diagram.	145
Figure 71: RAMEP general Design Reference Mission (DRM).	146
Figure 72: variation of the orbit inclination for an SSO dawn-dusk orbit.	147
Figure 73: modes of operation at the system level.	151
Figure 74: alternative spacecraft configuration options.	154
Figure 75: VLEO-MAGNETO software functional structure.	156
Figure 76: VLEO-MAGNETO user-interactive interface.	157
Figure 77: ramEP spacecraft MDO process.	158
Figure 78: general definition of the launch vehicle fairing dimensions.	163
Figure 79: general definition of the spacecraft dimensions. Only half spacecraft is represented in the figure.	163
Figure 80: definition of the spacecraft body dimension. In the most generic case, the spacecraft body section is represented with a square section.	164
Figure 81: solar activity between 1997 and 2019 (23° and 24° Solar Cycle).	168
Figure 82: example of the result obtained from the adopted NRLMSISE-00 highlighting the strong variation of the temperature at 230km.	170
Figure 83: averaged temperature variation in the considered altitude range for the different solar activity periods.	170
Figure 84: averaged atmospheric composition variations in the considered altitude range considering the different solar activity periods.	171

Figure 85: ramEP control logic for altitude maintenance.....	177
Figure 86: eclipse model, geometrical construction.....	178
Figure 87: ESA – GOCE first global gravitational model [196]......	182
Figure 88: altitude definition for the different Earth models.....	183
Figure 89: definition of the target altitude range with the main altitude limits considered in the thruster control logic.....	184
Figure 90: MDO Pareto front.....	190
Figure 91: optimal configurations for the different criterion (i) min FVAL, (ii) max P_{ramEP} and (iii) max T/D.....	193
Figure 92: trends of the thrust-over-drag ratio for the selected configuration (top- left) max (T/D), (top-right) max ($PramEP$) and (bottom) min($FVAL$).	195
Figure 93 trends of the generated spacecraft drag for the selected configuration (top- left) max (T/D), (top-right) max ($PramEP$) and (bottom) min($FVAL$).	196
Figure 94: trends of the generated ramEP thrust for the selected configuration (top- left) max (T/D), (top-right) max ($PramEP$) and (bottom) min($FVAL$). The points on the trends fulfilling the acceleration voltage constraint are highlighted in green.	197
Figure 95: trends of the thrust-over-drag ratio for the selected configuration (top- left) max (T/D), (top-right) max ($PramEP$) and (bottom) min($FVAL$). The points on the trends fulfilling the acceleration voltage constraint are highlighted in green.	198
Figure 96: trends of the thrust-over-drag ratios considering alternative deployed wing configurations investigated for max $PramEP$ solution.	201
Figure 97 trends of the thrust-over-drag ratios considering alternative deployed wing configurations investigated for max T/D solution.	201
Figure 98 trends of the thrust-over-drag ratios considering alternative deployed wing configurations investigated for min $FVAL$ solution.	202
Figure 99: High Solar Activity propagation. (a) Altitude w.r.t. long, medium and short step averaging process, (b) thruster acceleration voltage, (c) activated thruster control modes, (d) T/D values.	204
Figure 100: Medium Solar Activity propagation. (a) Altitude w.r.t. long, medium and short step averaging process, (b) thruster acceleration voltage, (c) activated thruster control modes, (d) T/D values.....	205
Figure 101: Low Solar Activity propagation. (a) Altitude w.r.t. long, medium and short step averaging process, (b) thruster acceleration voltage, (c) activated thruster control modes, (d) T/D values.	205

Figure 102:: Relation between physical degradation effects, component condition changes, and observable thruster performance parameters.....	209
Figure 103: Non-Linear Gas Path representation [209].....	213
Figure 104: representative schematic of the voltage distribution in a Hall thruster discharge chamber.....	221
Figure 105: schematic of a simplified Hall thruster magnetic circuit [222].....	223
Figure 106: (Top picture) IV10 vacuum facility rendering; (Bottom-Left) IV10 laboratory and (Bottom-Right) movable cap equipped with conical Grafoil targets (credits: SITAEL).....	227
Figure 107: Schematic of the IV10 propellant feeding system.	229
Figure 108: the three HT20k DM2 configurations (S,M and L) operated at 25mg/s @300V [43]	232
Figure 109:EHM based on GPA approach HT application process.	236
Figure 110: ICM coefficient values.	237
Figure 111: ICM coefficient distributions.	237
Figure 112: normalized delta of faulty operative points with respect to the nominal operative points.	241
Figure 113: delta flow rate of the faulty points with respect to the nominal operative points.	241
Figure 114-ANNEX-A: Functional tree at subsystem/component level of a space tug operated in the OOS scenario.	264

Abbreviations

ADCS	Attitude Determination and Control Subsystem
AMFR	Anodic Mass Flow Rate
ANN	Artificial Neural Network
BBN	Bayesian Belief Network
C&DH	Command and Data Handling
COTS	Commercial-off-the-Shelf
DD	Direct Drive
DDU	Direct Drive Unit
DM	Demonstration Model
DRM	Design Reference Mission
EHM	Engine Health Monitoring
EoL	End of Life
EOR	Electric Orbit Raising
EP	Electric Propulsion
FCM	Failure Coefficient Matrix
FCU	Flow Control Unit
FDIR	Failure Detection Identification and Recovery
FMEA	Failure Mode and Effect Analysis
FMECA	Failure Mode and Effect Criticality Analysis
GEO	Geostationary Orbit
GIE	Gridded Ion Engine
GPA	Gas Path Analysis
GTO	Geostationary Transfer Orbit
HT	Hall Thruster
ICM	Influence Coefficient Matrix
IoD	In Orbit Demonstration
ISRU	In Situ Resources Utilization

KMFR	Cathode Mass Flow Rate
LEO	Low Earth Orbit
LEOP	Launch and Early Operating Phase
LGPA	Linear Gas Path
MAGNETO	MultidisciplinAry desiGN Electric Tug tOol
MCC	Mission Control Centre
MDO	Multi-Objective Optimisation
MEOP	Maximum allowable operating pressure
MMOD	Micro-Meteoroids and Orbital Debris
MOC	Mission operation Centre
MS	Mission Scenario
MSC	Mission Support Centre
NLGPA	Non-linear Gas Path
OORS	On Orbit Refuelling System
OOS	On Orbit Servicing
PCDU	Power Control And Distribution Unit
PFCV	Proportional Flow Control Valve
PMA	Pressure Management Assembly
PO	Parking Orbit
PO	Parking Orbit Electric Power Distribution and Control
POW	Subsystem
PPU	Power Processing Unit
RRM	Robotic Refuelling Mission
RVD	Rendezvous and Docking
SA	Solar Array
SCC	Spacecraft Control Centre
SE	System Engineering
SOC	Science Control Centre
SSO	Sun Synchronous Orbit
TCS	Thermal Control System

TPM	Thruster Point Mechanism
TRL	Technological Readiness Level
TT&C	Telemetry, Tracking and Communication
TTV	ThermoThrottle valve
TU	Thruster Unit
VLEO	Very Low Earth Orbit

Chapter 1

Introduction

The utilization of space is still in its infancy compared to the number of thinkable possibilities. Several steps have been already taken, but many are still to come.

With different global responses, the current space scenarios may be embraced in the so-called New Space Economy. In this context, several worldwide endeavours will improve or develop economically sustainable approaches to access, exploit and explore space. Unofficially identified with the Space Shuttle retirement in 2011, the beginning of this new space era opened new opportunities through the emerging of decentralized companies actively operating in new born space commercialization scenarios. First, the launch of mega-constellation in Low Earth Orbit (LEO) represents one example of how commercial operators translated the arising stakeholder needs of global coverage services into innovative mission architectures. Nowadays, OneWeb and Starlink are largely deployed and have started their operational phase, highlighting the benefits brought by the constellation concept mainly in terms of pervasive connectivity and operational versatility. The second path impacted by this new space renaissance is the opportunities beyond the LEO. The introduction of the constellations influenced the typical approach followed by the main space operators to the geostationary orbits, considered a steady-state reference market so far.

Smaller satellites are gradually replacing heavy platforms because of the higher versatility obtained by introducing both multifunctional and reconfigurable payloads. Far in space, the international community is focused on the Moon scenario with the so-called "return and stay" approach. One example is the American's leading Artemis programme. Officially started in 2017, it implements the previous outcomes of the major American projects and missions cancelled mainly for budget limitations. The final political and economic endorsement arrived in 2021 thanks to Biden's administration with the assignment of the first commercial contracts to support the development and manufacturing of the necessary technologies.

A multimodular space station placed in cis-lunar space, the so-called "Lunar Gateway" (formerly Deep Space Gateway) will be the centre of a complex mission architecture based on different space systems. They will cooperate in providing support for its construction, resupply and all the operations on the lunar surface. With the challenging objective of a first Moon landing in 2024, this ambitious programme required international cooperation involving public and private organisations to overcome the major criticalities dictated by the extensive costs. Despite everything, the lunar scenario is considered an exceptional environment to prove technologies and operations for enabling even far away targets around other celestial bodies of the Solar System. The future vision of the space community was outlined by the International Space Exploration Coordination Group (ISECG), funded in 2006 to derive a shared strategy for robotic and space exploration. Subsequent updates of the Global Exploration Roadmap with a final release in 2018 [1], followed by an additional supplement in 2020[2], defined the reference mission scenarios for both Moon and Mars, providing a general overview of the incremental technological developments necessary to fulfil these ambitious targets successfully. With this objective, the world-leading space agencies and international organisations would be setting priorities for the technological building blocks that are considered an enabler for future space endeavours. One of the later examples is the investigation performed by NASA in 2020.

NASA's Technological Taxonomy [3] identified 17 technological areas organised in a detailed taxonomy to facilitate the management and the cross-communication among the different sectors. Among them, the TX01 Propulsion Systems results have a prominent position due to the crucial importance of the identified functionalities, technologies and methods. Indeed, this area embraces all aspects of the chemical, non-chemical propulsion devices, systems and possible related propulsion ground technologies. In specific, a fundamental category included in the area TX01.2 is the Electric Space Propulsion consisting of (i) Integrated Systems and Ancillary technologies, (ii) Electrostatic devices, (iii) Electromagnetic devices and (iv) Electrothermal devices, which represents a complete coverage of the different development activities in this propulsion field.

As a matter of fact, electric propulsion systems provide specific impulse values at least an order of magnitude higher than the chemical systems, implying huge mass advantages at the platform level. This prominent evidence is of particular importance for spacecraft intended for on-orbit servicing and transportation missions. Furthermore, high-power EP systems have an additional value for the spacecraft. Their higher power translates into higher thrust values, allowing the commercially viable duration of the missions and higher economic revenues prospected.

On-orbit satellite servicing and transferring spacecraft are few examples of the number of architectures under study to tackle the benefits coming from the adoption of such performing and reliable high-power electric propulsion systems.

Increasing the TRL of these propulsion systems is fundamental, but it is not the only advancement necessary to fully exploit such systems for future scenarios. Several other criticalities at both the satellite system and propulsion subsystem levels should be faced with EP system development. At the component level, the main issues are related to the expensive qualification campaigns necessary to reach an adequate confidence level, which corresponds to a higher TRL for flying the specific propulsion device onboard the satellite. The key example is represented by the qualification process of the thruster, which is the most impacting in terms of costs and time. Based on the safety margin of the mission total impulse and the number of on/off cycles, the classical approach shall be revamped with more efficient, reliable and cost-effective processes. Several concepts have been studied at the subsystem level during the decades to strengthen electric propulsion benefits further. However, alternative solutions envisage a radical modification for the traditional propulsive string to avoid, for example, extensive qualification campaign and optimized manufacturing processes.

Even though the introduction of new architecture concepts increases the subsystem's overall complexity, it can benefit from higher performance and reliability.

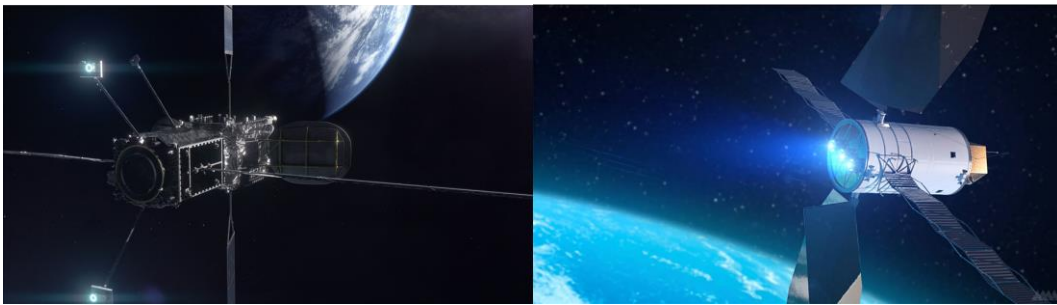


Figure 1: (Left) Artistic rendering of the Mission Extension Vehicle-2 (MEV-2) to the Intelsat 10-02 (IS-10-02) commercial communications satellite occurred in February 2020 (credits: Northrop Grumman). (Right) NASA's BIG Idea Challenge space tug concept (credits: NASA).

In addition to the technological-based criticalities, the mission applications previously mentioned further push the requirements impacting the design of the electric propulsion subsystems. Often, the main impacted aspect could be reconducted to (i) higher thrust levels, provided by more powerful systems, augmented operational reliability, and (ii) an extended operative lifetime, for sustain high total impulses, are required to fulfil the mission objectives. Alternative architectures could represent viable solutions to mitigate possible criticalities merging the two different requests previously highlighted. One example is the adoption of cluster configuration as an alternative to the typical monolithic architectures. The required performance could be reached and exceeded with lower power thrusters arranged in multiple propulsive strings simultaneously operated. Another aspect nowadays of particular interest is the adoption of alternative propellant instead of the commonly used xenon. Reducing the costs of procurement and management of the propellant is fundamental to cut the overall mission's costs,

particularly when high propellant demand missions are conceived, such as for reusable or long-range (and extended duration) scenarios.

Despite the possible criticalities highlighted at the subsystem level, the persisting struggle of the space community is the reduction of the dry mass of a spacecraft. Even for this market need, an innovative architecture solution, specifically introduced in the electric propulsion field, has been envisioned for a substantial decrease in spacecraft mass and power consumption. The so-called “Direct Drive” approach allows a direct interface of the thruster with the solar panels, which results in a higher power processing efficiency. This approach impacts more than one spacecraft onboard subsystems: (i) the EPS with the simplification of the component in charge of the power processing and control, (ii) the Electric Power Subsystem (EPS) due to the required operation at high voltage, and (iii) the Thermal Control Subsystem (TCS) due to the lower wasted power budget.

In this work, an extended analysis of on-orbit servicing scenarios is considered as one of the most interesting applications nowadays foreseen for adopting high power electric propulsion systems. To investigate all the architecture alternatives highlighting their impact at subsystem, spacecraft and mission level, a dedicated design and simulation environment, so-called “Multidisciplinary design Electric Tug tool” (MAGNETO), has been developed for these scenarios. This tool is conceived for targeting a consolidation of the TRL 5 (beta version), defined for software products, which is established after completing an end-to-end software elements implementation, verification of interfacing with other software/systems, and testing in a relevant environment.

Two main aspects drove the development of MAGNETO: the possibility of multi-inputs/outputs options and the modularity of the different subroutines.

The adopted user-friendly approach for managing the inputs parameters and the related output results was considered an essential property to handle multi simulations and analyses easily. Moreover, the segmentation of the software structure in independent subroutines allowed the tool's versatility to include additional design modules to extend the software functionalities further.

The different architecture alternatives are instead introduced with a proper setting of control flags. A set of excel input files interfaced with the software allows a straightforward definition of the mission and analysis parameters. The design modules introduced in MAGNETO can then process the input data and simulate the mission profile with a dedicated trajectory propagation module based on a low-thrust trajectory sub-optimal model. The data provided in output mainly concern both mission and spacecraft budgets that can be eventually processed by the last software module dedicated to the trade-off of different simulation outputs.

The flexibility of design and simulating mission scenarios based on electric propulsion technologies was further extended, considering an innovative electric propulsion system based on the air-breathing concept. So-called “ramEP”, this thruster technology opens a new range of mission scenarios below the traditional LEO altitudes. In a range between 180 km and 250 km, the Very Low Earth Orbit (VLEO) are nowadays an unexploited region mainly because of the high levels of

drag that a dedicated propulsion system shall continuously counteract to avoid a quick spacecraft's re-entry. Except for a few past missions, such as GOCE and SLATS, designed for relatively short mission lifetimes, the amount of propellant required for fulfilling extended mission operations strongly limits the design of the VLEO mission resulting in most of the cases in an unfeasible result. On the contrary, the ramEP concept offers the possibility to exploit the incoming flow as a propellant, avoiding all the fluidical components. The atmospheric residuals are collected through an intake and then processed by a double-stage thruster composed of ionization and an acceleration stage that generates thrust.

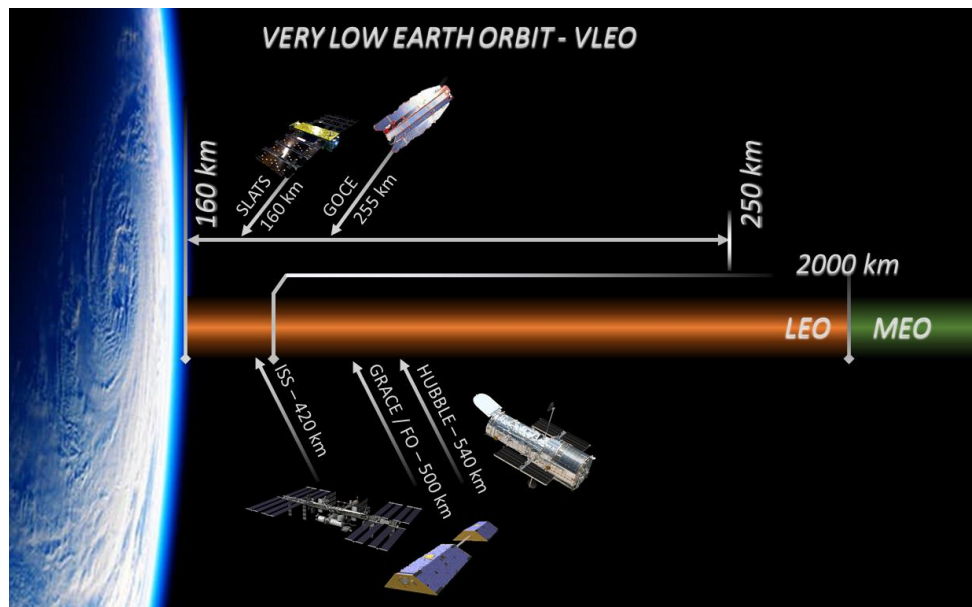


Figure 2: General overview of the past mission at very low altitudes with some reference mission as ISS, GRACE/FCO and Hubble.

An In-Orbit Demonstration mission (IoD) embarking ramEP thruster was conceived to demonstrate the feasibility of exploiting the VLEO region. However, the spacecraft design cannot follow the typical spacecraft design approach due to the peculiar operational environment. As a consequence, MAGNETO was modified with dedicated routines to guarantee the representativeness of the simulated environment and the consequence cross-effects on the critical onboard subsystems such as propulsion subsystem, electric power subsystem and structure. The main modification concerns introducing a multi-objective optimisation (MDO) process to derive the optimal spacecraft configuration, aiming to minimize the generated drag providing the required power and volume for both thruster and other onboard subsystems. Relying on the weighted method, the MDO was exploited for generating the Pareto front of the optimal solutions. A set of the possible optimal solutions was then selected accordingly to rationales introduced to represent the stakeholder needs. The operative altitude range was investigated to assess the altitude at which the designed spacecraft were able to fly, maintaining a thrust-over-drag ratio greater than one.

This preparatory phase was exploited to determine the minimum operability altitudes, for each selected configuration, given then in input to the trajectory propagation module, already developed for the space tug case study but updated with a complex thruster control law to chase the pre-selected optimal operative altitude.

Besides the technological development activities, the possibility of fully adopt such novel thruster and system concepts shall be supported by a series of side improvements included in the TX01.1.1 of the NASA Technological Taxonomy in terms of Health Management and Sensors. In the electric propulsion field, the monitoring of the subsystem health condition usually relies on the telemetries collected by the Power Processing Unit (PPU) processed by the ground control centre. However, with the onboard system's increased complexities, the adoption of improved Failure Detection Isolation and Recovery (FDIR) functions shall further stress to avoid possibly dangerous situations. The complexities in the definition of the FDIR functions are related to failure modes usually identified and opportunely mitigated during the design phase exploiting the standard Failure Mode and Effect Analysis (FMEA) and Failure Mode and Effect Criticality Analysis (FMECA) procedures. However, due to the lack of knowledge in the complete understanding of the failure that can occur, other methods could be considered. In particular, taking inspiration from methods already developed in the aeronautic field, the entire subsystem's operation can be monitored, and possible failure can be detected. The so-called Engine Health Monitoring Method based on the Gas Path Analysis is applied to Hall Thrusters in this work. The basic principle of these model is the derivation of the so-called "Influence Coefficient Matrix" (ICM) opportunely calibrated on a set nominal operative data of the thruster. This process consists of relating the deviations of a set of thruster parameters, considered measurable, with a second set of unmeasured parameters considered representative of the thruster's health status. The derived ICM is then inverted to obtain the "Failure Coefficient Matrix" (FCM) exploited to detect a possible failure.

This methodology has been applied in this work on the dataset collected during the development phase of the SITAEL's HT20k. Thanks to several test activities included in the framework of different development programmes, this 20-kW class was tested over its extended operative range allowing the collection of a large set of experimental data. Moreover, a failure that occurred to the test setup provided a unique opportunity to exploit the derived FCM on a real case to verify its capability to detect the failure.

The contents of this thesis are organised as follows. Chapter 2 is dedicated to the mission analysis performed on the space tug taken as a case study to develop a mission design and analysis tool called MAGNETO. The reference application considered for the design of the space tug is the OOS, for which two reference scenarios were derived. After a detailed introduction on the OOS scenarios possibilities, a complete mission analysis is presented to derive the necessary

mission and spacecraft requirement and constraints. Following this preparatory phase, the structure of MAGNETO is presented with the details on the implemented sizing mathematical models. Particular focus is given to the mathematical models introduced to investigate the alternative EPS architectures. The results of the two different performed simulations branches are presented at the end of the chapter.

The ramEP mission analysis and platform design are presented in Chapter 3.

A detailed mission analysis was performed for an IoD scenario introduced to investigate the feasibility of the innovative VLEO platform based on air-breathing propulsion. Though the inputs provided by the mission analysis and considering the critical aspects mainly concerned the environmental effects on the mission and spacecraft design, the main modification in MAGNETO (for the VLEO scenario called "VLEO-MAGNETO") were reported.

As a part of the tool modification, a central role is given to the MDO process. A complete overview of the objective definition and exploited design models is provided.

The presentation of the atmospheric model, the thruster performance model and the eclipse model are followed by the thruster control law because of fundamental importance to guarantee the altitude control capability along the trajectory through the operational cycle of the thruster itself. At the end of the chapter, the main MDO results are presented with the selection of three optimal configurations according to different selection rationale. Therefore, then results related to the altitude feasibility analysis and trajectory propagation analysis are presented to verify the identified solutions' operational feasibility even considering alternative spacecraft configurations.

The development of the Engine Health Monitoring (EHM) method applied to Hall thrusters is presented in Chapter 4. As previously mentioned, this work relies on a methodological approach exploited in the other fields of propulsion introduced in an extensive literature review. Then, the methodology applied to the Hall thruster is explained, introducing the theoretical process exploited to identify the involved parameters considered representative of the nominal thruster operation. This was performed through performance relations properly introduce and elaborated in the so-called ICM. The capability of the ICM of identifying possible faulty situation was presented at the end of the chapter after the overview of the test facility, diagnostics, and the general followed test plan.

Finally, in Chapter 7, conclusions, open problems and suggestions for further improvements about this thesis are discussed.

Chapter 2

CASE STUDY: the SPACE TUG

2.1 Space Tug concept & Mission Opportunities

The future of space utilization is rapidly changing, including new mission opportunities to satisfy the differentiation of the stakeholder needs growing in time. Due to a higher maturity level, the disruptiveness of new technology has renewed the interest in past concepts pushing toward their technical feasibility and economic sustainability. As anticipated, this is the case of the electric propulsion identified as an enabler for several mission concepts nowadays under particular interest. In this context, the development of a new approach to space operations is represented by the possible realization of a "space infrastructure" able to sustain On-Orbit Servicing (OOS) concepts. The term infrastructure is used in this case with a broader meaning embracing ground and space systems for an end-to-end approach to the provision of OOS capabilities. While the present infrastructures could be exploited with minor adaptations for ground systems, the space system shall be specifically designed with specific functionalities to cover the possible application scenarios. The design could be driven by single or multiple applications depending on the envisaged technical and economic feasibility. The space systems generally involved in OOS scenarios are commonly subdivided into (i) the space system which provides OOS capabilities, the so-called "servicer system/vehicle", and (ii) the space system object of service, called "serviced system".

These can embrace a wide range of applications [4] that could be subdivided in:

- Inspection of space objects: this function refers to the possibility of exploiting remote sensing for supporting the assessment in case of anomalies, health monitoring status or providing a contactless connection for ground communication. Any mate or docking capabilities are required by the servicer vehicle.
- Relocation of space system: in this application class, all possible scenarios where the orbit of the space objects is actively modified. The envisaged scenarios consist of relocating a satellite from an initial orbit to its final operative position, rescue operation of a space system subjected to a launch failure, transfers for disposal operation at End-of-Life (EoL) toward graveyard orbits as well as directly onto a re-entry trajectory. Besides the mentioned scenarios, another possibility considers the grasping and transferring of non-collaborative objects with the objective of decrease their decay time. This latter scenario is one of the

possible solutions to engage the critical issue represented by the increasing number of junk objects.

Furthermore, repositioning operation could be foreseen for modifications of constellation configuration. Additional functionality included in this category is the provision of attitude control capability to extend the operative lifetime once the satellite onboard propellant has run out. All the scenarios mentioned above are enabled by the capability given to the servicer vehicle to perform safe rendezvous and docking operation with the serviced object.

- **Restoration:** the general definition of the scenarios included in this functional class is returning the serviced space system to its previous nominal status. This embraces a set of operations such as refuelling, replacing or refurbishing failed components and movable mechanisms that failed during the early operation phase. The servicer vehicle shall be equipped with advanced tools developed to perform these operations on a serviced space system not specifically designed to sustain OOS.
- **Augmentation:** embrace all the operations where the serviced space system capabilities are increased. This includes mainly the change of both payload and bus components with upgraded versions. In this case, the serviced system shall be designed with a robust modular approach to enable this kind of operations.
- **Assemble:** considering the limited launch capability in term of payload mass launchable, space assembling could represent the only option for an extensive space system. In this case, the servicer system shall provide transport capability and, eventually, construction capabilities for specific assembly operations.

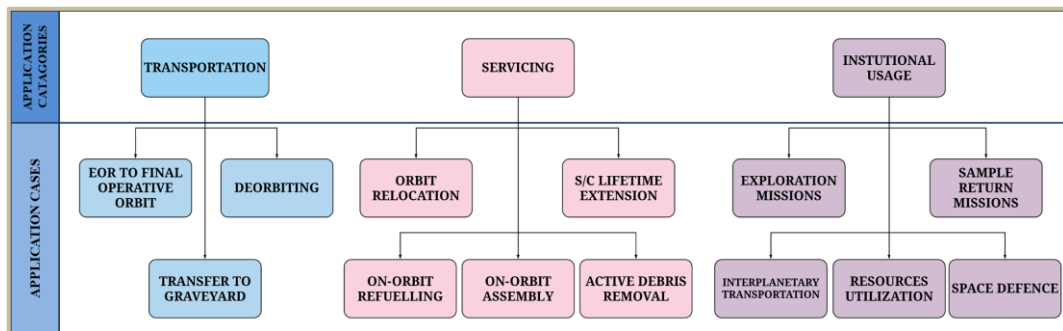


Figure 3: possible application range for the space tug concept.

A possible space system specifically designed to address these functionalities is the space tug. This reusable system can provide thrusting capability and eventually equipped with a specific payload to enable servicing operations.

The maturity of the involved technologies strongly limits the feasibility proven of the different application. In addition, the typical design process followed nowadays is typically based on both technologies and devices selected for a determined operative lifetime over which their operation might result too risky or expensive. In addition, the architecture itself of the satellites does not consider requirements or mission constraints specifically introduced to drive the design of the satellite itself toward reliable servicing operations.

Consequently, the analysis presented in the following sections was based on relocation scenarios considered feasible in the short term due to the low level of interaction between the service provider, hence the space tug, and the serviced satellite. The two selected scenarios are briefly described below:

Mission Scenario 1 (MS.1): in this scenario, the service provision consists of transferring a telecommunication satellite from its initial release orbit to its final operative location in GEO. The space tug will return in a parking orbit in the proximity of the release orbit of another commercial satellite to be served. During the waiting phase, all necessary maintenance and refuelling operation will be performed.

Mission Scenario 2 (MS.2): this scenario is an extension of the previous ones. After the first transfer phase transferring a telecommunication satellite, the space tug will approach the second satellite in the GEO location to perform a phasing manoeuvre aimed to relocate it to a new GEO position. With the conclusion of this phase, the space tug returns in LEO for the following transfer. Even in this scenario, maintenance and refuelling operations are foreseen in the waiting period in between two consecutive missions. This latter scenario was introduced to highlight the capability of the tug to perform a relocation manoeuvre with a heavy payload represented by the serviced satellite.

2.2 Mission definition

Considering the OOS space tug mission opportunities detailed in the previous section, the System Engineering (SE) design process (described in [5–7]) of a new space system starts with the definition of the *Mission Statement*. It represents a helpful statement in which goals and rationale for fulfilling the mission itself are defined together with the possible mission and programmatic constraints [5]. According to these characteristics, the mission statement shared for the OOS space tug mission scenarios is the following:

To exploit high-power electric propulsion to provide on-orbit servicing for telecommunication satellites released in LEO and to be operated in GEO or already operated in GEO.

From the mission statement, the primary mission objectives can be directly derived:

- I. To provide launch capabilities
- II. To perform in space operations enhancing servicing operation
- III. To provide ground support

In the standard approach to a mission definition, the primary objective hereabove identified might be reconducted to the main functions allocated to the segment level derived from the mission statement, which interests the "System of System" level. Therefore, exploiting the functional tree derivation procedure, the Segment

objectives are flowed down at the system level. The high-level functions are identified for the mission elements that cooperate to fulfil the mission goals. In Figure 4, the functional tree down to the system level is shown.

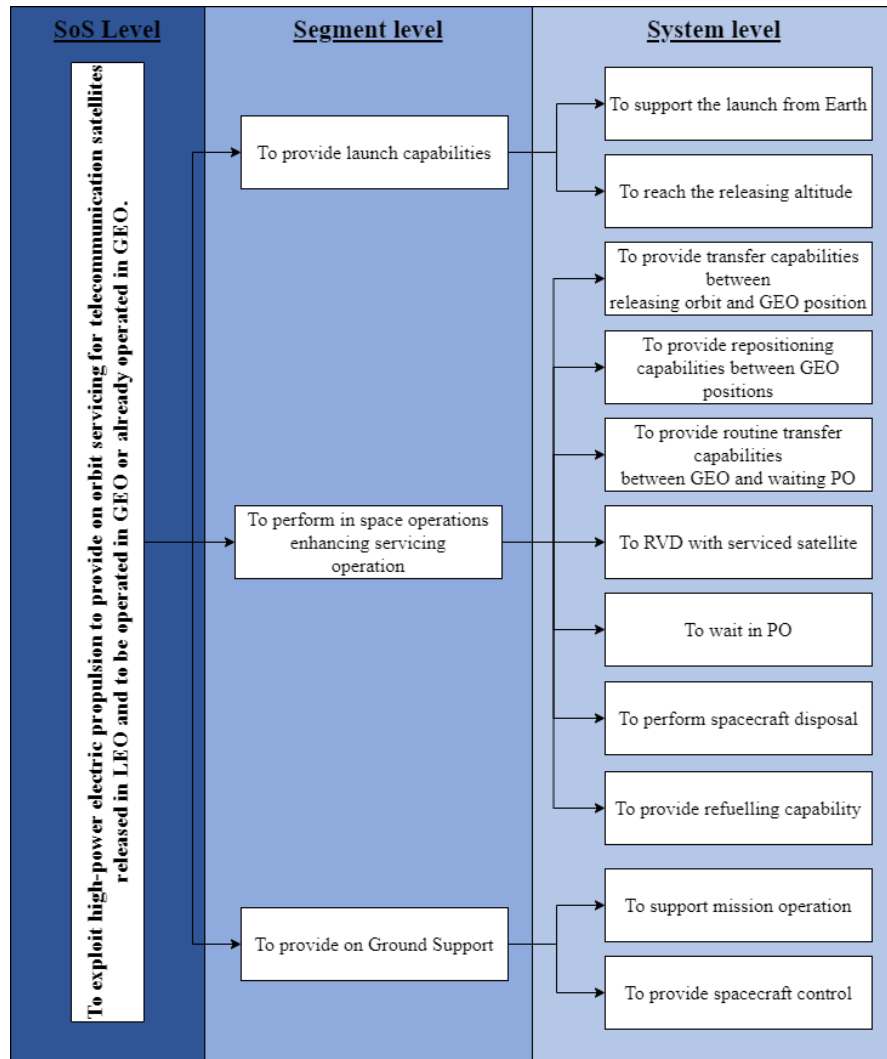


Figure 4: space tug for OOS Functional Tree.

Once the Functional Tree has been derived, a Function Product Matrix can be exploited to define which product could perform the requested functionalities. In this case, considering that the analysis here reported refers to Systems and Subsystems Level, it means that the Matrix (Figure 5) allows identifying the Subsystems of the Transportations System. Then, similarly to the Functional Tree, a Product Tree can be drafted (Figure 6).

One of the critical functions that shall be included in the definition of the reusability approach of the space tug is to ensure its refuelling. The Product Tree reported in

Figure 4 widens the scope to a higher level, revealing that a proper refuelling infrastructure shall be considered within the space segment.

		<i>Products@ Segment Level</i>		
		Launch Segment	Space Segment	Ground Segment
<i>Functions@ Segment Level</i>	To provide launch capabilities from Earth			
	To perform in space operations enhancing servicing operation			
	To provide on Ground Support			

Figure 5: Functions/Products matrix at Segment level.

			<i>Products@ System Level</i>					
			Launch Segment	Space Segment	Ground Segment			
<i>Functions @ System Level</i>	Fun@SysLevel		Launch Infrastructure	Launcher	Space tug	On-Orbit refuelling System	Mission Support Centre	Mission Control Centre
	1	To support the launch from Earth						
	2	To reach the releasing altitude in Earth proximity						
	3	To provide transfer capabilities between releasing orbit and GEO position						
	4	To provide repositioning capabilities between GEO positions						
	5	To provide routine transfer capabilities between GEO and waiting PO						
	6	To RVD with serviced satellite						
	7	To wait in PO						
	8	To perform spacecraft disposal						
	9	To provide refuelling capability						
	10	To provide spacecraft control						
	11	To provide spacecraft control						

Figure 6: Functions/products Matrix at System level.

The last step of the design process is to arrange the mission elements in each segment into a graphical representation in which the mutual relationships existing among them are highlighted. This can be done by exploiting the Interconnection Block Diagram (IBD), where the derivation of the existing interfaces is graphically enabled.

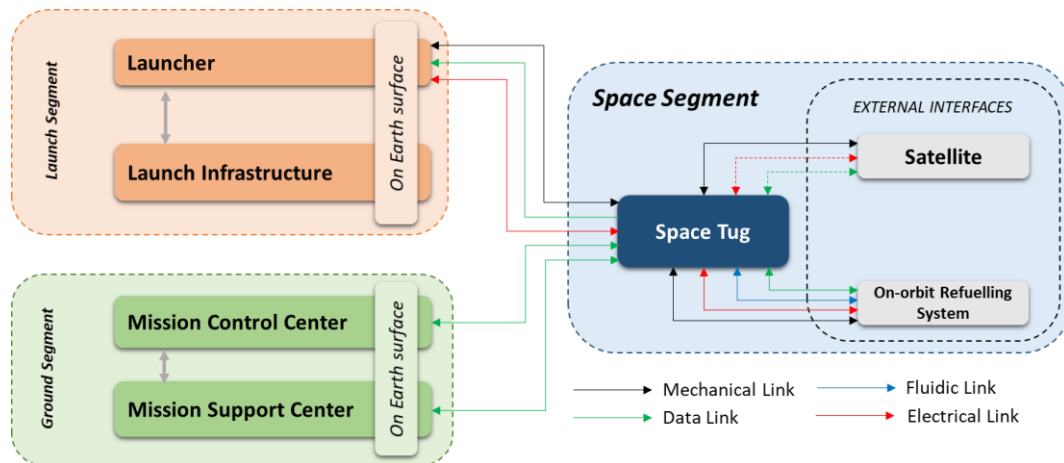


Figure 7: OOS space tug Interconnection Block Diagram at segment level.

Figure 7 shows the mission elements identified through the Functional analysis and the Functions/Product matrices for each mission segment. The space tug and the OORS, and the serviced satellite are instead included in the space segment for which an additional sub-segment has been introduced for the latter two mission elements. This approach allows focusing the analysis on the space tug while both the serviced spacecraft and the OORS are included as external interfaces for which specific requirement and constraints are introduced to drive the design of the tug itself. In the next section, the so-called "Mission architecture" is detailed, focusing on the functional definition of the space tug.

2.3 Space tug: mission architecture and spacecraft definition

- **Ground segment**

As shown in

Figure 7, the Ground Segment consists of two main facilities: Mission Control Centre (MCC) and Mission Support Centre (MSC). The MCC is in charge of receiving telemetry and housekeeping data, tracking and ranging operation, and transmitting commands to the tug. Moreover, it is in charge of the management of spacecraft operations. The interface with the end-user (i.e., satellite operators) is instead guaranteed by the MSC, which collects and elaborates the stakeholder needs providing processed information regarding the status of the overall mission and the serviced satellite.

In the ground segment, antennas and other remote facilities necessary to fulfil mission link requirements are also included.

- **Launch segment**

The launch segment consists of the launch vehicle and all necessary ground support facilities to support the final spacecraft integration, pre-launch operation and launch operations. The selection of the launch vehicle shall be driver by several evaluations. Despite the complex selection process, the first step is defining the payload mass available for each vehicle. The typical subdivision identifies four main launch classes (considering LEO and GTO-GEO release orbit):

- Small launch vehicles: with a payload capability <2000 kg
- Medium launch vehicles: with a payload capability from 2t up to 20t
- Heavy launch vehicles: with a payload capability from 20t up to 50t
- Super heavy launch vehicles: with a payload capability >50t

In space tug mission architecture, the launch segment regards the launch operation of the tug, excluding, therefore, the launch phase of the serviced satellite.

- **Space Segment: On-Orbit Refuelling System (OORS)**

As previously defined, one of the main characteristics of the space tug is its reusability for multiple missions. In addition to the specific feature to sustain long terms operation and overlong exposure to the space environment, the introduction of this mission property has a strong impact on the mission architecture. The space tug scenario is translated into the needs of performing multiple transfers either to move serviced satellites in GEO or relocate them on different GEO longitude slots. Despite the main advantages in term of propellant consumption due to the adoption of electric propulsion in the design of the space tug, the overall propellant budget to cover the space tug lifetime could lead to an unrealistic volume to be stored onboard the spacecraft. Consequently, the need for refuelling operations became a fundamental enabler for these types of space system performing such peculiar operations.

In order to fulfil this mission constraint, different strategies and mission architectures could be foreseen, including traditional and unusual mission elements. In the past several concepts have been proposed considering as drivers for the evaluation of both architectural and economic impacts [8,9,18,10–17] and the possibility to introduce new interfaces and production technologies such as the exploitation of ISRU capabilities [14,19].

On the one hand, a first possibility could be represented by a dedicated space system with large propellant storage capability launched to sustain the reusable system's operation or extend the launch capability. An example of the latter function has been recently developed by SpaceX, where a dedicated vehicle is used to refill the tanks of the main spacecraft called "Starship" before its injection on transfer trajectories toward the Moon and Mars [20] (see Figure 8).

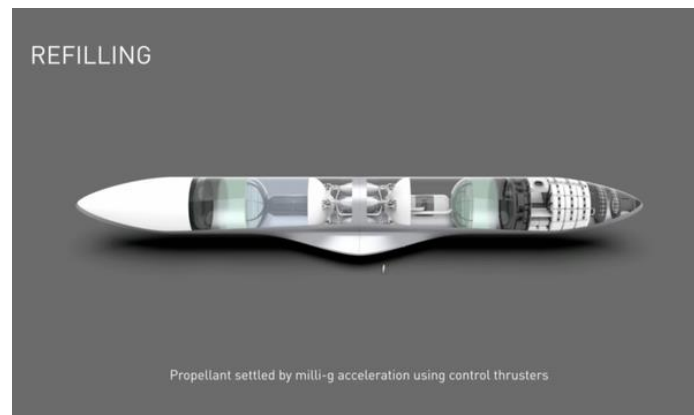


Figure 8: SpaceX’s refuelling concept for Starship operation (credits: SpaceX).

On the other hand, another possible architecture proposed for the scenario in which refuelling operations are foreseen is to rely on permanent orbital infrastructure. Comparable to a gas station, this infrastructure is capable of storing enough propellant for multiple visiting satellites. The U.S has published an extended analysis of the advantages of having refuelling facilities in LEO: Huma Space Flight Plans Committee supported by NASA in 2009 [21] and a NASA's report on the emerging space activities [22]. Both reports identified the capability to provide on-orbit refuelling as a cornerstone for extended mission operation in the Solar System, owing to the strong increase of the launchable payload rather than propellant.

It is important to highlight that most developed concepts have been designed to store chemical propellants, even in cryogenic conditions. For electric propulsion, xenon is usually exploited as a propellant. It is usually stored in supercritical conditions (186 bar between 20° and 50°C). Any criticalities have been identified for long-term storing of even a large propellant volume if the tank's thermal control can be guaranteed. Nevertheless, specific attention shall be given during refuelling operation in xenon of either the propellant depot or the visiting spacecraft. A specific temperature control solution might be necessary to dissipate the heat generated by this exothermal process. This impact also the duration of the refuelling operations.

According to Figure 7, the LEO On-Orbit Refuelling System (OORS) considered in the space tug mission architecture is considered an external interface. It is not further analysed in this work.

- **Space Segment: Serviced satellite**

Another fundamental element of the foreseen space tug mission architecture is the serviced satellite. As previously introduced, this mission element has been defined as an external interface. Consequently, a set of analyses have been performed to identify mission requirements and constraints impacted by the characteristics of the serviced satellite. In particular, in both scenarios introduced

as possible space tug application (MS1 and MS2), the fundamental information necessary for the analysis of the OOS operations are: (i) the mass of the serviced satellites and (ii) its location.

In order to generalize the analysis and enabling possible comparisons, the considered mass values of the serviced satellite mass have been derived with trend analysis. Relying on the UCS database [23], the complete list of satellites has been filtered, selecting the GEO orbiting satellites with respect to their launch date. As shown in Figure 9, three main trends might be identified (so-called "series" in the figure): (i) Light (<2500 kg), (ii) Medium (2500 kg \leq \cdot \leq 4500kg) and (iii) heavy (>5000 kg) series. These trends show how most of the GEO satellites is design with a target launch mass greater than 3 tons. After 2000, despite the larger number of satellites belonging to this mass range, a substantial increment of the number of small satellites occurred. This might be justified by the miniaturization of the electronic components and the introduction of new technologies, as well as the gradual implementation of software-based rather than hardware-based functionalities.

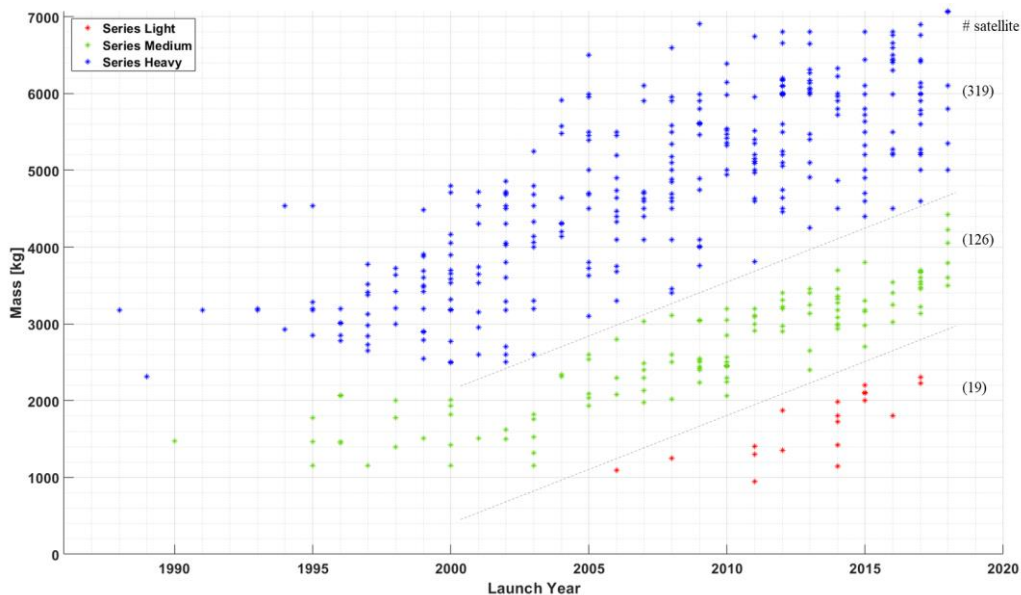


Figure 9: GEO satellite mass trend with respect to the year of launch.

Therefore, three mass values have been derived from this analysis: (i) very small GEO satellites with a mass equal to 1000kg, (ii) small GEO satellites with a mass equal to 3000kg and (iii) standard size GEO satellite, with a mass equal to 5000 kg. These three options have been considered representative of the main trends identified in

Figure 7.

Another fundamental characteristic of the GEO satellite is their longitude position in GEO which defines a certain surface coverage according to the payload performance. Exploiting the same rationale using for the derivation of the mass-

trends, the longitude of the satellites currently in operation has been derived, as shown in Figure 10.

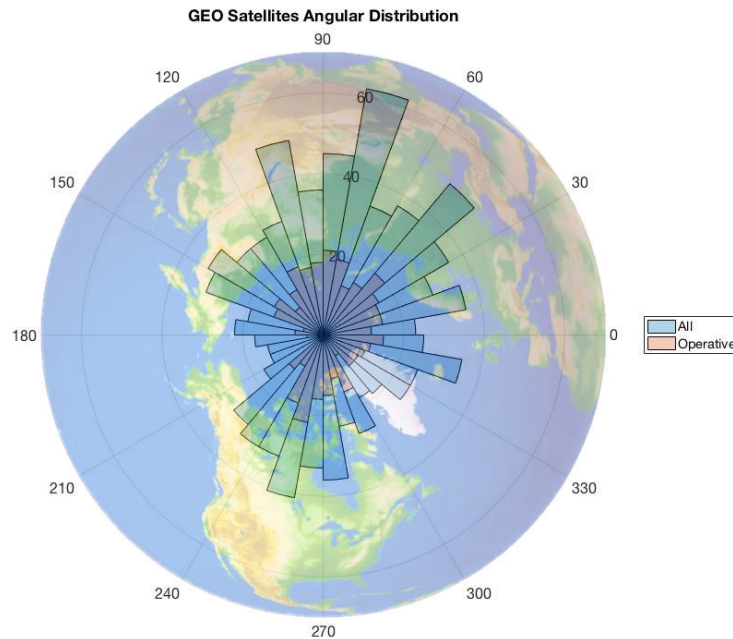


Figure 10: GEO satellite angular distribution.

The GEO region has been portioned with an angular step of 10° in order to highlight the angular region with a higher number of satellites. However, how shown in Figure 10, the distribution of the satellites results almost uniform with few peaks in particular over the Asian and American continent.

- **Space Segment: Space tug**

The space tug represents the main mission element. This transportation space system is designed for multiple operations, among which common functionalities are shared. After the deployment of the tug itself, it is designed to dock the serviced satellite performing a rendezvous manoeuvre and, after verification of the health status of both systems, move it into its target position where it will be released. Consequently, the design of the space tug shall be driven by critical functionalities that enabled the operations mentioned above. In particular, the possibility of interfacing the spacecraft with other mission elements and the capability of performing multiple transfer manoeuvres are the critical spacecraft design driver.

- *Interfaces with other mission elements:* the OOS operation required the capability of the system to establish different interfaces between the system itself and the serviced spacecraft. In addition, the same interfaces shall be guaranteed with the OORS during the refuelling operation. Specifically, the space tug shall provide mechanical, fluidical, electrical and data interfaces. The docking operations between the space tug and the client satellite can be classified as cooperative operation since both spacecraft has their own attitude control capability actively used during this phase. Hence, while specific interfaces or technologies shall be

foreseen for uncontrolled target, the space tug can rely on a solid development background of the mechanical interfaces already exploited for the ISS visiting spacecraft. In a cross-field attention to the standardization of the space technologies, also the current interfaces options have been revised by the international entities (e.g., NASA, ESA) with the final target of providing a single adaptable design solution. Despite this effort, in the next future, with the possibility offers by the OOS applications, the satellites themselves will be equipped with specific standard mechanisms.

While the mechanical interfaces are aspects not directly derived from the introduction of the OOS scenario, for what concern propellant, power, and data interfaces, a technological gap should be filled in the next future to guarantee safety and repeatable operations. A first successful attempt to pave the way toward the demonstration of refuelling tools, technologies and techniques was successfully performed by NASA in 2013, with the Robotic Refuelling Mission (RRM) exploiting the ISS as a test-bench [24,25]. Further development steps are foreseen in the next future, targeting a real mission in 2023 to restore the operation of Landsat-7 that will run out of fuel in 2021 [26].

- *Electric propulsion technologies:* another fundamental design driver for the space tug concept is the selection of suitable propulsion technology. According to the needs identified for space tug operations, the electric propulsion technology is selected to cover the mission's total impulse, split among the different mission phases. Hence the propulsion subsystem based on electric propulsion technology consists of the thruster, which the main function is to provide thrust and all other components necessary to store and regulate the propellant feeding and to guarantee an adequate electrical and telemetry interface with the other spacecraft subsystems. The Hall thruster (HT) represents the most advanced technology suitable for space tug operation among all the electric propulsion device options. In fact, considering the time constraints often associated with the OOS service for increasing the availability of the serviced satellite, these electric propulsion devices offer a higher thrust level with an adequate specific impulse value with respect to the other electric thrusters as the Gridded Ion Engine (GIE). Moreover, it guarantees a moderately extended lifetime, in particular considering the recent introduction of the magnetically shielded configuration and relatively high reliability.

As will be presented in the following section, the architecture of the electric propulsion subsystem will be investigated considering different design option introduced to optimize the system investigated at the mission and spacecraft level.

After the definition of the functionalities at the system level, the Same approach has been exploited to flow down the function at subsystem and component level. In Annex A, the mission analysis tools, already presented in the previous section, are used for the definition of the functionalities of the different subsystems composing the spacecraft.

2.4 Space tug OOS scenario

As a part of mission characterization activities, following the classical mission analysis methodology presented by different authors [5], a fundamental step is the assessment of the operation that the spacecraft will perform during its entire life-cycle in the fulfilment of the mission objectives. This is allowed by the derivation of the Concept of Operation (so-called "ConOps") analysis through which the operational profile of the space tug is described in terms of (i) mission phases: a set of subsequent phases are identified and classified according to the characteristic spacecraft operation, identifying starting/ending events for each phase, involved internal/external mission elements (along with the related interfaces) and the operative environment (ii) Modes of operation, representing the status of operation of the spacecraft in each phase for which pre-determined functionalities are enabled, (iii) foreseen traffic plan: a graphical representation of the mission phase organized in a mission timeline. In the following paragraphs, the ConOps of the space tug in the foreseen OOS scenarios is presented.

2.4.1 Mission phases

In this section, the space tug mission phases identified for both OOS scenarios are presented. Each mission phase is briefly described highlighting the main functionalities provided by the identified mission elements. Those mission elements classified as external interfaces (see Figure 7) are not further analysed, with the exception of the refuelling operation of the OORS to include the constraint imposed by the tug refuelling operation on its mission schedule. Finally, the mission phases are reported in a Design Reference Mission (DRM) for a graphical representation of the mission profile.

Considering the operative commonalities of the space tug for both mission scenarios, the mission phases are presented in two steps. Hereafter, the mission phases in common to both scenarios are reported.

MS1.1-MS2.1 Telecom satellite launch

All the operation necessary to launch and release the telecom satellite in a PO are performed.

MS1.2-MS2.2 Space tug RVD & docking to telecom satellite

The space tug starts the RVD manoeuvres to dock with the telecom satellite. This phase is characterized by an initial approach phase performed by the electric thrusters and close-range operations performed by chemical thrusters for avoiding possible collision risks.

MS1.3-MS2.3 EOR to GEO

After a check status of the health status of both spacecraft, the space tug starts to provide thrust to transfer the telecom satellite in GEO orbit.

MS1.4-MS2.4 GEO phasing

The space tug performs phasing manoeuvres to reach the target GEO longitude slot of the telecom satellite. This phase is considered optional if the transfer phase did not allow to directly reach the target GEO longitude position.

MS1.5-MS2.5 Telecom satellite release

The telecom satellite is released by the space tug unlocking the docking mechanism. Then, through the chemical thrusters, the space tug performs a separation manoeuvre to reach a safe position far enough to avoid any collision with the telecom satellite.

MS1.6-MS2.10 Space tug EOR down to LEO-PO

The space tug starts the return trip down to LEO-PO, exploiting the electric thrusters.

MS1.7-MS2.11 RVD approach to OORS

The space tug starts the RVD manoeuvres to dock with the OORS. This phase is characterized by an initial approach phase performed by the electric thrusters and close-range operations performed by chemical thrusters for avoiding possible collision risks.

MS1.8-MS2.12 Space tug refuelling operation

After the verification of the health status of the space tug, the refuelling operations may start through a dedicated fluidic interface.

MS1.9-MS2.13 Space tug waiting phase

In between two consecutive missions, the Space tug could wait docked to the OORS (if the OORS is designed to sustain its operations with the visiting space tug docked) or wait on a dedicated PO. In the case of the waiting phase of the space tug docked to the OORS, all possible maintenance operations could be considered. Otherwise, in case of waiting on a PO, the space tug will perform a departure manoeuvre, reaching a safety position after the conclusion of the refuelling operation.

Considering the additional mission objective included in MS2, the supplementary phases are the following:

MS2.6 Space Tug repositioning manoeuvre

After the release of the first serviced spacecraft, the Space tug moves from the first GEO target position (target position of the first serviced satellite) and relocate itself in a close region around the second GEO satellite to be serviced. Hence, the space tug performs a phasing manoeuvre within the necessary correction manoeuvres.

MS2.7 RVD approach & docking with serviced satellite

The space tug starts the RVD manoeuvres to dock with the second serviced. This phase is characterized by an initial approach phase performed by the electric thrusters and close-range operations performed by chemical thruster for avoiding possible collision risks until the full docking condition with the serviced satellite.

MS2.8 Serviced spacecraft repositioning manoeuvre

Exploiting the electric thrusters, the space tug will move the serviced satellite toward its second GEO position performing a phasing manoeuvre.

MS2.9 Serviced spacecraft release

The serviced spacecraft is release in its GEO target position. The chemical propulsion is used for performing the departure manoeuvre targeting a safety position far from the released satellite avoiding possible collision hazard.

Even though the OORS is considered an external interface, with respect to the definition of the mission element interactions, an additional mission phase is introduced to include its reloading operations. As previously specified, the OORS is foreseen as an orbiting space system with autonomous capability able to be docked by visiting spacecraft.

R* Propellant Reload System launch

In this phase, a dedicated system to reload the OORS is launch through a launch vehicle.

In Figure 11 and Figure 12, the DRMs of the two defined scenarios are shown. In both scenarios, the tug transfers the serviced satellite from an LEO up to its GEO final longitude slot. The departure LEO orbit shall coincide with the releasing orbit of the serviced satellite. This orbit is defined with respect to the used launch vehicles. The launch vehicle selection depends on the serviced satellite launch mass for which different launcher classes might be foreseen. Consequently, the release orbit could slightly vary. With different launch mass capabilities, even small launchers, such as VEGA and VEGA C, capable of reaching an equatorial orbit at 300 km of altitude. For example, the European VEGA launcher, currently providing commercial launch, is designed to launch a payload mass up to 2500kg in an

equatorial 200x1500 km orbit [27]. The upgraded VEGA version, designated VEGA C, is able to inject up to 3500 kg in a circular LEO of 600km [28]. Considering a heavy-lift vehicle such as the Ariane V, the payload weight deployable can reach a value up to 21t on a circular orbit between 200km and 400km with an inclination of 51.6° (ISS orbit) [29].

Taking into account the average lift capabilities of the operational launchers, the departure orbit, as well as the parking orbit (PO) in which the space tug could wait in between two consecutive transfers, is assumed at an altitude of 300km with $i=0^\circ$. The final target region for the servicing operation of the space tug is the geostationary orbit class with an altitude of 35786 km and an equatorial inclination. For what concern the repositioning manoeuvres based on consecutive phasing operations, the altitude reached by the tug can be higher and lower with respect to the GEO altitude. However, as will be further detailed, the scenario selected considers a variation of 100 km down w.r.t. GEO owing to the lower risk of collisions with other GEO objects.

Lastly, the tug waiting orbit coincides with the departure orbit, where also the OORS is located. An additional scenario, not included in this work, considers the OORS orbiting in a stable orbit 300km higher with respect to the tug PO.

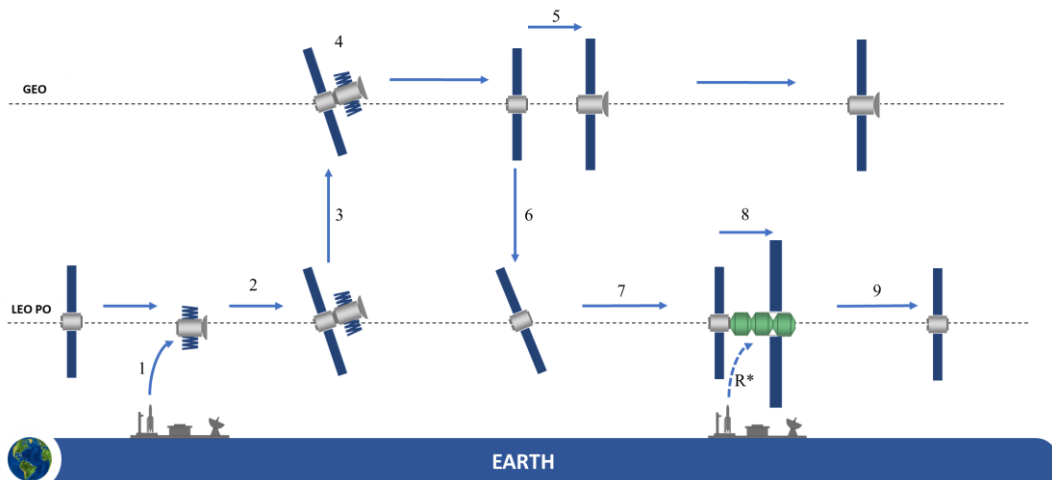


Figure 11: MS1 Design Reference Mission.

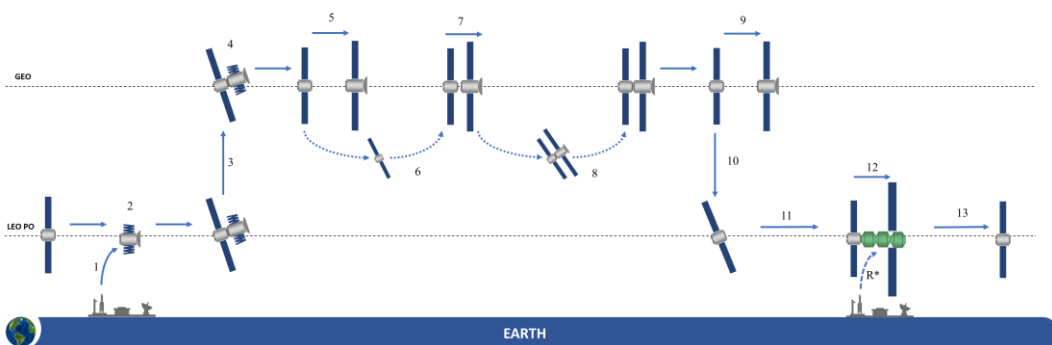


Figure 12: MS2 Design Reference Mission.

2.4.2 Modes of operation

Considering the two mission profiles introduced in the previous section, a set of modes of operation has been identified. According to the foreseen operations, the same set of modes can be taken into account for both scenarios (MS1 & MS2). As a matter of fact, the same operations as performed in a different operative environment with constraints compatible with the modes of operation hereafter presented.

Their general subdivision has been made according to the four main operational segments encountered through the lifetime of the space tug in the fulfilment of its mission requirements and constraints.

The different operational environment and the characteristic operations performed by the space tug were considered rational for the identification of the segments. As a consequence, they are: (I)AIT & ground operations, (II) Launch and early operations, (III) Space operation (Nominal phase) and (IV) End-of-Life (EoL) and Disposal phase. Despite the full characterization of the modes of operation, this work is focused on the main modes on which the space tug can be operated. In particular, the space tug active operations starting with the conclusion of the launch and Early operation phase, with the commissioning of the spacecraft, until the reception of the EoL/disposal command.

The five major modes (see Figure 14) of operation at the spacecraft level for the in-orbit phase are:

- **NOMINAL:** in which IDLE and the CHECK sub-modes could be triggered. These sub-modes are considered transient modes because they are triggered before switching to another mode.
 - when in IDLE, all the subsystems of the spacecraft are activated at minimum power, necessary to guarantee the survival of the spacecraft itself, and they are ready to go to another mode. This mode is typically triggered during the waiting phases.
 - when in CHECK mode, all the watchdog and housekeeping functions are performed to check the health status of either one single subsystem or the entire spacecraft. This sub-mode is usually triggered before and after the transfer phase, at least on critical subsystems such as the electric propulsion subsystem. Moreover, it could be occasionally triggered in case of the danger of a specific component.
- **EP MANOEUVRE:** this mode is triggered when the EPS subsystem is fully operated. In this operating mode, not only EPS is activated but also all the subsystems necessary to perform the electric transfers are operated to guarantee the housekeeping and communication functions.
- **CP MANOEUVRE:** this mode is triggered during the proximity operations (such as RDV, docking and undocking phase). This mode could be occasionally activated also during the EOR phases for attitude control purposes. In the CP

MANOEUVRE, the necessary subsystems to fire the chemical thrusters are activated as well as to guarantee the safe operation and the survival of the spacecraft.

- **STAND_BY**: only the essential subsystems (EPS, COMM, TCS, C&DH) are activated in order to ensure the survival of the spacecraft.
- **SAFE**: this mode is invoked after failure detection. With its switching, all the operations of the spacecraft are suspended. In particular, the SAFE MODE implies the safe mode for the AOCS as the first action, ensuring the electric power generation. After that, the SAFE MODE allows performing all Failure Detection Identification and Recovery (FDIR) actions.

Moreover, the transition between modes have been investigated, and the results are graphically summarized in Figure 13.

		Spacecraft Modes of Operations (in-orbit)			
		Safe	Stand-By	Nominal EP mode	Nominal CP mode
Mission Phases	Ground				
	LEOP				
	MS1.2-MS2.2 Space tug RVD & docking to telecom satellite				
	MS1.3-MS2.3 EOR to GEO				
	MS1.4-MS2.4 GEO phasing				
	MS1.5-MS2.5 Telecom satellite release				
	MS1.6-MS2.10 Space tug EOR down to LEO PO				
	MS1.7-MS2.11 RVD approach to refuelling system				
	MS1.8-MS2.12 Space tug refuelling operation				
	MS1.9-MS2.13 Space tug waiting phase in LEO PO				
	MS2.6 Space Tug repositioning manoeuvre				
	MS2.7 RVD approach & docking with serviced satellite				
	MS2.8 Serviced spacecraft repositioning manoeuvre				
	MS2.9 Serviced spacecraft release				
	TS disposal				

Figure 13: activation of the modes of operation with respect to the foreseen operation in both scenarios. The coloured boxes refer to the modes of operation that can be triggered during the related mission phase. The dashed boxes highlight the modes of operation that could be eventually triggered in case of necessity.

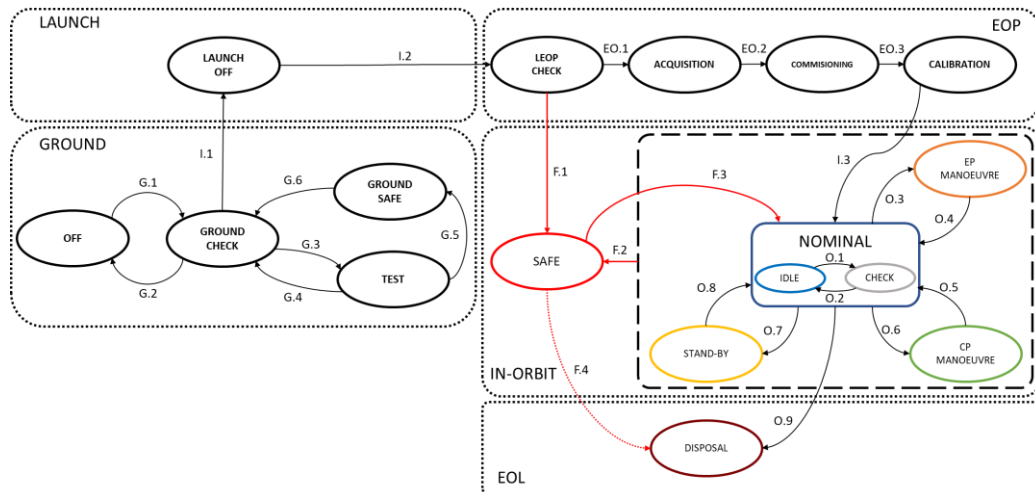


Figure 14: Space tug modes of operation.

The Mode Diagram is reported in Figure 14. In this diagram, the nominal mode transitions (black arrows) and safe mode transitions (red arrows) are shown. It is important to specify that from all the modes contained in the inner dashed box direct switch to the SAFE mode is possible. The transition modes are subdivided into two main categories: In-Orbit (labelled with O) and Safe (labelled with F). For each transition, the triggering event has been identified accordingly with the current mode compared to the related mission phase.

Table 1 summarizes the trigger events for each mode of transitions. Five different categories of transitions have been identified:

- Ground Commanded (GC): the mode of transition is triggered after the reception of a specific command from the MCC.
- Automatic Commanded (AC): the mode of transition is triggered after the reception of a specific command from an automatic decision process.
- Time-Triggered (TT): the mode of transition is triggered after the reception of a specific command from a process in which a certain time value is considered.
- Station Command (SC): this category is similar to the GC ones. However, the authority for the command transmission is now delegated to a control centre on a station. This is particularly important for the mission far from the Earth, in which a high delay period for the transmission is not always acceptable.
- Failure Detection (FD): this category includes all the mode of transitions to the SAFE mode from all the other modes.

Following the categories defined above, the eight different modes of transition have been identified. In particular, the O.1 transitions between IDLE and CHECK mode is usually automatically commanded. However, if expressly requested by the ground control, the automatic command can be overridden with a specific command transmission. The return transition from the CHECK to IDLE mode is automatically commanded, and it happens after the transmission of the telemetries collected to the ground. The EP MANOEUVRE mode ensures the possibility to perform the EOR manoeuvres. The transition to this mode is identified with the O.3 transition, which takes place only after the reception of the specific command from ground control.

Once the space tug reaches the target orbit, the O.4 transition allows the return to the NOMINAL mode. However, if necessary, the automatically commanded transition can be overridden with a command transmitted from the ground. The same logic is adopted for the manoeuvres performed utilizing chemical propulsion. In this case, the CP MANOEUVRE shall be triggered. The O.6 is the transition to switch on this mode, while the O.5 ensures the return to the NOMINAL mode. In details, the switching to CP MANOEUVRE for the proximity operations, such as RDV and docking, is commanded by a ground transmission. All the others possible transitions can occur either automatically commanded, such as the nominal operations of the AOCS, or ground commanded. The last mode of transitions for the in-space operations is those related to the STAND-BY mode. The switching on this mode is ensured by O.7 transition commanded by either a target orbit command reception or a ground command received. The O.8 transition occurs after the reception of a specific command from the ground.

The set of the modes of transition analysed is related to the SAFE mode. The F.2 transition connects all the modes of the in-orbit phase with the safe mode. This transition is usually automatically commanded. However, the ground control can override the automatic switching and set the SAFE mode for the system through the transmission of a specific command. The return to NOMINAL mode is then ensured by the F.2 transition, which can be commanded only from the ground control.

Table 1: Modes of transition.

MODES of TRANSITION							
	ID	DESCRIPTION	GC	AC	TT	SC	FD
IN-ORBIT	O.1	Check command received / O.3, O.6, O.7 mode of transitions triggered	X	X			
	O.2	Telemetry transmitted		X			
	O.3	EP manoeuvre command received	X				
	O.4	Target orbit reached / EP manoeuvre end command received	X	X			
	O.5	The final position reached / Final attitude reached / CP manoeuvre command received	X	X			
	O.6	CP manoeuvre command received	X			X	
	O.7	Target orbit reached / Stand-by command received	X	X			
	O.8	Nominal operation command received	X				
IN-ORBIT SAFE	F.1	Fault detected	X				X
	F.3	Restart nominal operation command received	X				

The operative modes are then specified in terms of electrical power supplied to the most consuming S/C systems, including all potential situations.

Considering the possible operation of the different onboard subsystems, four different states were identified depending on the power consumption allowed:

- On – operating.
- Off – excluded from power distribution.
- DC – discontinuous operating, where DC means Duty Cycle.
- (DC) – potential discontinuous operating.

The following Table 2 summarises the various power combinations for each operative mode.

Table 2: subsystem status for the different modes of operation.

	[EPS]	[PROP]	[TCS]	[AOCS]	[COMM]	[C&DH]
EP MANOEUVRE	On	On	On	On	(DC)	On
SAFE	On	Off	(DC)	(DC)	DC	On
CP MANOEUVRE	On	Off	On	On	(DC)	On
STAND-BY	On	Off	On	Off	DC	On
CHECK	DC	DC	DC	DC	DC	DC
IDLE	On	(DC)	On	On	DC	On

The further analysis of the operational modes, a percentage value will be defined in order to determine the power consumption for each subsystem of the space tug.

2.4.3 OOS traffic plan

Another fundamental step in the definition of the space tug ConOps is the derivation of the possible mission traffic plan, the so-called "Mission timeline". It defines the temporal sequence of the mission phases specifying each phase's duration by identifying their starting and ending dates and possible time constraints dictated by contingency operations with their related duration.

Considering the spacecraft operations mentioned above performed by the space tug in both the introduced mission scenario, the most impacting phases in the time demanding are represented by the EOR up to the GEO, the EOR down to the PO and the phasing manoeuvre associated with the relocation of the serviced satellite between two GEO slots. The duration of these phases is certainly impacted by the departing and arrival locations but also by the performance provided by the selected architecture of the propulsion subsystem. Consequently, the approach followed in this work was based on maintained unconstrained the duration of these phases for a full investigation of the capabilities obtainable by the different system architectures introduced. This approach is also supported by the incapability to define mission durations for intercepting the profitable market demand. Examples of market forecast uncertainties can be found looking on the variability of the telecom GEO market considered as a reference for the space tug scenario.

Despite the limitation introduced by the followed approach, in Figure 15 and Figure 16, the mission timeline of MS.1 and MS.2 are presented. The duration of the following phases has been defined considering:

- Telecom satellite launch: this phase is considered the T0 of the space tug scenario. At T+1, after one day, the early commissioning of the critical system onboard the serviced satellite is performed.
- RVD & docking of the space tug with the serviced satellite: this phase begins with the close-range manoeuvre up to the complete docking with the service satellite. The duration of this phase cannot be longer than one day. Contingency operations are included in the maximum duration of this phase.
- Serviced satellite releasing: the release of the serviced satellite and the subsequent space tug separation shall not exceed the maximum duration of 12 h. This maximum phase duration includes possible contingency manoeuvre.
- Refuelling and maintenance operation at OORS: during this phase, the space tug is docked at the OORS. After the confirmation of the stable connection of the interfaces between the tug and the OORS, a safety check is performed to authorize the initiation of the propellant transfer. A xenon tank is usually loaded with a low xenon flow rate in order to respect thermal constraints [30]. As a consequence, the overall refuelling operation is foreseen to be concluded in a maximum period of one week.
- Waiting phase: as previously specified, the space tug can either wait for the launch of the satellite to be served docked at the OORS or in a dedicated PO. The first option is chosen if a maintenance operation would be performed. Any specific time constraints have been assumed since the waiting phase depends on the serviced satellites launch schedule.

The mission timeline of MS.1 is presented in Figure 15, while Figure 16 shows the MS.2 timeline.

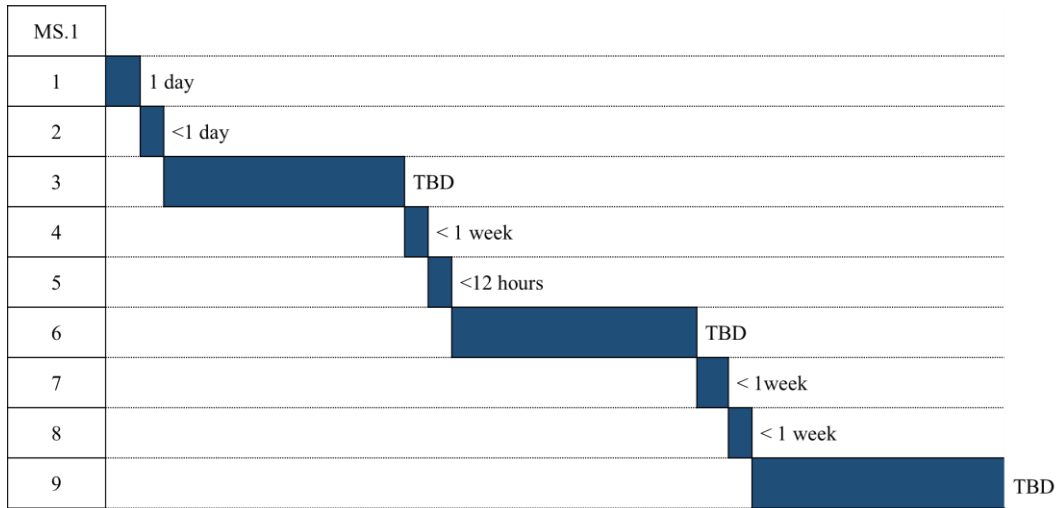


Figure 15: MS1 operational timeline- The TBD phase durations are related to the low thrust transfer (phase 3 and 6) and waiting phase (phase 9)

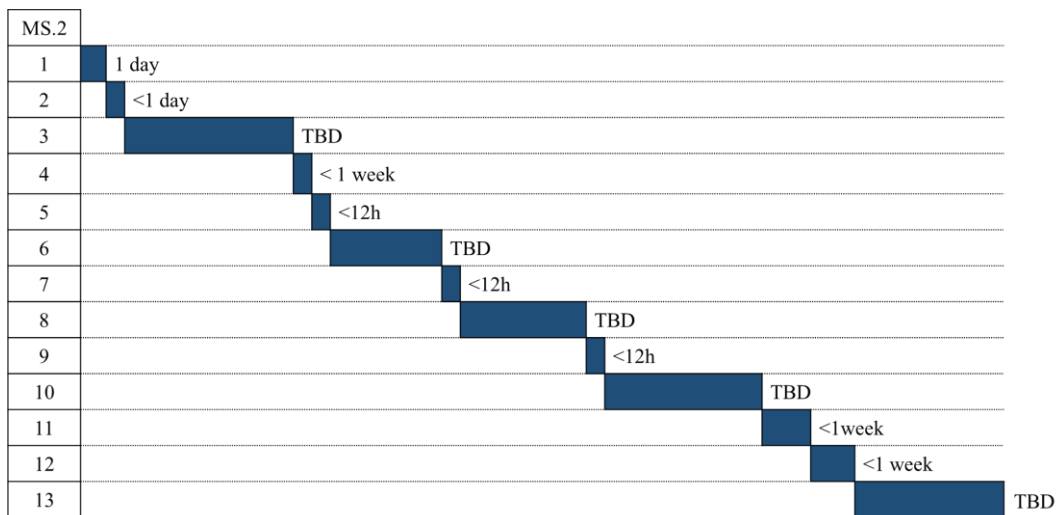


Figure 16: MS2 operational timeline. The TBD phase durations are related to the low thrust transfer (phase 3, 6, 8 and 10) and waiting phase (phase 13).

2.5 MAGNETO – Multidisciplinary design Electric Tug Tool

Exploiting the functional, physical and operational definition of the space tug, all the information necessary to proceed with the sizing process are provided.

The main objective of this phase is the derivation of the spacecraft and mission budgets, particularly important for the evaluation of the different design solution during the preliminary mission analysis phase.

This latter phase requires the interaction of different disciplines in an iterative process usually aimed to minimize the spacecraft mass while maximizing the mission utility in fulfilling its objectives.

As previously mentioned, the main design driver of the space tug is represented by the adoption of electric propulsion for providing transfer capability, essential for performing OOS operations. In addition to the complex design interactions among the spacecraft subsystems for their sizing, the objective of this study consists of the understanding of the possible impacts that the introduction of different architectures of the propulsion subsystem based on electric propulsion devices in the different scenario introduced.

Under those circumstances, the developed software-based tool called MAGNETO provides a flexible environment where the user can easily change the mission parameters related to both mission operations and spacecraft design and compare the obtained results. The MATLAB environment used for the development of the tool allows a higher level of flexibility, enabling the software's interaction with other parallel tool commonly used during the mission analysis. Different file formats are supported by the tool for the input uploading and, after the simulation, for storing the selected output. Another fundamental characteristic of the tool, intrinsically introduced in the pursuit of its development objectives, is the modular approach followed for the coding of the routines that facilitate future improvements with additional software functionalities.

The main structure of the software is organized in three main blocks following the key mission analysis step: (i) in the scenario definition block, all the information coming from the previous steps (i.e. functional analysis and ConOps) are introduced in the software, (ii) scenario analysis block, based on design modules where the space tug is preliminary sized, (iii) scenario optimization block, where the space tug design is optimized exploiting detailed design module and a trajectory propagation module for the minimization of the overall spacecraft mass and (iv) a dedicated module consisting in post-processing of the tool outputs for the evaluation of the final results.

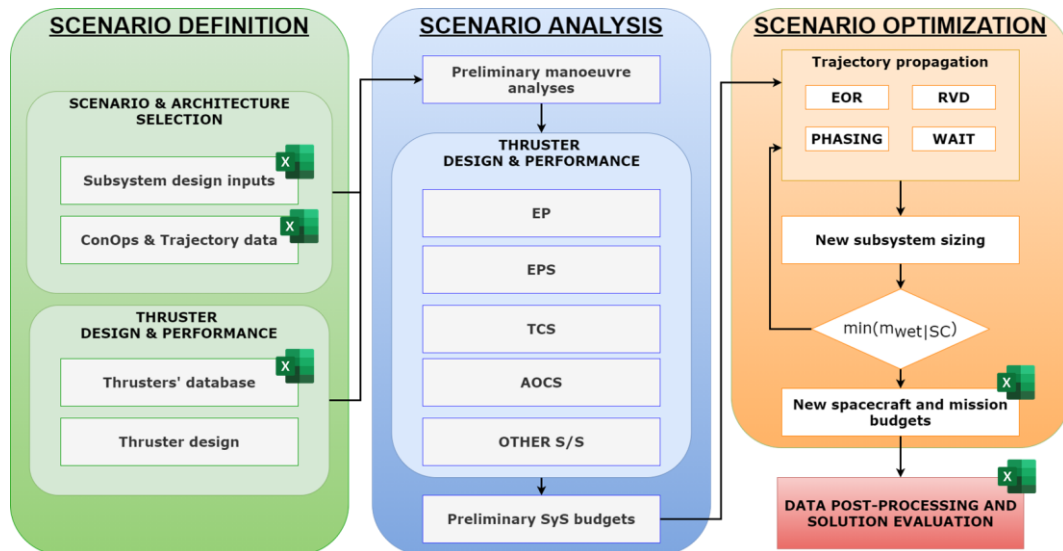


Figure 17: functional structure of MAGNETO.

The current development activities on MAGNETO target the consolidation of the guidelines defined for TRL5 (beta version) define for the software development status according to ECSS standard [31] and the NASA standard [32]. The main related activities concern the production of the full software documentation and quality standards in which both test case and examples are reported. The bunch of tasks derived from this objective are partially performed in the framework of a GSTP project funded by ESA aimed to push the development of the HT20k designed by SITAEL. Politecnico di Torino is in charge of the mission and system analysis work packages where MAGNETO is currently exploited for investigation possible future scenario enabled by high power electric propulsion.

The following paragraphs report the explanation of the main routines introduced in MAGNETO. In particular, the focus is given to the design of the electric propulsion subsystem and its possible architectural alternatives. In addition, a complete description of the trajectory propagator exploited to provide a suboptimal solution for the low-thrust trajectory, forced by the adoption of the electric propulsion, is reported.

2.5.1 Scenario definition: the input module

As previously mentioned, the development of MAGNETO was strongly driven by a modular approach to the single routine of the software. This aspect was also implemented in the input module, called “Scenario definition”. This software segment represents the user interface through which the functional, design and ConOps inputs, defined exploiting the classical mission analysis tools, are introduced in the software. The overall initialization procedure consists of two phases. The first step is based on an offline setting of the design and operational inputs based on structured Excel spreadsheets where main parameters concerning spacecraft architecture and design, mission phases and manoeuvres and trajectory propagation setting can be modified and set.

- **Mission scenario ConOps**

This spreadsheet is organized to introduce all the necessary parameters which characterized a specific phase of a mission. Besides the general scenario information, such as mission scenario denomination, starting date and number of phases, the main part of the table consists of a double input column where the initial and final orbital parameters are defined. In addition, for each phase, a single cell of the table is dedicated to (i) define the typology of manoeuvre to perform (see Section 2.5.4), (ii) the duration of the phase (if necessary), (iii) either phasing altitude variation or phasing longitude (if the phasing manoeuvre is required), (iv) a flag for the identification of the phases in which the mass of the serviced satellite shall be taken into account and (iv) the additional mass of xenon loaded during the refuelling operation and the related phase number in which it is performed.

The online setup up phase allows the selection of a specific mission scenario ConOps spreadsheet. Hence, it can be defined for a set of simulations.

- **Constant and safety margin**

A dedicated spreadsheet is introduced for the definition of the constant and safety margins. Throughout the design phase of a space mission, the implementation of a margin philosophy on the budgeting activities allows the accommodation of uncertainties and changes [5]. Therefore, considering the preliminary mission design phase targeted for MAGNETO development, the possibility of introducing margins on power, mass and delta-V budget was implemented according to the guidelines detailed in [33] and [34].

In particular, the following percentage has been considered:

Table 3: safety margin on S/C budgets.

Budget	Percentage
Margin on mass budgets	20%
Margin on power budget contributions	10%
Margin on propellant budgets (electric & chemical propellants)	15%

The safety margin can be modified through the input spreadsheet to perform prevision on final budget values.

- **Thruster operative points database**

According to the peculiarities of the space tug mission, a dedicated database was created to collect all performance and design characteristics of high-power thrusters selected with respect to lower powerful thrusters. The performed literature review focused on the available data related to the thruster characterization campaigns considering the parameters reported in Table 4.

If not present in the tabulated form, the values were highlighted over the graphical performance envelope. Since few thrusters were also tested with alternative propellant, the related test data were also collected in the database.

Table 4: thruster parameters collected in the database.

PARAMETERS	U.M.	SYMBOLS
Discharge Voltage	[V]	V_d
Discharge Current	[A]	I_d
Anode Mass Low Rate	[mg/s]	\dot{m}_a
Cathode Mass Flow Rate	[mg/s]	\dot{m}_c
Cathode Reference Potential (*)	[V]	V_{CRP}
Thrust	[mN]	T
Anodic Specific Impulse (*)	[s]	$I_{sp a}$
Total Specific Impulse	[s]	$I_{sp tot}$
Anodic Efficiency (*)	[-]	η_a
Total Efficiency (*)	[-]	η_t
Discharge Power	[W]	P_d
Total Power	[W]	P_{TOT}
(*) if reported in the published papers		

Both prototype and already qualified thrusters were considered, which includes: (i) SITAEL HT5k, (ii) SITAEL HT20k, (iii) Safran PPS1350, (iv) Safran PPS5000, (v) Busek BHT-8000, (vi) Busek BHT-20K, (vii) NASA H6, (viii) NASA T220, (ix) NASA 400M, (x) NASA 457M, (xi) Aerojet XR-12 (AEPS) (xii) Fakel SPT140, (xiii) Fakel SPT200, (xiv) Fakel SPT290, (xv) TsNIIMASH TM50, (xvi) TsNIIMASH D200.

Particular focus was given to the SITAEL's thrusters for which the entire performance envelopes were available through the collaborations in the framework of the GTSP HT20k project and thanks to the contributions in the context of the H2020 Consortium for Hall Effect Orbital Propulsion System (CHEOPS).

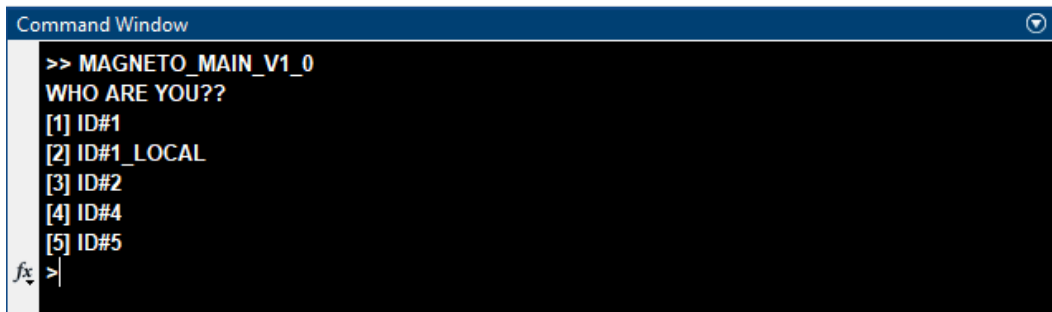
Other design features of the considered thrusters will be presented in Section 2.5.2.1.

Propagation setup parameters

The last group of settings to be defined before the initialization of the software are related to trajectory propagation. In particular, it is possible to set which kind of orbital disturbances considered among (i) Gravitation J2, (ii) Third body perturbation, (iii) solar pressure, (iv) drag. Additional details will be given in Section 3.6.1.2.

The eclipse condition is introduced during the trajectory propagation through a dedicated flag that shall be set to one. In this case, a short propagation step is advisable to intercept the light/shadow boundary effectively.

The second setting phase is performed when the software is initialized. Bullet menus are directly shown on the MATLAB command window enabling the user to select the subsequent options. An example of this phase is shown in Figure 18, where the selection of the correct folder link is required by the user for proper uploading of the input files.



```
Command Window
>> MAGNETO_MAIN_V1_0
WHO ARE YOU??
[1] ID#1
[2] ID#1_LOCAL
[3] ID#2
[4] ID#4
[5] ID#5
>
```

Figure 18: MATLAB user interface, user folder selection.

Other selections proposed to the user concern: (i) reference scenario, (ii) reference thruster among those previously listed, (iii) specific thruster performance requirements, in terms of (thrust specific impulse and discharge volta and (iv) propulsion subsystem architecture (see Section 2.5.2.1).

2.5.2 Scenario analysis: design module of the Space Tug

The following section briefly describes the main design routines introduced in MAGNETO, focusing on the main design parameters considered.

2.5.2.1 Electric propulsion subsystem design module

The propulsion subsystem represents one of the fundamental subsystems of the space tug through which most of the foreseen manoeuvres are performed. As previously mentioned, for a subsystem based on Hall devices, a series of components shall be included to operate the thruster properly. These are commonly divided into fluidical and power/control components. Hereafter, a brief description of the components included in the EPS of the space tug is provided with the related sizing models:

Tank assembly

The tanks are used to store propellant in the proper storage condition. If the selected propellant is xenon, it is usually maintained at the supercritical state to ensure a reasonable tankage fraction, defined as the ratio between the propellant and tank mass and a high storage density. The supercritical condition is reached with a temperature greater than 289.75 K and a density of 1.155 g/cm³, according to NIST [35,36]. The transition of the xenon from the supercritical condition to the liquid state shall be avoided. If this transition occurred, the operation of the downstream fluidical components could be jeopardized or degraded, such as the pressure and temperature sensors adopted for monitoring the conditions of the tanks. Consequently, at 186 bars of pressure, usually selected as Maximum allowable operating pressure (MEOP), the temperature range shall always be in a range of 27°C and 50°C for all mission phases.

The developed subroutine allows to size the tank, following the procedure presented in [37], or to select it in a database where the main feature of large tanks (>100l) able to store xenon are collected. The tank assembly is isolated from the downstream fluidic branches through two parallel pyrotechnic valves during the ground and launch phases. One valve is then fired during the LEOP operation of the tug, enabling the downstream propellant flow.

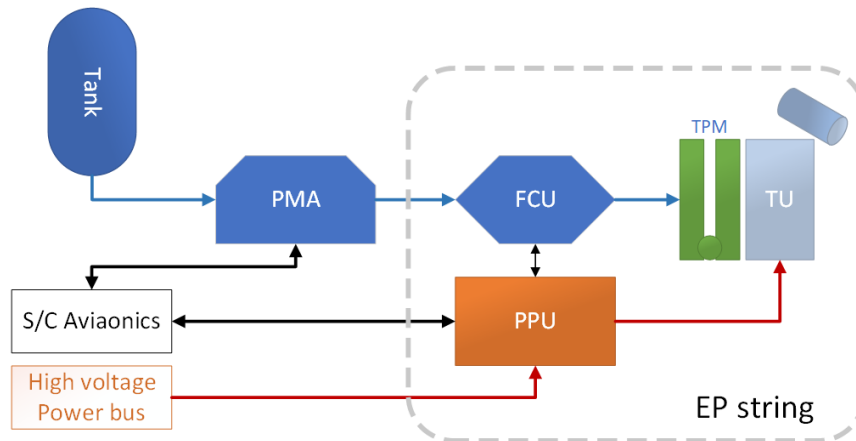


Figure 19: simplified scheme of a monolithic propulsion subsystem based on Hall thruster technology.

Propellant Management Assembly (PMA)

From the high-pressure storage condition, the pressure of the propellant shall be regulated to meet the inlet requirement of the thrusters. This functionality is usually guaranteed by a pressure regulator that can operate in a mechanical single or double stage or through an electronic regulation based on the bang-bang concept, as that exploited on SMART-1 [38].

The general architecture is usually based on an operative branch where the regulator is upstream and downstream isolated through a latch valve and one redundant branch.

The sizing routine introduced for the sizing of the PMA components has an internal check to verify if the mass flow required downstream by the thruster meets the performance of the pressure regulator. If the requirement is not fulfilled, an additional operative branch is added.

During the regulation action of the pressure regulator (both mechanical and electronic typology), the Joule-Thompson effect shall be counteracted, avoiding the reduction of the propellant temperature below the supercritical region. Therefore, heaters placed directly on the component are considered with their related consumption.

Even in this case, the developed subroutine relies on a dedicated database or on a custom sizing model in which the mass of the PMA components is estimated considering the propellant flow rate required [39] (see Table 7)

Flow Control Unit (FCU)

The FCU is usually based on a single subassembly in charge to regulate the propellant flow rate fed to the thruster at the proper thruster inlet condition. The assembly can be based on either a Proportional Flow Control Valve (PFCV) or a Thermo-throttle valve (TTV). With different control logic implemented in the PPU, both valves are suitable for regulating the propellant flow rate. The developed subroutine relies on a dedicated database or on a custom sizing model in which the mass of the FCU is estimated considering the propellant flow rate required [39] (see Table 7)

Power Processing Unit (PPU)

The PPU is an electronic unit that provides the control and power conditioning for the thruster and the FCU elements. In particular, it supplies the electrical power to the TU elements (Anode, Magnets and Cathode), providing isolation in between the input power bus and the TU. A dedicated module is introduced in the PPU architecture to feed the FCU elements (valves, heaters, and sensors). The control authority is held on the two components mentioned above by the control module, which is designed to operate the PPU according to the operative mode command received from the spacecraft OBC. All the telemetries are collected, managed for enabling the thruster control loop and eventually forwarded to the OBC of the spacecraft. The PPU is also in charge to detect possible failures and trigger the safe mode at the spacecraft level if necessary. For its preliminary design, the dedicated subroutine relies on an empirical relation based on publisher data where both mass and volume are considered dependent on the required thruster power loads required [39] (see Table 7).

The PPU can also be equipped with a Thruster Switching Unit (TSU), which interfaces up to 4 thrusters on the same PPU. However, it is possible to operate one thruster at a time. The TSU mass is always estimated equal to 1 kg. An additional functionality, particularly relevant if a redundant PPU is considered, is the possibility of a cross strapping among the PPU's, which allows transferring thruster and FCU supplies to another PPU.

Thruster Pointing mechanism (TPM)

The thruster pointing mechanism (TPM) shall hold, arrange, and point the thruster with respect to the different operation required throughout the mission phases. Two main configurations are usually adopted: (i) the TPM supporting the thruster directly interfacing the spacecraft structure or (ii) the TPM based on a robotic arm with the thruster mounted at the tip of it. Both configurations could eventually be considered for the space tug architecture. According to the preliminary design phase, despite the available design module based on [39], this component is not included in the architecture introduced for the analyses performed in this work.

Thruster Unit (TU)

The TU represents the core of the EPS. It provides thrust according to the imposed settings from the PPU. Presented as sub-assembly, it consists of the anodic section and the cathode, external or central mounted. Among the thrusters listed in the previous section, the SITAEL's 5kW-class HT5k and the 20kW-class HT20k have been considered as reference thrusters for the following analyses.

Since 2013, SITAEL represents a prominent reality in the field of high-power electric propulsion with the beginning of the development activities on the HT5k. Supported by several programs, this thruster undergone several design iterations and test campaigns aimed to optimize the thruster design and at the same time enlarge its operative envelope. In particular, low and high voltage operation were delved deeply to fully address the potential application of this thruster onboard telecom satellites. A significant advancement introduced in the design of the HT5k was the magnetically shielded configuration. This particular magnetic field shape allows the mitigation of the erosion phenomena, which represent the main criticality of this typology of thrusters.

The development status of the thruster has recently reached the Engineering Qualification Model in the framework of the ItalGovSatCom (IGSC) project. In the next future, the HT5k will undergo a whole qualification campaign. More details can be found in [40,41].

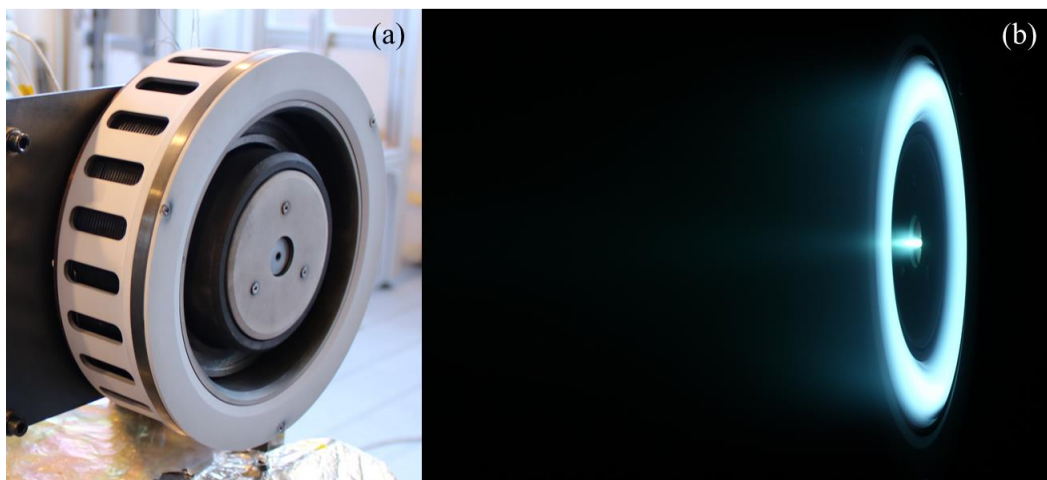


Figure 20: (a) HT5k during integration on thrust stand; (b) HT5k during characterization campaign.

A set of parallel development activities was instead focused on developing a dedicated hollow cathode called HC20. In the current TU configuration, the cathode is central mounted.

The main performance specification of both the HT5k and the HC20 are summarized in Table 5.

Table 5: Ht5k and HC20 main specification [40].

HT5 K main performance specification	
Total mass flow rate	9-24 mg/s
Discharge power range	2500-7500 W
Thrust range	120-410 mN
Total Specific impulse	$\leq 2300s$
Discharge voltage range	250-500 V
HC20 main specification	
Current emission	8-25 V
Keeper current	$\leq 4 A$
Heater Current	$\leq 12 A$
Mass flowrate	0-8-2 mg/s
Estimated number of cycles	>10000 cycles

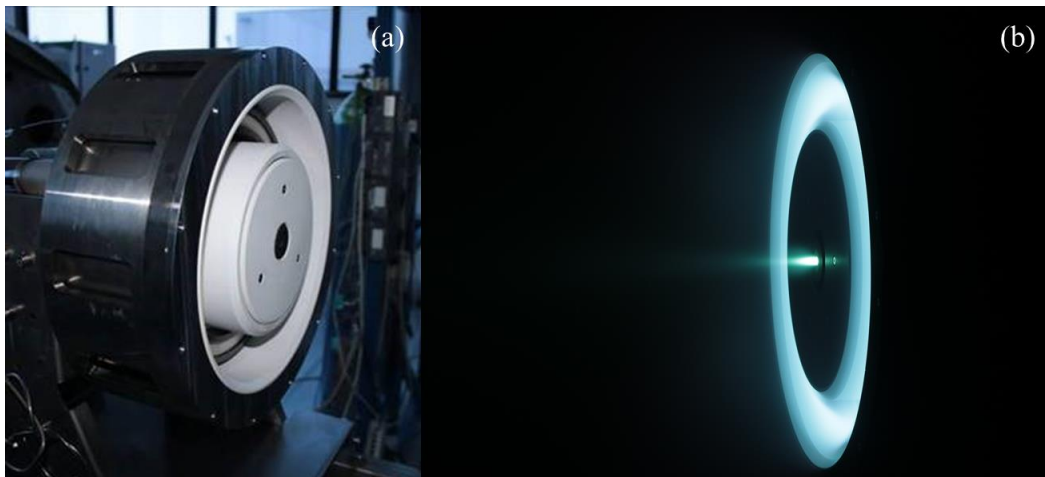


Figure 21: (a) HT20k DM2-L; (b) HT20k DM2-L during the first characterization campaign [42].

The development of the most powerful HT20k begins in 2015 to intercept future in-space transportation and space exploration needs. In the framework of different European projects and relying on the experience gained on the HT5k, this 20kW-class thruster reached the engineering model maturity for which environmental and endurance tests are scheduled in the next future. As happened for the previous thruster, the HC60 hollow cathode has been developed to meet the operative condition necessary for the operation of the thruster.

A detailed explanation of the subsequent design phases and test activities is reported in Section 4.7. A summary of the HT20k and HC60 specification is shown in Table 6.

Table 6: HT20k and HC60 specifications.

HT20k performance specification	
Total mass flow rate	20-40 mg/s
Discharge power range	10-25 kW
Thrust range	300-1300 mN
Total specific impulse	2000-3800s
Discharge voltage range	300-1000 V
HC60 specifications [43][44]	
Discharge current	30-60A
Mass flow rate	Up to 6 mg/s
Discharge voltage	10-18 V
Lifetime	>10000h

According to both design drivers and constraints reported above, a summary for the estimation of the EPS components is reported in Table 7. The user can select the default mass values reported in the table, or for the custom architecture design process, scaling models are introduced, as already specified. In the latter case. More details on the developed custom model for the EPS string can be found in [39].

Table 7: EPS component sizing features.

Component	Custom	HT5k	HT20k
Tank	It is sized considering a tankage fraction on the propellant budget.		
PMA	$M_{PMA} = 0.1366 \cdot \log(\dot{m}_p) + 0.1599$ (**)	4 kg (*)	4 kg (*)
(*) A redundant pressure regulation branch is considered in the mass budget. (**) As \dot{m}_p is considered the total propellant mass flow to the thrusters.			
FCU	$M_{FCU} = 0.0105 \cdot \dot{m}_{thr} + 0.4052$ (**)	2.1 kg	2.1 kg
(*) Pressure and Temperature sensors, filter and anode/cathode solenoid valves are included. (**) With \dot{m}_{thr} is considered the mass flow to every single thruster. It is the sum of the cathode and anode mass flow rate.			
PPU	$M_{PPU} = 0.003 \cdot P_{thr} + 4.7385$ (*)	17 kg	40 kg
(*) P_{thr} is the power that shall be provided in input to the thruster.			
TSU	1 kg		
TU	w.r.t. thruster database	12.5 kg (*)	49.5kg (*)
(*) The mass of the cathode is included			

The capability of the EPS sizing module is extended, including the cluster configuration. This specific design choice could be selected for three main complementary reasons. The first possibility considers the mission requirements, which usually impact the thrust level provided by the EPS. In this case, instead of design a more powerful thruster (that in the first approximation could be considered proportional to the thrust generated), the approach is to cluster an adequate number of thrusters. The second rationale for introducing a cluster configuration is the need to reach a certain reliability level to fulfil the mission and spacecraft requirements. The last reason which forces the architecture toward a cluster approach is to provide thrust toward multiple thrust vectors not reachable by a TPM.

Today's typical solution is based on a cluster approach where some of the thrusters are operated in parallel while others are added to mitigate possible failures.

Besides the advantages for which the cluster approach represents the best option, additional benefits can be identified. As extensively explained in [45], this architecture allows a reduction of the overall development and qualification costs of a new thruster. Higher scalability of the propulsion subsystem is attained with a consequent extension of the operative envelope of the subsystem.

A further benefit may come from the possibility to adequately integrate the single thruster in a cluster avoiding the need for a TPM.

Nevertheless, even though this solution could bring several advantages, critical drawbacks could jeopardize its adoption. One example is the complexities that might be encountered for integrating the cluster onto the platform and the needs to control the thermal condition of the different components to avoid local hot spots thermally.

In Figure 19, the subassembly composed of PPU, FCU and TU is called EP-string. This sub-assembly is introduced for each thruster for the basic cluster architecture while tank assembly and PMA are shared among the EP-strings. Figure 22 show a possible cluster subsystem based on two strings.

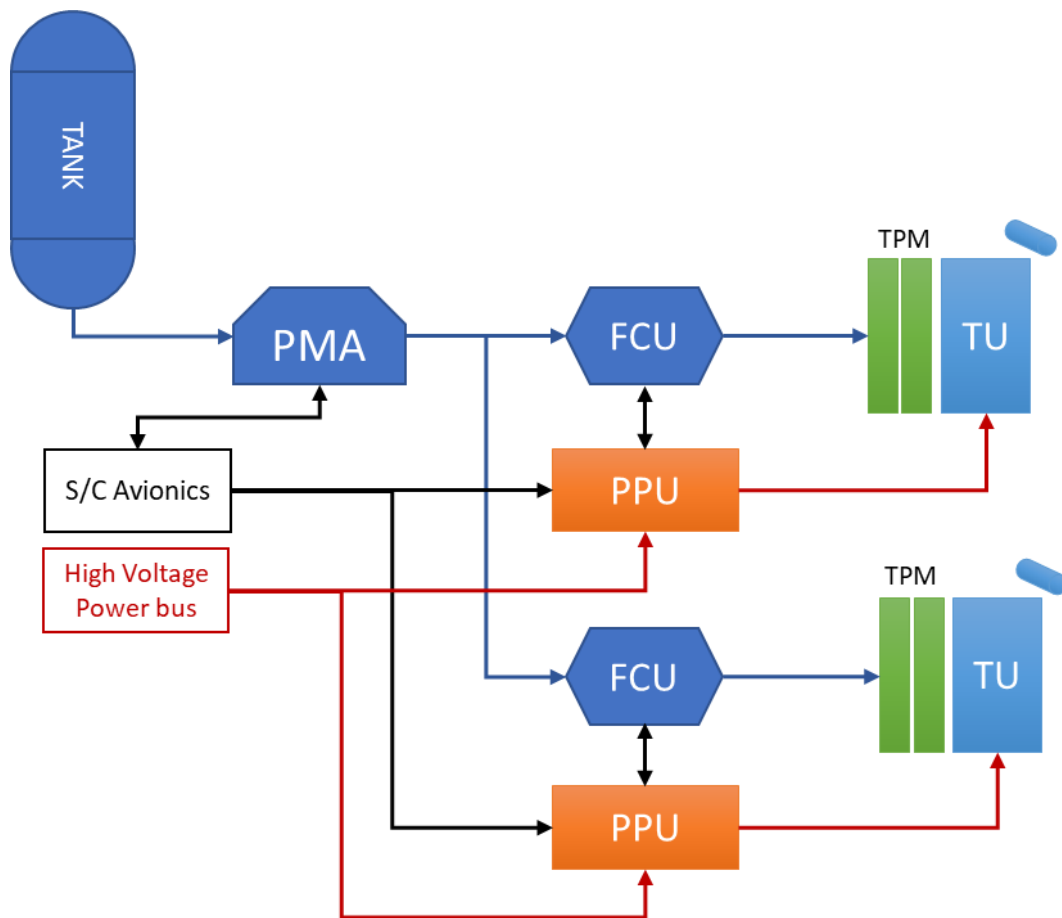


Figure 22: Simplified block diagram of an EPS based on cluster architecture.

The development of the EPS sizing routine allows both architectures, for which:

- N_{PMA} : as previously reported, the baseline architecture foresaw two PMA branches.
- N_{THR} : is defined in input by the user where it is possible to specify the number of operative ($N_{THR|op}$), stand-by ($N_{THR|std}$) and redundant thrusters ($N_{THR|red}$). In the case of cluster comparison, the number of operative thrusters could be introduced for the target available power ($P_{SC|available}$) defined, as:

$$N_{THR|op} = \left\lceil \frac{P_{SC|available}}{P_{THR}} \right\rceil \quad (2.1)$$

As a result, the total number of thrusters is given by:

$$N_{THR} = N_{THR|op} + N_{THR|std} + N_{THR|red} \quad (2.2)$$

- N_{FCU} : the number of the FCU is always equal to the number of the thrusters. In the baseline architecture, the number of PPU and FCU is equal to the number of thrusters.
- The number of thrusters controlled by a PPU up to four thanks to the adoption of the TSU. Defining the number of TU interfaced by the TSU as $N_{TSU|TU}$, the number of the PPU will be:

$$N_{PPU} = \left\lceil \frac{N_{THR}}{N_{TSU|TU}} \right\rceil \quad (2.3)$$

An additional user input option, introduced to extend the versatility of MAGNETO in intercepting alternative input requirement defined at the subsystem level, is the derivation of the EP string components' number with respect to the reliability of this subassembly. The generalized approach is based on the “*k out of n model*” [46–48]. The number of parallel strings which shall survive or succeed is k_{thr} over the number of available strings (n_{thr}). If with $R_{EPstring}$ is identified the reliability calculated on the single string, the reliability of the overall strings is:

$$R_{EPstring|TOT} = \sum_{m=k_{thr}}^{n_{thr}} \frac{n_{thr}!}{m!(n_{thr}-m)!} (R_{EPstring})^m (1 - R_{EPstring})^{n_{thr}-m} \quad (2.4)$$

Thus, through an iterative process, the number of EP strings that fulfilled the reliability at the subsystem level is derived. It is essential to highlight that Eq. (2.4) is valid for the active-standby condition of the considered components. Furthermore, in the case of the selection of this input option, the reliability foreseen for the single component shall be defined and introduced in a dedicated section of the input file. For the EP string sub-assembly, the reliability block diagram considers a series architecture of PPU, FCU and TU.

2.5.2.2 Direct Drive configuration

The Direct-Drive (DD) approach allows simplification of the electrical scheme of an electric propulsion system. Noting that an electric thruster is among the highest power-demanding components onboard a spacecraft, this simplification translates into the possibility of using lighter and smaller components for power regulation and distribution, and it could be effectively adopted in the case of a space tug.

Additionally, the possible stringent requirements and constraints derived from the adoption of high-power EPS that impact the other subsystems' design (i.e., the TCS) can be relaxed, which also brings mass and cost savings.

Nevertheless, besides the above gains from the direct-drive approach, it is also necessary to note that its implementation necessitates the development of specific technologies, such as high-voltage solar arrays, and incorporating new components in the spacecraft power system architecture. The cost, mass and eventual complexity of both technologies and components shall be fully addressed to guarantee the profitable adoption of the DD architecture.

As a result, although the advantages of a direct-drive system are known, the actual savings at the system level in terms of mass and cost can be made only after weighing the direct benefits of DD against the additional requirements that its application may introduce.

Furthermore, it is important to underline that, according to several system characterization campaigns in the past years performed on Hall thrusters operated in DD mode [49–51], the implementation of the direct-drive approach may introduce some constraints on the propulsion system. However, as far as the thruster is operated within its stable and high-efficiency domain, the influence of the direct drive is not significant on the performance of the Hall thruster. The capability of the direct-drive system in supplying power and regulating the thruster behaviour to ensure the above requirement over the entire mission lifetime is by itself a challenge with possible system-level implications. Thus, it is imperative to consider these aspects and investigate them thoroughly before opting for the direct-drive approach. Adopting a direct-drive electric propulsion system has several direct advantages that, in general, may allow about a 5-10% reduction in the mass of multiple spacecraft components, such as harness and cabling, power regulation and distribution system and the thermal control system. This, in turn, translates into a lower mass of launch, with a consequent decrease in the total project cost of the system.

In particular, the mass of the power processing unit (PPU) is significantly reduced because of the direct-drive approach. A PPU constitutes a significant contribution of electric propulsion system mass and size because it includes high-power converters on the anode power line to regulate the low-bus voltage at a level suitable for thruster operation. These modules also serve as galvanic isolators to decouple the anode current oscillations from the bus and the power system. As a result, these components are of considerable mass, cost, and complexity. In addition, an increase

in the thruster discharge power translates into even heavier, bulkier, and more complex PPUs. The direct-drive approach allows simplifying the PPU greatly, removing all power converters and implementing a simplified filter unit on the anode power line. Consequently, the mass of the PPU could be reduced by more than 50%, cutting the overall component cost by an average factor of four.

The remaining electronics of the original PPU, i.e., all components apart from the anode power module(s), form a new system component called the Direct Drive Unit (DDU). It is important to note that a DDU has a notably higher efficiency than conventional PPUs, exceeding 99%, as will be seen later in this document. This higher efficiency results in lower heat dissipation and allows the application of a simplified thermal control system (TCS) with consequent mass and cost savings.

In addition to the direct advantages due to the reduction of PPU mass and volume and the reduction of thermal load to be dissipated by the TCS, other indirect advantages not directly related to the implementation of a DD system can be considered. These indirect advantages can be obtained by implementing the high-voltage power bus. The high-voltage bus can, of course, be adopted, even though the Direct Drive approach is followed. Nevertheless, the high-voltage solar arrays and high-voltage bus are enabling technologies of a DD system. In particular, an HV bus implies that a fixed power can be delivered to subsystems by a lower current. This also results in lower heat dissipation and allows further reduction in the mass, complexity, and cost of the TCS.

Furthermore, the higher efficiency of the direct-drive unit in the DD scheme translates, to some extent, into a reduced power demand of the propulsion system. Thus, the area of the solar arrays can be reduced. This reduction also implies notable mass savings. In this respect, besides the lowered cost due to the need for a smaller area of solar arrays, the high-voltage solar array technologies, under development today, are cost-effective solutions with a specific cost (\$/W) of only 1/4 of the conventional high-efficiency planar arrays.

Direct Advantages of DD implementation

As briefly discussed above, the principal benefit of the DD configuration compared with the conventional PPU is the removal of the anodic module(s). Thus, the mass savings provided by the DD system can be evaluated as the difference in mass for a classical PPU configuration, mainly due to the removal of the anode power module(s). To proceed with the analysis, we, therefore, define a single anode module of a conventional PPU in terms of a DC-DC converter, considered to be constituted by: (i) a chopper stage, which converts fixed DC input to a variable DC output voltage, (ii) an inverter transformer stage, to change the voltage output and provide isolation between input and output load, and (iii) a rectifier stage that provides rectified AC to (iv) a downstream DC filter, whose output is a DC to the TU. A DC filter is placed upstream of all components to isolate the EPS from the Electric Power Distribution and Control Subsystem (POW).

Figure 23 shows the conceptual arrangement of the components that form the PPU.



Figure 23: Conceptual functional block diagram of a conventional PPU.

The NASA Glenn Research Centre model is used to estimate the mass of a single anodic module [52]. This model provides the mass trend evaluation of all electronic components, which constitute a typical electric power subsystem of a spacecraft, considering its main sizing variables. According to the models related to the components in Figure 23, the overall anodic module mass is obtained by summing over the corresponding mass of all components.

The design parameters are reported in the table below:

Table 8: Anodic module assumed design parameters.

	Parameter	Description	Value		NOTE
DC Filter Stages			Upstream filter	Downstream filter	
	FSVO	Input voltage [V]	100	300 (*)	(*) Default value
	FSPO	Power [kW]	Depending on analysis inputs		
	FSRF	Ripple factor [%]	5 (*)		
	FSE	Efficiency [%]	99,8		
	SF	Switching frequency [kHz]	100		
	AM	Available module	3		
	RM	Required module	4		
	(*) Payload buck converter (0,04%)				
Chopper Stage	CSE	Efficiency	97,67		
	CSPO	Power [kW]	5,24		
	CSVI	Input voltage [V]	80		
	SF	Switching Frequency [kHz]	80		
	AM	Available module	3		
	RM	Required module	4		
Inverter/Transformer Stage	ITSVI	Input voltage [V]	90		
	ITSVO	Output voltage [V]	300		
	TF	Frequency [kHz]	55		
	ITSP0	Input Power [kW]	5,11		
	ITSE	Efficiency	99,2		
	AM	Available module	3		
	RM	Required module	4		
Rectifier Stage	RSPO	Power [kW]	5,07		
	PSVI	Input voltage [V]	300		
	RSE	Efficiency	98,7		
	AM	Available module	3		
	RM	Required module	4		
			For voltages > 110V		

The Switching Frequency (SF) for both the Chopper and the Inverter/Transformer were derived using the suggested values in [52], which provides the SF values with respect to the component output power, as is shown in Figure 24.

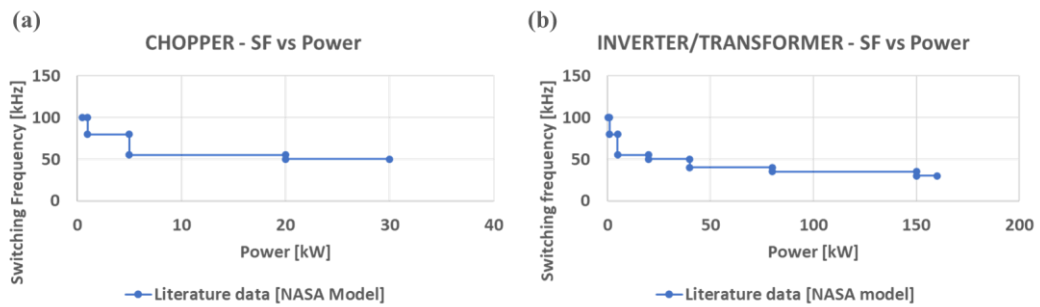


Figure 24: (a) Chopper Switching Frequency (SF) vs component power; (b) Inverter transformer Switching Frequency (SF) vs component power [53].

Figure 25 summarises the design parameters and variables at each step of the power conditioning by a conventional PPU, as presented in Table 8.

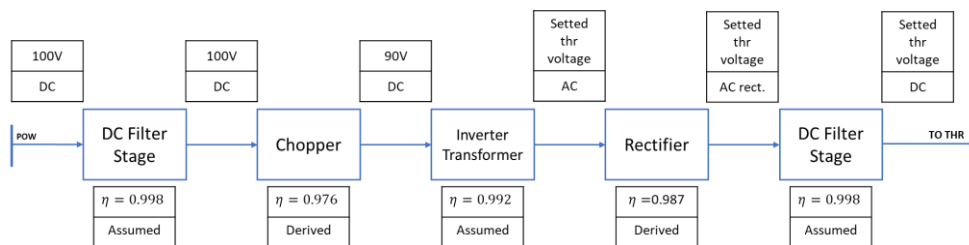


Figure 25: Anodic module block diagram power conditioning steps.

Another advantage of the DD system implementation is a reduction in the mass of the TCS. As previously mentioned, the higher efficiency of the DD system lowers the generated heat that needs to be dissipated by the TCS, which reduces the mass of the Thermal Control System. In particular, the design solution usually adopted for the conventional PPU architectures is loops of heat pipes through which the PPU generated heat flux flows to either deployable or body-mounted radiators. The PPU is placed in contact with body-mounted radiators in peculiar architectures where stringent thermal requirement shall be fulfilled, avoiding the heat pipes loops. In this analysis, the scheme with the heat pipe loops is being considered. The TCS mass saving is assessed considering an average power specific mass of 28 kg/kW for the radiators and 14 kg/kW for the heat pipes loops.

As briefly discussed in the previous paragraphs, the indirect advantages are not directly linked with implementing a DD scheme. These advantages are, in fact, due to design solutions that can be implemented regardless of the EPS architecture. In this respect, the high-voltage Electric Power Subsystem design, which provides high-voltage power to the EPS and other subsystems on-board a spacecraft, can serve as a major source of mass and cost benefits. However, despite several advantages that may be obtained, some technological limitations exist that shall be carefully investigated. They are mainly related to (i) high-voltage solar arrays, (ii)

high voltage batteries and (iii) high-voltage power bus. In the next paragraphs, a brief description of the design assumption in the case of DD architecture selection is reported. It is important to highlight that the user can modify all the parameters involved for the design of both the impacted components and the PPU anodic module elements.

- **High-voltage solar arrays**

The selection of a high-voltage power bus necessitates the use of high-voltage solar arrays. Despite the issues caused by the plasma environment surrounding the SA, as well as possible electric charging and arcing events, the implementation of a DD system allows a notable reduction in the SA area because of the higher efficiency of the DDU, and thus, the consequent reduction in the power demand required from the SA. A state-of-the-art high-power SA review showed that Ultraflex and Megaflex solar arrays developed by Orbital ATK are suitable for high-voltage operations [54–56]. These SAs have a specific architecture of the cells to increase the specific power, thus, increase the scalability to high power levels and feature an innovative deployable system based on folding spar joints and panel extension hinges, allowing very high packing efficiency.

To estimate the indirect advantage of the DD system coming from the high-voltage SA, the methodology presented in [52] is followed. Table 9 summarizes the design parameters used in the analysis. The SA area was calculated for the power levels required in both the PPU and DDU configuration.

Table 9: SA design parameters.

SA Design Parameters			NOTE
	PPU configuration	DDU configuration	
Sunlight power required [W]	6415	6026	Derived considering a margin of 5%;
Eclipse power required [W]	641.5	602.6	Assumed 10% of sunlight power for thrusting phases;
Daylight time [s]	5400		Derived for the worst condition in LEO>GEO transfer
Eclipse time [s]	1800		Derived for the worst condition in LEO>GEO transfer
Daylight path efficiency (X _D)	0.85		[5]
Eclipse path efficiency (X _E)	0.65		[5]
Cell efficiency (BoL)	33 %		Multijunction GaAS
Inherent degradation	0.805		[5]
Specific power [W/kg]	120		[54], [55]

As shown in Table 9, lower input power is required by the platform because the DD is characterized by system higher efficiency and lower losses through the power bus, which translates into a reduction of the SA area. This directly affects the Attitude Determination and Control Subsystem (ADCS) since the requirements on the torque force that it should counteract will be relaxed, resulting in reducing the subsystem mass.

High-voltage battery

The batteries represent one of the most critical issues for high-voltage POW design. On the one hand, this is because the high-voltage bus could require several cells in series, which increases the design complexity of this subsystem. On the other hand, adopting low-voltage batteries requires the use of a step-down converter. In this case, the subsystem mass savings and the reduction of generated heat load are lowered. The Li-ion batteries were selected with an energy density of 130 Wh/kg [5]. This adoption of this typology of cells allows reducing the number of cells necessary to operate at a high-voltage level. The design of the batteries considers the worst-case scenario of eclipse during LEO to GEO transfer. The power to be provided during the eclipse time is assumed to be 10% of the maximum power of the spacecraft. It is also pointed out that if a high-voltage POW is selected, it allows the relaxation of this requirement due to the lower power dissipation of the power bus. Following the design methodology presented in [5], the design parameters taken into account are reported in Table 10.

Table 10: battery design parameters.

Battery Design Parameters		NOTE
	PPU configuration	DDU configuration
Eclipse time [s]	1800	
DOD	0.75	
Transmission efficiency	0.9	
Energy density [Wh/kg]	130	
		[5]
		[5,57]

High-voltage power bus

Adopting a high-voltage power bus for the POW brings about other advantages at the spacecraft level. In fact, a higher voltage bus can provide the same power level with a lower current compared to a lower voltage bus. Consequently, the ohmic heat dissipations ($P_D = RI^2$) are reduced, and thus, less heat shall be managed by the TCS. Assuming that 7% of total power is dissipated as heat [5] for a system based on PPU, the following ratio is defined to derive the power dissipated by a DDU-based system ($P_{D,HV}$):

$$\frac{P_{D,HV}}{P_{D,LV}} = \frac{R I_{HV}^2}{R I_{LV}^2} = \frac{\left(\frac{V_{LV}}{V_{HV}} I_{LV}\right)^2}{I_{LV}^2} = \left(\frac{V_{LV}}{V_{HV}}\right)^2 \quad (2.5)$$

in which the indexes HV and LV denote High Voltage and Low Voltage, respectively.

As another critical point, when a high-voltage power bus is selected, it can also be possible to reduce the cross-section of the wires because of the lower current level that they need to carry. This design choice allows reducing the mass of the power bus. However, this design option results in the same values of the heat to be dissipated by the TCS. Therefore, reducing the bus mass by selecting smaller-diameter wires or reducing the TCS mass by lowering the ohmic power dissipation in the wires while keeping the wires' diameter constant presents two design options at the S/C-level. The selection of one option over the other requires more detailed trade-off analyses beyond the current high-level analysis scope. Accordingly, to present an overall estimate of DD system advantages, and with no further investigations on the spacecraft harness, the design solution of constant wire cross-section is selected.

Figure 26 summarizes the system benefits and potential challenges and/or risks related to implementing a DD system. The benefits are subdivided between direct and indirect advantages, as previously defined. More specifically, on the left-hand side of the black dashed line in Figure 26, the indirect effects on the S/C subsystems are shown, while the direct effects on the EPS are presented on the right side.

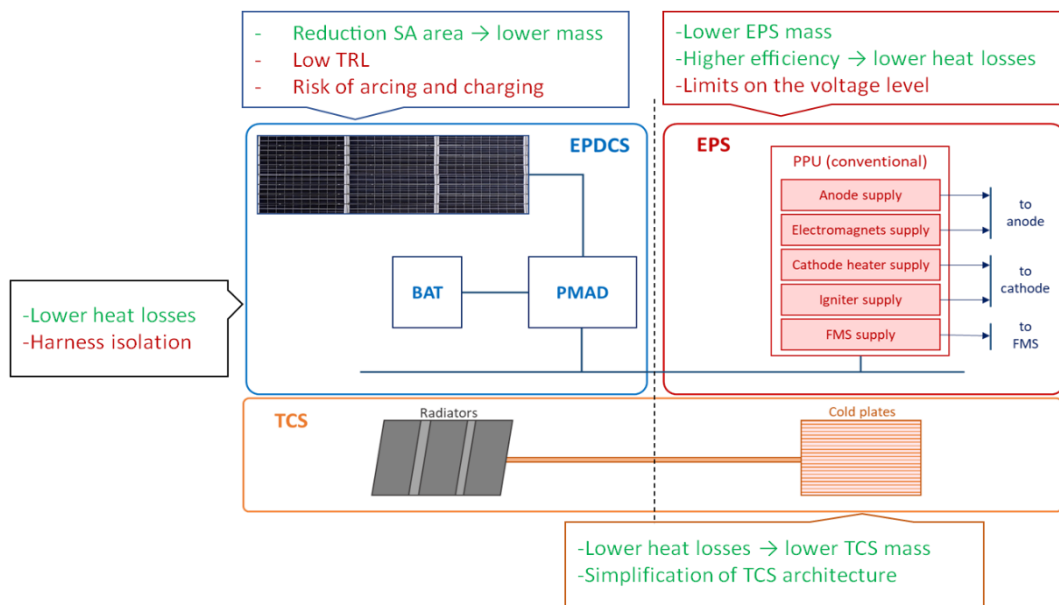


Figure 26: block diagram with the components considered in the DD approach.

An example of the different mass model project at a given power level required by a monolithic EPS string is shown in Figure 27.

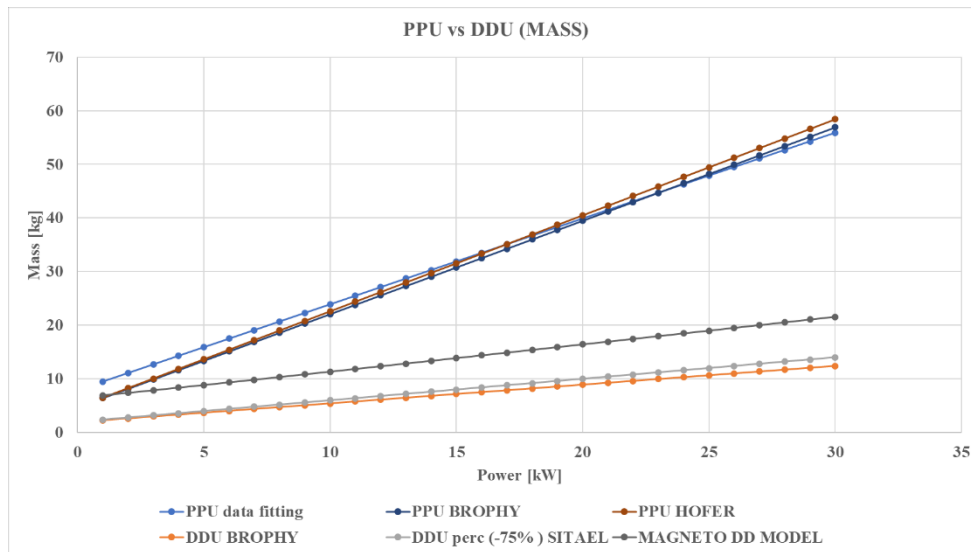


Figure 27: projection of the PPU mass vs DDU mass with respect to the input power of the EP string.

The mass models exploited for the PPU are: (i) PPU mass model obtained through a data fitting of the existing PPU [39], (ii) PPU mass model developed by Brophy [58], (iii) PPU mass model developed by Hofer [59], (iv) DDU mass model developed by Brophy and reported in [58], (v) DDU mass model developed by SITAEL in the framework of the CHEOPS project and (vi) the DDU mass model introduced in MAGNETO. As shown in the figure, the final mass trend resulted in having the same trend on those estimated through Brophy's and SITAEL's model. Despite this, the higher value is consequent to the different modularity approach followed.

2.5.2.3 Alternative propellant selection

Considering the mission requirements and constraints imposed by the foreseen space tug scenarios, the possibility to exploit alternative propellant instead of the commonly used xenon could result in strong cost-saving. However, before the selection of possible options to trade-off, high-level design constraints shall be first considered.

These are mainly related to performance aspects (e.g., thrust efficiency and thrust-to-power ratio) and compatibility with the materials in contact with the propellant gas. The considerations regarding the cost of procurement and handling are also crucial.

Moreover, for ease of handling, the propellant should be non-corrosive, with a low boiling point, and preferably non-toxic, according to [60,61]. The chemical properties of the noble gases meet a large number of the propellant requirements, like those mentioned above.

Among the noble gases, xenon is considered an optimal choice and has been used as the propellant in a large number of Hall and ion thrusters. A multitude of reasons exists that justifies the use of xenon. First of all, xenon is chemically inert and non-toxic. The high boiling temperature and density of xenon make it storable. Xenon has relatively low first ionization energy that results in low ionization cost compared to other potential propellants. Besides its compelling properties, however, xenon prices have surged significantly in the past years due to its scarcity in nature and the increasing demand in other industrial sectors. The augmented cost, in turn, brought to attention some other gases as possible substitutes for xenon. A valid alternative is represented by krypton which has comparable physical properties with respect to the xenon. The most relevant features which make this propellant an interesting alternative is its low price. In fact, while the xenon is today quoted at 2200€/kg, the krypton is in turn procured at 120 €/kg [62].

Despite the substantial benefit in terms of cost-saving, the utilization of the krypton brings some drawbacks that, even in this case, shall be carefully evaluated. The first concern is represented by a reduction of around 5-10% of the thruster performance, because the lower efficiencies due to the different ion mass and the higher neutrals' ionization energy. Concerning xenon, the lower atomic results in a higher specific impulse if the ions are accelerated at the same potential drop. For this reason, the thruster operated in krypton is stronger affected by erosion phenomena due to the higher ion velocities.

The lower storability of the krypton represents another important disadvantage. As a consequence, having a lower density, this mobile gas could be stored at a supercritical condition, increasing the pressure at 250 bar that corresponds to its triple point. Therefore, the design of the tank assembly and the PMA in charge of the pressure regulator could present some difficulties.

In MAGNETO, the user can choose the adoption of krypton with a dedicated flag in the input file. The constraints in particular related to the design of the tanks are therefore taken into account.

2.5.3 S/C subsystems design module

In this paragraph, the main assumptions introduced for the subsystem's design of the space tug (excluding the EPS) are presented. Specific MAGNETO subroutines are introduced following a modular approach to allow future development of the models. The models refer to those introduced in [5] suitable for the preliminary spacecraft design.

The focus of this section is given to the Power and Management subsystem (POW), chemical propulsion subsystem (cPROP) and Thermal control subsystem (TCS) because of their higher impacts foreseen during the space tug operations.

The rest of the subsystems are then sized considering a relative mass allocation percentage, as will be later detailed.

2.5.3.1 Electric Power and Management Subsystem (POW)

The POW is in charge of generating, manage, store and distribute the electric power necessary to sustain onboard loads according to the operational profile of the space tug. Deployable solar arrays guarantee, consisting of two steerable wings, the generation of the power. The baseline selection introduced in the design module is the Orbital ATK Ultraflex arrays [54] developed to provide high specific power (<220 W/kg) and high storability density (> 33 kW/m³). With a circular configuration, each six meters wing (prototype configuration) was developed to provide more than 15 kW. The introduced set of safety margins followed the indication suggested in the SMAD [5] for a conservative approach to the sizing of the solar arrays. The inherent degradation was estimated considering the product of (i) design and assembly inefficiency ($I_A = 0.95$), (ii) temperature inefficiency ($I_T = 0.94$) and (iii) shadowing inefficiency ($I_S = 0.99$). An additional margin considers the degradation of the cell performance during the operational lifetime fixed at 15 years. Its value increased up to 3%, which deviates compared to what suggested in the SMAD to take into account the degradation due to the repeated crossings of the Van Allen belt.

The power generated by the solar arrays is fed to a central electronic unit called Power Management and distribution unit (PMAD). This component is introduced to provide properly allocated power to sustain the different load and provide regulation with a filtering block. Furthermore, the PMAD is in charge to manage the operation of the battery pack. The baseline selection, proposed as a default option to the MAGNETO user, is the Li-ion battery adopted for upgrading the Eurostar 3000 GEO platform [63]. This battery technology has 175 Wh/kg of power density, an overall efficiency of 0,97 and a capacity of 50 Ah. Considering the mission profiles of the selected scenarios, the power required during the eclipse is calculated considering the loads coming for all the S/C subsystems with the EPS in idle mode (See section 2.4.2).

According to the SMAD, the mass of the harness is estimated as a fraction of the overall S/C dry mas. The adopted percentage is $MR_{harness} = 7\%$. Additional safety margins, already presented in Table 3, were included in the final mass budget.

2.5.3.2 Thermal Control Subsystem (TCS)

The TCS has the function to monitor and control the thermal condition of the onboard components to maintain the temperature in the operative ranges. Due to the adoption of electric propulsion, the accomplishment of this function shall be carefully investigated due to the possible hot spots caused by high heat fluxes, which usually characterized power electronics and TU. The design of the TCS considers three main components introduced to provide a passive thermal control strategy; they are (i) cold plates, placed in contact with the high-dissipative components, (ii) heat pipes, to transfer heat fluxes from the cold plates to (iii) radiators which are directly exposed along either the spacecraft external surface or

deployed through movable structures. Following the design procedure described in [64]. The temperature boundaries defined for cold and hot cases. This range was set with $T_{min} = -15^{\circ}C$ and $T_{max} = 50^{\circ}C$ derived for the average worst case conditions. The evaluation of the heat flux dissipated through the radiators was calculated considering the sum of the internal and external heat fluxes, Q_{int} and Q_{ext} respectively. In the design of the space tug, considering the impact of the high-power propulsion subsystem, the main contribution comes from the PPU dissipation due to its power processing efficiency set at 94%. The external heat contributions are defined by the operational environment of the space tug. The four contributions identified are (i) solar flux, (ii) albedo, (iii) Earth IR and (iv) S/C surface irradiance. Each term is evaluated for the related view factor updated at each iteration step during the propagation.

Therefore, once the total flux that shall be dissipated is calculated (Q_{rad}), the area of the radiators is derived considering the classical approach of a radiative surface for which:

$$A_{rad} = \frac{Q_{rad}}{\epsilon \sigma T_{max}^4} \quad (2.6)$$

with the ϵ is the emissivity of the radiators and σ is Stefan-Boltzmann constant. The mass of the radiators is then calculated considering a mass for the unit of area of 3.3 kg/m^2 [65].

2.5.3.3 Chemical Propulsion Subsystem (cPROP)

As already presented in the previous paragraphs, the chemical propulsion subsystem is introduced to provide thrust, in particular during RVD manoeuvres. Moreover, it can be used to desaturate the active attitude control actuators (e.g., reaction wheels). The architecture sets by default in the MAGNETO dedicated subroutine is based on the same configuration adopted for the European Automated Transfer Vehicle (ATV). A total of 28 thrusters are organized in 4 clusters of 2 thruster and 4 clusters of 5 thrusters. The 20N monopropellant thruster developed by ArianeGroup is assumed as the baseline option. A possible upgrade of the system architecture could be envisaged considering cold gas thruster directly operated with Xenon. In this latter case, the adoption of dedicated chemical propulsion is avoided with a consequent simplification of the spacecraft architecture and the related refuelling operation at the OORS. However, the performance provided by monopropellant thrusters operated with xenon are strongly reduced compared to the chemical-based architecture, which results in turn in possibly dangerous situations in case of collision avoidance manoeuvres during RVD operation with both the serviced satellite and the OORS.

- **Other subsystems onboard the space tug**

The mass budgeting process exploits the sizing models derived following the sizing models defined in [5,64] with the assumptions introduced in the previous paragraph. For the definition of the TT&C, C&DH Struct&Mech mass budget relative percentage relative to the dry mass of EPS, POW, cPROP and TCS, considering the mass ratio value (MR):

$$MR_{S/C} = \frac{M_{EPS|dry} + M_{TCS|dry} + M_{cPROP|dry} + M_{POW|dry}}{MR_{EPS} + MR_{TCS} + MR_{cPROP} + MR_{POW}} \quad (2.7)$$

Consequently, the mass of the other subsystem is then calculated as:

$$M_{TT\&C|dry} = MR_{TT\&C} * MR_{S/C} \quad (2.8)$$

$$(2.9)$$

$$M_{C\&DH|dry} = MR_{C\&DH} * MR_{S/C}$$

$$(2.10)$$

$$M_{Struct\&Mech|dry} = MR_{Struct\&Mech} * MR_{S/C}$$

The relative dry mass percentages of the subsystems are reported in the following table:

Table 11: relative dry mass fraction for each space tug subsystem.

Subsystem	Percentage
POW	0,3
PROP (cPROP+EPS)	0,24
AOCS	0,09
TCS	0,13
CDH	0,04
COMMSYS	0,05
STRUCT	0,15

The final total dry mass is then derived with the sum of the single subsystem dry mass budgets. Considering the preliminary design phase presented in this work, the dry mass is augmented through an imposed safety margin (see Table 3).

2.5.4 Scenario optimization: Trajectory Propagation Module

The scenario optimization module received input from the previous module in terms of preliminary mission budgets. However, considering the adoption of the electric propulsion, the computation of the transfer time, the delta-V and the related propellant mass shall be optimized through a specific subroutine. Therefore, a propagation routine is introduced in a for-loop through which the spacecraft budgets are minimized. The core of this MAGNETO block is the propagation module able to provide a sub-optimal solution for the transfer parameters mentioned above. This subroutine implements an orbital dynamics model based on modified equinoctial elements. This approach improves the computational efficiency and avoids tedious numerical singularities [66,67].

The model includes different orbital disturbances to fully characterise the space tug's operative environment since their related acceleration magnitudes can reach values comparable to those related to the thrust accelerations. Therefore, dedicated models were introduced for the evaluation at each integration point of (i) gravitational zonal harmonic J2, (ii) solar pressure (SP), (iii) atmospheric drag (D) and (iv) third-body perturbation (TB) (considering only Sun and Moon contributions).

Starting from the second-order differential equation that described the orbital motion and exploiting the relation presented in [68], it is possible to write the orbital dynamics of the spacecraft in terms of equinoctial elements:

$$y = [p, f, g, h, k, L] \quad (2.11)$$

Therefore, the equation becomes the following equation of motion:

$$\dot{y} = A(y)\Delta + b \quad (2.12)$$

Where the coefficient matrix $A(y)$, the accelerations' vector Δ and the vector b are:

$$A(y) = \begin{bmatrix} 0 & \frac{2p}{q} \sqrt{\frac{p}{\mu}} & 0 \\ \sqrt{\frac{p}{\mu}} \sin L & \sqrt{\frac{p}{\mu}} \frac{1}{q} \{(q+1) \cos L + f\} & -\sqrt{\frac{p}{\mu}} \frac{g}{q} \{h \sin L - k \cos L\} \\ -\sqrt{\frac{p}{\mu}} \cos L & \sqrt{\frac{p}{\mu}} \frac{1}{q} \{(q+1) \sin L + g\} & \sqrt{\frac{p}{\mu}} \frac{f}{q} \{h \sin L - k \cos L\} \\ 0 & 0 & \sqrt{\frac{p}{\mu}} \frac{s^2 \cos L}{2q} \\ 0 & 0 & \sqrt{\frac{p}{\mu}} \frac{s^2 \sin L}{2q} \\ 0 & 0 & \sqrt{\frac{p}{\mu}} \frac{1}{q} \{h \sin L - k \cos L\} \end{bmatrix} \quad (2.13)$$

$$\Delta = [a_r \ a_t \ a_n] = \Delta_{J_2} + \Delta_{TB} + \Delta_T + \Delta_D + \Delta_{SP} \quad (2.14)$$

where: (Δ_{J_2}) J_2 acceleration, (Δ_{TB}) Third body acceleration, (Δ_T) thrust acceleration, (Δ_D) drag acceleration and (Δ_{SP}) Solar Pressure acceleration.

$$b = \left[0 \ 0 \ 0 \ 0 \ 0 \ 0 \ \sqrt{2\mu p} \left(\frac{q}{p}\right)^2 \right] \quad (2.15)$$

And the terms q and s^2 defined as the combination of the equinoctial elements as

$$q = 1 + f \cos L + g \sin L \quad (2.16)$$

$$s^2 = 1 + \sqrt{h^2 + k^2} \quad (2.17)$$

For the definition of the 5x3 vector Δ containing the disturbances components, different models were used. Most of the models are based on the ECI frame, for which a transformation matrix was introduced to convert the results in the LVLH reference frame.

- Gravitational perturbation: the gravitational perturbation included in the model refers only to the contribution of the zonal harmonic J_2 , which introduced the effects caused by the Earth oblateness. This approximation

is justified by the value of the J2 coefficient, which results in orders of magnitude higher than the other coefficients.

- **Atmospheric Drag:** for mission phases in proximity to the Earth (in particular for LEO operations), the drag generated with the interaction between the spacecraft and the atmospheric residuals cannot be neglected. For estimating its value, Eq. (3.21) (detailed in Section 3.6.1.2) is used considering a reference derived considering the solar array's surface including an additional safety margin. The drag coefficient was set at $C_D = 2.2$ [5] as a standard value exploited for the preliminary drag estimation.
- **Solar pressure:** the solar pressure acts on the spacecraft during sunlight conditions. The model exploited is based on the reference surface of the spacecraft (A_{ref}), the reflectivity coefficient (C_R) and the solar pressure value (p_S).
- **Third Body:** this acceleration was calculated exploiting Battin's method [69], which allows neglecting second-order effects. The gravitational influences of the Sun and Moon are considered.
- **Thrust acceleration:** the components of the thrust acceleration are evaluated about the EPS architecture and the operative point selected, and the total wet mass of the spacecraft updated each integration step due to the propellant consumption. The thrust value is maintained constant along the trajectory.

In order to perform the desired manoeuvre selected in the input file, a weighted method based on the normalized relative deltas among the final and initial values of each orbital parameter is used. The relative computed weight W_i is therefore defined as:

$$W_i = \frac{k_{orbital}(t) - k_{target}}{|k_{initial} - k_{target}|} \quad (2.18)$$

where $k_{orbital}(t)$ is the value of the orbital parameter at each integration step while k_{target} is the final target value. The thrust management function tries to minimize the weights at each integration step to find the optimal local trajectory. This process is repeated at each integration step, for which a suboptimal global trajectory is obtained when each orbital parameter weight approaches the set tolerance limits. In order to enable the trajectory control, thrust steering capability is given through the specification of in-plane and out-of-plane thrust angles as

Table 12: in-plane and out-of-plane angles for each controlled orbital parameter.

In-plane angle	Out-of-plane angle
Semi-major axis a	
$\alpha = \tan^{-1}\left(e \cdot \frac{\sin v}{1 + e \cdot \cos v}\right)$	$\beta = 0$
Eccentricity e	
$\alpha = \tan^{-1}\left(e \cdot \frac{\sin v}{\cos v + \cos E}\right)$	$\beta = 0$
Inclination i	
$\alpha = 0$	$\beta = \text{sgn}(\cos(\omega + v)) \cdot \frac{\pi}{2}$
Right Ascension of Ascending Node RAAN Ω	
$\alpha = 0$	$\beta = \text{sgn}(\sin(\omega + v)) \cdot \frac{\pi}{2}$
Argument of Perigee ω	
$\alpha = \tan^{-1}\left(\frac{1 + e \cdot \cos v}{2 + e \cdot \cos v} \cdot \cot v\right)$	$\beta = \tan^{-1}\left(\frac{e \cdot \cot i \sin(\omega + v)}{\sin(\alpha - v) \cdot (1 + e \cdot \cos v) - \cos \alpha \cdot \cos v}\right)$

The calculated weights with Eq. (2.18) are summed for tangential, radial, and normal direction, including the thrust steering relation for each orbital parameter to find the resultant weighted vector.

(2.19)

$$u_r = W_a \cdot \cos(\beta_{max_a}) \cdot \sin(\alpha_{max_a}) + W_e \cdot \cos(\beta_{max_e}) \cdot \sin(\alpha_{max_e}) + W_w \cdot \cos(\beta_{max_w}) \cdot \sin(\alpha_{max_w})$$

$$u_t = W_a \cdot \cos(\beta_{max_a}) \cdot \cos(\alpha_{max_a}) + W_e \cdot \cos(\beta_{max_e}) \cdot \cos(\alpha_{max_e}) + W_w \cdot \cos(\beta_{max_w}) \cdot \cos(\alpha_{max_w})$$

(2.20)

$$u_n = W_a \cdot \sin(\beta_{max_a}) + W_e \cdot \sin(\beta_{max_e}) + W_w \cdot \sin(\beta_{max_w}) + W_i \cdot \sin(\beta_{max_i}) + W_{RAAN} \cdot \sin(\beta_{max_{RAAN}})$$

(2.21)

The resultant components are then normalized for the maximum value among u_r , u_t and u_n .

At the end of this process, the effective thrust angles α and β can be computed from the components of \vec{u} :

$$\alpha = \text{atan2}\left(\frac{u_r}{u_t}\right)$$

(2.22)

$$\beta = \text{asin}(u_n)$$

(2.23)

The thrust angles are computed exploiting the relations in Eq (2.22) and Eq. (2.23). Table 12 can be limited for the tilt range allowable by the design of the TPM. Another design option is to provide the functionalities of the TPM through an articulated robotic arm already adopted onboard a commercial satellite, such as the Eutelsat-172b [62] Electra [63]. This possibility is included in MAGNETO with a dedicated input setting with which the mass and the solid angle range can be defined.

The dynamic orbital model is introduced in four different sub-modules, one for each manoeuvre foreseen for the space tug to fulfil its mission objectives.

The key differences among them are the condition at which the trajectory propagation is terminated and if the thrust acceleration (considering the thrust provided by electric thrusters) is considered or not.

They are:

- Electric Orbit Raising (EOR): the integration process is terminated when the target orbital position is reached. Any time constraint is considered.
- Rendezvous and Docking (RVD): if this manoeuvre is selected, the thrust acceleration is neglected in Eq. (2.19), Eq. (2.20) and Eq. (2.21). The propagation is terminated through the phase duration limit defined in the input file by the user.
- WAIT: the waiting phase is terminated when the phase duration limit defined in the input file by the user is reached. The thrust acceleration term is neglected in Eq. (2.19), Eq. (2.20) and Eq. (2.21).
- PHASING: this manoeuvre is selected during tug relocation service operations. The trajectory propagation is terminated once the tug reaches the target position. This manoeuvre is characterized by two possible user input options. The first possibility is to set the delta altitude that the tug shall reach to perform the phasing manoeuvres. In this case, the first propagation is performed to fix the initial guess of an optimization process introduced to minimize the period $t_{wait|PHASING}$ that the tug shall wait before starting the return phasing transfer.

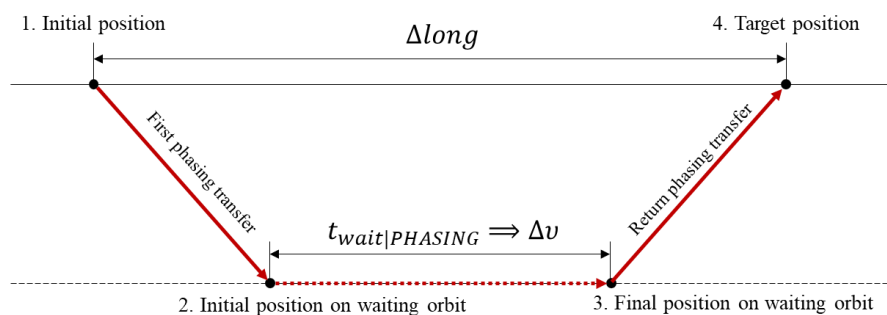


Figure 28: phasing phases.

The second option selectable by the user relies on the definition of the maximum duration of the phasing manoeuvre. The optimization process

consists of series of iteration to match the set duration, minimizing the propellant consumption. In this case, the propagation is terminated when the target position is reached under the duration limitation. More details on the phasing manoeuvre can be found in [70].

2.5.5 Output and result analysis module

To complete the mission analysis procedure is fundamental to elaborating the raw data for a clear understanding of the results obtained and eventually for comparison among different simulations. This capability is provided in MAGNETO through the last module of the software, specifically developed with a dedicated process for fulfilling the user needs of output analyses.

The first step allows the user to save the raw data with the desire format and name. Then, a list is proposed to the user for the selection of the typology of analysis to execute.

The main options are related to the possibility to plot the different output values also uploading other result datasets for direct comparisons. The other key capability introduced is a trade-off process aimed to select the best design options.

This process follows the Analytic Hierarchy Process (AHP) commonly used during the preliminary design phases, where the high-level selection of the best design options shall be performed to steer the subsequent analysis phases.

The AHP consists of the definition of Figures of Merit (FoM) that are exploited as quantitative terms to highlight specific features of both mission and system design results.

These parameters are used to drive the evaluation to guarantee the representativeness of the stakeholder needs in the selection of the optimal solutions. Each FoM can have a different priority in ranking the result alternatives included in the trade-off. To intercept how the stakeholder judge whether each FoM has lower or higher importance, the weights are selected between 1 and 9 [71].

However, most of the time, the assessment of the weight is strongly driven by individual feeling, usually resulting in a spread of weight value if a group of stakeholders is surveyed. Therefore, in MAGNETO, the trade-off module, a Monte-Carlo process was implemented to properly evaluate the weights' set. As a result of a stakeholders' survey, the minimum and maximum values of the weight spread range are considered. The final FoM weight is consequently derived according to Eq. (2.24).

$$W_h = \frac{\sum_{k=1}^N \left(\frac{rand(W_{\min |i}, W_{\max |i})_k}{\sum_{q=1}^M rand(W_{\min |i}, W_{\max |i})_q} \right)}{N} \quad (2.24)$$

Where: N is the MonteCarlo random cases, $W_{\min |i}$ is the i^{th} FoM lower weight and $W_{\max |i}$ is the i^{th} FoM maximum weight.

The last characteristics associated with each FoM is the direction of the evaluation. Again, the evaluation is in charge of the stakeholders who can judge if a specific FoM shall be minimized (LOW) or maximized (HIGH).

The FoM list with the related weights and direction can be defined in a dedicated section of the input file. Once the user selects the trade-off analysis, MAGNETO can upload this information and process the trade-off elaborating the raw data from different simulations.

For what concern the evaluation of the space tug, a list of FoM is defined by default (see Table 13).

Table 13: trade-off FoM, weights direction and results' source.

Figure of Merit	W_{MIN}	W_{MAX}	Dir	Source
S/C dry mass	8	9	LOW	S
Propellant mass	8	9	LOW	S
Total S/C power	7	9	LOW	S
Delta-V	6	8	LOW	S
Total transfer time	8	9	LOW	S
Return transfer time	5	6	LOW	S
EPS cost	7	8	LOW	PP
Propellant cost	7	8	LOW	PP
EPS reliability	6	9	HIGH	PP
EPS TRL	7	9	HIGH	PP
EPS Complexity	6	8	LOW	PP
Source:				
S: simulation. Values directly collected from MAGNETO simulation results.				
PP: post-processing. A specific model was introduced for the assessment of this FoM.				

Some of the FoMs listed in Table 13 are evaluated with specific models during the post-processing of the raw data resulting from the simulation performed with MAGNETO. The main assumption made on these models are listed below:

- **EPS STRING COST:** this FoM consists of an estimation of the recurrent cost (RC) of the EPS components, and it is numerically evaluated through the model introduced by Hofer in [59]. The growth percentage considered in the model foreseen an increase of two times the total cost of the string every 10 kW of EPS power budget.
- **PROPELLANT COST:** of particular relevance when a trade-off of a system presenting the utilization of alternative propellant is performed. The quotations of 2200 €/kg and 120 €/kg are used for xenon and krypton, respectively. The

user can be modified in the input file values to updated them according to the last market quotation.

- **EPS RELIABILITY:** the reliability of the EPS architecture is defined Through the “K out of n” model, which processes the reliability of the EPS string. As previously defined, the tank assembly and the PMA component are then considered with a series approach.
- **EPS TRL:** this value can be related either to specific components or the overall system. Its definition follows what detailed in [72]
- **EPS COMPLEXITY:** this FoM takes into account the (i) integration, (ii) validation and (iii) operational complexities. Moreover, it depends on the number of components involved in the EPS string and their arrangement.

The final trade-off ranking is obtained ranking the resulted scored computed with the following expression:

$$S_i = \sum_{h=1}^M \delta_h \cdot W_h \cdot V_{hi} \quad (2.25)$$

where S_i represents the final score of the i^{th} case under comparison, δ_h is the direction of trade-off defined for each h^{th} FoM, V_{hi} is the i^{th} FoM normalized value.

2.6 Main case study results

To prove the effective utility of MAGNETO, two different investigations were performed. The first analysis compares different space tug EPS architectures designed for an LEO-GEO OSS scenario. This analysis was introduced to validate the single sizing models and prove the effectiveness of the trade-off process module in selecting the optimal architectural solution. The second introduced case study was instead related to complete analysis of multiple LEO-GEO scenario where alternative architectures of the space tug were included in complex OOS operations.

2.6.1 EPS architecture comparison

As previously introduced, the adoption of electric propulsion devices brings a series of criticalities impacting the design of the platform and the consequent mission analysis in term of planning and operations. This is particularly relevant for high-power Hall thrusters such as the 5kW and 20kW. All the different typology of budgets (e.g., mass, power, thermal) and mission constraints such as launchable spacecraft mass, transfer time, and spacecraft operation shall be carefully evaluated during the preliminary design of a space tug targeting a sustainable OOS scenario. In particular, the comparison analysis consists of three trade-offs specifically developed to assess the design of alternative EPS string architecture, adopted propellant and electric power feeding architecture. The description of these alternatives and the design model introduced in the sizing routine of MAGNETO are detailed in Section 2.5. The first trade-off considered the evaluation of the EPOS string based on a monolithic architecture (single EPS string) and cluster architecture (multiple EPS string). This comparison was performed, keeping the overall power consumption constant. Therefore, while the 20-kW class (HT20k) was considered for the monolithic configuration, the cluster configuration was based on four 5kW-class thrusters (HT5K). As previously mentioned, the amount of propellant necessary for OOS scenarios could jeopardize both the economic and the technological feasibility of the mission itself. Therefore, the adoption of an alternative propellant represents a valid solution to carefully investigate. In particular, the adoption of krypton as an alternative propellant with respect to the commonly used xenon is nowadays envisioned for the future electric propulsion base spacecraft as the space tug. The last alternative architecture assessed with the following trade-off is the impact at the system and subsystem level of the DDU architecture.

The reference mission scenarios introduced for the derivation of the mission parameters impacted by the different design alternatives is the MS.1, where a 2 tons telecommunication satellite is transferred from LEO up to its final operative position in GEO orbits.

The design of the servicer space tug was reiterated for each architecture alternatives following the cases reported in Table 14:

Table 14: alternative design options under analysis.

	MONOL.	CLUSTER	PPU	DDU	XENON	KRYPTON	
1	X		X		X		CASE#1
2	X		X			X	CASE#2
3	X			X	X		CASE#3
4		X	X		X		CASE#4

Two subsets of thruster operative points were selected for this analysis in order to identify the cross effects of the different cases under study. The four cases reported in Table 14 were analysed considering both sets. In specific, SET#1 consists of operative point derived fixing the specific impulse (I_{sp}) and the the total thrust generated by the EPS. As a consequence, the cluster architecture considers four 5kW thrusters for a total thrust level equivalent to that generated by the 20kW-class thruster operated at 20kW. The other parameters involved in the definition of the operative points have been identified over the operational envelopes of the HT5k and HT20k operated with both xenon and xrypton.

Table 15: SET#1 of operative points for HT5k and HT20k.

SET#1	POWER	THRUST	SPECIFIC IMPULSE	VOLTAGE	PROPELLANT MASS FLOWRATE
	[kW]	[N]	[s]	[V]	[mg/s]
HT20k Xe	21	1	2500	450	40.5
HT20k Kr	22,5	1	2500	375	40.5
HT20k Xe (DDU case)	21	1	2500	450	40.5
HT5k Xe	6	0,25	2250	600	10.2

Fixing the thrust level and the specific impulse of the thruster, for krypton operation, the discharge voltage results to be lower due to the higher atomic mass of the Kr neutrals compared to the Xe neutrals. On the contrary, the discharge power

of the thruster operating with krypton results higher because of the higher ionization losses compared to the xenon.

The SET#2 was instead derived, keeping constant both the thruster discharge voltage and the thruster discharge power, as indicated in Table 16. In this case, the krypton case presents a higher specific impulse and a reduced thrust compared with the performance obtained with xenon.

Table 16: SET#2 of operative points for HT5k and HT20k

SET#2	POWER	THRUST	SPECIFIC IMPULSE	VOLTAGE	PROPELLANT MASS FLOWRATE
	[kW]	[N]	[s]	[V]	[mg/s]
HT20k Xe	21	1	2500	450	40.5
HT20k Kr	21	0,77	3000	450	26.4
HT20k Xe DDU	22,2	1,06	2550	450	42.4
HT5k Xe	5,25	0,26	2130	450	12.4

Through the custom input file, the two datasets were introduced in MAGNETO while the mission scenario, as well as the selection of the alternative architectures, were selected to the standard user interface.

The direct comparisons were firstly performed to highlight the intrinsic feature of the alternative options, in specific: (i) monolithic vs cluster using both SET#1 and SET#2 of operative points, (ii) PPU vs DDU using both SET#1 and SET#2 of operative points and (iii) krypton vs xenon using both SET#1 and SET#2 of operative points. For these simulations performed with MAGNETO, the trade-off was based on the FoM defined in Section 2.5.5.

- *RESULT FOR THE OPERATIVE POINTS OF SET#1*

First, the comparison between monolithic and cluster architecture is shown in Table 17. As expected, considering the higher number of components, the S/C dry mass for the platform based on a cluster architecture is higher than the dry mass resulting in the monolithic architecture. As a direct consequence, the trajectory propagation results in a longer transfer time, a higher propellant mass that further impacts with an increment of the related costs. The delta-V values result comparable. An important FoM which presents a significant variation between the two architecture

is the reliability of the EPS. The cluster results to be more reliable due to the higher number of components present in the system, which allows the mitigation of multiple failures.

Table 17: Monolithic vs Cluster architecture, SET#1 operative points, comparison results. The bolded value results in the optimal trade-off solution.

EPS architecture	Monolithic	Cluster
EPDCS architecture	PPU	PPU
Propellant typology	Xe	Xe
S/C dry mass, kg	882,0	1051,6
Propellant mass, kg	801,3	876,6
Total transfer time, days	277,2	302,6
Round transfer time, days	214,7	228,5
Delta-V, m/s	9179,8	9177,4
Complexity	1	4
Thruster Cost, M€	8	15,9
Reliability	0,95	0,99
Final rank	-0,3025	-0,4317

The second comparison was performed considering the classical PPU architecture counterposed with the DDU approach. The main benefit obtained with the adoption of the DDU is the reduction of the spacecraft dry mass of about 10% compared to the mass on an EPS based on PPUs. As a consequence, the time necessary to transfer the telecom satellite decreases with a consequent reduction of the propellant mass employed for the end-to-end mission. As previously mentioned in the DDU description, the adoption of the DDU architecture forces the operation entire power bus and the solar arrays at a higher voltage level. Considering both the higher efficiencies of the modified PPU and the lower losses in the bus lines, the total power consumption is reduced. The main disadvantages of this architecture are the lower TRL level of the impacted components, such as the solar arrays.

Table 18: PPU cs DDU, SET-1 operative points, comparison results.

EPS architecture	Monolithic	Monolithic
POW architecture	PPU	DDU
Propellant typology	Xe	Xe
S/C dry mass, kg	882,0	806,5
Propellant mass, kg	801,3	766,9
Total Power, W	25607,3	24359,6
Total transfer time, days	277,2	265,2
Round transfer time, days	214,7	208,2
Delta-V, m/s	9179,8	9178,9
Complexity	1	0,5
TRL	9	5
Final rank	-0,3763	-0,3561

The last trade-off considers the alternative propellant utilization. The main outputs from the mission simulation and the score resulting from the trade-off are reported in Table 19. The storage condition of the krypton results in a higher tankage fraction that, in association with the higher thruster discharge power for the selected operative points, implicates a higher dry mass of the spacecraft. For most of the FoMs involved in the trade-off, an average increment of 9% occurred compared with the xenon-based system. Despite these negative trends, the saving of over 90% on the propellant costs results in the main benefit for considering krypton as the best alternative option to the classical used xenon.

Table 19: Xe vs Kr, SET#1 operative points.

EPS architecture	Monolithic	Monolithic
POW architecture	PPU	PPU
Propellant typology	Xe	Kr
S/C dry mass, kg	882,0	1010,4
Propellant mass, kg	801,3	859,6
Total Power, W	25607,3	27432,7
Total transfer time, days	277,2	297,2
Round transfer time, days	214,7	225,7
Delta-V, m/s	9179,8	9178,2
Propellant cost, M€	1,763	0,103
Final rank	-0,5522	-0,4406

In Figure 29, a summary of the trade-off main results for (i) dry and propellant mass, (ii) transfer time, (iii) propellant cost and (iv) total spacecraft power FoMs, with the related percentages, are graphically represented.

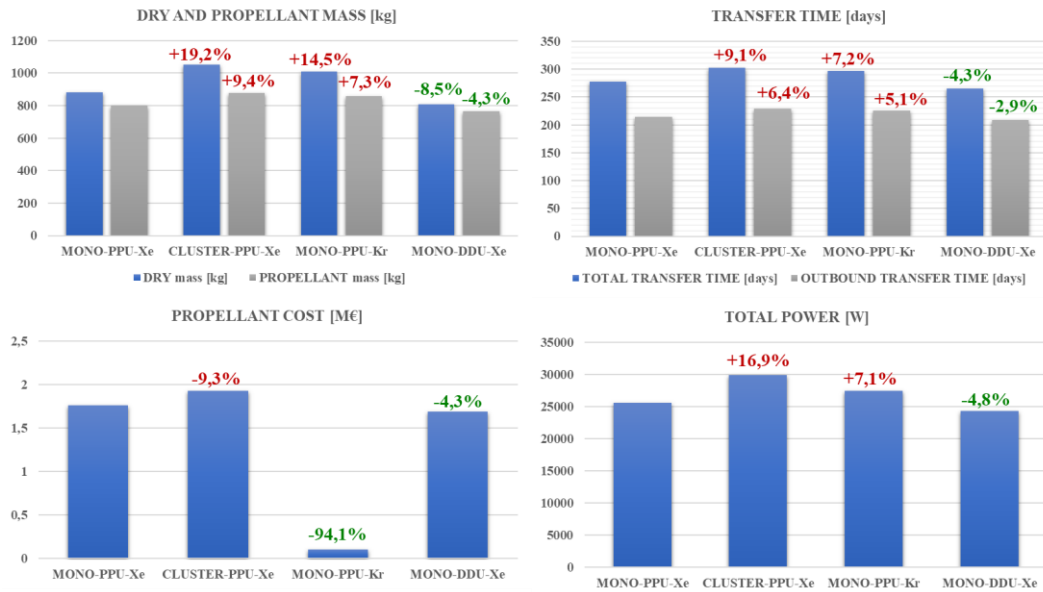


Figure 29: graphical comparisons with the related percentage for (i) dry and propellant mass budget (top-left), (ii) transfer time (top-right), (iii) propellant cost (bottom-left), (iv) total power (bottom-right).

- *RESULT FOR THE OPERATIVE POINTS OF SET#2*

In this paragraph, the architecture results simulated considering the SET#2 of operative points (constant discharge voltage and power) are compared.

The first comparison is between the EPS architecture alternative based on monolithic vs cluster configuration as performed with the previous analysis.

The main results concerning the FoMs exploited for the trade-off are reported in Table 20. The data show that the greater advantages are obtained through the propellant mass saving, of over 140kg, obtained with the monolithic configuration owing to the higher specific impulse reachable by the more powerful HT20k introduced in a monolithic configuration. This performance is intrinsically obtained by higher powerful thrusters, which operate with higher efficiencies.

In addition to the higher propellant mass necessary to complete the mission, the cluster architecture presents a higher dry mass caused by the higher number of components. As a result, the transfer time of the servicing transfer performed with a space tug equipped with a cluster of HT5k is 287,5 days against 277,2 days obtained with the monolithic HT20k architecture.

Table 20: Monolithic vs Cluster, SET-2 operative points, comparison results.

EPS architecture	Monolithic	Cluster
EPDCS architecture	PPU	PPU
Propellant typology	Xe	Xe
S/C dry mass, kg	882,0	935,6
Propellant mass, kg	801,3	1016,8
Total transfer time, days	277,2	287,5
Round transfer time, days	214,7	220,1
Delta-V, m/s	9179,8	9180,4
Complexity	1	4
Thruster Cost, M€	8	15,9
Reliability	0,95	0,99
Final rank	-0,2359	-0,3697

The second comparison concerning the PPU vs DDU architecture highlights that the latter is the optimal design solution of the POW and EPS subsystems. Also, with SET#2 of operative points, the same consideration can be derived. However, through the analysis of DDU with this second set of points, a lower propellant budget is obtained as well as a lower value for transfer time and delta-V owing to the higher value of specific impulse reachable with the higher efficiency of the entire EPS line. On the contrary, the higher thruster powers considered for the SET#2 turn in a higher power budget and an overall higher total dry mass. The trade-off FoM values are summarized in Table 21.

Table 21: PPU vs DDU, SET-2 operative points, comparison results.

EPS architecture	Monolithic	Monolithic
EPDCS architecture	PPU	DDU
Propellant typology	Xe	Xe
S/C dry mass, kg	882,0	835,2
Propellant mass, kg	801,3	762,1
Total Power, W	25607,3	25048,6
Total transfer time, days	277,2	253,3
Round transfer time, days	214,7	197,9
Delta-V, m/s	9179,8	9175
Complexity	1	0,5
TRL	9	5
Final rank	-0,3763	-0,3553

Finally, Table 22 collects the results of the comparison between alternative propellant. The optimal solution identified through the trade-off shows the advantages in the adoption of the krypton as the best alternative.

The higher specific impulse reachable with the thruster operated with krypton, around 3000s, allows a reduction of propellant mass consumption of 180 kg. The lower propellant budget reduced the spacecraft's dry mass, mainly owing to the lower tank mass. Selecting the operative points at constant voltage and discharge power to have comparable points, the operation with krypton results in a lower thrust level equal to 0,77 N, resulting in an additional 20% on transfer time xenon operation. Even in this case, the trade-off is strongly impacted by the cost of the propellant itself, for which an overall saving of 1.6M€ is obtained.

Table 22: Xe vs Kr, SET#2 operative points, comparison results.

EPS architecture	Monolithic	Monolithic
POW architecture	PPU	PPU
Propellant typology	Xe	Kr
S/C dry mass, kg	882,0	935,7
Propellant mass, kg	801,3	671,9
Total Power, W	25607,3	25607,3
Total transfer time, days	277,2	361,7
Round transfer time, days	214,7	276,8
Delta-V, m/s	9179,8	9177,8
Propellant cost, m€	1,763	0,081
Final rank	-0,5522	-0,4415

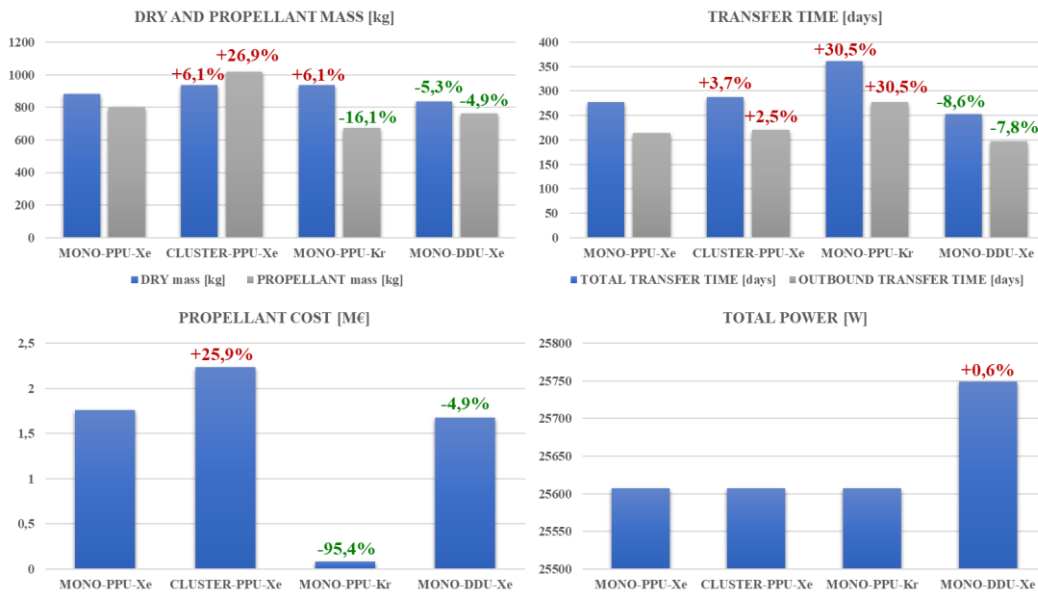


Figure 30 graphical comparisons with related percentage for (i) dry and propellant mass budget (top-left), (ii) transfer time (top-right), (iii) propellant cost (bottom-left), (iv) total power (bottom-right).

- *MERGED TRADE-OFF RESULTS*

To fully highlight the advantages, also including the different rationale exploited to derive the two set of operative points, a merged trade-off was performed, merging the trade-offs.

The final score shows that the krypton-based system is the best architecture option for the OOS. The krypton operative point belongs to SET#1 (1N, the 2500s and 22,5 kW), highlights a good balance between the propellant mass, transfer time and propellant cost. As well described, the propellant cost played a key role in the determination of the final score of the trade-off.

Table 23: comparison of all the cases under analysis.

Operative Points	EPS architecture	EPCDS architecture	Propellant	SCORE	RAN K
SET_1	Monolithic	PPU	Xe	-0,0707	5
	Monolithic	PPU	Kr	-0,0653	1
	Monolithic	DDU	Xe	-0,0703	3
	Cluster	PPU	Xe	-0,0923	6
SET_2	Monolithic	PPU	Xe	-0,0707	5
	Monolithic	PPU	Kr	-0,0660	2
	Monolithic	DDU	Xe	-0,0701	4
	Cluster	PPU	Xe	-0,0932	7

2.6.2 Scenario comparisons

This second branch of analyses was performed to assess the effectiveness of the propagation module introduced in MAGNETO for the different manoeuvres foreseen for a space tug. Both mission profiles were considered for these analyses. As specified in Section 2.4, the MS.1 consists of a mission profile where the space tug offers a transferring service for a telecommunication satellite from its LEO released orbit up to its final GEO location. After the correct positioning of the serviced satellite, the space tug performs a return transfer down to a parking orbit where it waits for the following service transfer. The second scenario adds an additional service operation consisting of relocating a second telecommunication satellite from one GEO location to a second location before returning to the parking orbit.

Thus, a set of alternative cases were selected considering the following alternative categories:

- Selection of the thruster: two thrusters were investigated, the HT5k and the HT20k.

- EPS architecture: to provide comparable results and extend the analysis to very high-power spacecraft, the cluster configuration was introduced for both thruster's selection.
- Payload mass: the serviced payload is represented by the telecommunication satellite transferred either from LEO up to GEO or during the relocation operation.
- Phasing longitude: in the case of MS.2, a set of delta longitude was considered for relocating the telecommunication satellite.

In Figure 31, the alternative cases under analysis are reported.

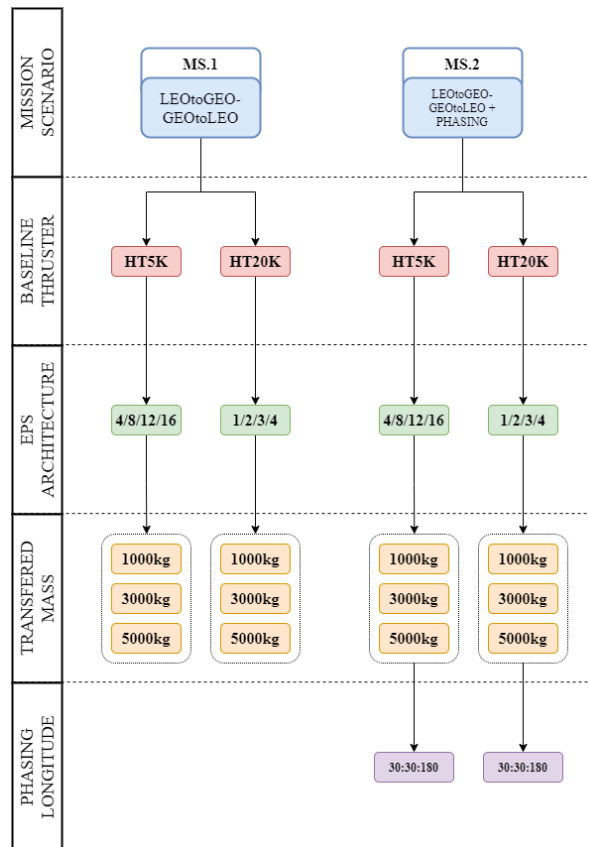


Figure 31: alternative tree of the simulations performed with MAGNETO on both scenarios.

For a direct comparison of the results, the 5kW-class HT5k was always considered as a part of a cluster of four HT5k to reach comparable performance in relation to the powerful HT20k.

Over the operative thruster map of both thrusters, an operative point subset was considered. In particular, the following requirements were imposed:

- The thrust of the EPS shall be between 1050 mN and 1350 mN.
- The specific impulse of the EPS shall be between 2050 s and 3000 s.
- The EPS input power shall be greater than 20kW.

According to [73] and considering the outputs of the analyses performed in the framework of the SITAEL's GSTP 20kW project, presented in [68,74,75], this range performance represent the most interesting for the future adoption of high power Hall thruster (>15 kW). The high thrust level required allows shorter transfer time, decreasing the period in with the serviced satellite results unexploited for revenue generation. Moreover, the transfer itself shows a higher efficiency due to the faster escape manoeuvre from the lower altitude orbits, which directly impacts the propellant consumed during the transfer. The possibility to increase the quantity of xenon necessary for the completion of the mission is further mitigated by the range of specific impulse value limited by the requirements. That range can be reached by operating the thrusters at high-voltage or high power. For example, the HT20k shall operate with a discharge voltage greater than 350V to exceed a specific impulse of 2200 s at 20kW of discharge power. Considering all these limitations, 21 operative points were identified, fulfilling the requirements on the operative envelope of the HT20k (see Table 24).

Table 24: HT20k selected operative points.

ID Operative Point	Thrust [N]	Isp [s]	Voltage [V]	Power [W]
<i>OP</i>₉₄	1,06	2303	400	21250
<i>OP</i>₉₄	1,08	2216	375	21250
<i>OP</i>₉₆	1,11	2123	350	21250
<i>OP</i>₁₀₄	1,06	2544	475	22500
<i>OP</i>₁₀₅	1,08	2473	450	22500
<i>OP</i>₁₀₆	1,10	2397	425	22500
<i>OP</i>₁₀₇	1,13	2315	400	22500
<i>OP</i>₁₀₈	1,15	2226	375	22500
<i>OP</i>₁₀₉	1,17	2132	350	22500
<i>OP</i>₁₁₄	1,06	2756	550	23750
<i>OP</i>₁₁₅	1,08	2695	525	23750
<i>OP</i>₁₁₆	1,10	2631	500	23750
<i>OP</i>₁₁₇	1,12	2562	475	23750
<i>OP</i>₁₁₈	1,14	2488	450	23750
<i>OP</i>₁₁₉	1,16	2409	425	23750
<i>OP</i>₁₂₀	1,19	2326	400	23750
<i>OP</i>₁₂₁	1,21	2235	375	23750
<i>OP</i>₁₂₂	1,24	2140	350	23750
<i>OP</i>₁₂₄	1,09	2892	600	25000
<i>OP</i>₁₂₅	1,10	2836	575	25000
<i>OP</i>₁₂₆	1,12	2776	550	25000
<i>OP</i>₁₂₇	1,14	2713	525	25000
<i>OP</i>₁₂₈	1,16	2646	500	25000
<i>OP</i>₁₂₉	1,18	2576	475	25000
<i>OP</i>₁₃₀	1,20	2500	450	25000
<i>OP</i>₁₃₁	1,23	2420	425	25000
<i>OP</i>₁₃₂	1,25	2335	400	25000
<i>OP</i>₁₃₃	1,28	2244	375	25000
<i>OP</i>₁₃₄	1,30	2146	350	25000

For what concern the HT5k, it was introduced in the analysis in a cluster configuration of four thrusters. In this case, the selection of the thruster operative points was performed considering four time the values of thruster power and generated thrust. The resulted performance were then filtered according to the imposed requirements. The selected operative points are collected in Table 25.

Table 25: HT5k selected operative points.

ID Operative Point	Thrust [N]	Isp [s]	Voltage [V]	Power [W]
<i>OP₁₄₆</i>	0,281014	2117,149	400	5500
<i>OP₁₄₇</i>	0,289758	2061,47	375	5500
<i>OP₁₄₈</i>	0,299212	2003,563	350	5500
<i>OP₁₆₆</i>	0,282432	2291,425	475	6000
<i>OP₁₆₇</i>	0,290231	2244,655	450	6000
<i>OP₁₆₈</i>	0,297558	2193,43	425	6000
<i>OP₁₆₉</i>	0,306539	2139,978	400	6000
<i>OP₁₇₀</i>	0,315756	2083,185	375	6000
<i>OP₁₇₁</i>	0,326155	2022,494	350	6000

For MS.1, considering the alternative cases reported in Figure 31, and including the limitations imposed on the EPS performance, a total of 357 cases were investigated with MAGNETO through a complete spacecraft sizing and mission profile propagation.

The main objective of this second analysis is to highlight the main trends in particular related to spacecraft budgets such as mass, propellant and power budget. In addition, the key result of the propagation is the derivation of the transfer time for each space tug design case.

The results are presented for a direct comparison of the space tug design based on both thrusters. The comparable values obtained are mainly driven by the approach followed in the identification of the alternative cases, whereas the cluster architecture of the EPS was intentionally selected for the thruster directly comparing the subsystem performance. Therefore, considering the coupled-cluster cases based on the 1:4 ratio between the HT20k and the HT5k architecture, the main impact on the results can be attributed to the number of components necessary to operate the EPS. Therefore, in Figure 32, Figure 33, Figure 34 and Figure 35, the results are grouped in four groups according to the introduced cluster architectures. As shown in Figure 32, the dry mass of the space tug has an overall range between 3.2 tons up to 16.1 tons. Considering that the propellant fraction over the wet mass varies between 20% up to 40%, the final wet mass has a range between 4.4 tons and 22.2 tons, as shown in Figure 33.

Starting for the cluster based on the lower number of thrusters, hence the configuration with one HT20k and that with for HT5k, for the following comparable architecture (based on 2 HT20k and eight HT5k), the average increment of the dry mass results around 50%. The subsequent cases implicate an

average increment of 66% (3 HT20k w.r.t. 2 HT20k, 12 HT5k w.r.t. 8 HT5k) and 75% (4 HT20k w.r.t. 3 HT20k, 16 HT5k w.r.t. 12 HT5k) of the space tug dry mass. For all configurations, particularly relevant is the mass allocated to the POW subsystem. With an average percentage of 47% over the dry mass of the different space tug solutions, it represents the highest mass allocation compared with the other subsystems. This characteristic is a direct consequence of the high power required to operate the EPS subsystem based on such power-class Hall thrusters. In Figure 34, the space tug power budget is reported showing that for the configuration based on 4 HT20k or 16 HT5k, the power required to be generated, managed and partially stored through the adoption of battery packs is around 100 kW. As a direct consequence, the greater number of operative thruster results in a lower transfer time for which, the completion of the mission is guaranteed. The total duration for these configurations' ranges between 194 days up to 275 days for 16 HT5k servicing the 1 ton telecom satellite and 16 HT5k transferring the 5 tons satellite respectively, depending on the selected operative point.

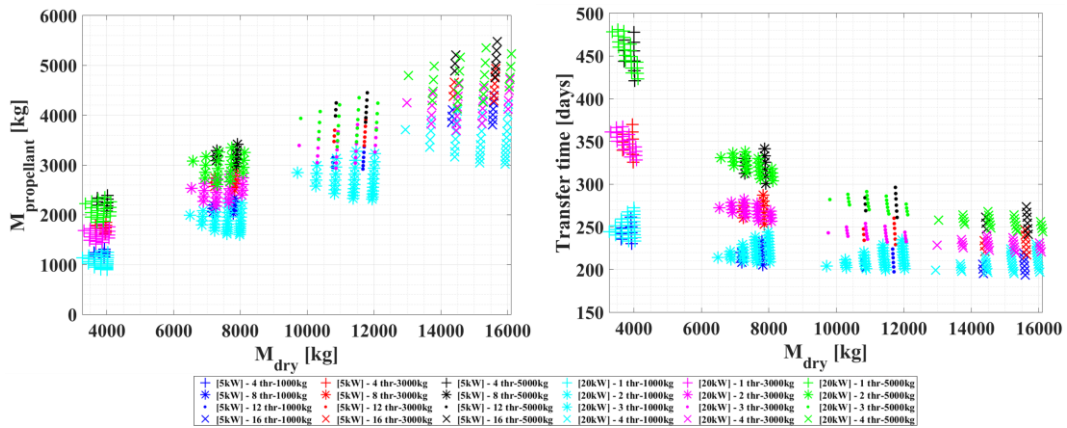


Figure 32: (left) propellant mass ($M_{propellant}$) and (right) transfer time ($t_{transfer|TOT}$) w.r.t. the space tug dry mass (M_{dry}) derived for MS.1 for the operative points of both HT5k and HT20k.

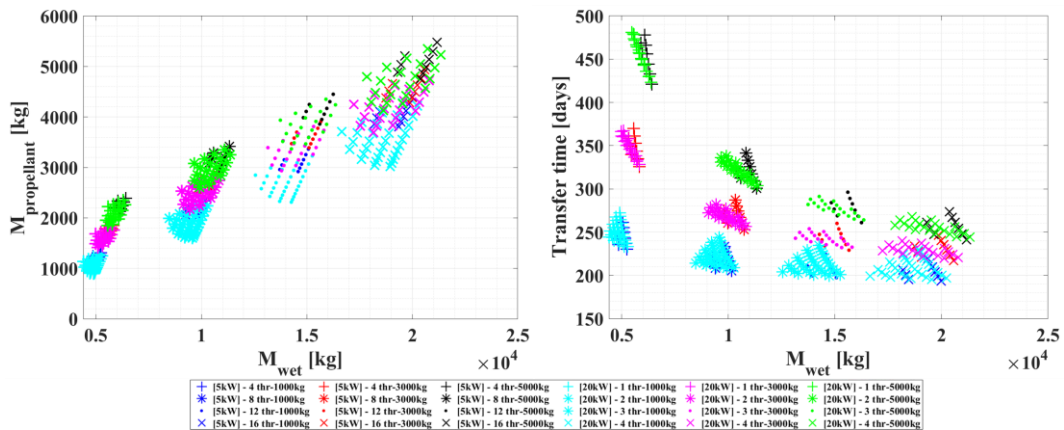


Figure 33: (left) propellant mass ($M_{propellant}$) and (right) transfer time ($t_{transfer|TOT}$) w.r.t. the space tug wet mass (M_{wet}) derived for MS.1 for the operative points of both HT5k and HT20k.

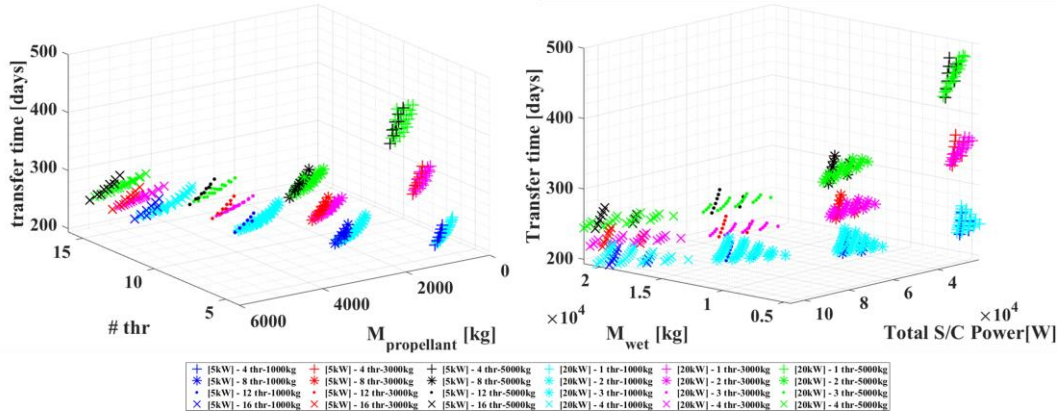


Figure 34: (left) transfer time ($t_{transfer|TOT}$) vs number of thrusters in the cluster (#thr) vs propellant mass ($M_{propellant}$) and (right) transfer time ($t_{transfer|TOT}$) vs wet mass (M_{wet}) vs total space tug power budget ($P_{S/C|TOT}$) derived for MS.1 for the operative points of both HT5k and HT20k.

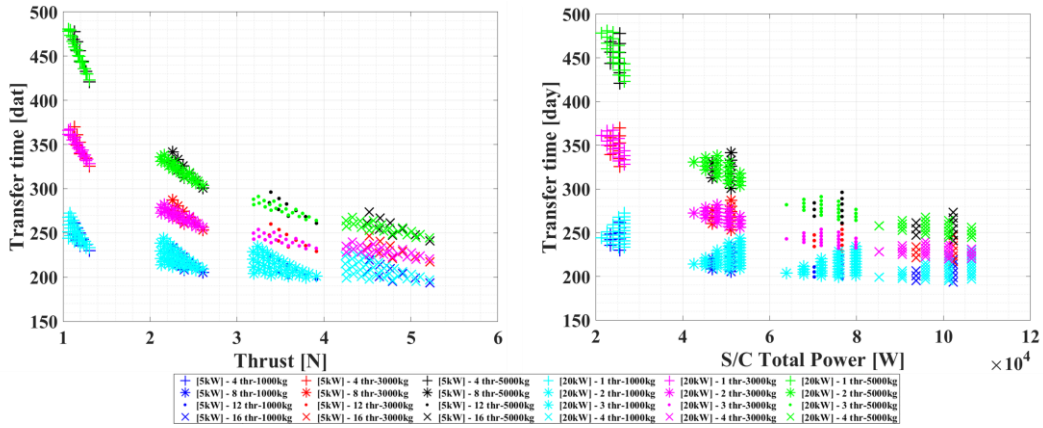


Figure 35: (left) transfer time ($t_{transfer|TOT}$) vs total generated thrust (T_{EPS}) (right) transfer time ($t_{transfer|TOT}$) vs total space tug power budget ($P_{S/C|TOT}$) derived for MS.1 for the operative points of both HT5k and HT20k.

As shown in Figure 35, reducing the number of thrusters, the solutions present higher mission periods up to 479 days for the configuration based on the 20kW HT20k transferring five tons telecom satellites.

The results related to the number of thrusters and the provided EPS performance concern only the thrusters actively operated to generate thrust. A redundancy logic was introduced to guarantee a minimum fail-safe condition in case of failure. In specific, the logic followed for the derivation of the number of stand-by thrusters was to introduce a redundant thruster for every 4 operative thrusters. In this way, a single failure event is complete mitigated for the baseline cluster of four thrusters introduced as a baseline for the HT5k cases. To further increase the level of reliability of the entire EPS, the PPUs were considered cross strapped with the PPU dedicated to the redundant thruster branch. With this option, in case of failure, the redundant PPU is used to feed the failed PPU on a nominal operative branch.

Following the simulation cases summarized in Figure 29, MS.2 has been simulated to highlight the impact of the relocation OOS on the overall preliminary mission budgeting.

In this scenario, the space tug mission profile consists of nine different mission phases (see Figure 12). First, the space tug starts the operation in its parking orbit, waiting for the launch of a telecommunication satellite to be serviced. After the rendezvous with the satellite, it performs an LEO-GEO manoeuvre thanks to the thrust provided by the electric thrusters. Then, after the release of the telecom satellite on its operative position, it performs a phasing manoeuvre to reach a second telecommunication satellite to be serviced. After its rendezvous and docking, a second phasing manoeuvre allows relocating the new satellite in its required position. Finally, the space tug will return to the parking orbit for the maintenance and refuelling operations and the waiting period before another OOS operation.

This study allows the investigation of the main properties at both mission and system level of the space tug in the function of the different delta longitude angles considered in the phasing manoeuvres performed for the relocation of the second serviced satellite. The following phasing angles (delta longitude) have been considered:

$$\Delta long = [30^\circ, 60^\circ, 90^\circ, 120^\circ, 150^\circ, 180^\circ]$$

In addition, the simulations consider different combinations of these angles for the first and second phasing manoeuvre to generalize the analysis.

A summary of the space tug configurations investigated with MS.2 is recalled in Table 26.

Table 26: space tug configurations simulated for MS.2.

	Thruster baseline	Propellant	Number of thrusters	EPS architecture
Configuration 1	HT20k	xenon	1,2,3,4	MIXED
Configuration 2	HT5k	xenon	4,8,12,16	CLUSTER

As already pointed out before, the number of thrusters in both power classes has been chosen to directly compare the selected architecture in terms of total power that shall be allocated to the EPS subsystem.

The operative points have been selected among those reported in Table 24 and Table 25 according to the requirements summarized in Table 27.

Table 27: Requirements for thruster operative points

		HT20k	HT5k
Thrust range	[N]	1,05-2	0,27-0,28
Specific impulse	[s]	2000-3000	2000-2200
Thruster discharge power	[W]	20000-21000	5000-6000

Following these boundaries, the operative points identified are:

Table 28: operative points.

Thruster	ID Operative Point	Thrust [N]	Isp [s]	Discharge Voltage [V]	Discharge Power [W]
HT20k	OP_{84}	1,064	2015,00112	325	20000
HT5k	OP_{145}	0,27	2168	425	5500

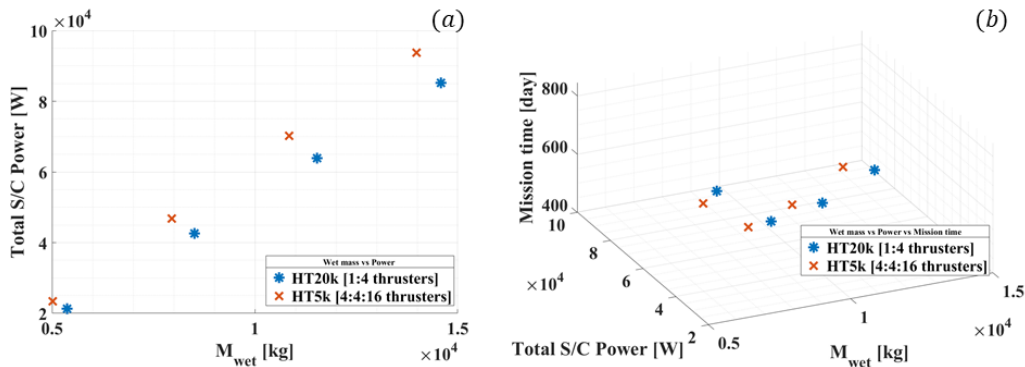


Figure 36. (a) The total power is compared with the total wet mass of the spacecraft [HT5k vs HT20k]. (b) The total power is compared with respect to wet mass and total mission time [HT5k vs HT20k]

Figure 36 shows how the total wet mass of the space tug changes in the function of the total power of the spacecraft. The first point figured from the left of each graph corresponds to:

- The blue marker is related to the space tug in which the EPS architecture is based on HT20k with 1 thruster;
- The red marker is related to the space tug in which the EPS architecture is based on HT5k with a baseline cluster-block of 4 thrusters.

As expected, the total wet mass increases with the increment of the total power mainly due to the higher mass of the electric power subsystem (POW) due to the higher power that shall be generated for the incremental number of the operative thruster. The power consumption for the architectures based on the HT5k is always greater than 11% with respect to the architectures based on the HT20k for all the cluster options.

Even though the solution with a higher power budget is characterized by higher complexity, dry mass and overall costs, it could represent the best solution for a mission with low durations need since the higher generated thrust.

The wet mass of the spacecraft increases by 3000kg for every thruster (or block of thrusters in the case of HT5k) added into the cluster for both configurations.

Figure 36 (b) shows how the mission time decreases when the total power, so the number of thrusters increases. The cluster configurations are analysed.

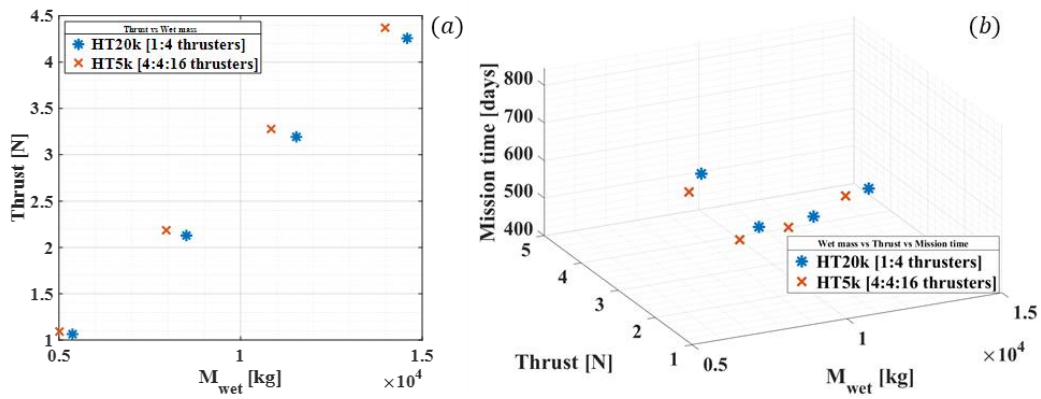


Figure 37. (a) Wet mass vs Total thrust. (b) Total thrust compared with mission time and wet mass

The total thrust of the different configurations follows the same behavior of the power trend. In Figure 37 (a), it is possible to see how the thrust increases with the decrease of the mission time. However, the configuration with high thrust and high power consists of higher dry mass values for the space tug. The highest thrust value equal to 4,4 N is obtained by the configuration having the HT5k as the baseline. As already mentioned, this configuration also presents a higher wet mass equal to 15t. Comparing the result with the dry mass shown in Figure 38, it is possible to notice that the propellant mass fraction, defined as the dry mass and wet mass ratio, is slightly lower than 50%.

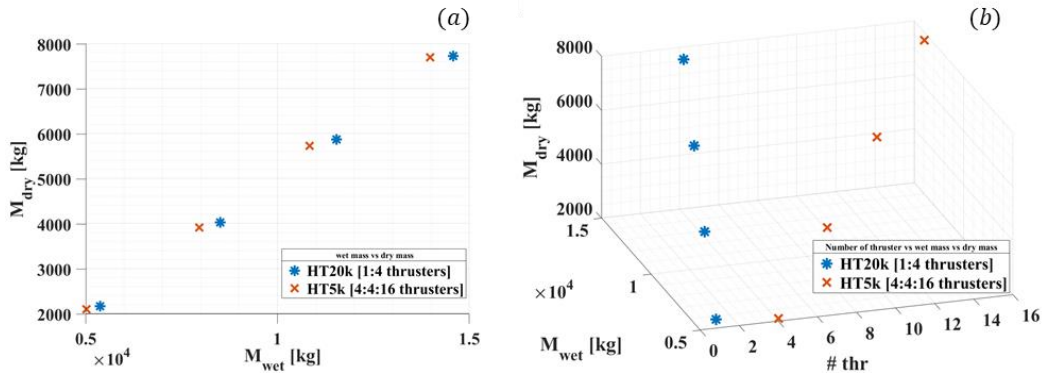


Figure 38. (a) Wet mass vs Dry mass. (b) Wet mass vs Dry mass vs number of thrusters

The payload mass considered for the study with different nine mission phases correspond to 3000 kg.

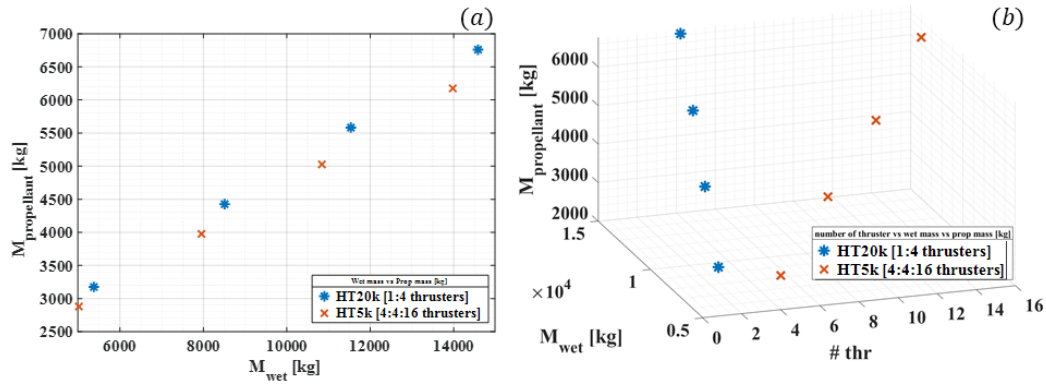


Figure 39. (a) Wet mass vs propellant mass. (b) Wet mass vs propellant mass vs number of thrusters

The propellant mass increase with the number of thrusters and the wet mass. It is possible to see that the prop mass starts to be 60 % of the wet mass for the configuration with the lowest number of thrusters and 42% for those configurations having the higher number of thrusters.

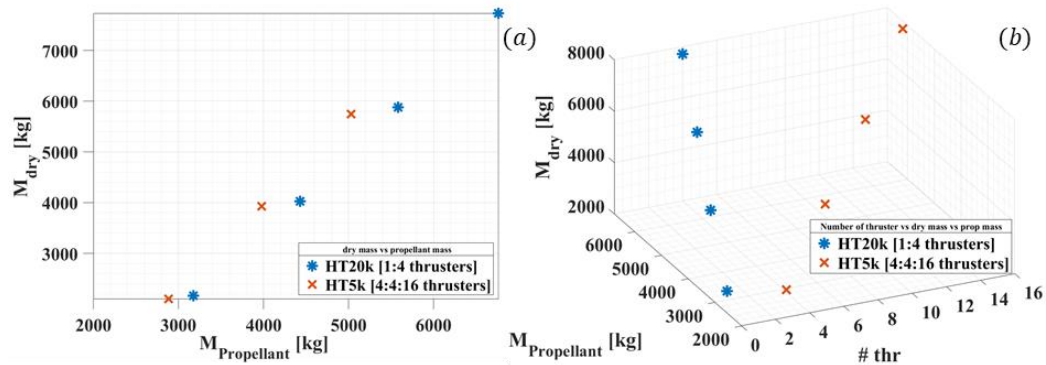


Figure 40. (a) Dry mass vs prop mass. (b) Dry mass vs prop mass vs Number of thrusters

The following results concern the main budgets and mission outputs of the Ms.2 relocation phase.

As previously presented, the MS.2 mission profile considered two phasing manoeuvres: the first one, performed by the space tug to reach the second serviced satellite while the second for relocating it in a new GEO longitude.

The general study consists of different simulation with all possible combinations of the main angles for the two phasing manoeuvres. The first relocation phase considered a fixed angle value of 30° . Table 29 reports the different delta longitude considered in the different simulated cases.

Table 29: Angles combinations

First phasing manoeuvre	Second phasing manoeuvre
30°	30°
30°	60°
30°	90°
30°	120°
30°	150°
30°	180°

This assumption was introduced to clearly highlight the main trends of the different mission and spacecraft main properties in function of the different delta longitude.

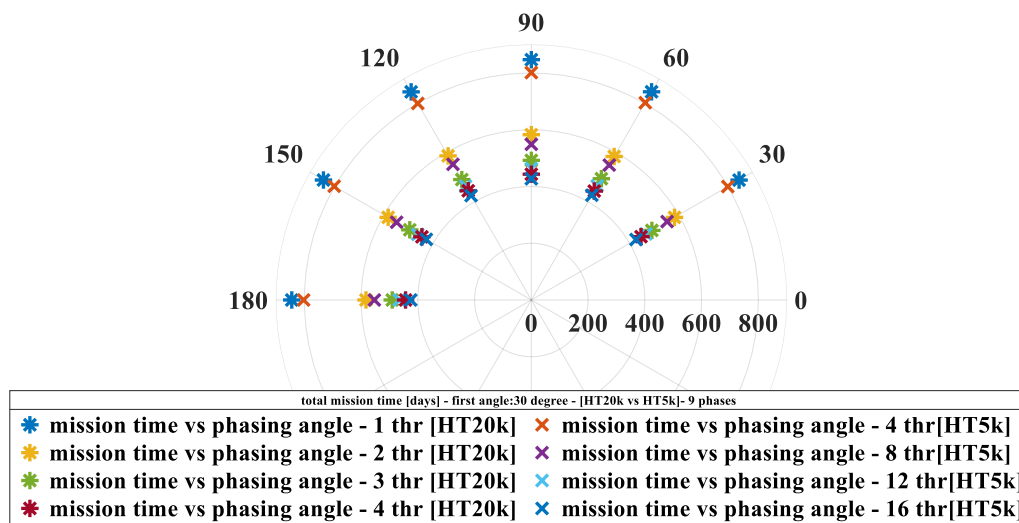


Figure 41. Total mission time vs second phasing manoeuvre angles [HT20k vs HT5k all n. thrusters configuration]

Figure 41 shows the HT20k and HT5k results obtained for the different EPS architectures. The mission time of the configuration with the lowest number of thrusters in the cluster is around 800 days for the total mission for both configurations. The mission time decreases with the number of thrusters up to 200 days for the configuration with 4 HT20k and 16 HT5k due to the higher thrust level available.

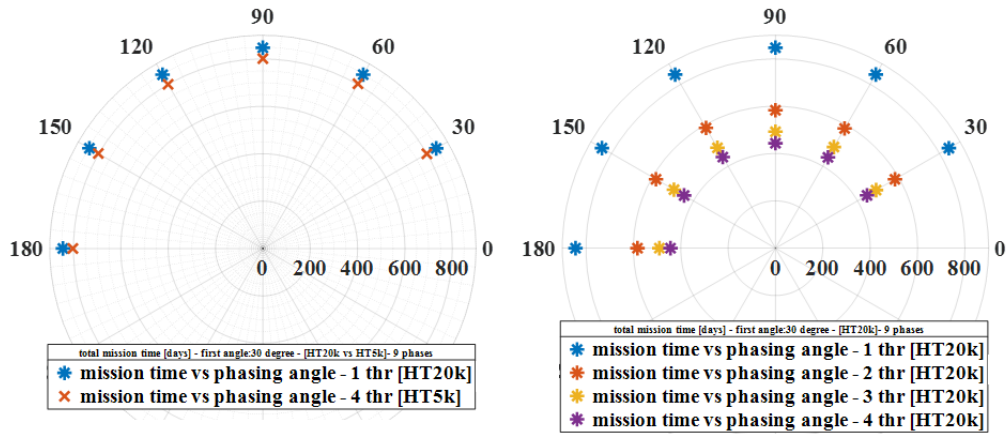


Figure 42. (a) Mission time [HT20k:1 thr vs HT5k:4 thr]; (b) Mission time for HT20k configurations.

The configurations' comparison is presented in Figure 43 (a), only considering the configurations with 1 HT20k and 4 HT5k. Thus, it is possible to see the difference between the mission time two configurations. Table 30 summarized the average mission durations for both configurations. The detailed results are presented in Appendix B.

Table 30: Total mission time data

Configuration	Average total mission time [day]
20 kw	845,26
5 kw	799,55

The satellite's dry mass includes all subsystems contributing to which a safety margin equal to 20% of the net mass has been considered due to the preliminary design phases.

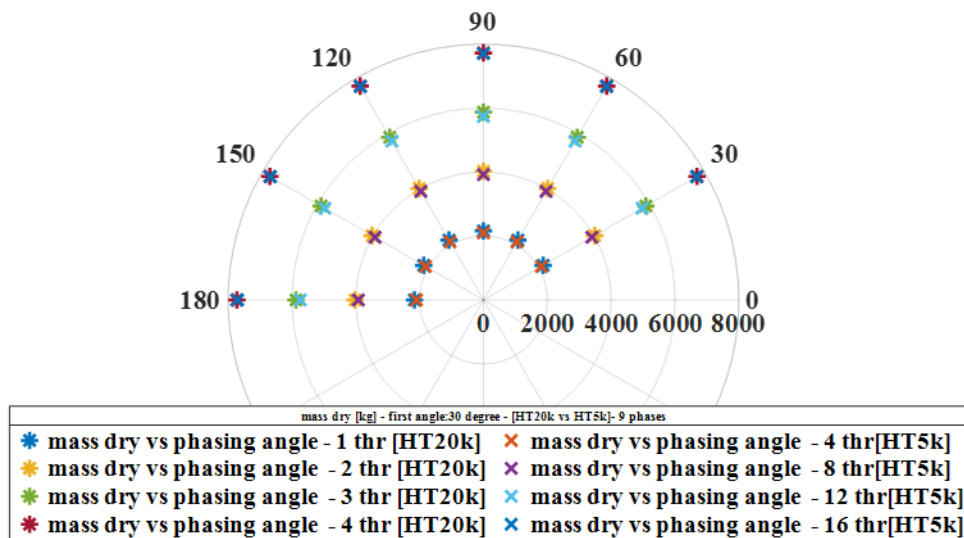


Figure 43. Dry mass vs second phasing manoeuver angles [HT20k vs HT5k all n. thrusters configuration]

In Figure 43, it is possible to see how the dry mass has the same values for the directly comparable cases in which for both configurations (based on HT5k and HT20k), total EPS power results comparable. As shown, the different delta longitude for the second phase with the first angle value fixed does not significantly change the total dry mass value.

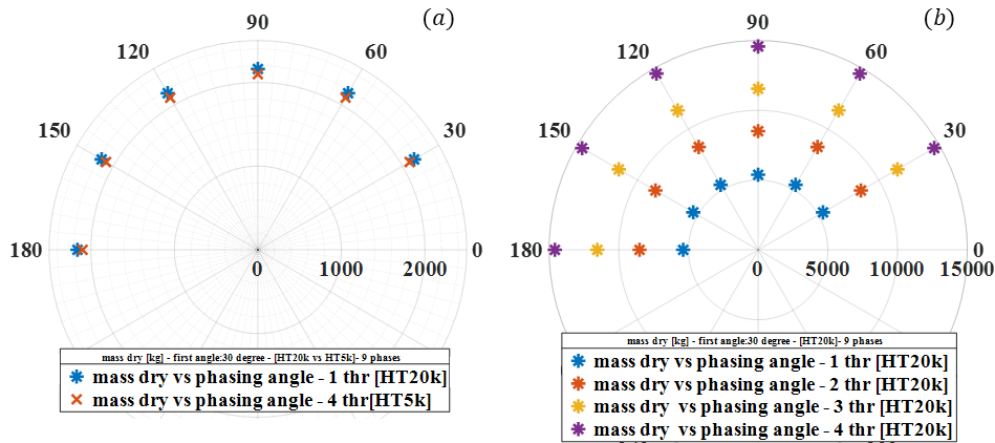


Figure 44.(a) Dry mass [HT20k:1 thr vs HT5k:4 thr]; (b) Dry mass for HT20k configuration

Even in Figure 44, the results are presented to compare the monolithic vs cluster configurations for 1 HT20k and 4 HT5k (a) and the comparison among all the architectures. In this case, the results refer to the spacecraft's wet mass, including the chemical propellant necessary for the close-range operations, the rendezvous and docking, and the undocking between the space tug and the serviced satellites.

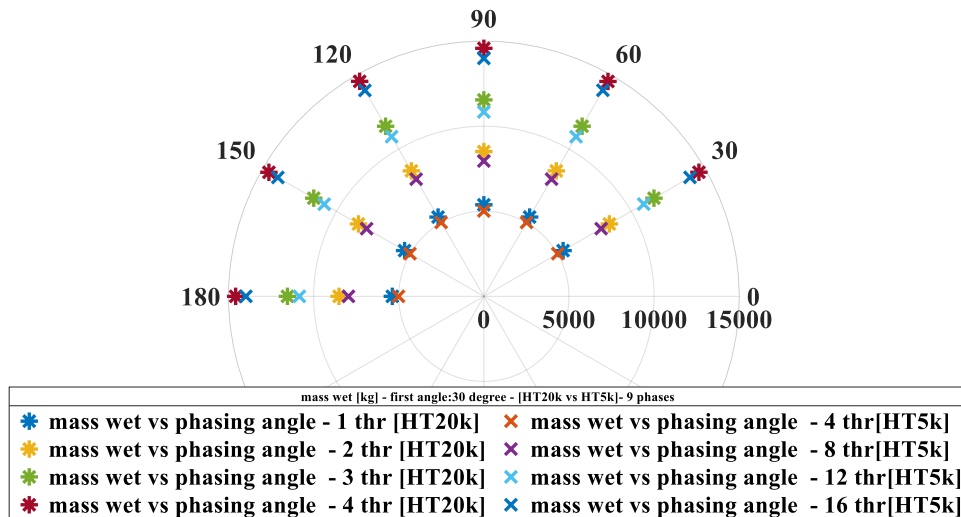


Figure 45. Wet mass vs second phasing maneuver angles [HT20k vs HT5k all n. thrusters configuration]

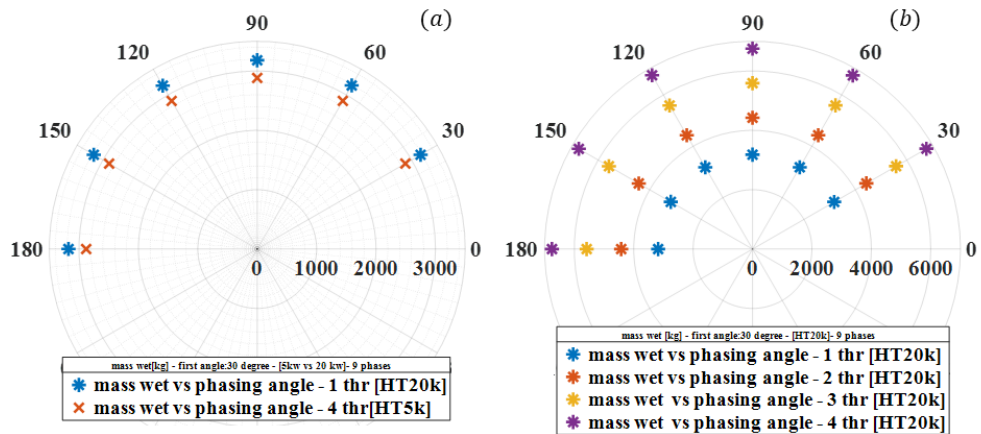


Figure 46.:(a) Wet mass [HT20k:1 thr vs HT5k:4 thr]; (b) Wet mass for HT20k configuration.

The wet mass of the space tug in the different configuration alternatives, including the telecom satellite wet mass equal to 3 tons, is presented in Figure 47. The final wet mass of the space-Tug considering payload mass. The mass values range from around 8300 kg for the configurations with the lowest number of thrusters (1 HT20k and 4 HT5k) up to around 15000kg (4 HT20k and 16 HT5k). Considering the launch capability of heavy and super-heavy launch vehicles, the possibility to launch the serviced satellite within the space tug for its first mission. This possibility could represent a substantial saving in terms of mission costs and propellant consumed by the space tug during the first phase of its mission.

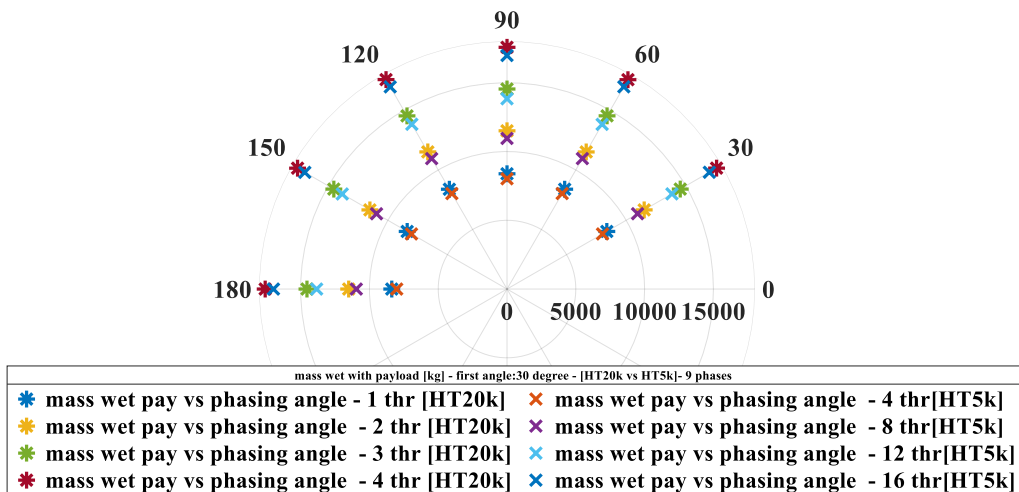


Figure 47. Wet mass with serviced satellite mass vs second phasing manoeuvre angles [HT20k vs HT5k all n. thrusters configuration]

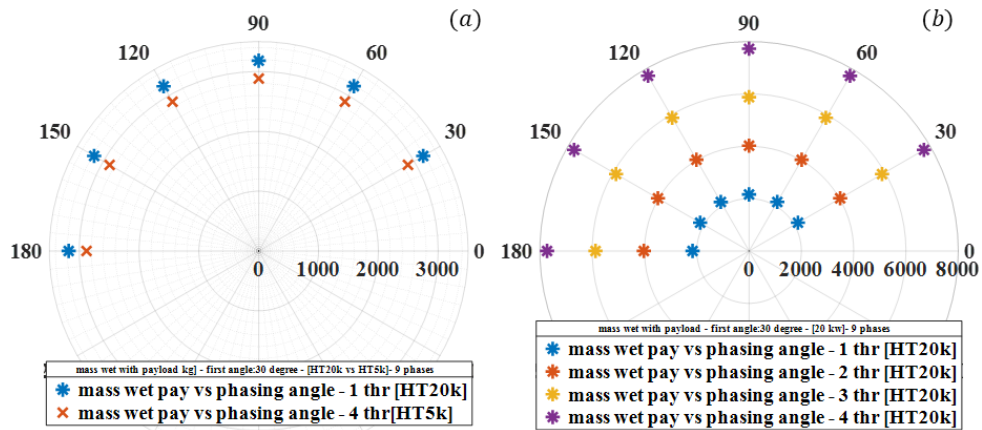


Figure 48: (a) Wet mass with serviced satellite mass [HT20k:1 thr vs HT5k:4 thr]; (b) Wet mass with serviced satellite mass for HT20k configuration.

In Figure 47, the propellant mass needed for the total mission scenario is presented. The results based on the configuration with HT20k present lower propellant mass values than those based on the HT5k thruster. This is mainly due to the higher thrust efficiency reached by the powerful thrusters, which decreases the propellant consumption. In fact, from Table 28, it is possible to observe that the operation point chosen for the HT20k presents a higher value of specific impulse, which determines the lower thruster consumption.

Consequently, the differences between the propellant mass values increase with the increment of the number of considered thrusters.

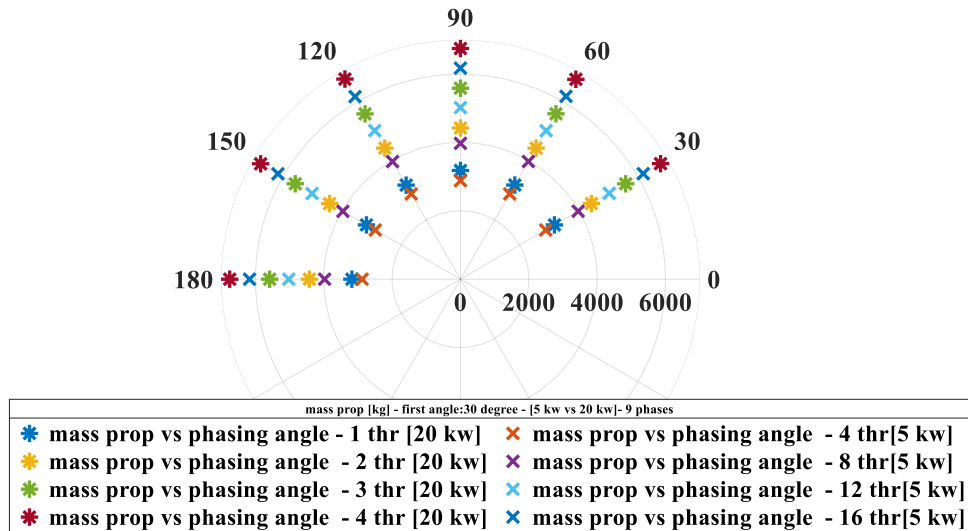


Figure 49. Propellant mass vs second phasing manoeuvre angles [HT20k vs HT5k all n. thrusters configuration]

The following results focused on the delta-V (only for electric propulsion transfers), the eclipse time, and the phase durations for the relocation angle cases report in Table 31.

Table 31: angle combinations for direct comparison of delta-V, phase durations, eclipse durations.

Thruster	1° phasing-Δ longitude [°]	2° phasing Δ longitude [°]
HT20k	30	180
HT5k	30	180

Table 32: results for HT5k configuration.

#	Phases MS.2 – HT5k conf.	delta-V [m/s]	Phase duration [day]	Eclipse duration [day]
1	Rendez-vous	0	0,20	0,08
2	LEO>GEO	4634,60	232,37	46,09
3	Rendez-vous (WP)	0	0,16	0,04
4	Rendez-vous	0	0,12	0
5	1° PHASING	0,50	1,08	0,04
6	Rendez-vous	0	0,20	0
7	2° PHASING	1,40	0,53	0
8	Rendez-vous	0	0,11	0,05
9	GEO>LEO	5038,50	190	28,88

Table 33: results for HT20k configuration.

#	Phases MS.2 – HT20k conf.	delta-V [m/s]	Phase duration [day]	Eclipse duration [day]
1	Rendez-vous	0	0,20	0,08
2	LEO>GEO	4630,0	245,14	48,85
3	Rendez-vous (WP)	0	0,17	0
4	Rendez-vous	0	0,11	0
5	1° PHASING	1,4	0,10	0
6	Rendez-vous	0	0,20	0
7	2° PHASING	1,3	0,44	0
8	Rendez-vous	0	0,12	0
9	GEO>LEO	5019,50	197	30,30

As shown in Table 32 and Table 33, the delta-V values for the phases in which the EPS is mainly exploited, such as LEO-GEO and GEO-LEO transfers, are similar. This is caused by the fact that the derivation delta-V is more dependent on the initial and final orbit set in input to MAGNETO rather than on the configuration investigated.

As previously defined, during the transfer from LEO to GEO, the space tug services a 3 tons telecom satellite. The higher mass of the overall space system (the space tug with telecom satellite docked) directly impacts the transfer durations, which results equal to 232 days for the HT5k configuration and 245 days for the HT20k configuration.

The duration of the first rendezvous manoeuvres (#1 in both tables) is considered as input data because the capability of MAGNETO does not allow the assessment of the relative position of the serviced satellite and the space tug. However, this capability will be added in the next release of the software.

The eclipse duration allows the calculation of the total time of the satellite in the shadow case. These data are different for each simulation because depending on the relative position of the Sun and the Earth during each manoeuvre. As previously specified, the operation of the EPS is assumed only during lighting conditions in order to avoid excessive battery weights. The general results indicate that the longest eclipse duration corresponds to LEO-GEO and GEO-LEO transfers. When the space tug operated close to the GEO position, the eclipse duration can be considered negligible.

Chapter 3

CASE STUDY: VLEO missions

Since the beginning of the space era, the introduction of innovative technologies pushed the limits on conceivable space activities further away.

Across the globe, the international community are working on many fundamental activities to pave the way for new mission scenarios. Multiple and various reasons are nowadays influencing this process, from improving the quality of life on Earth to the satisfaction of the human need of exploring new far places. Despite every honourable intention and objective, after the proof of its feasibility, introducing a new concept shall be driven by a careful analysis of its impacts on long-term space activities.

Focusing on the Earth-related missions, one of the most interesting concepts is the exploitation of a new range of orbit altitude: the Very Low Earth Orbits (VLEO). Below the commonly used Low Earth Orbit (LEO), this region of space ranging from 160km up to 250km offers considerable benefits, in particular for space observation and other space-based services such as telecommunication and GNSS. However, at this range of altitude, the generated drag will strongly reduce the orbital energy setting a critical limitation to the mission lifetime. Therefore, a dedicated propulsion system shall be adopted to provide the necessary compensation force, prevent the spacecraft's re-entry, and guarantee all mission operations necessary to fulfil the mission objectives. Nevertheless, with a traditional propulsion system, the mission lifetime is directly impacted by the quantity of propellant stored onboard the spacecraft, which determine its limit. With the introduction of the air-breathing electric propulsion, so-called ramEP, this limitation could be avoided. These systems can generate thrust without the need for an onboard propellant. In fact, their key operating principle is the scooping and utilization of the atmospheric residuals present in the considered range of altitudes. This characteristic will theoretically allow extending the mission operations, increasing both economic and scientific revenue and extending the overall mission opportunities. Other criticalities such as the cost of the ground services, the revenues coming from the mission product to the end-users and the degradation of the spacecraft surface and components (due to the harsh environment) will define the breakeven point on the maximum mission lifetime.

Even though the enabling of VLEO are nowadays of main interest, the flexibility of a ramEP thruster to operate with different gas mixture extends its range of adoption around other planets which present a suitable atmosphere.

The ramEP thruster is based on two main parts: an intake and an electric thruster. The intake can collect the incoming flow and direct it toward the inlet section of the electric thruster, meanwhile compressing the flow to reach the optimal thruster inlet pressure. Then, the flow is ionized and accelerated. The ionization and acceleration mechanism depends on the typology of thruster used.

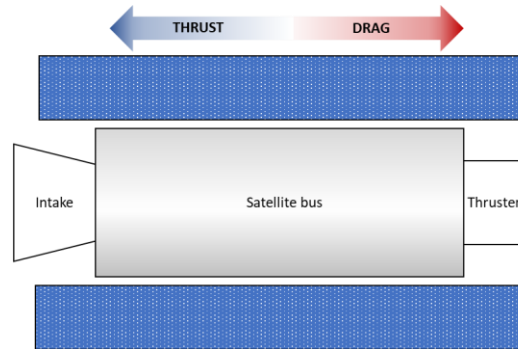


Figure 50: ramEP S/C concept.

The general spacecraft shape, presented in Figure 50, as well as the integration alternatives and constraints considered in this study, are presented later in this chapter within the sizing and analyses activities performed in this study to prove the concept feasibility.

In the following section, the benefit of the exploitation of a region of altitudes closer to the Earth is described.

3.1 The ramEP concept & VLEO environment

The advantages identified for the LEO orbits are further improved for specific applications lowering the orbit altitude. If exploited, these orbits could represent a true cornerstone for the “New Space Economy” actors in opening a new mission scenario. Several authors have already reported most of the advantages [76,77], hereafter listed.

- **Resolution of optical payloads:** considering constant the design of an optical payload, the theoretical resolution could be improved by lowering the observation altitude. This trend is ruled by the Rayleigh criterion, which relates the ground resolution of an object in a proportional relation with the observation altitude, also considering the design of the optical payload in terms of aperture and observation frequency length. It is technically possible to act these parameters improving the quality characteristics of the optics, enlarging the aperture of the optic or, in the case of VLEO application, reducing the observation altitude. A second approach could also be followed: reducing the optical performance, which allows a size down of the payload with a subsequent reduction of envelope and consumption maintaining constant the optical performance owing to the reduced altitude. This approach guarantees both a reduction of the payload mass, downrating

the mass class of the payload, and allows a possible extension of mission capabilities.

- **Radiometric performance:** as the distance from the Earth is reduced, the radiometric performance is improved due to the higher power density irradiated, allowing a higher signal to noise ratio. This effect can be translated either in higher performance or in less sensitive and cheaper sensors to be adopted.

- **Communication latency:** this key parameter represents a crucial characteristic for communication missions and, specifically, for peculiar missions where the transmission where the data transmission shall be as close as possible to a real-time condition. Lowering the satellite orbit could reduce by orders of magnitude this value improving current applications and enabling a full set of real-time based communication services.

- **Geospatial position accuracy:** the shorter path length defined by the lower altitude allows a more accurate imagery location due to the shorter arm length where the attitude uncertainties can propagate.

- **Mass budget:** two main figures of evaluation can be taken into account for the mass reduction allows by the lower altitude flown with an air-breathing based platform: the impact either on the payload design or on the bus design. First, assuming the payload requirements constant, the reduction of altitude allows a reduction in the dimensions and mass of the payload itself. For example, for optical payload, this reduction could be translated into smaller optics and payload system. On the other hand, the bus mass can be reduced owing to the “propellant-free” system enabled by this technology. This has impacted the satellite's dry and wet mass, evaluated case by case considering mission requirements and constraints.

- **Simple deorbiting strategy:** due to the relevant aerodynamic braking effects, the de-orbit strategy results strongly simplified. In fact, it results in to stop of counteracting the drag with the thruster. For the same reason, the risk of debris creation is fully eliminated due to their rapid re-entry period.

- **Low radiation level:** such low orbit altitudes offer significant protection from space radiation because of the coupled contributions of the Van Allen belt and the Earth magnetic field. This would lead to the possibility of using COTS electronic components instead of space-qualified components to reduce the costs of these systems.

- **Space accessibility:** due to the lower altitude to be reached by the launch vehicle, the VLEO has the characteristics to have easier accessibility than the other orbits. This is one of the main benefits that directly influence the reduction of the launch costs due to the possibility of exploiting smaller or different launch vehicles. In addition, the launch performance provided by innovative launch vehicles such as spaceplanes and air-launch rockets.

In this first phase of the VLEO market assessment, a preliminary selection of small/medium launchers was performed considering a launcher payload capability of up to 3000 kg.

The following launch vehicles were identified:

Table 34: Small/medium launch vehicle list.

Launcher name	Version	Launch mass SSO [kg] (*)	Manufacturer	Nation	REF.
Angara	1.2	2490	Khronichev	RUS	[78]
PSLV		1750	ISRO	IND	[79]
Long March	2C	1900	CALT	CHN	[80]
	2D	1300			[81]
	4B	2800			[82]
	4C	2800			[82]
	6	1080			[83]
Minotaur	IV	1735	Orbital	USA	[84]
	C	1050			[85]
Epsilon	-	1500		JAP	[86]
VEGA	-	1500	Avio	ITA	[27]
VEGA C	-	2200	Avi006F	ITA	[28]
CYCLONE	4M LV	3350		UKR	[87]
SOYUZ	2-1v	1400		RUS	[88]
Antares	230	3000		USA	[89]
(*) In this table, the included launchers belong to the small/medium launch vehicle class with a launcher mass in SSO between 1000 kg and 3000 kg. Both operational and under-development vehicle are included.					

3.2 Literature review: in between of thruster concept and new mission scenarios

The genesis work on air-breathing electric propulsion can be traced back to the Cold War period as a part of the strong proliferation of advanced concepts developed with the intent of winning the space race.

Due to the massive spreading of nuclear exploitation idea, most of these early proposed ideas relied upon nuclear power sources with just marginal mentions on the solar-based system. Moreover, the primitive proposed concept foreseen “self-refuelling rocket” instead of “air-breathing spacecraft. This approach suggests the focus of the research community was focused on the development of an easier space access capability to overcome technical limitations imposed by the quantity of propellant necessary to reach the orbit with a sustainable amount of carried payload.

The first researcher to propose a device to collect atmospheric propellant was Sterge Demetriades in a seminal paper published in 1959 [90]. In this paper, the concept named **PROpulsive Fluid ACcelerator (PROFAC)**, in its simplest definition, consists of a system able to collect incident atmosphere, compress, and cool it to extract oxygen to be used as propellant. That allowed to strongly reduce the propellant mass necessary to be carried from the ground.

The 11-ton vehicle designed to collect 400kg of atmospheric flow per day through a 10 m² collector at an orbital altitude of 100km. The generated drag would counteract by mean of a magnetoplasmadynamic thruster (MHC) which is fed with electric power by a nuclear reactor with a total power of 6MW. In a second paper published in 1962, Demetriades further developed the PROFAC concept defining the concept of operations of the vehicle judged feasible in terms of economic impact and technological development below 135 km, even if Demetriades did not provide any details on how it arrived at this conclusion.

On the wave of this unconventional concept, Bussard envisioned the possibility to scoop hydrogen during an interstellar journey to be exploited as a propellant in a fusion reactor that allows using the generated fusion product to generate thrust. As pointed out by various authors, Bussard’s concept, also called “Bussard Ramjet”, was more a sci-fi movie concept than a feasible system.

In the sixties, an important contribution in a definition of a feasible system able to collect propellant from the air came from Berner and Camac. In their work published in 1961 [91], they also investigated the possibility to exploit solar power in addition to nuclear power. A key parameter was introduced in this publication, the “weight-doubling time”, which represents the amount of time necessary to collect propellant from air to equalize the spacecraft's dry mass. The real cornerstone of this novel parameter consists of the delineation of a new way of evaluation for this typology of spacecraft where the mass of the launch vehicle is compared to the spacecraft costs to estimate the breakeven point where the scenario became sustain under an economic point of view.

The period to reach the breakeven point was estimated in less than one year for both solar and nuclear-powered spacecraft. Despite the encouraging results, the Berner and Camac analyses were based on basic atmospheric data and a mission scenario with missed eclipse condition. These inaccuracies put some doubts on the validity of the result because both aforementioned aspects strongly affect the feasibility of their concept.

In 1962, Reichel and his research group pushed further Berner and Camac's concepts of designing a nuclear-powered system rely on an electric propulsion system fed by propellant obtained through a scooping system followed by a liquefaction stage. With a 5-MW power source, the system was able to collect nearly 60k/hour of air flying at 110km [92,93].

In parallel with the Space Race era, the air-breathing concept also spread at the international level with research works published by Soviet Union scientists. Their works tried to prove the feasibility in terms of power generation considering both solar and nuclear-powered systems. The first researcher to propose a concept of an "air-breathing propulsion system was Cann in a paper published in 1975 [94]. Called Space Electric Ramjet (SERJ), the spacecraft concept relied on an electromagnetic engine (MHD) operated through the airflow collected by an intake, ionized in a dedicated stage, and accelerated employing an electromagnetic field. In his study, Cann adopted only solar panel aligned to the flow to generate the required power to sustain the continuous thrusting of the spacecraft flying at 160 km of altitude. As could be found in the previous studies, Cann's research suffers from inaccuracies coming for the impact of not considers the eclipse effects, which impose a strong limitation on the possibility of a constant power provision. Moreover, the solar array efficiency used to derive the power budget is considered outdated regarding the currently available solar array technology [95].

Another important soviet research who worked on air-breathing system concepts was Minovitch. As most of the research paper published in that period, he designed a system able to refuel a rocket to extend its mission lifetime improving lift-off performances. Another innovative concept developed by the researcher was a complex mission architecture based on the flying air-breathing spacecraft, a relay satellite, and a solar ground station. In this concept, a power of around 10 GW was irradiated by the ground station and relayed by the satellite to continuously reach the flying spacecraft, avoiding one of the main critical problems of this system represented by power generation. In his work, Minovitch proposed to use this mission architecture for multiple air-breathing assets. Moreover, he was the first to propose to use the air-breathing concept around other planets with a massive nuclear-powered system able to be refuelled during aerocapture manoeuvres able to perform the return trip. These concepts were published in a couple of conference papers in 1983 [96].

After these last Minovitch's works, the international community lost interest in these systems' typologies due to the end of the Cold War that had slowed down the concept proposals aimed to win the international "space competition. Moreover, the dissolution of the Soviet Union at the beginning of the last decade of the nineteenth

centuries represented a narrowing of the Russian involvement in space activities, then strictly focused on the international cooperation toward the early borne concept of the international space station. In addition, the number of technological criticalities identified in different seminal studies, such as the thruster technologies and the onboard power source and generation, was considered excessively challenging to be effectively addressed. As a consequence, while the air-breathing technology was temporarily abandoned, leaving the field to other classes of “less critical” mission scenarios.

The unstoppable improvement of the technologies had gradually opened new mission scenarios, even derived from previous mission concepts. This was the case of air-breathing systems, which were “rediscovered” by the international community with newly funded research in the first half of the twentieth century.

The approach followed by all the researchers was focused on “airbreathing spacecraft” instead of “air-scooping rocket”. This latter concept was definitively abandoned in the modern due to the lower efficiency of the scooping technology and the extended collection period necessary. However, other typologies of reusable space systems were instead introduced even if limited to the ascending phase and not intended to be exploited for interplanetary transfers.

However, in this new interest wave in “air-breathing” spacecraft, most of the published works presented a “technology-push” in which the main focus was usually given to a feasibility analysis in the adoption of a specific thruster device around which the spacecraft is designed. This approach could be easily explained considering the criticalities in the development of a thruster able to be operated with an atmospheric mixture as well as the scooping stage. While one of the main thruster criticalities is the limited operative lifetime due to the intense corrosion phenomena during the operation with atmospheric mixtures, the scooping devices suffer from low collection efficiency. Consequently, most of the recent research work tried to deal with these issues by introducing alternative design solutions.

For what concern the propulsion field, different thruster technologies involved such as (i) Hall Thrusters (HT), (ii) Gridded Ion Thruster (GIT), Radiofrequency Ion Thruster (RIT), Pulsed Plasma Thruster (PPT) Radiofrequency Plasma Thruster (RPT) and Helicon Plasma Thruster (HPT).

ABIE

In 2003, Nishiyama, Fujita, and Hisamoto of the Japan Aerospace Exploration Agency (JAXA) developed what was called Air-Breathing Ion Engine (ABIE) [97,98]. An intake stage consisting of a honeycomb parallel pipeline and the following collector section was designed to collect and compress the incoming flow in order to provide a pressure of 0.5 Pa to an Electron Cyclotron Resonance (ECR) Ion Thruster. In this thruster, a strong magnetic field generated by magnets, and an electric field generated by a microwave antenna, are exploited to ionize the incoming flow accelerated downstream by charged grids. The plume is then

neutralized through a cathode neutralizer. To guarantee the correct operation of the thruster, its estimated inlet pressure shall be greater than 0.5 Pa.

The Japanese researchers placed the intake around the spacecraft bus with a ring-shaped design. Consequently, the so-called “satellite core represented the available volume for all spacecraft subsystems (See Figure 51).

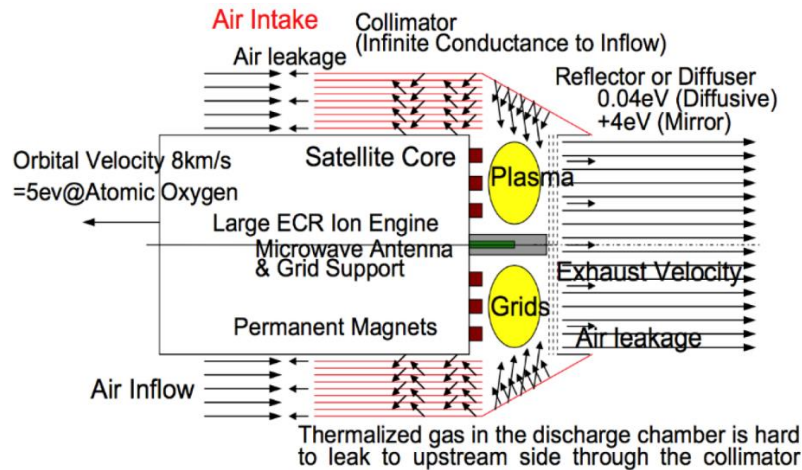


Figure 51: ABIE intake concept [99].

With an operating altitude between 150 and 200 km, the designed spacecraft was able of a full drag compensation at an altitude of 170 km, requiring a total power between 4 kW up to 5.59 kW. The frontal area was estimated at 1.5 m², developing a C_d=2. In the range of altitude considered, the thruster was capable of being operated with a thrust-to-power ratio between 10 and 13.7 mN/kW.

The Japanese research group focused the analysis on the intake design performing a direct Monte-Carlo simulation to assess its characteristics and the influence of the flight altitude and its geometrical design [93,94].

More recently, to pave the way for a full ground testing of the ECR thruster, an atomic oxygen ion source was developed and tested [97]. Meanwhile, the design activities on ECR thruster proceed with a numerical investigation of the thruster [97], which allows assessing the effects on metal boundaries, neutrals behaviour and plume-spacecraft interactions with, for example, a different configuration of antennas, magnets and metal boundaries.

ESA-RAMEP

With a conference publication in 2007[100], ESA presented the main results of their RAMEP spacecraft concept developed in an extensive study performed with a Concurrent Design approach (CDF). Their concept consists of medium size spacecraft designed for operating at an altitude between 180 and 250 km for a period between 3 and 8 years. The study was based on an estimation of the thruster performances using theoretical models that exploit available thruster data with the atmospheric mixture. The lack of an experimental campaign of a thruster specifically designed was mitigated considering multiple datasets coming from

different thrusters. In addition, the predictive theoretical models allow the investigation of various operative point with different discharge pressure. Another key point of the study was the detailed investigation of the intake design to assess its downstream performances' main design parameters.

The design of the intake was tailored for providing adequate flow inlet conditions to an RIT thruster that operates at lower flow densities with respect to an HT. This aspect relaxed the requirement of the compression capability of the intake, permitting a simpler design of the intake itself.

The selected ASTRUM RIT-10 GIE (Radio Frequency Ion Thruster) was thought to be operated in a cluster of four for a total power of 1 kW, generating a thruster range between 2-20 mN depending on the atmospheric properties along the orbit.

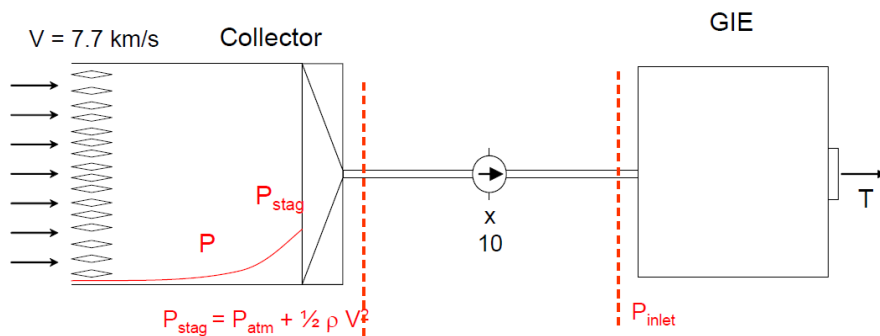


Figure 52: Schematic diagram of the ESA RAMEP intake concept [100].

After a qualitative trade-off on the main concept layout at the mission and system level, they evaluated the needs to operate with a continuous thruster without the needs for an additional tank for storing propellant. The selected reference mission was an In-Orbit Demonstration (IoD) with the possibility to accommodate an observation payload. The selected reference scenario consists of an SSO Dawn-Dusk orbit @6am in which the spacecraft was supposed to vary its altitude between 180 and 250km. The durations of the eclipse, both long and short, have been taken into account in the study. The estimated 16 min and 29 min long duration for short and long period respectively, the power system has been designed to sustain the operation of the thruster up to 17 min through the adoption of 612 Wh Li-Ion batteries.

The design of the spacecraft was conceived for the minimization of the generated drag and the maximization of the collecting capabilities. Those drivers resulted in a GOCE-like shape of the spacecraft with a frontal area of 1 m² with a total collecting area of 0.6 m². The selected solar array configuration consisted of 8 deployable solar mounted preferred with respect to the fixed GOCE wings and three body-mounted solar Arrays covering the octagonal-section body. The final projected mass was estimated lower than 1000 kg, considered as a constraint for the adoption of small-medium class launch vehicles.

The study was concluded with a set of high-level mission objective for an IoD mission for a full demonstration of the RAMEP concept capabilities. Moreover, they suggested a possible mission profile, identifying three mission phases at

different operative altitudes and a preliminary system design layout derived thanks to the performed study.

Martian Atmosphere Hall-Effect Thruster (MAHBET), BUSEK

Busek developed its air-breathing concept for a martian scenario [101,102]. Called Martian Atmosphere-Breathing Hall Effect Thruster (MABHET), this small spacecraft consists of a cylindrical intake externally placed in front of the spacecraft's main body in which all other subsystems of the spacecraft are hosted. The power required for operating the spacecraft is guaranteed by two solar array wings laterally deployed (see Figure 53). The coefficient drag of the vehicle was assumed equal to 3 due to the large solar array surfaces necessary to generate 1.2 kW. It is important to notice the criticalities concerning the distance of Mars from the Sun, which further stressed the need for large solar arrays. This was partially mitigated in the Busek study, assuming an efficiency of the solar cell of 35%, which represents a slightly high value even with the recent improvement and without the adoption of alternative architecture, as the solar concentrators. Even in this study, the analyses on mission scenarios allows providing useful data for the operation of the selected thruster.

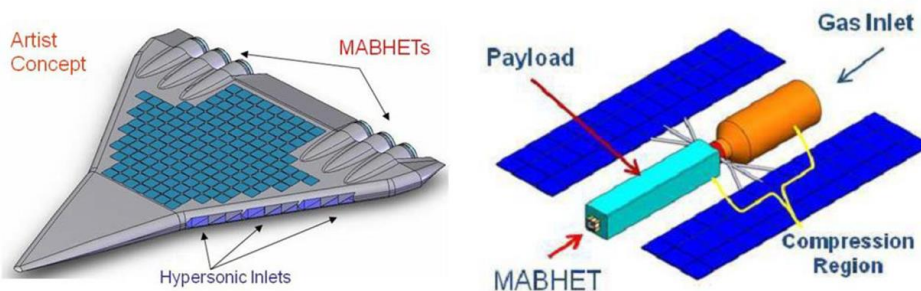


Figure 53:MAHBET spacecraft concept (credits: [101]).

The 1500kW HT developed by BUSEK was operated with an atmospheric mixture representative of the Martian atmosphere (95.7% CO₂, 2.7% N₂ and 1.6% Ar). The test aimed to investigate the peak values of the thrust-to-power ratio, considered key-driver due to the power limitation imposed by the spacecraft design itself. The thruster demonstrated the capability to reach a thruster-to-power ratio between 19 and 33 mN/kW. The results showed the feasibility of a full drag compensation in an altitude range between 150 and 180km.

Ceccanti, Marcuccio EP

In 2003 Ceccanti and Marcuccio presented a conference paper [103] conceiving multiple launches based on three identical small spacecraft of 450 kg each. The selected launcher was VEGA which allows to injection of the satellite at 500 km of altitude. The study aimed to prove the possibility for a fully drag compensation on a circular SSO orbit with an altitude between 220-296 km. and an inclination of $i=69.52^\circ$ for a total mission lifetime of 8 years.

The bus system consisting of a 2m long spacecraft with a hexagonal section of 1m in diameter. Considering a frontal area equal to 0.8 m^2 , the drag coefficient was fixed at $C_D=3$. Through 2 solar panels of 2.5 m^2 , the electric power subsystem was able to generate a total power between 200 W and 400 W, with possible power peaks up to 660 W. The spacecraft was also equipped with a Li-Ion battery to deal with short eclipse periods. For what concern the propulsion subsystem, 2 HT of 650W each guarantees a total thrust of 40mN. It is important to highlight that most of the study is focused on the orbital dynamics evolution rather than air-breathing system design.

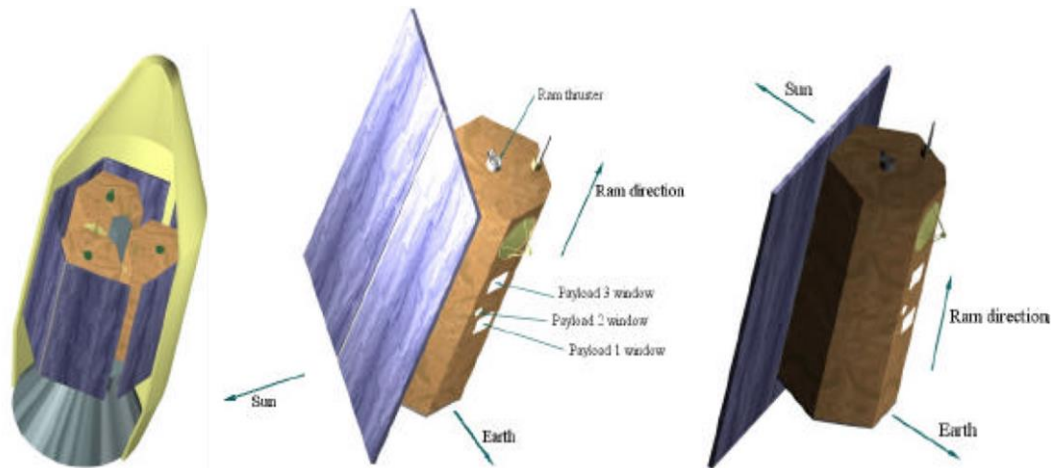


Figure 54: spacecraft concept (credit: [103])

Shabshelowitz RF RAMEP concept

With his PhD dissertation at the University of Michigan [104], Adam Shabshelowitz presented a detailed study on RF plasma technology for air-breathing operation.

The envisioned spacecraft has a total mass of $M_0=325 \text{ kg}$ operating on a circular orbit at $h=200\text{km}$. The minimum lifetime duration was assumed of 3 years. To generate the necessary power level for the operation of the thruster and the other loads onboard the spacecraft, the S/C cylindrical body of length $L=2.1\text{m}$ and diameter of 0.7m was covered by solar cells without additional lateral wings (such as in a GOCE-like configuration). The resultant frontal area was equal to 0.34 m^2 . The investigated single-stage HHT was foreseen to operate at a minimum of 33V and 306W, generating a total thrust up to 8.8 mN for a total thrust density of 29-59 mN/kW. Shabshelowitz adopted a particular design solution to counteract the atmospheric variation in term of flow density consisted in a ballast tank.

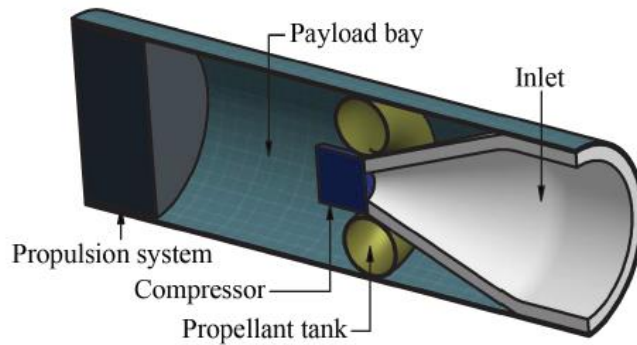


Figure 55: internal RF thruster main concept location (credit: [104]).

The last part of this section is dedicated to the two main mission specifically designed to operate in the VLEO region. The performed review is mainly focused on mission and spacecraft features introduced to fulfil the mission objectives and the operation in the challenging VLEO environment according to system requirements.

GOCE

Launched in 2009 with a ROCKOT launcher from Plesetsk Cosmodrome (RU), the Gravity Field and Steady-State Ocean Circulation Explorer (GOCE) represented one of the core missions in the context of the ESA Earth Explorer programme [105]. The mission objectives were to determine the geomagnetic field distribution over the geoid and gravity anomalies with higher accuracy (1cm and 1mgal). This allows reaching multiple science objectives such as (i) an improvement in the understanding of Earth physics and, in specific its geodynamics (ii) the determination of the marine geoid in order to establish marine dynamics and transport of mass (iii) the determination of the polar ice thickness derived from its influence on space gravity (iv) and the update with high-accuracy data of the reference earth surface. Three key spacecraft features allow determining the mission's success and even go beyond the objectives reported here above. They are the following:

- The satellite-to-satellite tracking for a precise orbit determination
- The embarked gradiometer, capable of measuring the components of the gradient tensor at each instant.
- The Drag-Free and Attitude Control System (DFACS), an S/C integrated subsystem that coupled both the propulsion subsystem and the attitude control system with the gradiometer, ensuring greater accuracy in the alignment of the local orbital frame with respect to the observation frame.



Figure 56:artistic impression of GOCE during thruster firing (credits: ESA)

Built by Thales Alenia Space Italia, as prime contractor and EADS Astrium, as responsible for the platform, GOCE represents the first space mission conceived for a long operation at an orbit altitude of 260 km on an SSO Dawn-Dusk @6am (the range of the flown altitude is 250-280 km). The selected propulsion was design to continuously counteract the drag in what so-called “drag-free mode” controlled in a closed-loop control through which the acceleration measurements were also exploited for generating science data.

The aerodynamic shape of the spacecraft was designed to minimize the drag along the direction of flight. The S/C presents a symmetrical architecture about the XY plane with a long central octagonal body (5.26.m in length with 0.9 m² of cross-section) with two lateral fixed wings introduced to increase the solar array surface without deployable parts. The total power generated by the 5 m² GaAs body-mounted solar cells was 1.6 kW EOL fed by a 24-32 VDC unregulated bud to the other S/C subsystems.

A primary structure, largely built with carbon fibre material, was adopted to reduce the overall weight while a high level of stiffness is guaranteed to sustain the high loads experienced during the launch phase. The total wet mass of the satellite was equal to 1077 kg considering the 100 kg of propellant necessary for a nominal mission lifetime of 20 months.

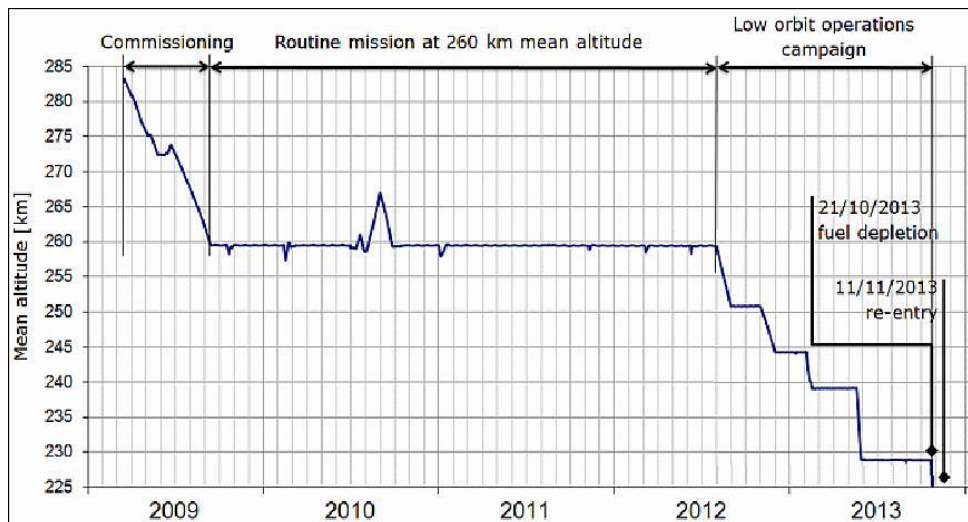


Figure 57: GOCE mission altitude variation (credit: ESA)

As previously introduced, the DFACS/AOCS was capable of providing drag-free operation and attitude control. The spacecraft's attitude was instead controlled by magnetorques driven by the central computer thanks to the telemetries collected by wide-field star trackers, coarse sun sensors and magnetometers (the latter two were introduced in case of safe mode). The intrinsic design of the spacecraft, which presents a centre of pressure behind the centre of mass, allows passive aerodynamic stability further increased winglets and trim masses.

The Ion Propulsion Assembly based on 2 T5 “Kaufman”-type thrusters, one operated and the second adopted for redundancy, allow compensating the drag force acting on an along-track direction. The thruster of the operative thruster could be controlled between 1 mN up to 20mN with a total power of 120-700 W.

For a specific impulse varying between 385s (@1mN) and 2870s (@20mN), the estimated propellant mass was 40 kg even if addition margins were considered to mitigate the uncertainties on the IPA operation [106,107].

The GOCE ConOps consisted of 8 different main phases: after the LEOP and commissioning operations, observation periods were alternated with a period dedicated for the calibration of the gradiometer payload. Considering the successful completion of the nominal pre-schedule mission duration, the GOCE mission was extended up to 4 years. A specific S/C mode of operation was adopted to deal with the long eclipse period during which the satellite performed an orbit-raising manoeuvre to sustain and orbit decay down to the subsequent operative altitude (POP2). Even though the nominal mission phase ended in April 2011, the onboard consumables (in particular the stored propellant) allowed to plan a mission extension until late 2013. In November 2013, GOCE ran out of propellant and performed an uncontrolled re-entry over the Falklands Islands. The extension of over 18 months proved the robustness of the spacecraft design operating in very low altitude orbit. In addition, it guaranteed remarkable scientific results, still investigated [108].

SLATS

With the objective of understanding the effects of the high-density atomic oxygen as well as the possibility to control a spacecraft in VLEO, JAXA designed and launched a dedicated mission in 2014. Called Super Low Altitude Test Satellite (SLATS), this mission was intended to fulfil the following mission objective in its two years mission lifetime. They are the following:

- Measure the atmospheric density at low altitude: to improve the current atmospheric model, for which their verification is guaranteed above the usual 400km of the nominal LEO missions, through additional data.
- Detect the atomic oxygen concentration and collect data on its effects on spacecraft materials: through a material sample payload, SLATS had the objective to study the degrading effects of the atomic oxygen, particularly presents around the altitude of 200 km.
- Validate and verify the design of the satellite for operation at very low altitude: as already mentioned for other missions, to fly a spacecraft at a constant altitude (around 200km), a constant thrust provision is required to counteract the constant effect of the drag force.

The S/C designed for a small-class satellite to be launched as a secondary payload with reduced dimensions (2.5 m x 5.2 m x 0.9 m, with SA deployed) and a total wet mass of 383kg.

The Ion Engine System (IES) consisted of a 1 x 20mN-class ion engine able to generate a thrust between 10 a 28 mN with a total power required of about 370 W (@10mN) [109]. The nominal specific impulse was 2000 s. For completing the mission operations, 10kg of xenon propellant stored in three tanks. An additional chemical reaction control system (RCS) was also adopted for the initial descent from 643 km to 393km what was identified as “initial orbit control” before the operation with the ion engine. As a consequence, 34kg of N₂H₄ propellant were embarked.

Thanks to the combination of electric and chemical thrusters, SLATS was able to operate on seven different altitudes (271.5 and 216.8 km for 38 days, 250, 240, 230, 181.1 and 167.4 km), maintaining a constant altitude for at least one week. To counteract the extreme drag force at the lower altitude, the RCS was operated to maintain both altitude and attitude. The mission ended in October 2019 after the decommissioning operation performed one day before.

SLATS was acknowledged as the lowest altitude reached by an Earth Observation satellite. More details can be found in [110–112]

Apart from the GOCE and SLATS mission, the literature review on the research work was focused only on the studies in which a mission concept was presented with a minimum of mission design and analysis of the spacecraft operation. However, vast scientific literature has been produced in the electric propulsion field during the last two decades, either proposing a new thruster concept for air-breathing operation or presenting an experimental campaign with conventional thrusters feed with the atmospheric mixture.

In particular, the demonstration of a stable operation with atmospheric mixtures is considered a fundamental milestone for an effective approach to the atmospheric scenarios, even without directly demonstrate the “air-breathing” operation concept. The conventional thruster successfully tested are reported in Table 35.

Table 35: conventional thrusters operated with oxygen-nitrogen mixtures.

Thruster Type Thruster	Nation	Man.	Year	Propellant	REF	NOTE
HET - PPS1350-TSD	ITA/FRA /GER	SNECMA/ SAFRAN, Giessen University, SITAEL	2011	N ₂ /O ₂ mixture	[113]	Due to the low ionization efficiency, both thrusters operated with reduced performance even if the stable mode has been reached.
RIT - RIT-10				N ₂ & O ₂		
TAL	RUS	TsNIIMAS H	1995	Xe/Air Mixture	[114]	Investigated the possibility to obtain a higher acceleration efficiency with a small addition of Xe without overheating the thruster.
HET	USA	BUSEK	NA	Air	[115]	No specific information has been released by BUSEK.
HET – Z-70	USA	Stanford University/ University of Surrey	2019	Xe/Air Mixture	[116]	The main aim of the work was to provide a clear understanding of the contribution to the performance of each species in thruster feeds with atmospheric mixtures.
Inductive plasma generation – IPG6-S	GER	IRS	2017	N ₂ /O ₂ mixture & single gases	[117]	The IPG6-S was successfully ignited, reaching a stable operation with a mixture and single gases. Interesting hysteresis phenomena were observed. Multiple ignition characterization tests were performed to fully understand the ignition procedure.

Microwave Electrothermal thruster	USA	Pennsylvania State University		N ₂ , H ₂ , NH ₃	[118]	Theoretical and experimental investigation of the 7.5-GHz MET at a power level between 70-1001 W
HHT – Helicon Hall Thruster	USA	University of Michigan	2012	N ₂ , Ar, Xe	[119]	Extensive investigation on the thruster performance in both single and double-stage modes. The main results indicate that the current utilization represents the major contribution to anode inefficiency, lower than the value reached with operation in Xe.
GIE -	RUS	TsAGI	2017	N ₂ , O ₂ , Xe	[120]	A theoretical investigation on the design and performance of a GIE thruster operating with atmospheric gases.
HDLT - Helicon Double-layer Thruster	AUS	Australian National University	2008	N ₂ , CH ₄ , NH ₃	[121]	Testing activities on HDLT operated with different chemical mixture have been performed. Plasma properties have been reported showing the possibility to operate the thruster with low inlet pressure.

CURRENT RESEARCH PROGRAMME

In the last decade, the European Commission, through Horizon 2020 programmes, and ESA, through either General Support Technology Programme (GSTP) or Technology Research Programme (TRP), have renewed the interest in the adoption of the air-breathing technology for opening new mission possibilities. As a consequence, a series of development programmes have been founded to further improve the readiness in different technological areas.

In particular, two main international groups are actively acting with this aim in projects named: DISCOVERER and AETHER. In the next paragraphs, a brief description of these project is given, highlighting the main achievements.

▪ DISCOVERER

Started in 2017, the H2020 DISCOVERER project [122,123] aims to introduce a novel design of Earth observation satellite in order to sustain operation at very low altitude. This object considers the adoption of new materials, innovative aerodynamic controls, and advances observation methods. The international group of partners aims to develop key technologies with a TRL around 1-2 through proof-

of-concept activities or validations for technology with a TRL of 4-5. After the project phase, the evolution of DISCOVERER, considered as a long-term objective, is the validation of such technologies in a real mission, which is not part of current project scopes.

The developed mission concept consists of a Cubesat standard spacecraft based on multiple cubes of a 10 cm side. In [124,125], some details on the spacecraft configuration used for aerodynamic and attitude analyses are provided, showing that a 3U configuration is selected (0.366x0.1x0.1 m) with four foldable wings deployed at the beginning of the mission along each side of the spacecraft (see Figure 58). Even not officially reported, the analysis on the satellite modelling reported in [126] suggested that the reference mission scenario based on a circular VLEO orbit at 350km with 50° of inclination. No additional information on both mission and S/C design have been published.

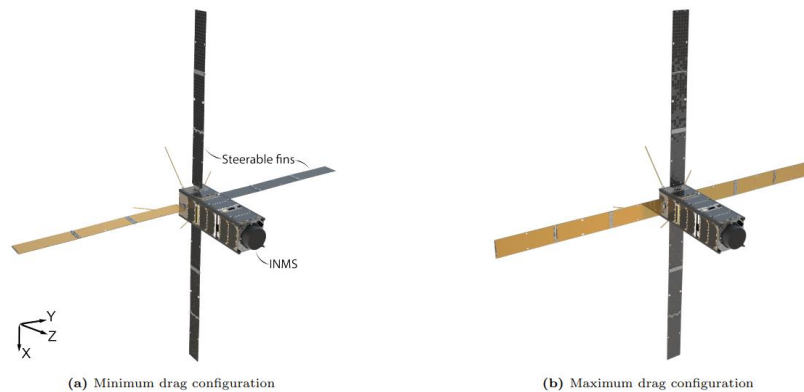


Figure 58: DISCOVERER spacecraft concept [124].

A key technology under development by the Institute of Space Systems (IRS) at the University of Stuttgart in the framework of this project is the electric thruster based on the Inductive Plasma Generator (IPG) [117,127–131]. In this thruster, a time-varying electric and magnetic field, generated through coil/birdcage-antenna fed with RF-current, is exploited to generate plasma. The shape of the electromagnetic field imposed with the antenna produces a drift velocity on the charged particles in the plasma bulk, which are accelerated in the same direction maintaining the quasi-neutral condition. As a result, this thruster does not require a dedicated neutralizer. The developed Inductive Plasma Generator (IPG) based on the previous IPG-6 has been designed for operation up to 3.5 kW.

Another important research topic introduced and developed in DISCOVERER is the possibility to steer the four fins to control both the attitude and orbit of the spacecraft with a differential control of the drag over the spacecraft surfaces. This approach has been exploited for the analysis in a formation flight scenario investigating the feasibility region of this option. This approach is interesting in particular because it allows providing a force out of the plane orbit, which is not a trivial aspect in the air-breathing concept where the intake of the propulsion system shall be aligned with the incoming air flux.

▪ SITAEL'S RAMEP DEVELOPMENT ACTIVITIES

The activities on air-breathing concepts started in SITAEL in 2017 when a TRP project funded by ESA paved the way up to the current development phase. Named “*Assessment of Key Aerothermodynamics Element for a RAMEP Concept*”, this project has the final objective of performing an experimental validation of an airbreathing thruster. Two main phases had been foreseen. The first phase included all the activities in order to: (i) define the requirements of the thruster concept, (ii) define a suitable scenario for the operation of the thruster and (iii) investigate the operation of the Particle Flow Generator (PFG) necessary for the on-ground testing of the RAMEP thruster. The project proceeds to the second phase consisting of: (iv) the optimization of the thruster design, (v) manufacturing and assembly of the thruster and (vi) its experimental validation. All these activities led to the first ignition of a fully integrated RAMEP system with a representative inlet flow generated by the PFG.

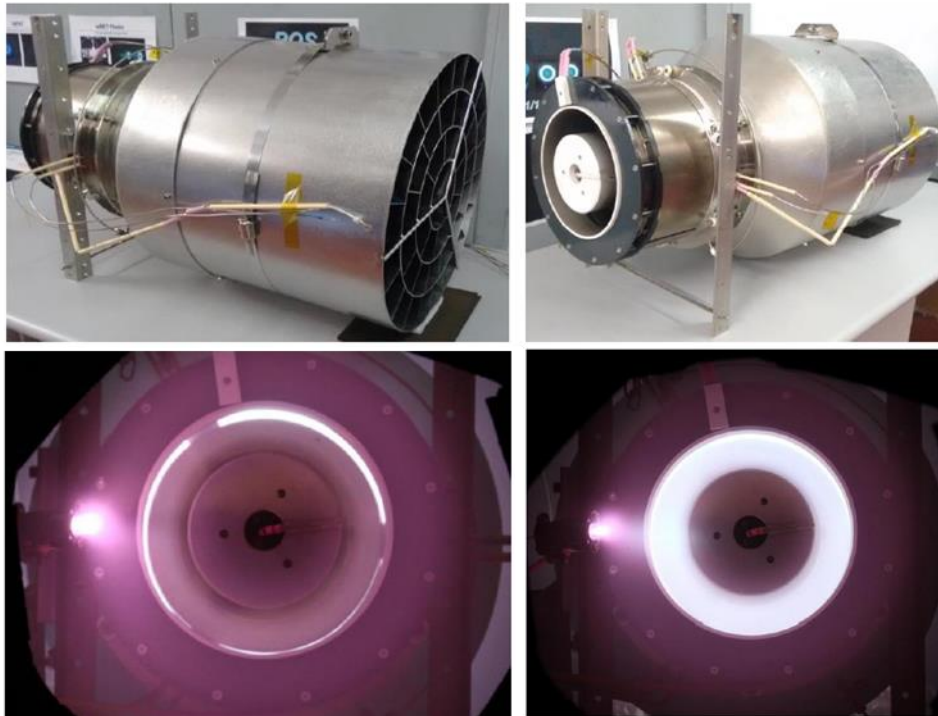


Figure 59: (top) prototype of the SITAEL's ramEP concept (bottom) SITAEL's ramEP prototype during the first firing test (credit: SITAEL) [132].

Several firings have been performed varying the inlet mixture between 8 mg/s of pure xenon to 4.7 mg/s of pure $1.27\text{N}_2+\text{O}_2$ flow. The ramEP assembly generated up to 6 ± 1 mN during operation with a pure atmospheric mixture. Even though the conducted test validated the functionality of the thruster as well as the possibility of its stable operation with atmospheric propellant, it was not capable of providing a Thrust-to-drag ratio greater than 1 due to the 26 ± 1 mN of measured drag [132]. Despite this preliminary result, the functional validation of the thruster concept

represented a significant achievement to prepare the following development steps toward an optimized design of the thruster itself.

To further proceed in the development of its RAMEP concept, SITAEL was selected for the H2020 AETHER project funded by the European Commission [133,134]. Composed by a multidisciplinary group of international partners, the Project consortium has the objective to push the technological development of the key technologies toward an In-Orbit demonstration (IoD) mission. The breakdown of this final objective consists of the achievement of technological milestones to shape the design of both the thruster and the platform able to host it and investigate the suitable mission scenarios in which this technology could represent a true cornerstone of future space missions.

Started in 2020, the first phase of the project was dedicated to high-level system trade-off, intake re-design and analyses on the foreseen performance of the thruster. This step ensured the derivation of a set of requirements (at different levels) which driven the subsequent hardware design phases. In particular, the collector/ionization stage will undergo an optimization phase to increase the collection efficiency, allowing an increment in ionizing particles (increment of the ionization efficiency) due to the higher density. Due to the selected thruster configuration based on GIE and HT technologies, a dedicated cathode is foreseen to be adopted. This represents a particular criticality for the corrosive action of the used atmospheric mixture on the cathode materials. As a consequence, a dedicated work package was introduced in the project to investigate alternative materials able to withstand these extreme degrading conditions.

Moreover, alternative cathode technologies will be considered, such as radio-frequency cathodes.

Other key activities will be performed on the ionization and acceleration stage to improve the reachable performance. An extensive experimental campaign will give the final proof of the goodness of the activities mentioned above through the validation in a representative test environment and the RAMEP thruster itself in a full-scale test. The conclusion of the testing phase will represent an important milestone for the maturity level of this technology, marking the possibility to target a real IoD mission efficiently.

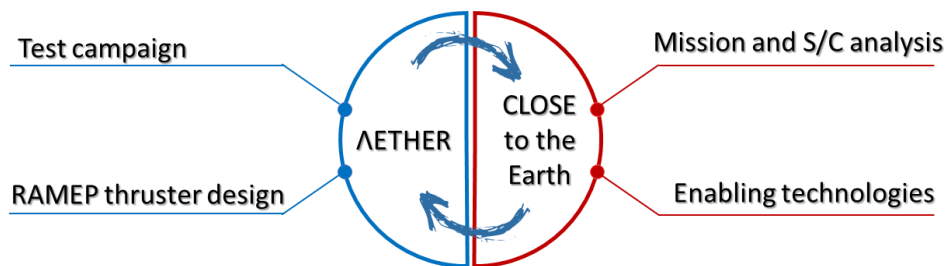


Figure 60: main objectives of the SITAEL projects about ramep technology.

A parallel “Close to the Earth” [135,136] is a program of an Italian consortium targeting to develop several technologies not only limited to the propulsion

technology and the related space platform able to host the ramEP thruster but also a set of technologies and process more intended toward the utilization of the VLEO products by the end-user. SITAEL leads the consortium of both private and public entities. Specifically, SITAEL is in charge of a preliminary design of a space platform that can operate observation payloads, whether they are optical or SAR payloads. The project is intrinsically linked with AETHER with a continuous exchange of input/output from both projects.

3.3 RAMEP future market opportunities

3.3.1 VLEO market: general description

The space sector is a dynamic environment continuously in evolution to respond to the different global needs. Over the past decade, the continuous growth of this sector has broadened the number of activities which become gradually integrated into multiple sectors. In the last decades, the eventual impact evaluation that space-based activities had on the “general” society has been appropriately included in what is now called the “New Space Economy”.

The related value chain of this novel economic environment is changing and growing with the inclusion of new operators and space-related entities. Traditionally based on the upstream-push approach, where technology developed by the upstream are exploited by the downstream in new applications, this evolution consists of a “market demand-pull” in which the downstream entities drive the development of new technologies to fulfil market needs.

Even though a strong economic impact, the space sector is still not clearly classified compared to the standard categories usually adopted for industrial classification. This undefined taxonomy causes some difficulties in the definition of the overall market revenues. Furthermore, most of the time, the proliferation of space-based activities integrated with classical ground-related activities and non-space activities have generated ambiguous boundaries among them. Consequently, the assessment, particularly for what concerns the downstream segment of the space value chain, which embraces all types of end-users, could be challenging. If the market sizing is performed with a quantitative approach, understanding the cross-relations among activities and their economic impact should be fully considered.

To provide an updated economic estimation of the current space market, in particular for outlying the incapability to provide a precise value, four different sources have been considered, already reported in [137] as shown in Figure 61. The uncertainties become more evident for long terms projects performed by several organizations to tailor investment and company decisions. In [138], a detailed work embracing the main financial institutions and rating companies has been developed. This survey shows that with a compound annual rate of growth ranging from 4.3% up to 9.5%, the space economy will be evaluated up to 2.7 trillion USD in 2040

thanks to the more involvement of private investors and a renewed government space policy.

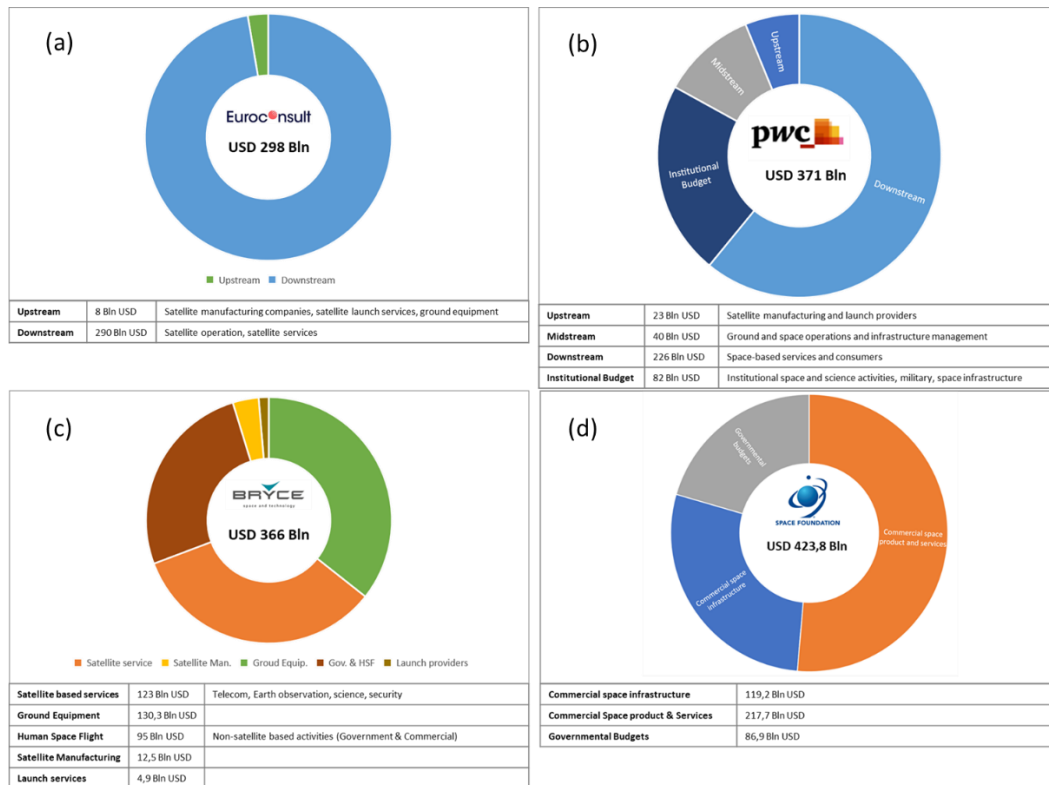


Figure 61: Space market revenues in 2020 (a) Source: [139–141] (b) Source:[137], (c) Source [142], (d) Source [143].

Different aspects force the rapid changes which characterized this environment. First, space-based services have already become essential in an integrated architecture exploited in different fields of the social-economic society. Several examples can be found looking at the roles of the satellite-based data in weather forecasting, navigation, management of resources (e.g., agriculture, forest management etc.), global timing as well as monitoring services such as disaster management security and defence activities sustained by the possible global coverage which represents a key design requirement for most of the Earth observation missions for example.

Second, due to the fusion of space-based data in terrestrial activities, the number of downstream space applications is expanding, enhancing innovation initiatives based on disruptive technologies, new business models, and novel spin-off of terrestrial applications. Consequently, new actors who are enlarging the space-related economic environment have substantially increased the rate of innovation and, at the same time, introduced new needs mainly associated with cost standardization, design standardization, sustainability, availability of the service/data provision and reliability.

Last, at the base of the “New Space Economy” approach, there is the so-called Commercial-off-the-Shelf (COTS) approach where standard terrestrial

technologies are either directly flown or subject to minor modifications to reach the spaceflight grade. This newly introduced approach ensures the reduction of both prototyping and low-volume productions, with the subsequent speed-up of the processes and development times, owing to the exploitation of mass-production approaches. Despite several benefits from this approach, it is not always applicable in particular technology areas such as payload and propulsion technologies, where the related issues can often be solved only with dedicated developments. Even though it could be seen as a blocking drawback, the improved benefits coming from increased performance and capabilities might push and sustain new space initiatives. Therefore, the combination of the market-pull and technology-pull approach characterized the space environment, particularly for disruptive innovations where different actors play each considers their own interests. This is the specific case of the airbreathing technology where the development and commercialization of the product cannot be straightforward without considering the needs of the end-users.

For outlining the VLEO market, the first activity performed is the identification of the related value chain, presented in Figure 62.

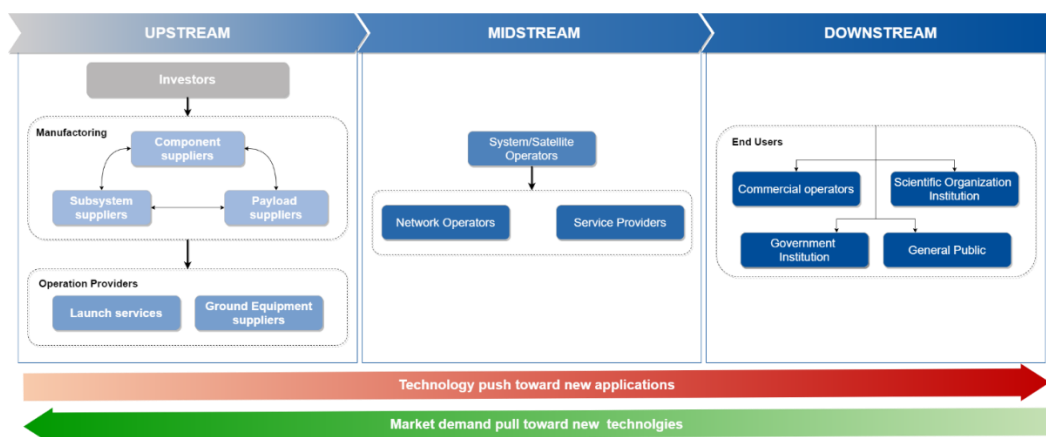


Figure 62: ramEP foreseen value chain.

As is possible appreciate from Figure 62, the value chain reports the complete range of activities undertaken for providing a product to the end-users. The upstream level includes investors able to economically support the development phase of a particular product, which is performed by a pool of components, subsystems, and payload suppliers. Large System Integrators (LSIs) are often considered overlapped to the manufacturing segment owing to their centralization capability in performing all the activities at different levels. Part of this section is also the operation providers represented by both ground and launch services providers.

The entities in charge to process the collected data and mission results are considered part of the midstream section. The system/satellite operators are also included because of their capability to operate the missions and elaborate raw data for the following section. Finally, the value chain is completed with the downstream section, which consists of all the different end-user. Characterized by a strong

mixed approach to the space data utilization, as previously reported, they are business and institutional players for which the derived product is created.

The analyses performed in the context of this study is focused on the end-users for the understanding of the possible application of the air-breathing technology as a novel product able to represent a game-changer in the VLEO region. Therefore, after the identification of the possible stakeholder acting in this sector, the analysis has been continued with the identification of the mass-class trends for LEO satellites. In addition, a general overview of the possible payload to be adopted has been performed in order to link them with the foreseen applications.

The rationales used for the stakeholder identification and grouping are the following: (i) who could have direct or indirect impacts on the activities in a VLEO scenario, (ii) who could receive benefit or advantages from the exploitation of a VLEO scenario, (iii) who could have interests in activities related to a VLEO scenario. Considering the transversal triggering effects that the enabling of this scenario could have, the stakeholder list has been generated following a generic approach not specifically addressed for a determined value chain level.

These “operators” could benefit from a cost-effective space platform able to provide lag-free, high-quality data with low-cost payloads. They could be:

Commercial operators	
Large System Integrators (LSI)	LSIs have a fundamental role in the space industry owing to their capability to assemble components/subsystems, ensuring the overall system function. Performing this function in the framework of the development and commercialization of air-breathing technology represents their main interests.
Industrial Group/Unions	The industrial players are mainly related to the upstream section, where the entire development and manufacturing cycles are performed. These stakeholders could be part of the LSIs.
Satellite operators	They are commercial players who operate the space system and, in most cases, elaborate raw data for the end-users. In the specific case of air-breathing technology, the possibility of providing a new product owing to the increase of system performance could represent a valuable benefit.
Private companies	This group represents all the entities sustained by private capitals. Mainly related to the end-user segment, they can gain benefit from the

	utilization of already elaborated data from their own business.
Governmental/Institutional	
Local institutional entities	The interest of the space sector for governmental and institutional entities at different levels include a wide range of possibilities mainly for specific interest not directly related to the monetization of a product/service. Included in this group are military interests.
National institutional entities	
International/Sovranational entities	
Public entities	
Private citizens / Groups	Mainly part of the end-users, private entities and non-governmental organizations could have different indirect interests in the exploitation of improved product coming for the utilization of air-breathing technology.
NGO	
Scientific Organization/Institutions	
Universities / Educational entities	In this group, all the organizations interested in the scientific exploitation of the products developed by the midstream are included.
National Research Centre/Group	
International research Centre/Group	

After the identification of the main application of interest for the future foreseen space-market trends, the general values chain characterized by Upstream, Midstream and Downstream are described. The analysis proceeds with a focus on small/medium satellite mass classes envisioned as the target category for air-breathing applications.

3.3.2 Application identification

The application areas have been based on an extensive literature review to embrace possible future trends of the public, governmental and commercial sector. The main considered drivers for the selection consisted of the benefits coming from the low altitudes of the VLEO region and the possible adoption of the related payload onboard a small/medium size platform. Any constraints coming from the mission architecture perspective were considered in the selection of the application.

This approach is justified by the possibility to tailor the future adoption of the airbreathing-based platform in different mission architecture such as multiple collaborative spacecraft or constellation. As a consequence, the possibility of introducing more exotic scenarios was considered as second step activity due to

critical peculiarities that characterise missions with extreme demanding payload requirements (e.g., high coverage capability or high revisit time).

Earth Observation [137,141,152–161,144–151]
Weather forecasting
Weather data to perform forecasting to support activities to all sectors (land and maritime transportation, aviation, agriculture).
Public authority services
Data exploited for governmental activities for regulation and policymaking and reinforcement, specific assets monitoring, urban and maritime monitoring
Environmental monitoring
Monitor of land, sea and air environment for monitoring, mapping, activities optimization, tracking and living species.
Security and Defense
Border control, general security (land, sea, and air), tactical surveillance, monitor of ground and tactical facilities.
Energy & resources monitoring
Different monitoring of asset for the exploitation of resources used for energy production. Optimization of the exploitation of the energy resource. Management and logistic monitoring. Renewable energy development, production, and optimization.
Industrial Services
Industrial infrastructure monitoring, tracking, and shipping service monitoring, performance monitoring.
Disaster Monitoring
Natural emergency response and management, humanitarian emergency monitoring and management
General services
They are mainly related to commercial services for mapping, geo-data acquisition, financial data acquisition for insurance and reinsurance.

Communication [137,140,160,146,149,151,153–155,158,159]
Data transfer
All end-to-end data transmission for communication. These applications include all possible typologies of data.
Data relay
Relay activities in an integrated architecture with other space applications/systems.
Secured communication & block-chain applications
Encrypted communication, high/ultra-fast communication. Provide updating blocks for blockchain application with decentralization and memory blocks.

Global Navigation Satellite System (GNSS) [137,140,160,146,149,151,153–155,158,159]
Location-Based Services
To provide an autonomous geospatial position for roads, aviation, railways, maritime and agriculture. Moreover, to provide specific location service for security military activities, science, private and commercial operators.
Time synchronization
To provide accurate and direct access to Coordinated Universal Time (UTC) [Timing] and to provide synchronization capabilities among receivers at a different location for several sectors such as Telecom, Energy and Finance

Science [137,140,160,146,149,151,153–155,158,159]
Earth Science
Range of applications aimed to study the structure and dynamics of the Earth. These can range from gravimetry applications to upper atmosphere study and monitoring. Moreover, this group includes scenarios aimed to study the composition and evolution of the soil and vegetation on lands.
Space Science
This group includes all the application aimed mainly at the investigation of the space weather caused by solar activities. Considering the range of altitude operated by the airbreathing-based platform, these applications can be reconducted to study the upper levels of the atmosphere.

- **On-orbit servicing** [137,140,160,146,149,151,153–155,158,159]

More exotic scenarios that the adoption of air-breathing technologies could enable are represented by the capability of these platforms of providing servicing operation such as space tugging and de-orbit services. The space tugging could represent a valuable solution to facilitate LEO accessibility meanwhile reducing the

overall mission costs. Even included in an end-to-end scenario, the capability of decreasing the deorbiting time could be beneficial to rapidly remove space objects and, at the same time, reduce the re-entry ground footprint improving the capability to control the re-entry trajectory. Even though these applications are considered of particular interest in recent years, they are considered far in time for their realization through certain feasibility prove.

- **Exploration** [137,151–155]

In the Solar System, the Earth is not the only planet to have an atmosphere that can be exploited as a propellant for the air-breathing system. These systems could be foreseen in their adoption around other planets with a suitable atmosphere (such as Mars and Titan) to provide most of the Earth applications (mainly for scientific purposes). Examples could be the study of the planetary atmosphere and analyses related to the geoscience field. Even in this case, the proven technical feasibility could represent an extreme challenge, in particular for the autonomous capability that these kinds of platforms shall have to be operated far from the Earth.

3.3.3 Current application market subdivision

To complete the market outlook presented in the previous section, a specific investigation has been performed to provide the space utilization status up to the current years. This analysis has been based on a database created including a set of sources among which: UCS Satellite Database [23], Observing System Capability Analysis and Review Tool (OSCAR) [162], ESA eoPortal Directory [163], SATCAT CelesTrak [164] and NSSDCA Master catalogue [165]. To verify the completeness of the final databased, the NORAD number as a unique identifier has been cross-checked and eventually, the database was updated. All the satellites parts of a constellation have been discarded by the main database and stored in a separate database for their specific analysis.

For a clear classification of the collected satellite information, the following skimming criteria have been adopted:

- Application classes: the application cases previously identified have been adapted in the subdivision approach adopted in the exploited database, consisting of:
 - Communication
 - Earth Observation
 - Earth & Space Science
 - GNSS
 - Technology Demonstration

Exploration and on-orbit services are application not considered in the database.

- Orbits: the orbit altitude has been considered as the only rationale for the orbit classification. They are the following:
 - Low Earth Orbit
 - Medium Earth Orbit
 - Geostationary Earth Orbit
 - Elliptical
- Period of time considered: the considered database collects satellite data since 1995. A timespan of about 4 years has been considered: (i) 1995-2000, (ii) 2011-2005, (iii) 2006-2010, (iv) 2011-2015 and (v) 2016-2020.

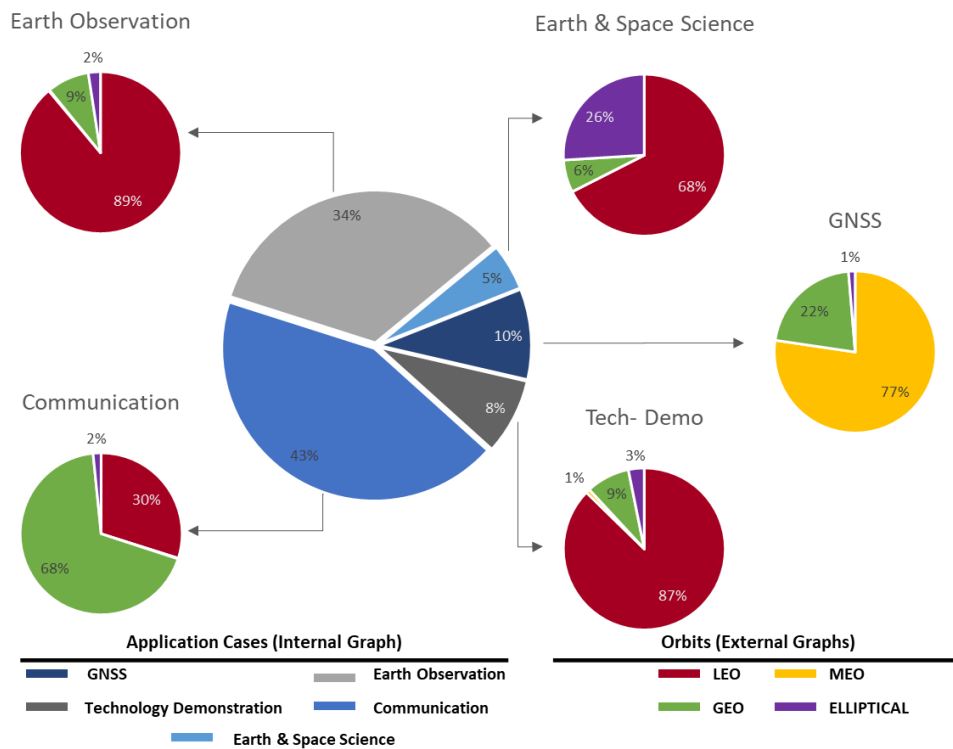


Figure 63: Space market economic segmentation for: (i) application (internal graph) and (ii) exploited orbits (external graphs).

Figure 63 shows the results of the database analysis. The application cases reported in the central graphs are then characterized for each application for the exploited orbits.

It is possible to appreciate that 43 % of the satellite currently operating in space are dedicated to communication. According to several public sources, this market will still dominate near-future forecasting. The reason for this implacable growth, with a 9.2% of growth rate between 2020 and 2027, can be identified in continuous needs for data, voice and broadcasting services targeting different end-users. Moreover, in recent years, internet-based activities strongly penetrate the space market, especially for what concern end-to-end data transfers [166].

Different worldwide players in this field are looking to this application and its growth capability to further developed its market estimated in USD 62.2 B in 2019 and USD 66.6 B in 2020 with a theoretical doubling capability in 2027, including

all segments of the value chain. The main market players who engaged the highest percentage of market share (nearly 42%) are the following: SES S.A.; Viasat, Inc.; Intelsat; Telesat; EchoStar Corporation; L3 Technologies, Inc.; Thuraya Telecommunications Company; SKY Perfect JSAT Group; GILAT SATELLITE NETWORKS. As it is possible to notice, they belong to the upper and mid-segment of the value-based classification due to the development of new applications, which influences the upper segment pushing toward new technological development and provide new services, which is an intrinsic characteristic of the mid-segment. Transversal to the objectives just reported, keeping the competitiveness on the market represents a key task translated in an optimization of the product costs and increment of their quality. This obvious market attitude pushes the communication space market toward a strong dynamism a quick change to react to new business opportunities promptly. A general overview of these effects could be reconducted to the number of satellites launched per year. As indicated in Figure 63, most of the communication satellites are placed in geostationary orbit (68%), for which coverage performance is maximized. According to Figure 66, the number of telecom satellites launched in the last period ranging from 2016 to 2020 has suffered a slight decline. It can be directly reconducted to the lowering of the orders since 2016 [167] and still ongoing with 14 orders in 2017-2018 and 15 in 2019 [168]. The slowdown of the double-digit GEO market growth is mainly caused by the uncertainties related to the future evolution of the technologies as well as to the effective approach to follow. On the one hand, the reborn of satellite constellation concepts could represent a true game-changer for the future of space commercial exploitation for communication purposes. Since its first pioneering proposals with the Globalstar and Iridium project launch, this mission architecture has been thought of with a moderate number (<100) of small/medium-size satellites. With the advancement in component miniaturization and with the gain in design experience, the major space operators are proposing and developing mega constellation with thousands of launched satellites. OneWeb (648 satellites), SpaceX's Starlink (4425 satellites) and Telesat (1160 satellites) are the most recent examples of how the potentiality of this architecture will become a reality in space soon. Even though several challenges shall be still addressed, such as regulations, traffic management and frequencies ownerships, the circumstances suggest a changing of the telecom market toward lower orbits (either LEO or MEO) and small spacecraft (<500kg) [169,170].

On the other hand, while multimedia data transfer has been the pillar of the GEO telecom market, nowadays, the user needs are moving toward internet-based services setting, in concurrent with the advancement of the technology, the obsolescence level of several satellites already operational. The large operators, such as Boeing and Airbus, are dealing with these aspects introducing flexible small GEO platforms able to minimize their ageing, guaranteeing the payload's reconfiguration capabilities. Examples could be found with Small-GEO [171], Electra [172], NEOSAT [173,174].

With the introduction of the satellite constellations with the consequent lowering of the operative orbits, the importance of the LEO and MEO regions are becoming relevant also for communication scenario. Up to nowadays, satellites for Earth Observation purposes dominated in this region, as shown in Figure 63, with constant growth in annual launches (Figure 64). Two main factors have influenced this sector: the widespread of observation products coming from remote sensing services and the increment of their utilization by the institution and governmental operators.

These public entities set up vast national and international programmes to coordinate all the EO opportunities with time. The NASA Earth Observing System (EOS) program and the European Copernicus embrace all possible EO scenario with a series of dedicated mission equipped with different payload technologies to cover all possible needs. With a total market of USD 4.6 B in 2019 [175], with the current estimated rate of growth, the total forecast market in 2029 is USD 8 B. These estimations include satellite constellations of small satellites. A positive margin could further increase the market size owing to the amount of investment of more than 50 companies. Furthermore, the impacts of EO in terms of economic revenue of the EO data products on the end-users is not fully assessed. As a result, even though not as quick as the communication market, the growth is ensured.

A different market, dominated by governmental/military programmes, is the GNSS applications. National and supranational programmes are currently ongoing with a future development roadmap mainly aimed at performance improvements. The main programmes are the American GPS, the European Galileo, the Russian GLONASS and the Chinese BeiDou. As shown in Figure 65, the class of orbits mainly used for these applications are the MEO owing to the complex orbital architecture to maximize the coverage capabilities with respect to a target receiver.

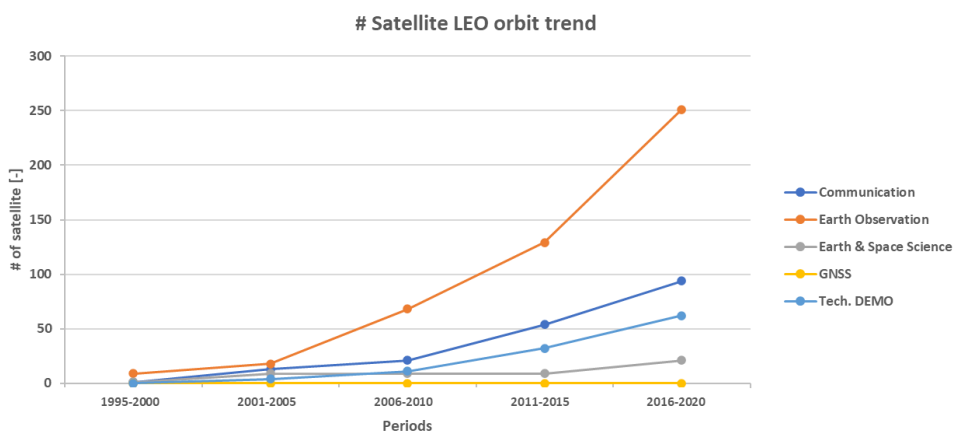


Figure 64: number of satellites in LEO w.r.t. their application.

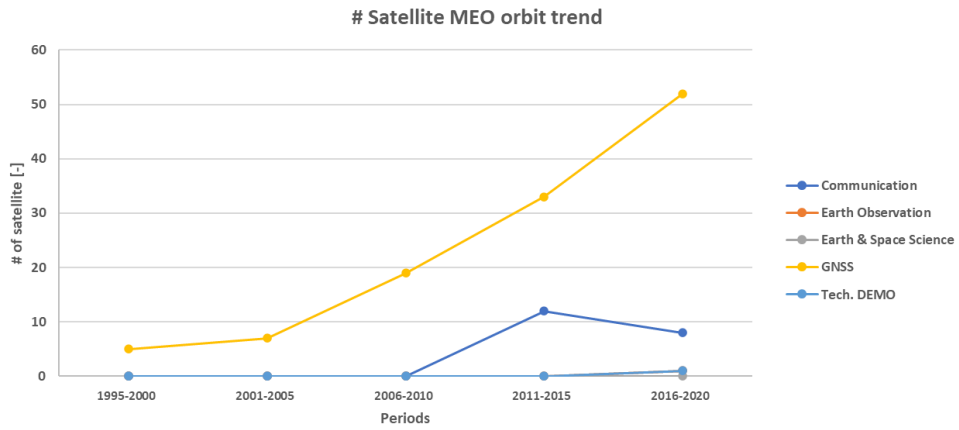


Figure 65 number of satellites in MEO w.r.t. their application.

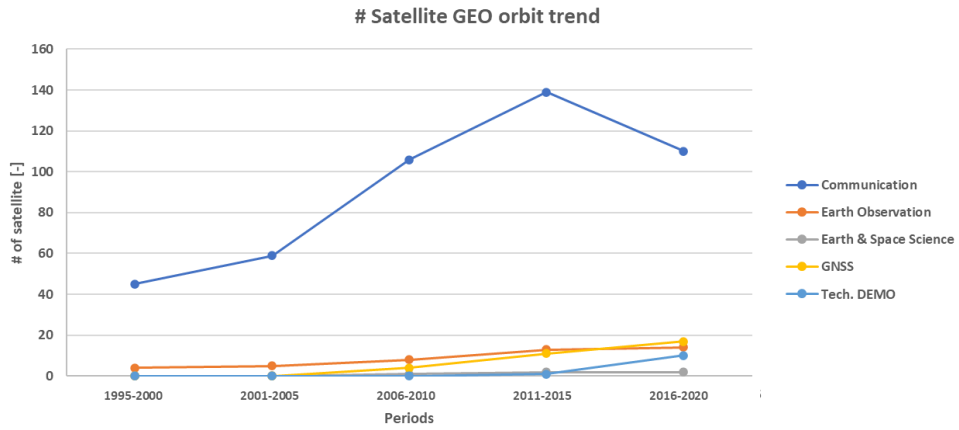


Figure 66: number of satellites in GEO w.r.t. their application.

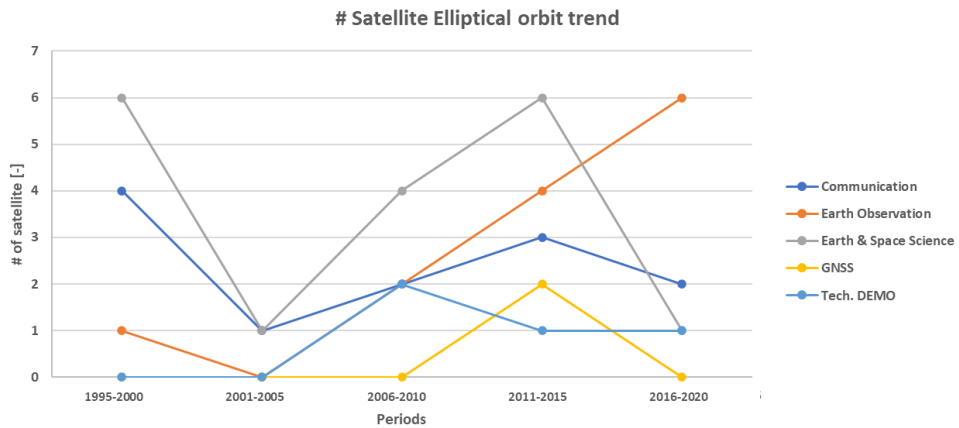


Figure 67: number of satellites on elliptical orbits w.r.t. their application.

3.4 VLEO scenario mission definition

3.4.1 VLEO IoD mission objectives

The most effective approach to fill the gap for a newly developed concept and its final space-proven status is represented by an In-Orbit demonstration mission. It is a critical decision since the high related risks. Therefore, it is usually not preferred by the LSI/operators that instead followed more conservative approaches adopting reliable components with flight heritage and already consolidated system design. Even though this latter design philosophy ensures a safe and cost-effective result, the bridge offers by a demonstration mission ensure a rapid infusion of revolutionary concepts and their quick gain of readiness (TRL) for fruitful commercialization.

The crucial aspect of the demonstration missions is the possibility of testing and qualifying the concept under a real operational environment, especially for what concern pressure, temperature, space radiation and EMC interactions. This is specifically evident on a ramEP concept due to the VLEO environment, which overlaps issues related to the space operation with those classically associated with atmospheric flight. Consequently, the following study has been centred on the feasibility analysis on a demonstration mission based on a ramEP technology, according to the objectives of the current SITAEI's ongoing projects. In particular, the study's objective is to suggest a possible scenario recommending relevant design and operation constraints to pave the way to the following detailed studies.

The primary objective of a ramEP demonstration mission consists of the full validation of the propulsion subsystem, based on a ramEP thruster, performing all its function of the ramEP in the fulfilment of all its functions and subfunctions.

These includes:

- the capability to counteract the atmospheric drag within its time variations.
- sustained the operation of the thruster dealing with the local environment variations.
- providing the expected performance along with the operative lifetime
- control the thruster with respect to the pre-determined control law.

Directly linked to the primary objective is the demonstration of the full operability of the ramEP platform during the operative mission lifetime. This is intended as the demonstration of flight operations and quantifies the performance of:

- spacecraft VLEO operations:
 - operation in eclipse
 - operation in daylight
 - operation in atmospheric variation
- autonomous onboard resource management and FDIR function
- autonomous navigation

- electric power subsystem operation and validation of specific architecture solutions
- consolidation of the communication architecture

Additionally, to the previous objectives, some secondary objectives could be considered as part of the demonstration mission:

- estimation of the degradation of the spacecraft material/surfaces due to the harsh environment
- validation of the performance of the thermal control system
- demonstration of the capability to operate the thruster in alternative and /or “exotic” operation.
- Re-entry trajectory forecasting capability.

Additional requirements have been imposed within these high-level objectives for the preliminary analysis performed on both the operative range of the thruster and on the foreseen operational timeframe.

- Altitude range: the altitude range of interest for the ramEP spacecraft operation is 180-250km. The capability of operating the thruster within this range shall be proven with the analyses presented in this work and the future test campaign [176].
- Reference orbit: the SSO Dawn-Dusk @6a.m. has been selected as reference orbit for the ramEP IoD mission. This baseline relies on the experience gained with GOCE [105,108] and the previous airbreathing studies [100,177].
- Mission lifetime: the mission lifetime has been set at 7 years. This mission duration is consistent with ESA expectations in the ramEP CDF investigation performed by the Agency [178]. After future evaluation on the capability of the spacecraft (and thruster) material to withstand the harsh VLEO environment, further extension of the lifetime requirement might be considered.
- Launch vehicle baseline/available launch mass: among different launch vehicle options (reported in Table 34), the launch vehicle considered as baseline for the ramEP IoD mission is the VEGA C. With the future first launch scheduled in 2021, the VEGA C will be able to deliver up to 2500 kg of payload on an SSO orbit [28]. Furthermore, among the small-medium class launchers, VEGA-C offers a higher cross-section fairing area. In addition, the available payload mass fulfils the foreseen small-mass spacecraft design, which is the target for an IoD mission. For preliminary estimation, the ramEP spacecraft mass was assumed equal to 1000kg.
- Thrust only during illumination period: to follow a worst-case approach, stressing the feasibility consideration on the onboard power generation as

well as the capability of the thruster to maintain a target altitude, the thrusting operations of the ramEP system were limited to lighting conditions without additional firing arcs during eclipse through the exploitation of the batteries.

This general design drivers have been introduced in the design process to steer the final result to guarantee representative design solutions in line with stakeholder expectation and based on the performed analysis. These have been included to narrow the design space a highlight the benefit/criticalities in the adoption of the ramEP technology.

3.4.2 Mission architecture

Following the classical subdivision of a space mission architecture, the ramEP mission comprises four main segments, each one including several building blocks to solve specific or share functionalities. These are namely: (i) Space segment, (ii) Ground segment, (iii) Launch segment and (iv) user segment, as shown in Figure 68. For each of these segments, main building blocks are identified to intercept both functions and expectation, which allow the fulfilment of the mission objectives. The architecture here presented includes elements not directly related to a demonstration mission but rather to one of the application scenarios presented in Section 3.3. This deviation is introduced to provide a clear overview of a foreseen ramEP mission architecture.

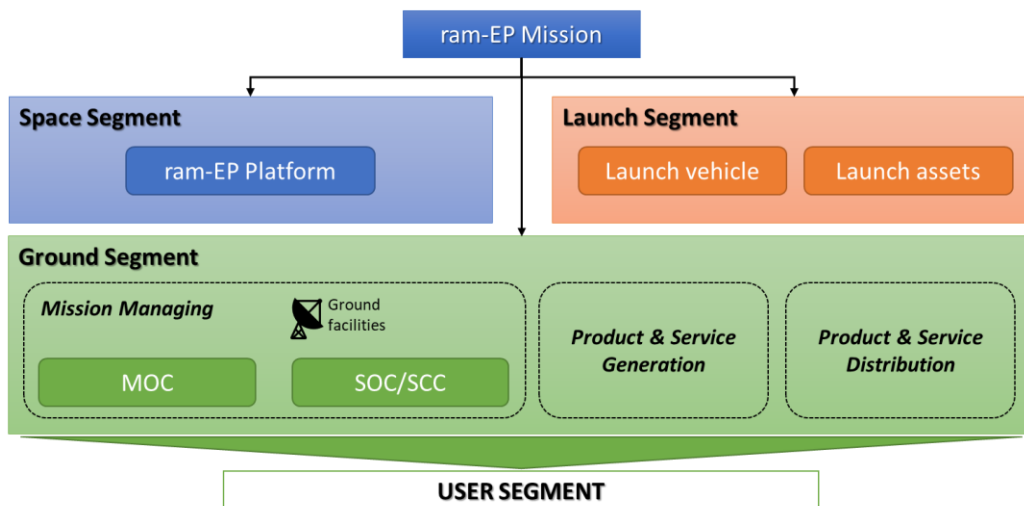


Figure 68: Notional system architecture block diagram.

The **Space Segment** consists of the ramEP platform, the payload, and the associated communication equipment. The platform is based on the ramEP thruster, the payload which interfaces with the objective of the mission and all the systems necessary for its survival and operation.

The **Launch Segment** includes all the assets and services associated with the launch vehicle, the payload integration and the spacecraft launch. The launch

element is the VEGA-C. The selection of the launch vehicle baseline has been carried out considering the preliminary mission and design analyses. Possible backup solutions have also been considered.

The **Ground Segment** elements are grouped concerning their functionalities in: Mission Management, Product and Service Generation, Product and Service Distribution. This subdivision based on functional attributes is not necessarily represented by the physical separation of the related functions. First, Mission Management comprises both physical and organizational assets for spacecraft and operation management. This group is based on two main centres: the Mission Operation Centre (MOC) and the Science Control Centre/Spacecraft Control Centre (SOC/SCC). The MOC is in charge of commanding spacecraft and instruments, ensuring its safety and health status, performing orbital analysis, providing uplink/downlink communications through ground stations (upload of spacecraft and payload telecommands and receive telemetry, providing raw telemetry and housekeeping data to the SOC/SCC, collecting data to the SOC/SCC, provide telecommand history to SOC/SCC).

Considering the different nature that the RAMEP mission could have in terms of final applications, the functionalities related to the SOC, and the SCC are grouped in one single entity. In particular, this centre has the function of mission operation planning and handling, process lower-level data, temporary storing of data (if needed). In this preliminary ground segment architecture, the POCC is considered as an optional centre to be included, if necessary, to operate a specific payload. Second, the Product and Service generation functions provide the capability of processing raw data operating regularly defined with respect to the availability of the final product/service: continuous, with latency and immediate. The generation processes on the raw data represent a key function to guarantee the fulfilment of mission requirements and stakeholders' satisfaction. Together with the main function above briefly described, the Product and Service generation functions also comprise the quality verification of the product, reporting to the SOC/SCC for corrective actions if needed. Last, the main Product and Service Distribution function are to provide an efficient interface with the User Segment. It is in charge of sharing data and services toward the End Users ensuring their reformatting, reprojection and subsetting.

The User Segment represents all possible end-users of RAMEP mission outputs instead. They have been categorised in: Commercial operators, Governments & Institutions, General Public, Scientific Organizations & Institutions, as shown in Section 3.3.1.

3.5 ramEP spacecraft concept

3.5.1 ramEP Platform Functional Definition

According to mission requirements and constraints as well as with the assumption made, the following functional analysis is derived (Figure 69). The analysis is limited to the subsystem level.

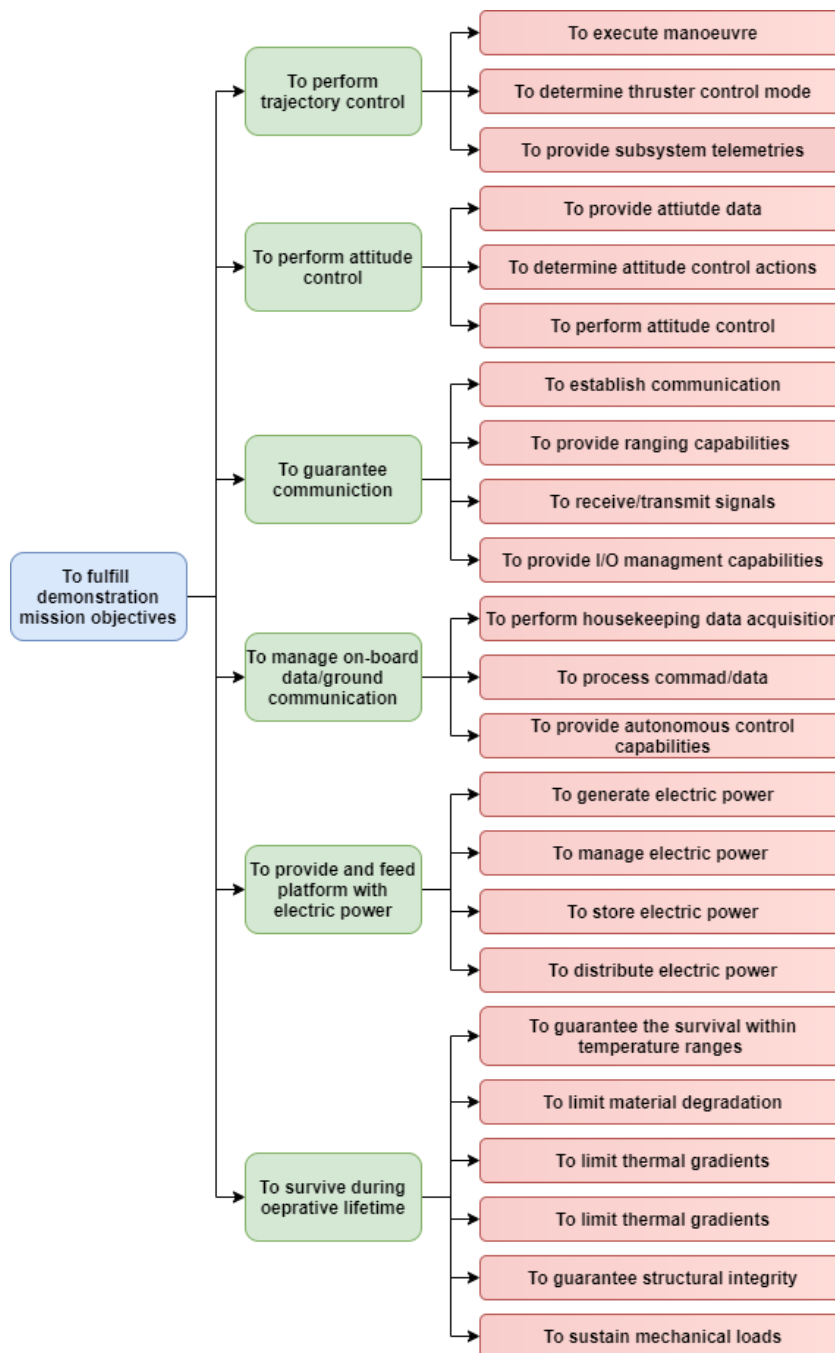


Figure 69: RAMEP Platform Functional Tree.

Following the classical system design definition exposed in [6,179], the consequent step is the function/product matrix, which allows allocating each function to a

specific product that shall be included in the spacecraft definition to fulfil the function itself. The Function/Product Matrix is shown in Table 36

Table 36: ramEP function/product matrix.

Functions - Subsystem level	Functions – Component level	ramEP Subsystem	Electric Power Subsystem	Thermal Control Subsystem	Attitude and Orbit Control Subsystem	Tracking & Telecommunication	Command & Data Handling	Structure
		ramEPS	EPS	TCS	AOCS	TT&C	C&DH	STRUCT
To perform trajectory control	To execute manoeuvre	x						
	To determine thruster control mode	x						
	To provide subsystem telemetries	x						
To perform attitude control	To provide attitude data				x			
	To determine control actions				x			
	To perform attitude control				x			
To guarantee communication	To establish communication					x		
	To provide ranging capabilities					x		
	To receive/transmit signals					x		
	To provide I/O management capabilities					x		
To manage on-board data/ground communication	To perform housekeeping data acquisition						x	
	To process command/data						x	
	To provide autonomous control capabilities						x	
To provide and feed platform with electric power	To generate electric power		x					
	To manage electric power		x					
	To store electric power		x					
	To distribute electric power		x					
To survive during operative lifetime	To guarantee survival within temperature ranges			x				
	To limit material degradation							x
	To limit thermal gradients			x				
	To guarantee the structural integrity							x
	To sustain mechanical loads							x

The identified platform subsystems are qualitatively detailed in the following paragraphs.

ramEP System: the propulsion system is based on several components that allow fulfilling all subsystem subfunctions to generate thrust. In general, the intake to thruster assembly has the function to provide thrust from the collected atmospheric particles. The electrical power necessary to operate the thruster is processed by the Power Processing Unit (PPU), which has the main function of conditioning the input power, provided by the Electric Power System, and supply it to the thruster. Moreover, it has control and FDIR capability. First, the control capabilities are defined with respect to the operative modes of the PPU, which

follows a dedicated control logic. Second, the FDIR functions guarantee the safety operation of the thruster through detection, identification and recovery actions which could be performed by the system, through autonomous actions, or platform level, triggering the safe/hold mode.

Electric Power System (EPS): this subsystem is most affected by the considerable power demand mainly related to the operation of the thruster. Thus, the first function allocated to the EPS is the onboard power generation employing solar cells arranged in arrays. The generated power is then managed by the Power Conditioning and Distribution Unit (PCDU), which allows the protection of the distribution power bus and conditionate the power to a controlled provision of electric power to the other platform loads. Moreover, this component allows regulating the recharge of the battery packs during the sunlight portion of the orbit. These components are in charge to sustain the operation during eclipse periods. Lastly, the distribution of the electrical power toward other onboard components is guaranteed by the power bus.

Thermal Control System (TCS): considering the orbital environment peculiarities and high power managed by some components associated with the formation of hot spots, the TCS shall ensure a thermal environment within the defined operative temperature ranges. This function can be split into several subfunctions allocated to a single component. The TCS shall guarantee proper insulation, heat rejection and generation, local sink, collection, and transportation of the heat. Temperature sensors are used to monitor the thermal environment. If the temperature level is close to the lower operative limit, it is increased or maintained by the mean of the heaters, placed in a strategic position to maximize heat generation to protect components from cold conditions. In specific cases, the MLI blankets are used either to thermally protect the component, regulating and keeping the heat fluxes, or to protect the component from external heat fluxes. On the contrary, for hot spots, mail generated by electric components (e.g., PPU) cold plates are exploited in association with heat pipes for heat transportation toward the radiators and efficiently dissipating the waste power flux.

Attitude and Orbit Control System (AOCS): the AOCS is another critical platform on-board system. It oversees attitude and orbit control for the whole mission duration, counteracting internal and external forces while providing 3-axis stabilization along the trajectory. Moreover, the AOCS functionalities comprise also the Guidance Navigation and Control (GNC) functions which allow operating the thruster following the pre-planned mission phase. These functions consist of: (i) provide telemetries of position, angular velocity rate and attitude, (ii) elaborate telemetries with respect to both desired phase operation/s and the defined control logic, (iii) determine necessary actions, verified, and validate the related commands to the control components (AOCS actuators and/or RAMEP thruster).

Environmental and operational disturbances impact the AOCS design. In specific, the drag generated by the atmospheric residuals continuously acts on the platform diminishing the orbital energy and generating torque forces around the inertial axes of the spacecraft itself. Thus, the ensuring of an efficient counteraction of the drag force, performed by the thruster and the possibility of providing a thrust over drag ratio greater than one, shall also be guaranteed by counteracting these torques according to the operative requirement of the thruster intake. In parallel to the influence of the incoming atmospheric flow, minor contributions of gravity gradient, solar pressure, third body and magnetic field are present. However, the latter external disturbance is exploited by the magnetometers that, in association with star-tracker and coarse Earth-Sun sensors, provide telemetry in every operative condition to derive the platform attitude. After the elaboration of the attitude status performed by a dedicated module of the On-Board Computer, the actuation of the control actions is demanded to the magnetorquers, placed along the principal inertial axes of the platform. In addition to the other sensors, an Inertial Measurement Unit (IMU) provides telemetries on acting body forces, angular rate and spacecraft orientation which are transmitted to the C&DH through a data bus.

Telemetry, Tracking & Communication (TT&C): this system provides a reliable interface between the ground segment and the spacecraft. The TT&C shall guarantee carrier tracking for ranging and tracking operations between ground stations and the spacecraft to know its position and velocity. Specific equipment is usually adopted for providing this function. The high gain antenna shall ensure the command reception in the uplink. The received signals shall be demodulated and transmitted to the C&DH through the data bus. The onboard telemetry composed of generic housekeeping and mission data shall be modulated and transmitted to the ground through the downlink process. This architecture is a two-way coherent mode that defines a turnaround frequency ratio between the uplink and downlink frequencies. The main criticality of the TT&C system is to deal with a short period for establishing a stable link between the ground station and the spacecraft. This constrains forces toward the adoption of a specific TT&C design for which high downlink data rates shall be considered.

Command and Data Handling (C&DH): this onboard system is based on different modules in charge of specific functions. An I/O board is adopted to interface the On-Board Computer with the other subsystem. The command received from the TT&C shall be validated, decrypted, processed, and distributed toward the other onboard systems. At the same time, the C&DH shall collect, process, store, encrypt and transmit housekeeping data, telemetry, and mission data. Moreover, specific OBC functions are keeping the spacecraft clocking and all the processing logic for the security and FDIR function. In the adopted OBC architecture, specific modules have been dedicated to TCS and AOCS due to their high level of complexity which required the implementation of specific capabilities. The ramEP system control capability is included in the AOCS module. All other functionalities

are allocated to the Command & Data Handling Management unit (CDMU). Last, a storage module composed of multiple storage units provides storage capability.

Structure (STRUCT): the spacecraft structure functions can be generally identified as the capability of providing loads paths for all operative loads, guaranteeing the spacecraft integrity and support internal/external components. The first functions are usually allocated to the primary structure, while the secondary structures are placed to mechanically interface the single components with the spacecraft. An additional function usually allocated to SRUCT is the protection from micro-meteoroids and orbital debris (MMOD).

ramEP Platform Physical Block Diagram

Starting from the functional analysis included in the previous paragraph, the functional block diagram of Figure 70 was derived.

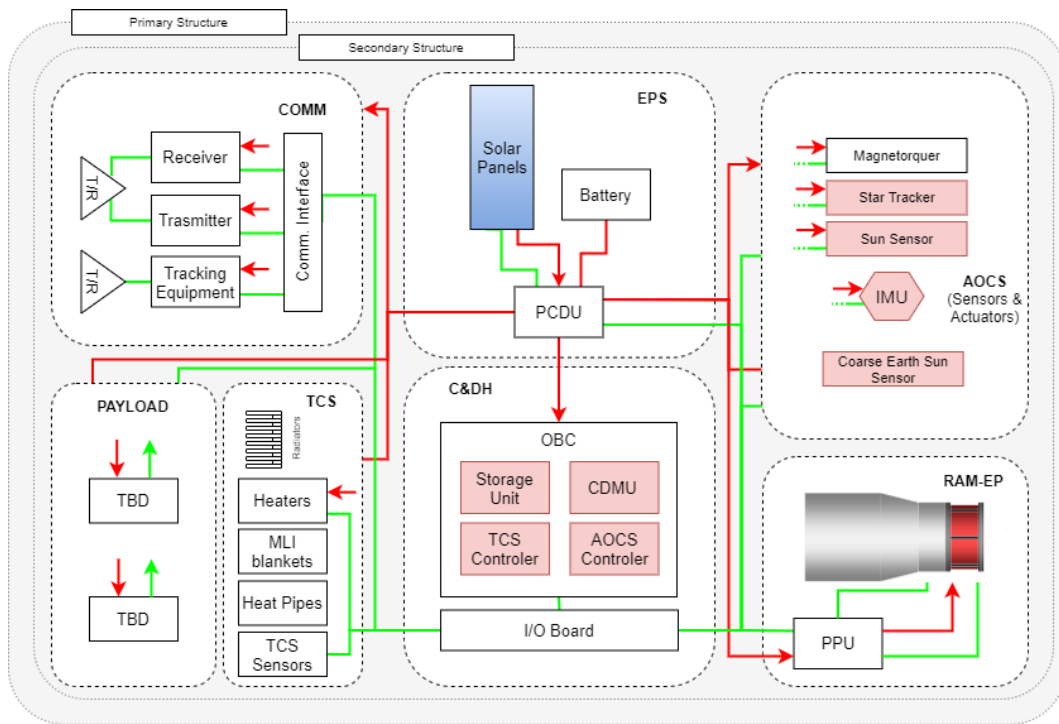


Figure 70: ramEP platform functional block diagram

The Functional Block Diagram reports the functional grouping of the derived components with the related output and input interconnections among the components themselves. The telemetry and command lines are represented with solid green lines. A central architecture focused on the C&DH is adopted.

3.5.2 ramEP ConOps: Design Reference Mission and mission phases

The Design Reference Mission (DRM) represents all the possible phases for a ramEP mission. The DRM reports three possible mission alternatives derived

considering: (i) the thrust over drag ratio, which can determine high/medium/low target altitudes, the number of phases where the average altitude is controlled around the selected target altitude and the duration of these phases; (ii) the operation during different solar periods (high, medium and low solar periods) with respect the possible launch date which determines the S/C capability to control the average altitude around the target altitude; (iii) the payload requirements and constraints in terms of altitudes, point accuracy and revisit period; (iv) launch capability of small-medium launchers.

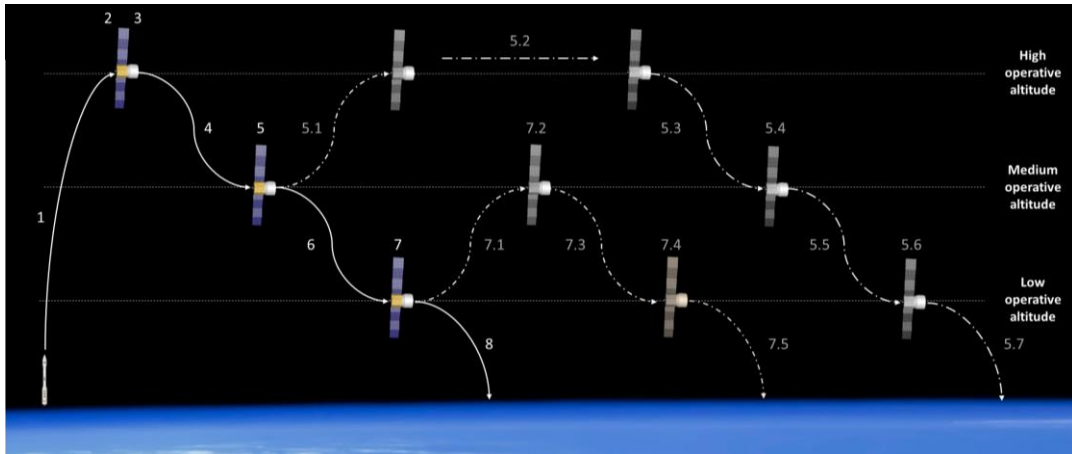


Figure 71: RAMEP general Design Reference Mission (DRM).

The generic approach followed in the definition of the ramEP DRM allows the exploitation of the same mission phases and operations in different orbits. However, in the next design iterations, mission and spacecraft operations shall be characterized and potentially constrained by a clear definition of the payload needs.

3.5.2.1 Reference orbits

A sun-synchronous orbit (SSO) is an almost polar orbit. A spacecraft in an SSO passes over any point of the central body's surface at the same local solar time. For example, a spacecraft in dusk-dawn orbit passes a specific region close to the equator always at sunrise in the morning, while a second region close to the equator but opposite in longitude by about 180 degrees is always passed at sunset. Besides, a dusk-dawn orbit puts the spacecraft in constant sunlight without encountering eclipses.

Because the central body (e.g., Earth) rotates around the Sun, the orbital plane of the SSO needs to rotate one revolution per year as well. This effect is called precession, and for the planet Earth, it is about 1 degree per day. Thus, a sun-synchronous orbit has always the same orientation w.r.t Sun, whereas other orbits typically stay inertially fixed. The precession of the orbital plane is achieved due to the J2 effect of the central body. The J2 effect is caused by the equatorial bulge, i.e., the difference between the equatorial and the polar radius of the central body. The angular precession of the orbital plane is a function of the orbit inclination:

$$\Delta\Omega = -3\pi \frac{J_2 R_E^2}{p^2} \cos i \quad (3.1)$$

Where Ω is the right ascension of the ascending node, J_2 is the coefficient for the second zonal term of the central body (e.g., 1.08263×10^{-3} for Earth), R_e is the equatorial radius of the central body (6378.137 km for Earth), p is the semi-latus rectum, and i is the inclination of the spacecraft's orbit. Considering a change in the right ascension of 360 degrees per year and a circular orbit, the inclination can be expressed as a function of the orbital altitude h :

$$\cos i \approx -\left(\frac{6378.137 \text{ km} + h}{12352 \text{ km}}\right)^{7/2} \quad (3.2)$$

The orbital inclination of an SSO is given in Figure 72: for an altitude regime from 160 to 250 km. Please note that the altitude is the one with respect to the equator.

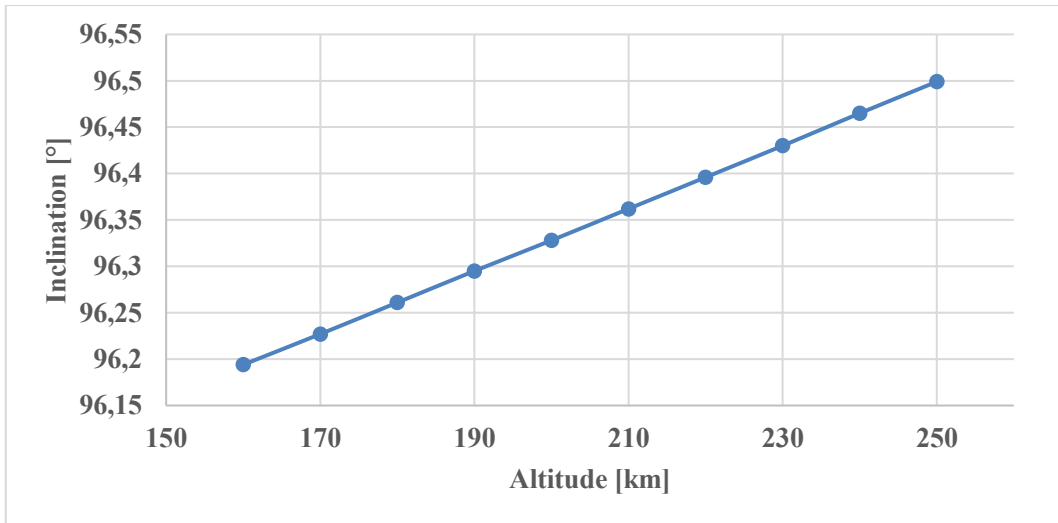


Figure 72: variation of the orbit inclination for an SSO dawn-dusk orbit.

The right ascension of the ascending node is chosen such that the SSO is a dusk-dawn orbit with continuous illumination by the Sun.

3.5.2.2 Mission Phases

Table 37 lists the main mission phases according to the mission objective and R /C functionalities.

Table 37: mission phases description.

	#	PHASE	SUB PHASE	PHASES
NOMINAL PHASES	1	Launch & Early Operation Phases (LEOP)	LNC	EOP – Launch
	2		EOP – COM	Early Operation Phase – Commissioning
	3	Nominal Operations (Nop)	Nop.AMP1	Altitude Maintenance phase – First thrusting phase
	4		Nop.AVP1	Altitude Variation phase – First altitude descend
	5		Nop.AMP2	Altitude Maintenance phase – Second thrusting phase
	6		Nop.AVP2	Altitude Variation phase – Second altitude descend
	7		Nop.AMP3	Altitude Maintenance phase – Third thrusting phase
	8	End of Life (EoL)	EoL	End of Life operations
MISSION EXTENSION POSSIBILITIES	5.1	Mission Extension (ME) – ME1	ME1.ASC1	ME – Ascend phase
	5.2		ME1.AMP1	ME – Altitude Maintenance phase – thrusting phase
	5.3		ME1-AVP1	ME – Altitude Variation phase – descend phase
	5.4		ME1.AMP2	ME – Altitude Maintenance phase – thrusting phase
	5.5		ME1-AVP1	ME – Altitude Variation phase – descend phase
	5.6		ME1.AMP3	ME – Altitude Maintenance phase – thrusting phase
	5.7		ME1.EoL	ME – End of Life operations
	7.1	Mission Extension (ME) – ME2	ME2.ASC1	ME – Ascend phase
	7.2		ME2.AMP1	ME – Altitude Maintenance phase – thrusting phase
	7.3		ME2.AVP1	ME – Altitude Variation phase – descend phase
7.4	ME2.AMP2		ME – Altitude Maintenance phase – thrusting phase	
7.5	ME2.De&R e		ME – End of Life operations	

A general identification of the mission phase is then characterized by the definition of the sub-phases. Each mission phases are characterized by starting and ending events, duration, environment and occurrence of particular event/s. Relevant mission phases and sub-phases are detailed in the following. Due to the level of the mission analysis and platform definition and design, the phase characteristics still under definition are reported with TBC/TBD. The future update of this document will provide more detailed information on the selected mission scenario.

Launch (LNC): all the operations that the selected launch vehicle shall perform to inject the S/C in its initial orbit. This phase includes launch, separation, acquisition, and initial check-out. The end event of this phase is the conclusion of the preliminary S/C activation and check-out.

Early Operation Phase – Commissioning (EOP-COM): S/C nominal operation and satellite check-out, payload activation and check-out, RAMEP system activation and check-out. The verification of the health status of the S/C and its systems represents the end event of this phase.

Altitude Maintenance Phase (AMP): this phase includes the operation of the RAMEP system in “Thrusting mode”, according to the adopted control logic, to maintain a constant average altitude. The altitude can vary for the different phases labelled with “AMP”. The payload is operated relative to the pre-planned duty cycle. The end event of this phase is represented by the switching to other operational modes commanded by the OBC, according to pre-planned mission operations.

Altitude Variation Phase (AVP): during this phase, the S/C mean altitude is varied. According to the planned mission operations, the S/C will vary its mean altitude, operating either in “thrusting mode” to raise the altitude or in “Fall mode” to decrease it. In both cases, the payload can be operated according to its duty cycle. The trigger of OBC commands which pushes the change of S/C mode represents the end event for the phases labelled with AVP. This event coincides with the achievement of the target mean altitude.

End of Life (EoL): in this phase, the end-of-life operation will be performed. The S/C is controlled as long as the thruster can be operated even though the generated thrust will inevitably be lower than the drag at lower altitudes. The orbit will be controlled, targeting an increment of the eccentricity to reduce the uncertainties in the estimation of the ground re-entry swath. Before losing the attitude control capability, all passivation actions will be performed. Then the uncontrolled atmospheric entry will completely burn up the satellite during re-entry. All the operations in this phase will be performed in the pre-planner “EoL mode”.

Additional mission phases include:

Mission Extension #1 (ME1): the optional mission extension #1 includes a single AVP phase to raise the average altitude to a higher altitude starting from the average operative altitude. Then, three AMP phases are planned, spaced out with two AVP phases. The EoL phase represents the final phase of the ME1.

Mission Extension #2 (ME2): the optional mission extension solution #2 foresees the possibility to raise the mean altitude starting from the lowest operative

altitude. The consequent AMP phase is followed by an AVP and the last AMP. The ME2 ends with the EoL phase.

Table 38 lists and characterizes the nominal phases considering the average altitude and starting/ending events description.

Table 38: mission phases characterization.

#	ACR:	Altitude [km]	Starting event	Ending event
1	LNC	--	Launch	Conclusion S/C preliminary check
2	EOP-COM	HOA	Conclusion S/C preliminary check	Conclusion of Commissioning phase – reception of nominal operation command
3	NOp.AMP1	HOA	Conclusion of Commissioning phase – reception of nominal operation command	AMP ending OBC command
4	Nop.AVP1	HOA>MOA	AMP ending OBC command	Reaching the target altitude
5	Nop.AMP2	MOA	Reaching the target altitude	AMP ending OBC command
6	Nop.AVP2	MOA>LOA	AMP ending OBC command	AMP ending OBC command
7	Nop.AMP3	LOA	Reaching the target altitude	Reception of the EoL entering command
8	EoL	LOA>re-entry	Reception of the EoL entering command	Re-entry

(*) During the commissioning phase, the RAMEP system will not be operated to maintain a constant average altitude but only for system health checks. As a result, the first thrusting phase could be performed to a lower altitude. However, the next design phases will characterize the launch performance with the period necessary for EOP.

HOA: High Operative Altitude
MOA: Medium Operative Altitude
LOA: Low Operative Altitude

3.5.3 Modes of Operation

Figure 73 identifies the RAMEP S/C modes of operation necessary to derive the power budget for each mission phase according to the duty cycles of the single subsystems. However, it is important to highlight that, as for the space tug case, the main consumption is represented by the propulsion subsystem based on the ramEP thruster.

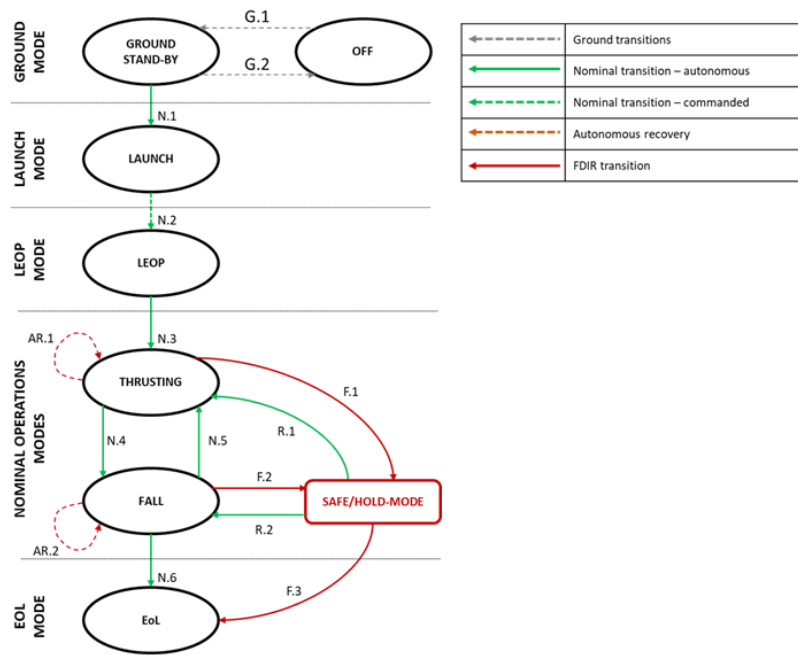


Figure 73: modes of operation at the system level.

The identified modes of operation are mainly characterized by the correspondent mission phase:

- **OFF:** in this mode, the S/C is fully OFF.
- **GROUND STAND-BY:** this mode is activated when one or more equipment is activated during on-ground to perform test activities.
- **LAUNCH:** during the launch phase up to its deployment, the S/C is in the off state to avoid potential hazards that could endanger both the spacecraft and the launch vehicle, jeopardizing this phase.
- **LEOP:** this mode is activated during early operation activities to perform the spacecraft commissioning while ensuring the full attitude control capability.
- **THRUSTING:** This phase is activated during altitude control operations. The average altitude is controlled to either keep it constant or increase it to a higher value. This mode of operation allows the operation of the payload according to its operative profile.
- **FALL:** the objective of this mode is to guarantee a controlled descend to a lower average altitude targeted according to the pre-planned mission operation. All S/C functions are guaranteed during this mode except for the ramEP system, which is switched off.

- **EOL:** this mode is activated at the end of nominal mission phases for ensuring a semi-controlled re-entry. It allows the operation RAMEP system as long as the attitude can be controlled, reducing both the risk of an uncontrolled re-entry in overpopulated regions and the area of the debris footprint. After the exceeding of the attitude control capability, passivation actions are taking place to avoid potential explosions.
- **SAFE/HOLD MODE:** this mode is reached autonomously after the detection of pre-defined operation conditions or event which could jeopardize S/C integrity and/or future operations causing either loss of the mission or damaging of the spacecraft. The safe/hold mode consists of the minimization of the power consumption, excluding the non-essential system. After the completion of FDIR functions, if the safe/hold trigger event is recovered, the mode is forced to a nominal mode after the reception of the proper ground command. If the safe/hold event cannot be recovered, the safe/hold mode is triggered to perform the platform passivation in EoL mode for S/C disposal.

In Table 39, the identified transitions are characterized by initial and final system mode.

Table 39: ramEP S/C mode transition characterization.

Transition type	Transition ID	Initial State	Final State
GROUND	G.1	OFF	Ground Stand-by
	G.2	Ground Stand-by	OFF
NOMINAL	N.1	Ground Stand-by	Launch
	N.2	Launch	LEOP
	N.3	LEOP	Thrusting
	N.4	Thrusting	Fall
	N.5	Fall	Thrusting
	N.6	Fall	EoL
RECOVERY	R.1	Safe/Hold-mode	Thrusting
	R.2	Safe/Hold-mode	Fall
AUTONOMOUS RECOVERY	AR.1	-	-
	AR.2	-	-
FAILURE	F.1	Thrusting	Safe/Hold-mode
	F.2	Fall	Safe/Hold-mode
	F.3	Safe/Hold-mode	EoL

3.6 Platform Definition

For the platform definition steps reported in the previous paragraphs, different design drivers have been identified and analysed, aiming at parameter quantification and, consequently, defining optimal spacecraft design solution.

As presented in the previous paragraphs, mission and platform definitions drive the evaluation of the performance achievable by the overall platform in terms of generated thrust and drag. To quantify both variables, the derivation and the analysis of alternative design solutions represents a fundamental activity to limit the design variable ranges according to mission requirements and constraints. Following these drivers, all possible configurations are identified considering the minimization of the frontal area through an aerodynamic shape, allowing the lowering of the generated drag. The selection of the most appropriate class of spacecraft shape has been carried out following the standard stepwise process by using multi-criteria decision analysis based on the definition of criteria and identification of alternatives. During this work, the following design drivers have been considered:

- ❖ System aerodynamic performances
 - Rationale: the criterion is to be intended as the need for maximization of fly-ability in every solar activity (low, medium, and high), lowering the generated drag fulfilling mission objectives.
 - Evaluation parameter/s: the evaluation parameter is the generated drag against the thrust level provided.

- ❖ Available internal volume
 - Rationale: the criterion is to maximize the internal volume available for all the platform systems, including the payload.
 - Evaluation parameter/s: the parameters are the internal volume evaluated against the generated drag, both volume and shape compatibility with the launcher.

- ❖ Configuration compatibility
 - Rationale: the criterion to choose a shape class that maximizes the compatibility with the selected launcher.
 - Evaluation parameter/s: the parameter based on which the alternative is evaluated against the criterion is, in this case, the shape interference with the available fairing dimensions, CoG.

- ❖ Aerodynamic stability
 - Rationale: the criterion consists of the minimization of external disturbances caused by the aerodynamic effects.
 - Evaluation parameter/s: the evaluation parameters are the disturbances forces and momentum against the internal volume,

generated drag, platform budgets, launcher compatibility and fulfilment of mission objectives.

As a consequence, the spacecraft configurations have been selected considering: (i) the general shape of the spacecraft obtained through the different relative position of the main spacecraft body, the solar arrays and the intake, (ii) the spacecraft body cross-section shape, which consider the minimization of the area not exploited by the intake itself, (iii) the architecture solutions of the solar arrays. A schematic overview of the class of alternatives is shown in Figure 74.

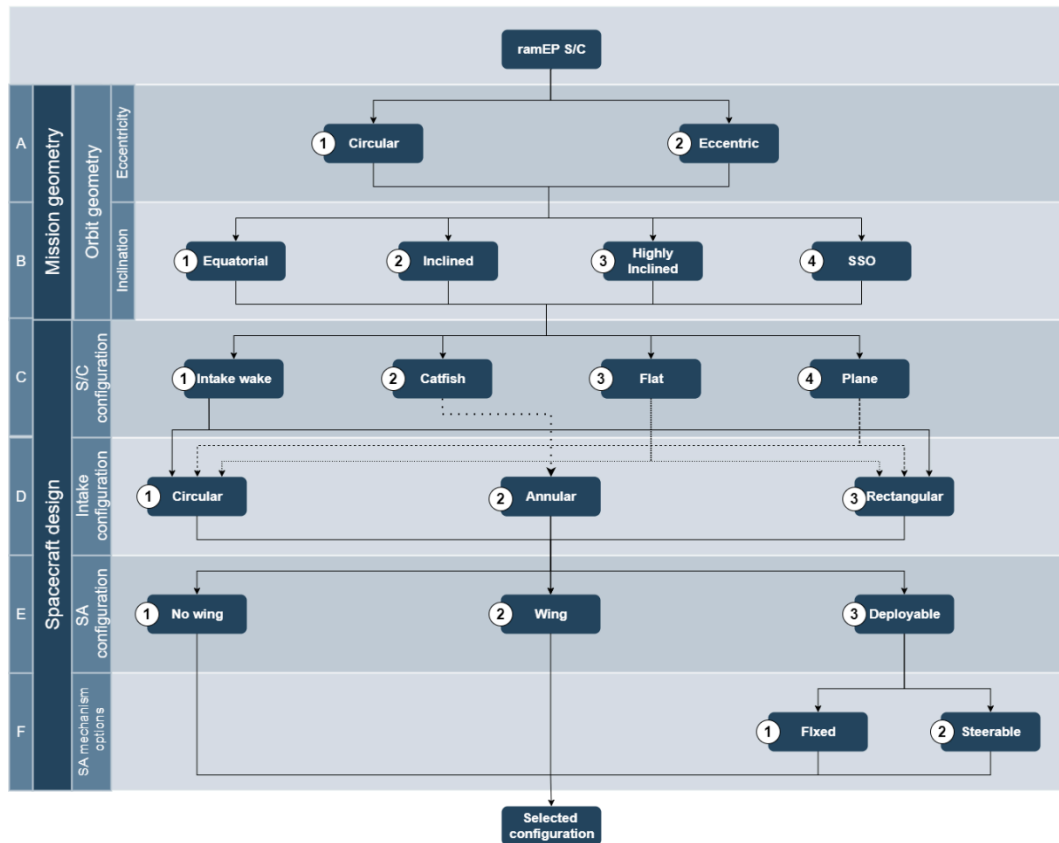


Figure 74: alternative spacecraft configuration options.

A qualitative evaluation has been performed to highlight the case of interest for the preliminary design of the ramEP spacecraft aimed at an IoD mission. The qualitative evaluation is shown in Table 40.

Table 40: mission and configuration trade-off.

Decision level	Alternatives			
A	Circular (1)		Eccentric (2)	
B	Equatorial (1)	Inclined (2)	Highly inclined (3)	SSO (4)
C	Intake Wake (1)	Catfish (2)	Flat (3)	Plane (4)
D	Circular (1)	Annular (2)		Ractangular (3)
E	No wing (1)	Wing (2)	Deployable (3)	
F	-		Fixed (1)	Steerable (2)

Several qualitative evaluations have been performed to highlight the advantages and disadvantages of each mission and configuration alternatives reported in Table 40. As a result, the circular SSO has been selected as a reference orbit, as already reported in Section 4.5.2.1.

The selection of the platform configuration has been based on the rationales reported above. It resulted in a general shape of the spacecraft in which the intake having a circular shape (D1) is integrated into the spacecraft body. The rest of the spacecraft subsystems are instead placed in the intake wake (C1) in order to minimize the exposed passive area, which caused a drag force increment. Moreover, this alternative allows the symmetry of the spacecraft is essential to minimized gravity and aerodynamic disturbances. For what concern the solar array configuration, multiple solutions have been considered. Following the GOCE-like concept, solution E2 consists of two fixed lateral structures covered with body-mounted solar cells. This option provides robustness to the structure avoiding complex mechanisms for the deployment of the solar arrays. Despite this limitation, it is limited by the available cross-section surface of the selected launch vehicle fairing. The capability of deploy solar arrays has also been considered with the option (E3) without steering capability (F1). Even though the latter possibility will enable the maximization of the power generation over the inclined orbit, the increasing of the generated drag due to the tilted surfaces will strongly reduce the capability of the system to produce a thrust over drag ratio equal or greater than one. As a consequence, this option has been discarded.

3.6.1 MAGNETO: software modifications

In order to prove the feasibility of the foreseen IoD mission in VLEO, the MAGNETO software developed in the context of space-tug analyses was expanded with several additional routines.

In Figure 75, the functional structure of the now-called “VLEO-MAGNETO” is shown. In the following sections, a general overview of the three main modules consisting of the structure of VLEO-MAGNETO is described.

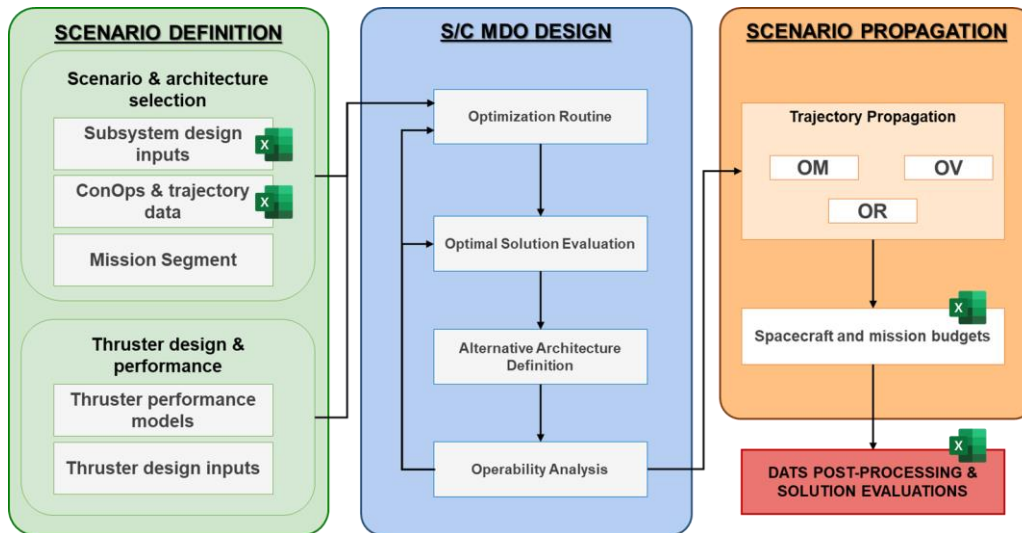


Figure 75: VLEO-MAGNETO software functional structure.

3.6.1.1 Input module

The input module's characteristic and the required user setup input during the simulation initialization are explained in this section. As already explained in the Space Tug case, a series of consecutive operations shall be performed to launch a new simulation in MAGNETO.

First, the offline modules consist of a set of Excel spreadsheet in which all the defined mission and spacecraft parameters needed for the following analyses are collected. This module is divided into two main routines: the spacecraft design and mission ConOps and the other specifically dedicated to the parameters necessary for both sizing and performance evaluation of the ramEP spacecraft. The software can read the spreadsheet opportunely compiled and save it as input in dedicated data structures.

Once the design and operational parameters are defined, the initialization of the online phases begins with the selection of the user local file folder path already defined in the source code (see Figure 75).

Through the definition of multiple spreadsheets, clearly labelled with a progressive integer number, it is possible to pre-define the entire set of simulations to be performed, then selected typing the related id number.

The successive inputs required from the user are related to the data saving and data plot procedures.

```

You have selected mission VLEO SCENARIO scenarios.
B.1
Trajectory propagation
WHICH SCENARIO DO YOU WANT RUN?
>1
B.1 - END
C.0 - DEFINITION OF THE DATA SAVING STRATEGY + PLOT
Long or short run?
>(0) ALL POINTS
>(1) EVERY PHASE
>(2) LONG RUN
>0
Saving process at the end of the run!\n

Do you want plot the data during the run?
>(1) YES
>(0) NO
>0
C.0 - end
C.1 - INPUT DATA IMPORT

```

Figure 76: VLEO-MAGNETO user-interactive interface.

Depending on both the duration of the single phases, defined in the operation input spreadsheet, and on the stopping condition reached within the simulation evolution, the computational time could strongly increase. To avoid out-of-memory issues, the large structures in which all the output parameters are collected are saved in three different ways. For short simulations, a single structure is saved at the end of the simulation itself. For long simulations time, the user can either select the option to save the output structure at the end of each mission phases (particularly useful when specific analyses shall be performed on a single phase) or select the option to save the output structure after a pre-define time (i.e., every hour of simulation). In the two latter cases, the data structures are saved on a single file, and the MATLAB data are deleted.

Furthermore, to quickly evaluate the trajectory evolution, a set of plots is proposed at each integration step. The user could enable or disable this function. At the end of the propagation phase, a dedicated plot subroutine is proposed in which the main mission parameters can be visualized.

3.6.1.2 PLATFORM DESIGN: Multidisciplinary design approach

A Multidisciplinary Design Optimization (MDO) process was set up to derive the optimal solution considering several objective functions for the generation of a Pareto front to include different optimal solutions for spacecraft design. The MDO process includes different specific tasks currently ongoing. The definition of the design space with the related design constraints is the main activity performed together with the derivation of the design modules for the preliminary sizing of each subsystem. This process is based on several design modules developed to size the main systems onboard the platform considering a variable configuration of the spacecraft.

In order to define the set of input and assigned parameters as well as constraint values among them, a series of parallel activities and analyses were carried out on specific design drivers. In particular, considering the general mission objectives reported in Section 4.4.1 and a set of assumptions has been introduced:

(i) Launch vehicle selection: a full set of launch vehicles (both rocket and innovative launch vehicle as spaceplane) were considered. The vehicle payload characteristics were listed and analysed with the main purposes of identified constraints impacting the ramEP satellite's dimensions and identifying the mass ranges allowed. For the following optimization activities, the VEGA-C has been considered as reference launchers because the highest fairing cross-lateral section surface available.

(ii) Eclipse condition: an extended eclipse analysis was carried out with a simplified orbital propagator to assess the worst eclipse condition (longest eclipse period). The set of orbits investigated was derived considering different altitudes over the ramEP operative altitude range (between 160 250km) over an SSO orbit Dawn-Dusk. The worst-case condition considered in the optimization process consists of an eclipse period of 1600s.

The coupling relationship for the optimization problem is organized in the design structure N2 diagram, as shown in Figure 77.

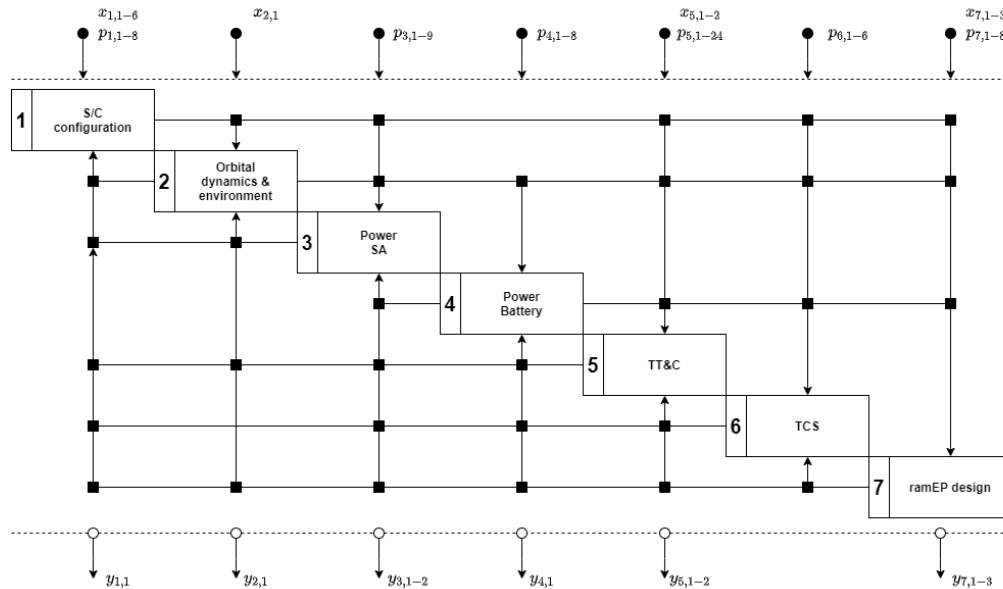


Figure 77: ramEP spacecraft MDO process.

In this process, four different types of variables are considered:

- $x_{i,k}$: k^{th} design variables
- $y_{i,k}$: k^{th} outputs for each discipline
- $y_{i|j,k}$: k^{th} coupled variables from design block i to design block j
- $p_{i,k}$: k^{th} fixed design parameters
- **DESIGN VARIABLES**

In this section, the input variables to Multidisciplinary Design Optimization are tabled. The range of variation of these parameters represents the overall design space in which feasible solution can be searched according to the constraints defined in the following sections.

In the table below, the design input variables are defined through their symbol used in the MDO-N2 diagram (see Figure 77), their physical meaning in the definition of the spacecraft design space, their unit of measurement and the value ranges.

Table 41: MDO design variables.

DB	$x_{i,k}$	Physical symbol	Physical meaning	Unit	Values	
					Min	Max
1	$x_{1,1}$	$W_{PLT tot}$	Width of the platform	[m]		
	$x_{1,2}$	$W_{PLT ratio}$	Ratio between the body and the wing widths	[-]		
	$x_{1,3}$	L_{PLT}	Length of the platform body	[m]		
	$x_{1,4}$	$L_{WING btm}$	Bottom length of the wing	[m]		
	$x_{1,5}$	$L_{WING top}$	Top length of the wing	[m]		
	$x_{1,6}$	$W_{FRONT ratio}$	Ratio between frontal sides	[-]		
2	$x_{2,1}$	h	Altitude	[km]		
5	$x_{5,1}$	$P_{TT\&C}$	Power of the antenna	[W]		
	$x_{5,2}$	L_{ANT}	Length of the antenna	[cm]		
7	$x_{7,1}$	V_{ramEP}	Discharge Voltage	[V]		
	$x_{7,2}$	$L_{ramEP int}$	Intake length	[m]		
	$x_{7,3}$	N	Number of intake ducts	[-]	1	100

In Table 42, the optimization output variables are summarized. These results are then combined for the definition of the optimization objective as following explained. The rest of the variables have been introduced for successive system evaluations.

Table 42: MDO output variables.,

DB	$y_{i,k}$	Physical symbol	Physical meaning	Unit
1	$y_{1,1}$	$V_{S/C}$	Payload/bus available module	$[m^3]$
2	$y_{2,1}$	$D_{S/C}$	Drag of the spacecraft	$[N]$
3	$y_{3,1}$	$P_{S/C}$	Spacecraft generated power	$[W]$
	$y_{3,2}$	S_{SA}	Solar array surfaces	$[m^2]$
4	$y_{4,1}$	P_{BATT}	Power of the battery pack	$[W]$
5	$y_{5,1}$	LM_{up}	Uplink margin	$[dB]$
	$y_{5,2}$	LM_{down}	Downlink margin	$[dB]$
7	$y_{7,1}$	T_{ramEP}	ramEP Thrust	$[N]$
	$y_{7,2}$	P_{ramEP}	ramEP Power	$[W]$
	$y_{7,3}$	ϕ_{ramEP}	ramEP acceleration voltage	$[V]$

Based on the aforementioned design variables reported in Table 41, the constrained MDO was set up.

The traditional objective of an optimization process applied to a space system design is reducing the overall system mass. This design goal is usually considered directly linked with the system cost, often introduced with proportional relations. Although the spacecraft mass is still fundamental for a comprehensive evaluation of the optimal design solution, a different approach has been followed. Considering the peculiarities of the VLEO scenario as well as the ramEP thruster, the preliminary system design targeted with this optimization considers a set of multiple objectives introduced for defined the optimal spacecraft configuration connected with optimal thruster operative range. First, the spacecraft configuration shall be conceived in order to minimize the generated drag.

On the contrary, it shall maximize the internal volume available for the spacecraft subsystems and eventually for the payload. Another key aspect to consider is the management of the onboard power. Increasing the thruster available power, a higher thruster value can potentially be reached. However, other onboard subsystems shall be fed with power as well as a possible payload. Nevertheless, the higher power level available onboard consists of larger solar arrays, generating a higher drag level. All these qualitative considerations have been translated into three design objectives, usually defined as attributes of the optimization process:

First, the drag over thrust ratio provides a clear indicator of the spacecraft shape goodness with respect to the obtainable thruster performance.

$$\widehat{OBJ}_1 = \frac{D_{S/C}}{T_{ramEP}}$$

where the $D_{S/C}$ is the total drag generated by the spacecraft and T_{ramEP} is the net thrust generate by the ramEP thruster.

The maximization of the internal volume is taken as the second objective. It depends on the geometrical configuration of the spacecraft and the design of the intake

section of the ramEP thruster. Taking the inverse of the volume, the optimization process can be implemented following the minimization approach.

$$\widehat{OBJ}_2 = 1/V$$

where V is the available internal volume.

The last objective is the minimization of the ratio between the ramEP thruster power and the overall platform power. This ratio shall be minimized to increase the capability of the system in sustaining additional power loads.

$$\widehat{OBJ}_3 = \frac{P_{ramEP}}{P_{S/C}}$$

where P_{ramEP} is the power of the ramEP thruster while $P_{S/C}$ is the total onboard power.

These objectives have been combined with a weighted sum approach to defining the following function:

$$J(y) = \alpha \widehat{OBJ}_1 + \beta \widehat{OBJ}_2 + \delta \widehat{OBJ}_3 \quad (3.3)$$

Where α , β and δ are the three scalar weights with $\alpha + \beta + \delta = 1$. These coefficients are chosen in the (0,1). To limit the computational demand, this range was spaced with an interval of 0,1. This allows reducing the number of cases to 34. As stated in [180], this is the classical procedure to generate the Pareto front in the objective space. An external for-loop introduced in the MDO process generates the different optimal values with respect to the triplet weight values, which classifies the solutions on the Pareto. By definition, the solution of the MDO that cannot be further improved at the same time is non-inferior and admissible solutions lying on a surface called Pareto front. This specific solution set is also defined as the group of non-dominated solutions.

The front generation process has been implemented in a dedicated subroutine based on a Pattern Search optimization algorithm introduced exploiting the customized MATLAB routine. This method foresees the definition of an initial values vector from which the algorithm defines a set of points around them, so-called “mesh”, created adding a scalar multiple to the initial values. At each point of the mesh, the objective function is evaluated to fit the best solutions taken as the initial point for the following iteration step. With the repetition of this process, the pattern of the best point is established, targeting the optimal result with the refinement of the optimization mesh. The number of iterations can be defined as well as the tolerance value after which this process is terminated.

At each interaction, the output values are compared with both predefined equalities and inequalities constraints through which the admissibility of the design result is evaluated.

$$\min J(\alpha, \beta, \delta, \widehat{OBJ}_1, \widehat{OBJ}_2, \widehat{OBJ}_3) \begin{cases} \widehat{OBJ}_1(\dots) \\ \widehat{OBJ}_2(\dots) \\ \widehat{OBJ}_3(\dots) \end{cases}$$

with

$$s. t. \left\{ \begin{array}{l} [y_{1,1}] = D_1(x_{1,1-6}, p_{1,1-8}) \\ [y_{2,1}] = D_2(x_{2,1}) \\ [y_{3,1}, y_{3,2}] = D_3(p_{3,1-9}) \\ [y_{4,1}] = D_4(p_{4,1-8}) \\ [y_{5,1}, y_{5,2}] = D_5(x_{5,1-2}, p_{5,1-24}) \\ [y_{7,1}, y_{7,2}, y_{7,3}] = D_7(x_{7,1-2}, p_{7,1-8}) \\ C_1(y_{7,1}, y_{2,1}) \leq 0 \\ C_2(y_{7,2}, y_{3,1}) \leq 0 \\ C_3(x_{1,1-6}, p_{1,1-8}) \leq 0 \\ C_4(x_{1,1-6}, p_{1,1-8}) \leq 0 \\ C_5(x_{1,1-6}, p_{1,1-8}) \leq 0 \\ C_6(x_{1,1-6}, p_{1,1-8}) \leq 0 \\ C_7(y_{1,1}) \leq 0 \\ C_8(y_{7,1}) \leq 0 \\ C_9(y_{2,1}) \leq 0 \\ C_{10}(y_{3,1}) \leq 0 \\ C_{11}(y_{7,2}) \leq 0 \\ C_{12}(y_{7,2}, y_{3,1}, y_{4,1}) \leq 0 \\ C_{13}(y_{5,1}) \leq 0 \\ C_{14}(y_{5,2}) \leq 0 \\ C_{15}(y_{5,1}) \leq 0 \\ C_{16}(y_{5,2}) \leq 0 \end{array} \right.$$

The set of constraints has been defined considering a mixture of both cross-check value, introduced to check the validity of a specific value, and constrained the output value in either feasible or target range.

- **Geometrical S/C modelling for aerodynamic definition**

The geometrical configuration of the spacecraft is defined through a set of input variables and constraints introduced in the previous section. It shall comply with general requirements introduced to constrain the configuration itself during the MDO process to those defined in Figure 74. The configuration driven requirements are:

- The S/C shall fit the fairing of VEGA C.
- The S/C shall consider the interface with the launcher.
- The S/C shall accommodate the required solar panels.
- The S/C design shall accommodate all subsystems required by the spacecraft to operate.

- The frontal area of the S/C shall be minimized with respect to the envelope of the thruster intake.
- The frontal area of the main body shall accommodate the ramEP intake.

The design drivers identified point toward a GOCE-like configuration based on a central body with an octagonal cross-section. The baseline for solar array configuration is two fixed wings with body-mounted solar cells. However, the possibility to consider a “clean” body configuration with deployable solar arrays has been considered for increasing the total power available. The overall spacecraft shape shall fit inside the fairing of the VEGA-C launcher. The envelope constraints have been introduced as fixed parameters in the MDO process. Moreover, the mechanical interface with the launch adapter has also been considered introducing a constraint on the minimum diameter circumscribed in the S/C body section.

Figure 78, Figure 79 and Figure 80 show the generic spacecraft envelopes that have been depicted, highlighting the main quantities involved in the optimization process. In Figure 78, the geometrical parameters related to the fairing interface has also been reported considering the fairing adapter. The focus on the S/C optimization quantities has been given in Figure 79 over a generic spacecraft profile.

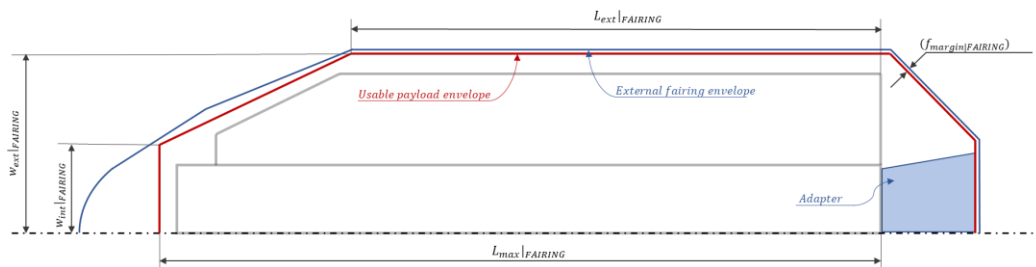


Figure 78: general definition of the launch vehicle fairing dimensions.

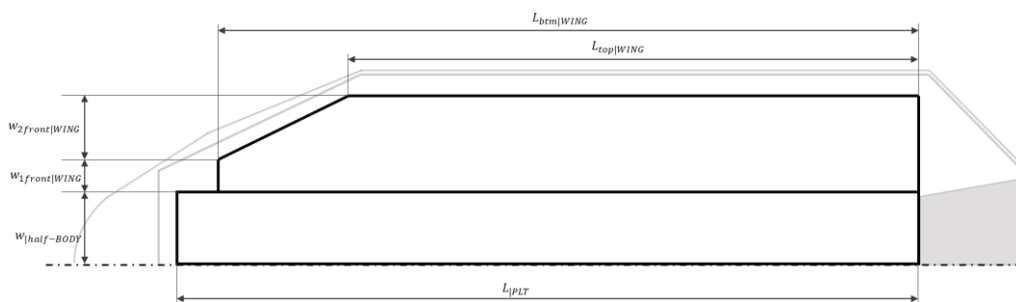


Figure 79: general definition of the spacecraft dimensions. Only half spacecraft is represented in the figure.

Figure 80 shows the main body cross-section introducing the circular intake shape as defined in Section 3.6.

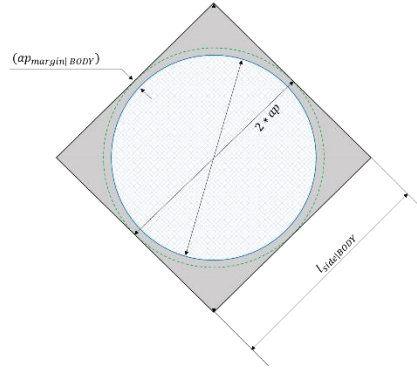


Figure 80: definition of the spacecraft body dimension. In the most generic case, the spacecraft body section is represented with a square section.

The geometrical relations linking the final design block output with the optimization variables have been derived by defining the variables and quantities hereabove presented. From equations (3.4) to (3.18), the main geometrical relations for areas and volume have been reported. For the notation exploited for the following equation, refers to Figure 78, Figure 79 and Figure 80.

- Overall S/C “wet” area

$$A_{lat|BODY} = l_{side|BODY} L_{PLT} n \quad (3.4)$$

where n is the number of the cross-section sides.

- S/C main body cross-sectional area

$$A_{front|SECT} = \frac{w_{BODY}^2}{4} \cos\left(\frac{\pi}{n}\right) \sin\left(\frac{\pi}{n}\right) \quad (3.5)$$

- Available intake area

$$A_{INT} = \pi \left(\frac{w_{BODY} \cos\left(\frac{\pi}{n}\right)}{2} \right)^2 (1 - ap_{margin|BODY})^2 \quad (3.6)$$

- Body frontal area (without intake area)

$$A_{front|BODY} = A_{front|SECT} - A_{INT} \quad (3.7)$$

- Fairing dimensions

$$\zeta = \frac{(W_{\text{ext|FAIRING}} - W_{\text{int|FAIRING}})}{(L_{\text{max|FAIRING}} - L_{\text{ext|FAIRING}})} \quad (3.8)$$

- S/C length

$$W_{\text{btm|MAX}} = \zeta(L_{\text{max|FAIRING}} - L_{\text{btm|WING}}) + W_{\text{int|FAIRING}} \quad (3.9)$$

$$(3.10)$$

$$W_{\text{top|MAX}} = \zeta(L_{\text{max|FAIRING}} - L_{\text{top|WING}}) + W_{\text{int|FAIRING}}$$

- S/C width

$$W_{\text{front|WING}} = W_{\text{btm|MAX}} - \frac{W_{\text{BODY}}}{2} \quad (3.11)$$

- Lateral wing area

$$A_1 = L_{\text{top|WING}} W_{\text{WING}} \quad (3.12)$$

$$(3.13)$$

$$A_2 = (W_{\text{front|WING}} - W_{\text{front|WING}})(L_{\text{btm|WING}} - L_{\text{top|WING}}) \quad (3.14)$$

$$A_3 = W_{\text{front|WING}}(L_{\text{btm|WING}} - L_{\text{top|WING}}) \quad (3.15)$$

$$A_{\text{lat|WING}} = A_1 + A_2 + A_3$$

- Frontal wing area

$$\begin{aligned} & A_{\text{front|WING}} \\ &= S_{\text{WING}} \sqrt{(L_{\text{btm|WING}} - L_{\text{top|WING}})^2 + (W_{\text{WING}} - W_{\text{front|WING}})^2} \quad (3.16) \\ &+ W_{\text{front|WING}} * S_{\text{WING}} \end{aligned}$$

- S/C Volume

$$V_{|BODY} = A_{|front|SECT} L_{|PLT} \quad (3.17)$$

$$V_{|WING} = A_{|lat|WING} S_{|WING} \quad (3.18)$$

As previously specified, the derivation of the platform configuration, depending on the optimization variables introduced as input of the MDO problem, impact other MDO (i.e., Drag evaluation module and electric power subsystem module) from which further outputs are calculated.

- **Thruster Performance Models (TPM)**

The thruster performance model represents one of the main design blocks introduced in the MDO problem through which the performance of the ramEP thruster is evaluated. SITAEL has developed this performance module in the framework of the AETHER project [135].

The model presents two main approaches that can be independently selected according to requirements and constraints evaluated at the platform level.

On the one hand, the called “*Constant Power Law*” provides the performance of the thruster in terms of generated thrust and discharge voltage. The variation of the number of particles collected by the intake and accelerated by the thruster caused a variation in the thruster discharge current along the trajectory. Consequently, the discharge voltage level (ϕ_{ramEP}) shall be varied to maintained constant the thruster input power (P_{ramEP}). The model input/output parameters are shown in Eq. (3.19):

$$[T_{ramEP}, \phi_{ramEP}] = \mathcal{F}(N_O, N_{N_2}, T_a, V_{rel}, A_{int}, N_{duct}, L_{ion}, L_C, P_{ramEP}) \quad (3.19)$$

where N_O , and N_{N_2} are the number densities of the oxygen and bi-atomic nitrogen and, T_a is the temperature of the incoming flow. These parameters are derived by exploiting the atmospheric model presented in the next section. A_{int} , N_{duct} , L_{ion} , and L_C are the set of input for the geometrical definition of the thruster, respectively: the intake area, the number of intake ducts, the length of the ionization stage and the length of the collector stage. V_{rel} is the orbital velocity calculated with respect to the altitude of the spacecraft while the P_{ramEP} is the thruster input power calculated considering the available onboard power provided by the solar arrays and the other busloads. An additional efficiency of 0.9 has been considered on the PPU.

The second performance model developed to provide the thrust level generated by the ramEP thruster and the power to guarantee that the thrust level gives in input the discharge voltage at which the thruster is operated.

The drawbacks in adopting this second thruster control law are mainly related to the variable power load required by the thruster along the trajectory that shall be guaranteed to sustain the thruster discharge. Consequently, the electric power subsystem of the spacecraft shall be designed to provide the higher power peaks and dissipate the power in excesses. To ensure this capability, the common operational approach is usually based on tilting the solar arrays designed for the maximum required power to increase the angle of incidence of the solar rays and consequently reduce the generated power. Considering the assumption made on the SSO, this solution is not considered practicable [6,7,181].

- **Atmospheric Modelling**

The introduction of an atmospheric model is essential for a full understanding of the ramEP spacecraft environment. According to the general mission requirements reported in Section 3.4.1, the nominal operation of the ramEP IoD mission is fully performed in a region of the upper atmosphere called the thermosphere. Ranging from about 90 km up to approximately 400 km depending on both solar and geomagnetic activity, a strong increment of the temperature characterizes this region due to the absorption of the EUV coming from the Sun. The evolution of the temperature profile and the numerical density of the atmospheric species is influenced by the amount of energy received from two main sources: the solar flux and the geomagnetic activity.

The major variation of both neutral density and temperature is caused by the solar flux, which follows the 11-years solar cycle period. This period is usually associated with the variable number of observed sunspots and related transient aperiodic phenomena (solar flares and Corona loops) that caused a variation in the solar radiation level and the quantity of jettisoned material.

An example of the solar activity is shown in Figure 81, in which the number of solar sunspots is reported for the two last complete cycles (23^o and 24^o cycle).

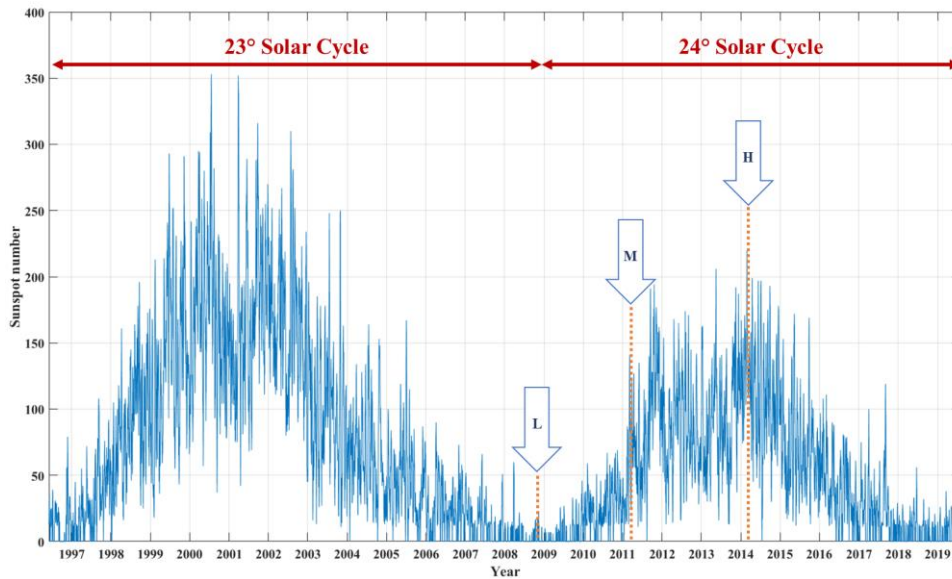


Figure 81: solar activity between 1997 and 2019 (23° and 24° Solar Cycle).

Over the past decades, many atmospheric models have been developed to properly estimate the dynamic composition and temperature of all the atmospheric layers, including the thermosphere. During this time, either improvement to older models or new models has been introduced exploiting newly available data. The model adopted for this study was developed through the Mass-Spectrometer-Incoherent-Scatter (MSIS) by Naval Research Laboratory (NRL) as an extension of the previous MSISE-90 [182] from ground to the exosphere. Moreover, this model improves the usually adopted Jaccia-70, in particular, to estimate the densities at low altitude. As a consequence, the NRLMSISE-00 (E stands for “extend”) was recognised as one of the reference atmospheric models by the European Cooperation for Space Standardization (ECSS). [183].

This model provides the atmospheric composition in terms of the number density of He, O, N₂, O₂, Ar, H and N, the total mass density, the total number density, and the temperature. Having in input the UTC, the altitude, and the geographical latitude and longitude, the model correlates these inputs to two types of indices: the solar indices F10.7 and the magnetic indices A_p.

The first indices, the F10.7, are the abbreviation of the solar flux at 10.7 cm, corresponding to a radio emission at 2800 MHz. The recorded data of sunspot number, ultraviolet (UV) and visible emission are interrelated for the definition of this term. Dependent on the solar cycle, the F10.7 can vary from 50 s.f.u. (solar flux unit) up to 300 s.f.u.

The geomagnetic activity is taken into account with the A_p-index, which represents the daily averaged variation of the geomagnetic field due to the cross-interaction among the solar wind, the Earth’s magnetosphere and the ionosphere.

With daily repetition, three hours of observation from 13 ground station collect the data of the geomagnetic activity from which value of K_p and a_p are derived. The

term A_p is then derived considering an averaging of eight a_p values selected near the net mean value.

In addition to these two main indices, other two parameters have been added to take into account the long period variations:

- $F10.7_{ctr81}$: the 81-day average value of F10.7 centred on the input time.
- $A_{p_{avg7}}$: the 7-day average value of A_p centred on the input time.

A specific subroutine has been developed and integrated into VLEO-MAGNETO. The database included in the model has been based on the NASA NOAA indices database [184]. NOAA has collected data from 1957 to today with a forecasting set of data up until 2044.

$$[n_{He}, n_O, n_{N_2}, n_{O_2}, n_{Ar}, n_H, n_N, T_\infty, \rho_\infty] = NRLMSISE00(UTC, h, lat, long) \quad (3.20)$$

As defined before, the NRLMSISE00 model has in input the time (UTC), the altitude and the geographical position in terms of latitude and longitude value as reported in Eq. (3.20). For the propagation phase in VLEO-MAGNETO, the inline values of these quantities are used. On the contrary, a reduced model is exploited for evaluating the different optimized configurations due to the less computational demand. Consequently, the analyses were performed considering the first semi cycle of the 24° solar cycle and comparing the obtained atmospheric variation result with the GOCE flight data. This last completed solar cycle began in December 2008 and ended in May 2020. To reduce the order of the model, three surrogate data-based models were developed averaging the data of three one-month periods, each one centred in high, medium, and low solar activity. The following dates have been considered (see Figure 81):

Table 43: selected solar period.

Solar cycle Period	Date
Low Solar Period	December 2008
Medium Solar Period	February 2011
High Solar Period	April 2014

For each of these periods, the atmospheric model was run providing in input (i) the periods summarized in Table 43, (ii) an altitude range between 160 km and 250 km with a span of 1 km and (iii) a grid over latitude and longitude direction with a resolution of 1° . The collected outputs were then averaged with respect to the period considering. An example of the obtained result is shown in Figure 82.

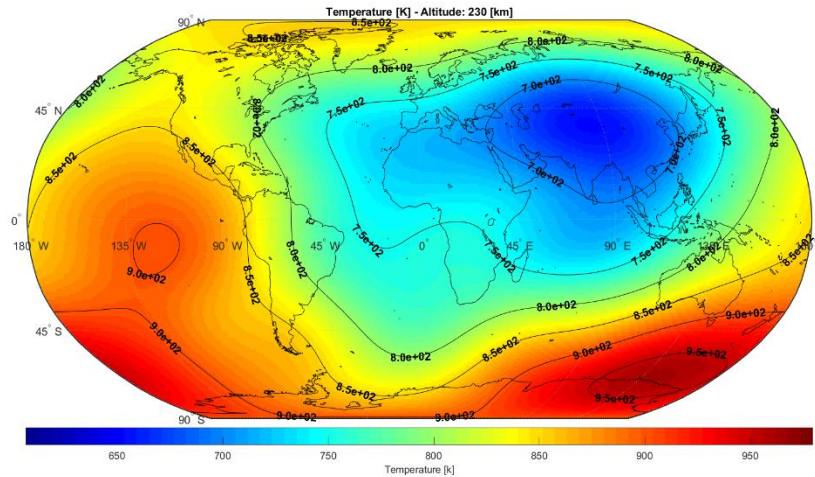


Figure 82: example of the result obtained from the adopted NRLMSISE-00 highlighting the strong variation of the temperature at 230km.

A second step for reaching the single altitude depended on the value, the matrix in which the time average data were stored for each lat/long combination was further averaged. This procedure was repeated for each altitude and each output quantity of the atmospheric model. Once obtained the single value dependent only on the altitude, the least square method was exploited for deriving an easy-handled polynomial function. Figure 82, Figure 83 and Figure 84 show the variation of temperature and numeric density concerning the considered altitude range.

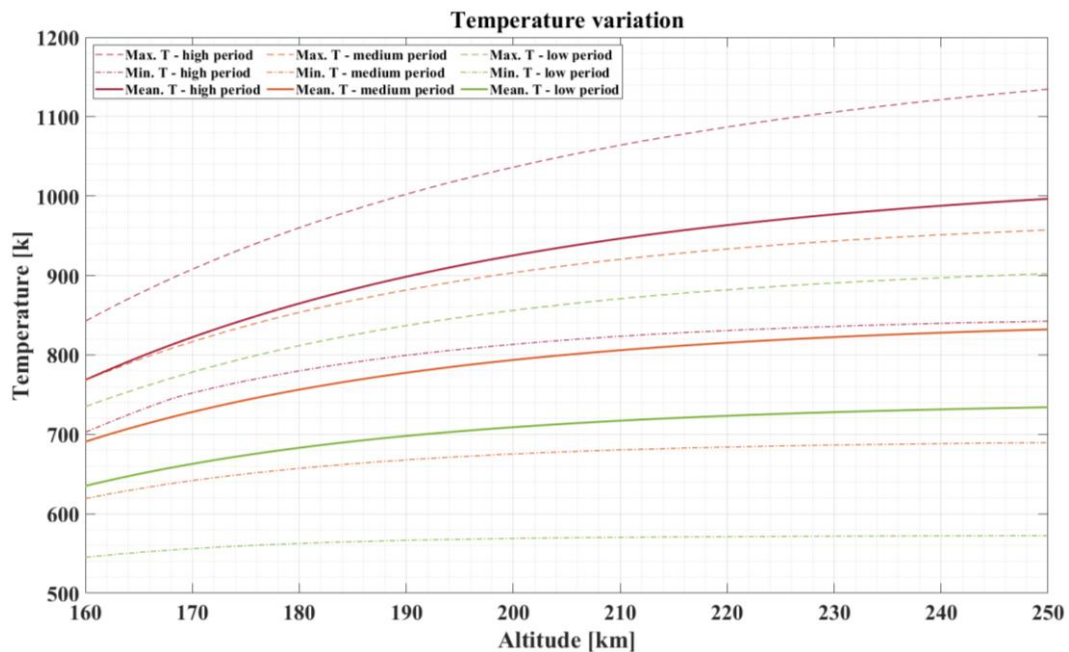


Figure 83: averaged temperature variation in the considered altitude range for the different solar activity periods.

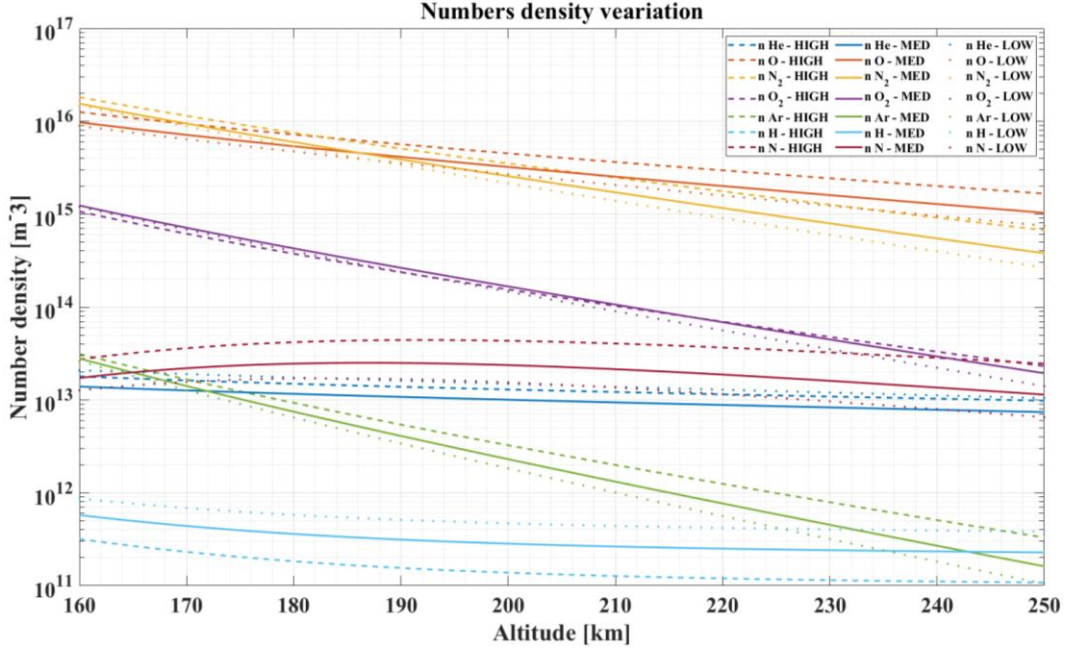


Figure 84: averaged atmospheric composition variations in the considered altitude range considering the different solar activity periods.

- **Drag Model**

As reported above, a VLEO mission is design to operate in a range of orbits significantly lower with respect to more common space missions. Over this range, the capability to predict with a higher level of accuracy the drag force generated by the spacecraft is fundamental to assess the influence that this perturbation force has on the spacecraft orbital dynamics. Opposite to the relative direction of motion of the spacecraft, this force is caused by the transfer of momentum of the impacting atmospheric particle on the spacecraft surfaces. The low fidelity approach usually adopted for the drag estimation consists of the assumption of the drag coefficient C_D commonly set at 2.2. Consequently, the well-known drag equation for the drag calculation is exploited:

$$a_D = \frac{1}{2} \rho V_{rel}^2 C_D \frac{S_{S/C}}{m_{S/C}} \quad (3.21)$$

where ρ is the atmospheric density, V_{rel} is the relative velocity of the spacecraft, $S_{S/C}$ is the equivalent (or reference) spacecraft surface and $m_{S/C}$ is the spacecraft total mass. Even though this approach allows a simple implementation process for preliminary estimation phases; it does not fully characterize the physical phenomena involved in the generation of this force and, in particular, in the derivation of the C_D .

Different concurrent factors drive the definition of this parameter.

The diffusive and specular dynamic of the particles impacting the spacecraft surfaces are ruled by their physical properties for which specific model should be exploited. However, it is possible to introduce novel analytical methods that

provide the estimation of the drag coefficient during the preliminary spacecraft design phases.

The different theories developed in the past years can be distinguished for the flow regime to which they are referring. These cases are the (i) continuous and the (ii) free molecular flow, separated by a transition region.

The criterion exploits for the distinguish of whether the spacecraft is in one of the two regimes is given by the analysis of the Knudsen number evolution. This dimensionless number links the mean free path length of the particles (λ) with the physical length (L) of the objects (in our case, the spacecraft) with the following relation:

$$Kn = \frac{\lambda}{L} \quad (3.22)$$

The mean particle free path is given by:

$$\lambda = \frac{1}{\sqrt{2}\pi d^2 n} \quad (3.23)$$

where d is the average particle diameter, and n is the numerical density. Both quantities are derived from the atmospheric model and can vary as a function of altitude, location, and observation date. Nevertheless, the average particle diameter is usually assumed equal to $d = 3.78 \cdot 10^{-10}m$, as stated in [185]. While in the first region, the continuity equation can be used, with the increment of the altitude, the rarefaction of the atmosphere increases the Knudsen number due to the higher value of λ which became either comparable or higher than the length of the spacecraft. The free molecular flow condition is indeed identified with a lower limit set at $Kn=10$.

From this lower boundary, the higher distances among the particles make the collisions among them difficult. As a consequence, the impact phenomena between the incoming particles and the spacecraft surfaces cannot be anymore described by the continuous equations. Moreover, in the range of altitude considered for the ramEP mission, all the spacecraft surfaces suffer from a quick coating caused by the atomic oxygen and its reaction products. This changes the re-emission properties of the surfaces themselves, which impact the C_D value [186].

For the estimation of the drag forces acting on the ramEP spacecraft, a dedicated subroutine has been introduced in VLEO-MAGNETO. While the other parameters of Eq. (3.21) are evaluated according to either the integration step (velocity of the spacecraft and atmospheric density) or on the spacecraft design (reference surface and mass). The drag coefficient is calculated through the analytical model developed by Schaff & Chambré in a published in 1961 [187,188].

Based on the free molecular condition assumption, the drag coefficient is derived for a flat surface as follow:

$$C_d = \sin\theta [1 + \operatorname{erf}(S\theta)] \left[(2 - \sigma_n) \left(\sin^2\theta + \frac{1}{2S^2} \right) + \sigma_t \cos^2\theta + \frac{\sigma_n \sin\theta}{2S} \sqrt{\frac{\pi T_w}{T_a}} \right] \\ + e^{-(S\theta)^2} \left[\frac{2 - \sigma_n}{\sqrt{\pi}S} \sin^2\theta + \frac{\sigma_t \cos^2\theta}{\sqrt{\pi}S} + \frac{\sigma_n \sin\theta}{2S^2} \sqrt{\frac{T_w}{T_a}} \right] \quad (3.24)$$

where:

- θ is the angle of attack defined as the complementary of the between the normal surface vector and the outward velocity vector at a given point on the surface;
- S is the mean molecular velocity, dependent on the incoming flow velocity and its temperature.

$$S = \sqrt{\frac{MV_{rel}^2}{2k_b T_a}} \quad (3.25)$$

where M is the mean molecular mass and k_b is the Boltzmann's constant.

- σ_n and σ_t : are the normal and the tangential accommodation coefficients. Both parameters are typically assumed equal to 0.9, according to [189]
- T_a and T_w : are respectively the temperature of the incoming flow and the temperature of the surface. While the first parameter is derived for the introduced NRLMSISE-00, the spacecraft surface temperature shall be calculated with further assumptions.

The temperature of the spacecraft surfaces varies along the orbit depending on the incoming heating contributions derived considering the spacecraft's attitude. However, as commonly performed in the preliminary design phases of the TCS, the worst condition is taken for the sizing to ensure the system's operability in all the other cases. Even in this case, the surface temperature has been calculated considering the worst-case condition for which the spacecraft is considered a black body. The equilibrium is then estimated over a flat plate with a nadir pointing. These assumptions allow us to define the total flux as the sum of the different heat flux contributions:

$$Q_T = Q_S + Q_A + Q_{IR} + Q_P + Q_{LOAD} = \sum_i Q_i F_i \quad (3.26)$$

where the different terms are: (i) Q_S is the Sun radiation, (ii) Q_A is the Albedo contribution due to the Sun radiation reflection on the Earth surface, (iii) Q_{IR} is the infrared radiation of the Earth, (iv) Q_p is the free molecular heating caused by the particle collisions, and (v) is the heat of the internal spacecraft components, derived considering a 96% of PPU efficiency and an overall spacecraft efficiency on the power feeding of 90%.

The parameters are reported in Table 44 with the related reference values [5,177]:

Table 44: summary of the heat fluxes formulation.

Contribution	Equation	Note	Ref
Sun	$Q_S = Q_{\odot} f_{\odot}$	$Q_{\odot} = 1367 \text{ W/m}^2$ $f_{\odot} = 0.5$	[6,7,64]
Albedo	$Q_S = a Q_{\odot} f_A$	Albedo reflection Coef. $a = 0.35$ $f_A = 0.3511$	
IR Earth	$Q_S = Q_{IR} f_{IR}$	$Q_{IR} = 275 \text{ W/m}^2$ $f_{IR} = 0.3471$	
Particle flux	$Q_P = \frac{1}{4} M n V_{rel}^2$	//	
Internal flux	Q_{LOAD}	//	

Then, the surface temperature is calculated with the following Stefan Boltzmann's equation:

$$T_w = \left(\frac{Q_{tot}}{\sigma} \right)^{1/4} \quad (3.27)$$

where σ is the Stefan Boltzmann constant. Even though this approach can be exploited for the design phases integrated into the MDO process, the variability of the orbital conditions encountered during the trajectory propagation can strongly affect the relative temperature of the spacecraft temperature generating strong heat fluxes that shall be minimized. In order to deal with these uncertainties, the propagation module considered the procedure reported above for the surface temperature computation for each surface of the spacecraft according to their specific orientation. The main impacting factor is the field of view value for each contribution which is calculated according to the procedure reported in [64]. If the surface presents a temperature gradient owing to its particular shape, the temperature is averaged, and the mean value is taken as a reference.

With the definition of all the parameters involved in the calculation of the C_D , and considering a generic surface (not necessarily flat), the drag coefficient is computed for the i^{th} surface as:

$$(3.28)$$

$$C_{D|i} = \frac{1}{A_{f|i}} \int_{A_i} C_{D|i}(\theta) dA_i$$

The followed method deals with the drag coefficients calculated independently for the different species which constitute the atmospheric flux. The final value is computed by adding each single contributions concerning the different surfaces.

3.6.1.3 SCENARIO PROPAGATION – Manoeuvres and altitude control logic

After the definition of the spacecraft design through the evaluation of the optimal configuration and the selection of the desired solutions, the analysis proceeds with the propagation of the trajectory. As previously mentioned, the definition of both initial (only for the propagation initiation) and final orbital parameters is included in the input module consisting of (i) altitude, (ii) eccentricity, (iii) inclination, (iv) RAAN, (v) argument of perigee and (vi) true anomaly.

Within the initialization of the orbital state vector, a special treatment has been considered for what concerns the orbital inclination. Considering the requirement reported in Section 3.4.1, the SSO shall have a precise inclination value in the function of the spacecraft's altitude to have a nodal procession able to maintain the angular momentum vector always aligned toward the Sun. With this specific aim, a separate module has been developed and integrated into the propagator. At each propagation step, the inclination at the current propagation altitude is derived and set as the final integration target value. Following the weighted procedure presented in 2.5.4, the “out-of-plane” thrust angle is derived and compared with the boundary value imposed by the maximum yaw and pitch angle allowable in the operability region of the intake. Therefore, even if the orbital inclination can be defined as an input to the software, it can vary with respect to the altitude. This constraint is set considering the maximum incidence angle for which the intake can operate with high air collection efficiency, and it is equal to 2°.

In the input spreadsheet related to the spacecraft operation, the user shall define the typology of manoeuvre foreseen for each phase. Consequently, the software can read the selection and set the appropriate propagator break conditions. Three manoeuvres have been introduced: (i) Orbital Maintenance (OM), (ii) Orbital Variation (OV) and (iii) Orbital Raising (OR).

The orbital maintenance module includes the full thruster control logic (presented later in this paragraph) to follow a predetermined altitude entry value. The period of propagation used as the stopping condition of the trajectory is introduced in the operation spreadsheet of the input file as an additional parameter setting by the user. Other propagation modules are instead introduced to enable altitude variations. The orbit raising disengages the constraints on altitude rate limitation as soon as the spacecraft approaches the target altitude zone (see Figure 89). The same approach is followed by the OV module, where the thruster is not operated until the approach to the upper limit of the target altitude zone when the limitations on the altitude variation rate are restored.

Including the differences among the three manoeuvres modules, a multilevel control law has been developed. Its structure includes three evaluation areas: (i) orbit environment, (ii) Thruster operative requirements and (iii) Trajectory state evaluation. The following decision levels are:

- Eclipse condition
- Trajectory calibration time (characteristic time derived with a PSD analysis of the initial altitude history)
- Delta altitude with respect to the target altitude
- Sign average altitude variation rate.
- Average altitude variation rate wrt variation limit
- Thruster Cool-down period
- Thruster system limitation

In Figure 85, the decision flow of the introduced thruster control logic is shown.

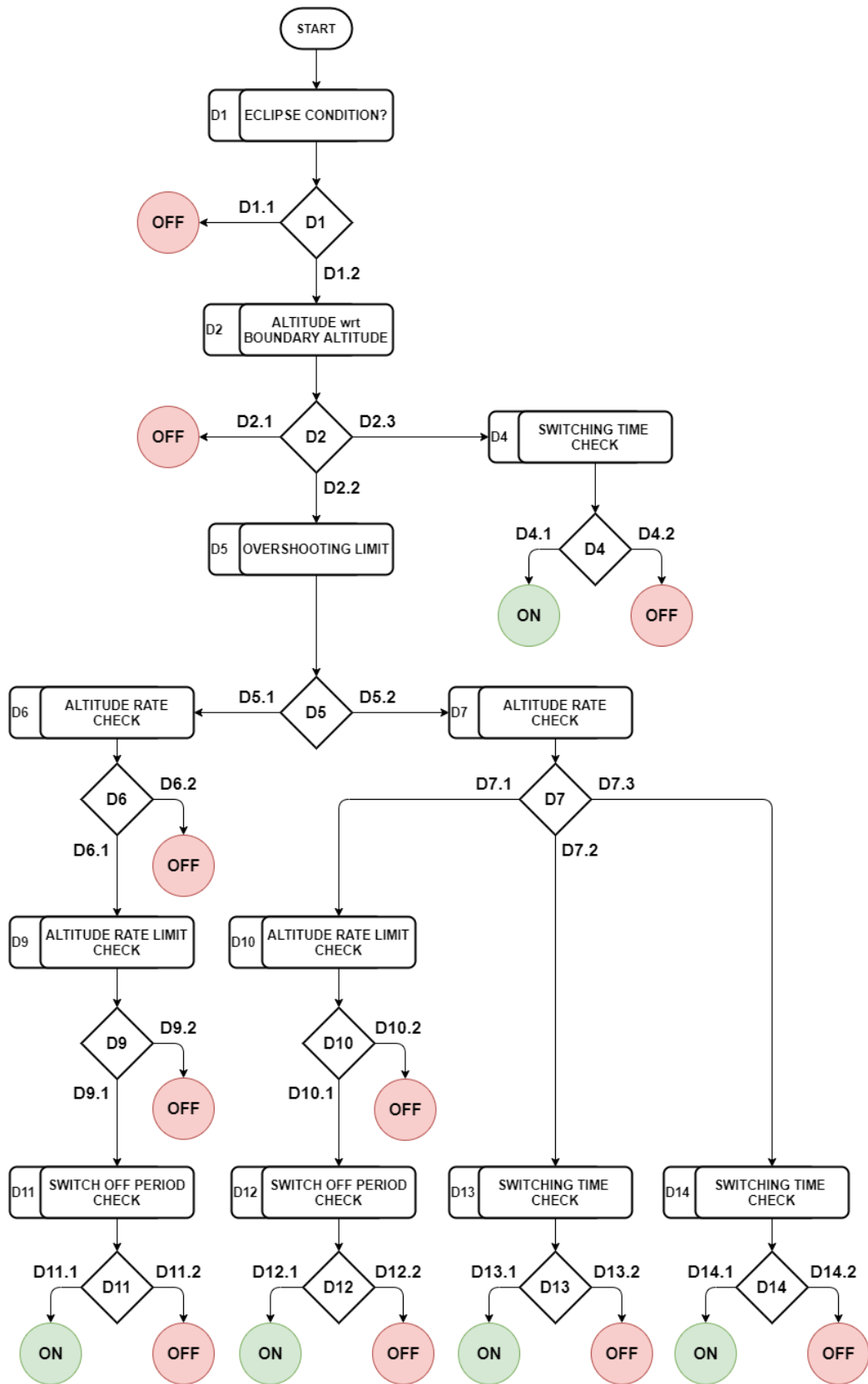


Figure 85: ramEP control logic for altitude maintenance.

➤ **ENVIRONMENT EVALUATION: Eclipse condition [Decision level D1]**

As defined in Section 3.4, the reference mission orbit for the ramEP IoD mission is the SSO at 6 a.m. Considering the range of operative altitude and the related inclination driven by Eq. (3.2), this orbit is affected by the period of no eclipse alternated to the period of relatively long eclipse up to 37.5 minutes.

Therefore, for the correct evaluation of the capability of the ramEP thruster in sustaining a constant altitude trajectory, it is essential to perform a detailed investigation on the light or eclipse condition with respect to the spacecraft orbital positions.

The eclipse model introduced in VLEO-MAGNETO follows the approach presented in [190]. In this work, the eclipse prediction method relies on a conical shadow model where penumbra and umbra conditions are dependent on the relative distance between the involved celestial bodies (Earth and Sun).

Considering two vectors \mathbf{r} and \mathbf{r}_s as the relative vector of the satellite and the Sun to the main reference (ECI) frame, the instantaneous plane S_0 could be geometrically constructed. In Figure 86 are shown the setpoints at a given epoch identified over the satellite orbit through this plane: (i) PU_1 and PU_2 represent the entry/exit penumbra points, (ii) U_1 and U_2 represents the entry/exit umbra points. The angles δ_U and δ_{PU} denotes the angle of $\overline{OU_1}$ and $\overline{OPU_1}$ respectively. A consequence the following geometrical expression can be derived under the assumption of the conical umbra geometry.

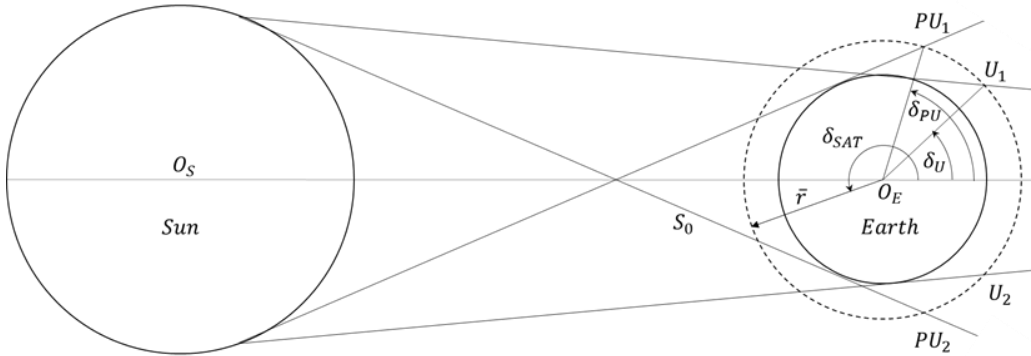


Figure 86: eclipse model, geometrical construction.

For the two possible conditions:

Umbra condition	Penumbra condition
$\begin{cases} \delta_U = \pi - \cos^{-1}\left(\frac{R_e}{x_U}\right) - \cos^{-1}\left(\frac{R_e}{ \bar{r} }\right) \\ x_U = \frac{R_e \overline{O_S O_E} }{R_s + R_e} \end{cases}$	$\begin{cases} \delta_{PU} = \pi - \cos^{-1}\left(\frac{R_e}{x_{PU}}\right) - \cos^{-1}\left(\frac{R_e}{ \bar{r} }\right) \\ x_{PU} = \frac{R_e \overline{O_S O_E} }{R_s - R_e} \end{cases}$

where R_e is the Earth radius, and R_s is the Sun radius (approximately 969000km) and $|\overline{O_S O_E}|$ is the distance between Sun and Earth.

Moreover, the position of the spacecraft identified to the vector \bar{r} is:

$$\delta_{SAT} = \pi - \cos^{-1} \left(\frac{\bar{r}_s \cdot \bar{r}}{|\bar{r}_s| |\bar{r}|} \right) \quad (3.29)$$

with the \bar{r}_s the Sun position vector in ECI frame and \bar{r} the spacecraft position vector. The penumbra condition is defined as $\delta_U < \delta_{SAT} < \delta_{PU}$ and the umbra condition is $\delta_U > \delta_{SAT}$. For the evaluation of these conditions, the determination of the angle δ_{SAT} is derived with respect to the orbital state vector:

For an inertial ECI system:

$$\bar{r} = \begin{pmatrix} \cos u \cos \Omega - \sin u \cos i \sin \Omega \\ \cos u \sin \Omega - \sin u \cos i \cos \Omega \\ \sin u \sin i \end{pmatrix} \quad (3.30)$$

where u is the argument of latitude, i is the inclination, Ω is the RAAN. Reporting the \bar{r}_s in the ECI frame, we can obtain:

$$\bar{r}_s = \begin{pmatrix} \cos \Phi \\ \sin \Phi \cos \varepsilon \\ \sin \Phi \sin \varepsilon \end{pmatrix} \quad (3.31)$$

With Φ as solar latitude and ε between the ecliptic and the equatorial plane. Combining the previous equations, we obtained the definition of δ_{SAT} :

$$\cos \delta_{SAT} = -A \sin u - B \cos u \quad (3.32)$$

with:

$$\begin{cases} A = A_1 \sin \Omega + A_2 \cos \Omega + A_3 \\ B = B_1 \sin \Omega + B_2 \cos \Omega \end{cases} \quad (3.33)$$

where:

$$(3.34)$$

$$\begin{cases} A_1 = -\cos i \cos \Phi \\ A_2 = \cos i \sin \Phi \cos \varepsilon \\ A_3 = \sin i \sin \Phi \sin \varepsilon \\ B_1 = \sin \Phi \cos \varepsilon \\ B_2 = \cos \Phi \end{cases}$$

With the same formulation angles δ_U and δ_{PU} can be obtained and evaluated. Following the previous steps, the eclipse condition is evaluated at each integration point. In the eclipse condition, the thruster is not operated due to the excessive loads required from the batteries for its operation. In the case of operation of the thruster during eclipse conditions, the power source relies on the power stored in the batteries. They shall be recharge during the sunlight orbital segment. This causes an increment of the solar arrays necessary to provide the additional recharge power and, consequently, an increment of the drag that shall be counteracted.

Table 45: D1 level, decision options.

Eclipse condition check		
Decision label	Description	Thruster status/Control decision
D1.1	The spacecraft is in eclipse.	The thruster is either maintained OFF or switched OFF.
D1.2	The spacecraft is in sunlight.	The control level D2 is triggered

➤ **ORBIT EVALUATION:** spacecraft altitudes

The core of the thruster control law is the evaluation of the attitude of the spacecraft during the trajectory propagation with respect to its predefined target value. In addition to the other decision levels, it has one of the main influences on both the feasibility demonstration of the ramEP concept and the definition of the thruster operability range.

Even though the scenario under consideration is an IoD mission, the mission constraint on keeping an average altitude value is included in the requirement to fulfil. It is considered a fundamental figure to demonstrate the feasibility of the mission itself.

In the classical definition of the Keplerian orbital elements, the semi-major axis represents one of the elements necessary for the definition of the orbit size; hence, it is usually adopted for a clear understanding of the orbit.

In a VLEO scenario, the more practical approach for specifying the ramEP spacecraft orbit is to report its altitude related to the Earth surface. This process is intrinsically caused by common human sense to compare the VLEO scenario to an atmospheric one where the aircraft altitude is usually adopted rather than its Earth-centred radius.

However, the altitude value is not univocally defined, but it depends on the adopted reference system. These concepts are included in a vast discipline called

“Geodesy”. It is considered the science branch exploited for the measurement and full understanding of the Earth's gravity field, shape, and orientation in space. The geodesy principles are exploited in the modern era to correct the positioning on the Earth surface provided by the Global positioning System (GPS), which represents the usually adopted reference frame for the global terrestrial reference.

In geodesy, the definition of the reference ellipsoid and the geoid is the first step for the derivation of an appropriate reference system.

The ellipsoid is a second-order approximation of the equipotential Earth rotating sphere. It is considered a “normal” gravity representation of the Earth gravity field, without complex mathematical formulations that shall be exploited to include both the geoid and the gravity anomalies caused by the internal Earth dynamics. It provides a relatively simple reference system that can be exploited for a vast set of geodesy and geophysics applications. The adoption of this reference system can benefit from the easy gravity field representation, which is easy to handle and does not have a critical deviation from the real gravity field.

Since its first definition by Pizzetti (1894), many updates were introduced up to the Geodetic Reference System 1980 (GRS80) and World Geodetic System 1984 (WGS84) that have been currently updated through the introduction of GPS data. All these systems allow the definition of several geometric and geophysical parameters through four independent parameters.

Although the ellipsoid provides a valuable approach for horizontal coordinates (i.e., the definition of latitude and longitude), the vertical datum is not fully representative. Therefore, a more complex approach can be exploited by introducing a surface over the gravitational field that best fit the mean sea level over the ocean [191], the geoid.

This surface represents the constant equipotential energy surface overlying the mean sea level. Its definition is not straightforward. In fact, the geoid depends on the oceanic dynamic processes, which introduced uncertainties ranges. Moreover, the overlaying of the masses does not allow the distinction of the single dynamical contributions.

The differences between the ellipsoid and the geoid pass through the definition of three different surfaces: (i) topographic surface, a highly irregular surface following terrain orography and sea bathymetry, (ii) the reference ellipsoid, consisting of a mathematical representation of the Earth shape and (iii) the geoid, which is the equipotential surface that follows the mean sea level.

Thanks to these surfaces, the gravitational interactions can be easily associated with respect to a certain elevation.

Considering a certain position over the Earth surface (located to GPS positioning), the following relation is given (see Figure 88):

$$h = H + N \tag{3.35}$$

where h is the height of the ellipsoid related to the ellipsoid, H is the elevation of the geoid relative to the geoid and N is called geoid undulation relative to the ellipsoid.

The geoid undulations are usually expressed through harmonic expansion of the gravitational potential. With several ground and satellite contributions, the Earth Gravitational Model 1984 (EGM84) was introduced by National Imagery and Mapping Agency (NIMA) and followed by the EGM96 in 1998 [192] developed in collaboration with NASA Goddard Space Flight Centre and Ohio State University. An international effort focused on expanding the understanding of the Earth gravity and its characteristics pushed toward a new space-based data source. One of the first examples of the update coming from data derived from GRACE was the release of the EGM08, in which a new level of gravity resolution was reached [193].

More recently, GOCE provided additional data used in a mixed approach with the terrestrial measurement [194]. The latter effort contributed to the definition of the Global Gravity Model [195].

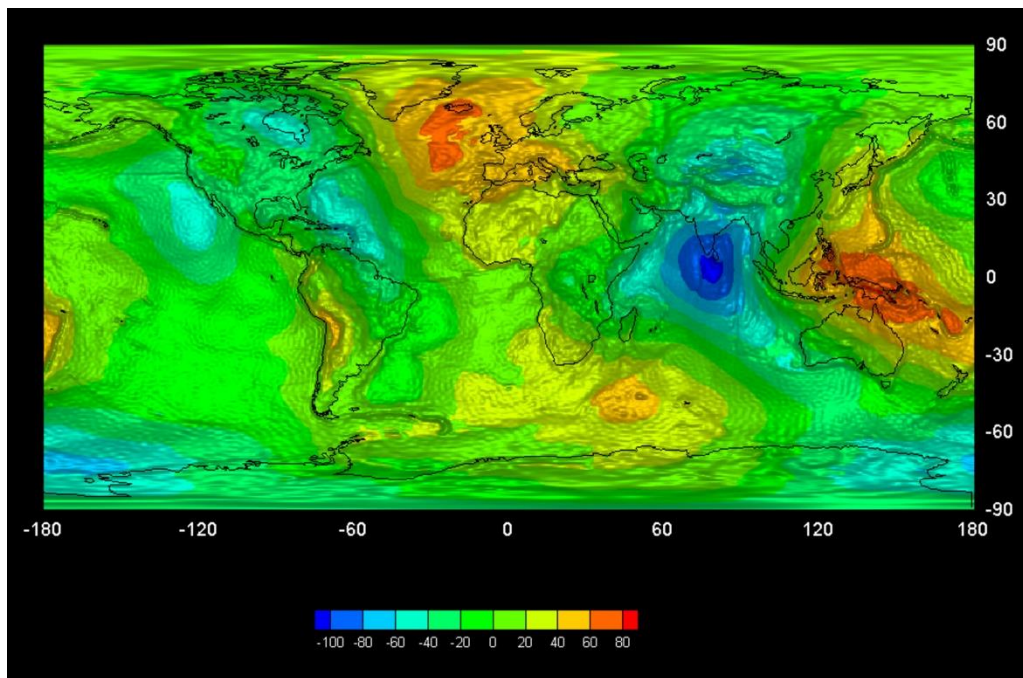


Figure 87: ESA – GOCE first global gravitational model [196].

In the thruster control law implemented in VLEO-MAGNETO, all these terms shall be defined to link the trajectory propagation to the used atmospheric model. In fact, while the gravity effects are included in the trajectory equations written in the ECI reference frame, which provides the altitude-related to the ellipsoid, the NRLMSISE-00.

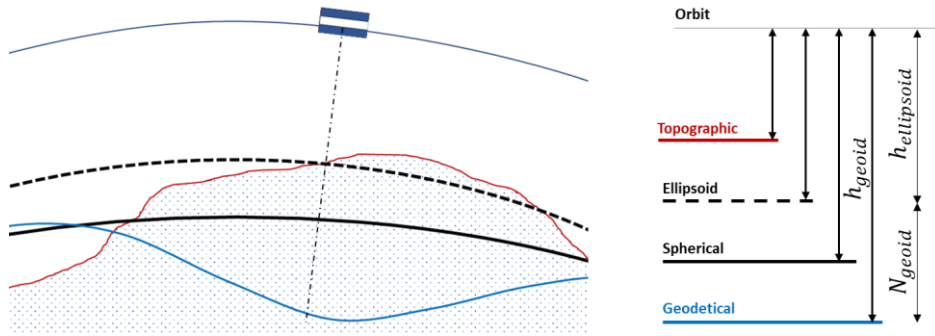


Figure 88: altitude definition for the different Earth models.

As previously reported, the propagation module introduced in VLEO-MAGNETO is based on a trajectory equation referred to ECI reference frame. Therefore, the control logic shall first import the ECI altitude, manage it to provide the control reference value to be considered in the control logic, and then provide an output flag that defines the thruster's operation.

The output at each integration step is an altitude value then saved in a dedicated vector. In the most general case, it has an undular non-regular behaviour. In order to derive a single altitude value to be exploited in the control logic, the altitude value collected in this vector shall be adequately averaged. Due to the impossibility of fully describing the spacecraft's behaviour a priori, other procedures shall be implemented. This particular procedure has been based on the Power Spectral Density (PSD) of the altitude vector, treated as a generic signal in the control module. The theoretical definition of this process is to find how the total power is distributed over frequencies. The objective is to exploit the PSD for analysing the altitude vector to derive the dominant frequencies of the altitude variation and exploit them for averaging the vector, obtaining a single output altitude value over a certain set of vector value. By definition, the dominant this kind of frequency carries the maximum energy among all the others. Therefore, through the PSD, the dominant frequencies are identified, selecting the highest peak over the spectrogram. The period has consequently derived inverting the frequency and called " σ ". The $(n-1)$ points taken over the calculated period are then simply averaged.

In the foreseen scenario, the spacecraft will spend the first phase performing all the required commissioning operation of the platform and its subsystems, as specified in Section 3.4. During this period, the thruster is not operated, causing a falling of the spacecraft that should be considered in the definition of the launch release altitude. Consequently, the averaging procedure can be performed to derive the initial control value of the altitude. Once this value approaches the target altitude, the thruster control logic will be engaged with subsequent on/off cycles that directly impact the altitude value itself. Consequently, the entire calibration procedure exploiting the dominant frequency period shall be repeated to ensure the inclusion of the thrust acceleration in the spacecraft orbital dynamics while reducing the intrinsic initial calibration error. The calibration repetition period is set with respect ten times the orbital period of the current average orbit, allowing a vast dataset of

altitude value provided to the PSD-based process. The width of the recalibration dataset has been decided according to the capability of embrace from very short up to secular orbital perturbations.

The thruster control module also allows us to consider a set of averaging possibilities introduced through multiple values of σ . In particular, the following periods are defined by default in the control loop and used differently averaging the altitude value set through the control steps: (i) 3σ used for “altitude boundary” control step, with the average altitude value called " h_{long} " (D2), (ii) 2σ used for “altitude overshoot limit”, for which the averaged altitude value derived is called " h_{med} " (D5) and finally (iii) σ used for the definition of the altitude change rate over the averaged altitude valued called " h_{short} " (D6/D7/D9/D10).

In Figure 89, a general approach to the boundaries definition over the target altitude is shown. The belt with a range ± 1 km with respect to the target altitude is called the “target altitude range”. Inside this bound, the altitude change rate control is engaged. Closer to the target altitude, an upper overshooting altitude is introduced. The latter boundary allows following the target orbit when the conditions of T/D are at the turn of 1. In fact, in that specific case, the variation of the atmosphere could push the spacecraft toward an altitude where recovery operation toward $T/D > 1$ range is impossible. Therefore, the safest approach to guarantee the operability of the system is to force the spacecraft to fly in a range of altitude where the T/D value is for most of the point greater than one.

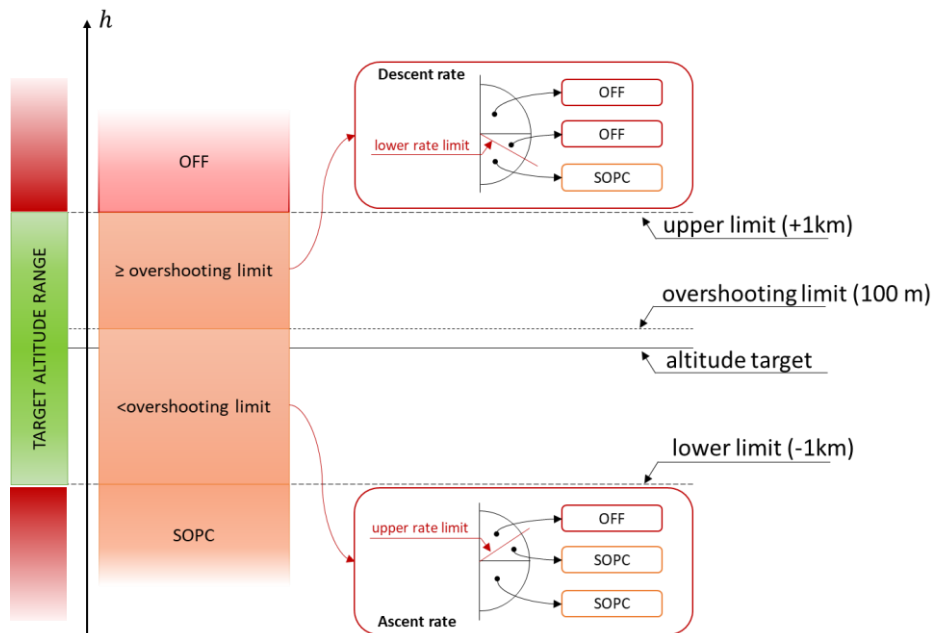


Figure 89: definition of the target altitude range with the main altitude limits considered in the thruster control logic.

- *S/C mean altitude wrt Altitude boundary limits [Decision level D2]*

This decision level of the thruster control module considers the target altitude range limited in between the upper and lower boundary. These are set at $h_{limit} = .1\text{km}$ from the target altitude that the spacecraft has to reach. For altitudes above the upper limit, the thruster is maintained in off condition except for both the commission phase, where it can be operated according to pre-planned verification operations and orbit adjustment manoeuvres if necessary. In Table 46, the output decision cases have been summarized with the consequent thruster operation status.

Table 46: D2 level, decision options.

Altitude wrt boundary limit		
Decision label	Description	Thruster status/Control logic decision
D2.1	The h_{long} value is higher than $h_{long} + h_{limit up}$. The thruster is maintained non-operative.	The thruster is either maintained OFF or switched OFF.
D2.2	The h_{long} value is included in the target altitude range. The following control steps are triggered	The control level D5 is triggered
D2.3	The h_{long} value is lower than $h_{long} - h_{limit up}$. The thruster is operated as much as possible considering the switching off period check decision step.	The control level D4 is triggered

- **Altitude overshooting limits [Decision level D5]**

The altitude overshoot limit has been introduced to avoid two main issues during the altitude tracking operation. First, once the spacecraft approaches the target altitude, the altitude rate slows down, triggering the inner decision steps. Second, the overshooting limit represents a safe margin when the target altitude is close to T/D=1, avoiding the decay of the spacecraft below an altitude where recovery could be not feasible.

The overshooting altitude is set to $h_{overshoot} = 100\text{m}$. In Table 47, the output decision cases have been summarized with the consequent thruster operation status.

Table 47: D5 level, decision options.

Altitude overshooting		
Decision label	Description	Thruster status/Control logic decision
D5.1	The h_{med} is higher than $h_{overshooting}$. The following control step is triggered.	The control level D6 is triggered
D5.2	The h_{med} is lower than $h_{overshooting}$. The following control step is triggered.	The control level D7 is triggered

○ **Altitude rate check [Decision level D6/D7]**

The derivation of the spacecraft altitude rate is introduced for completing the understanding of the spacecraft orbital dynamics.

The altitude rate is calculated at each integration loop with respect to the integration step and the altitude value h_{short} . This decision level evaluates either the ascend or descend behaviour of the spacecraft. In Table 48, the output decision cases have been summarized with the consequent thruster operation status.

Table 48: D6 and D7 levels, decision options.

Altitude rate check		
Decision label	Description	Thruster status/Control logic decision
D6.1	The altitude rate is negative. The control level is triggered.	The control level D9 is triggered
D6.2	The altitude rate is positive. The spacecraft has an ascend behaviour.	The thruster is either maintained OFF or switched OFF.
D7.1	The altitude rate is positive. The spacecraft has an ascend behaviour. The following control step is triggered.	The control level D10 is triggered
D7.2	The altitude rate is negative. The spacecraft has a descend behaviour. The following control step is triggered.	The control level D13 is triggered
D7.3	The altitude rate is zero. The following control step is triggered.	The control level D14 is triggered

○ **Altitude rate limit check [Decision level D9/D10]**

In order to guarantee a smooth approach to the target altitude facilitating the dumping actions of possible unstable dynamics, the spacecraft altitude rate is limited. The limitation can be varied in the different mission phases. During the nominal mission phases, the finest control is given, setting the altitude rate limitation at $\dot{h}_{limit|rate} = 1.93 \cdot 10^{-5} m/s$.

This strong requirement has been derived considering GOCE's operations [197]. This limitation can be triggered for both ascending of descending approaches. In Table 49, the output decision cases have been summarized with the consequent thruster operation status.

Table 49: D9 and D10 levels, decision options.

Altitude rate limit check		
Decision label	Description	Thruster status/Control logic decision
D9.1	The spacecraft is descending with an altitude rate higher than the set $\dot{h}_{limit rate}$. The altitude rate shall be reduced. The following decision level is triggered.	The control level D11 is triggered
D9.2	The spacecraft is descending with an altitude rate lower than the set $\dot{h}_{limit rate}$. The altitude rate could be increased.	The thruster is either maintained OFF or switched OFF.
D10.1	The spacecraft is ascending with an altitude rate lower than the set $\dot{h}_{limit rate}$. The altitude rate could be increased. The following decision level is triggered.	The control level D12 is triggered
D10.2	The spacecraft is ascending with an altitude rate higher than the set $\dot{h}_{limit rate}$. The altitude rate shall be reduced.	The thruster is either maintained OFF or switched OFF.

➤ **ramEP THRUSTER CONSTRAINT:** Switching of period check [Decision level D4/D11/12/13/14]

The preliminary design phase of the ramEP thruster force a conservative approach to the thruster operations, introducing additional safe margin to avoid possible criticalities. This approach has been followed by setting a minimum switch-off time to allow the cooldown of the thruster. This time is required mainly to avoid the overheating of the cathode heater before starting the following ignition sequence. This time could be minimized by introducing a heater temperature sensing, thanks to which an algorithm in the PPU control block can manage both the cooldown and heat time of the cathode. However, the capability to perform these types of operations is strongly impacted by the design of the cathode that is not currently

defined. Moreover, a dedicated test campaign shall be performed for a detailed assessment of temperature reference point characteristic according to the foreseen mission profile.

In the current switch off limitation time, a period of $t_{off|limit}=1000s$. In Table 50, the output decision cases have been summarized with the consequent thruster operation status.

Table 50: D4, D11, D12, D13 and D14 levels, decision options.

Switching time check		
Decision label	Description	Thruster status/Control logic decision
D4.1	$t_{off} \geq t_{off limit}$. The thruster could be re-ignited. If already firing, the thruster is maintained operative.	The thruster is either maintained ON or switched ON.
D4.2	$t_{off} < t_{off limit}$. The thruster is maintained off. The thruster ignition procedure cannot be performed.	The thruster is either maintained OFF or switched OFF.
D11.1	$t_{off} \geq t_{off limit}$. The thruster could be re-ignited. If already firing, the thruster is maintained operative.	The thruster is either maintained ON or switched ON.
D11.2	$t_{off} < t_{off limit}$. The thruster is maintained off. The thruster ignition procedure cannot be performed.	The thruster is either maintained OFF or switched OFF.
D12.1	$t_{off} \geq t_{off limit}$. The thruster could be re-ignited. If already firing, the thruster is maintained operative.	The thruster is either maintained ON or switched ON.
D12.2	$t_{off} < t_{off limit}$. The thruster is maintained off. The thruster ignition procedure cannot be performed.	The thruster is either maintained OFF or switched OFF.
D13.1	$t_{off} \geq t_{off limit}$. The thruster could be re-ignited. If already firing, the thruster is maintained operative.	The thruster is either maintained ON or switched ON.
D13.2	$t_{off} < t_{off limit}$. The thruster is maintained off. The thruster ignition procedure cannot be performed.	The thruster is either maintained OFF or switched OFF.
D14.1	$t_{off} \geq t_{off limit}$. The thruster could be re-ignited. If already firing, the thruster is maintained operative.	The thruster is either maintained ON or switched ON.
D14.2	$t_{off} < t_{off limit}$. The thruster is maintained off. The thruster ignition procedure cannot be performed.	The thruster is either maintained OFF or switched OFF.

3.7 MDO and trajectory propagation results

This section focused on the main results obtained exploiting the different modules of VLEO-MAGNETO for the derivation of an optimal platform configuration and the related orbital analysis performed aimed to demonstrate the feasibility of the air-breathing concept. As presented in Section 3.6.1, the analysis of the configuration is subdivided into three main steps. Considering the mission requirements and constraints as well as qualitative design considerations reported in Section 3.4.1, the MDO process presented in Section 3.6.1.2 is set up. The design and operational constraints are provided to the MDO process through the input module, called “Scenario definition”, presented in Section 3.4. Recalling the process introduced in VLEO MAGNETO, the results of the Pareto front resulting from the optimization process are analysed with respect to multiple criteria. The selection phase of the optimal solution foreseen a second decision level for further characterization of the alternative solar array architectures. These are specifically adapted to the optimal solutions on the Pareto front.

Each derived alternative is investigated with the average atmospheric model presented in Section 3.6.1.2. After this phase, the user can select the final optimal configuration according to the mission operational requirements, even in this case with a multi-criteria selection.

Once that the configuration is selected, it propagated thrust the last module of VLE-MAGNETO to verify the goodness of the resulted configurations in a pre-selected mission profile.

Following the MDO process defined in Section 3.6.1.2, the related MATLAB routine was executed on a common laptop PC equipped with an Intel i7 655U processor running Windows 10 with the MATLAB version 2020a.

As previously introduced, the number of MDO solutions depends on how the input variables are introduced and on both linear and non-linear constraints, which defined the admissibility of the solutions in the feasible design space. For the analysis performed, the derivation of the Pareto front was obtained through a weighted method for which a set of 34 weight triplets was defined in the range $[0-1]$ with a step of 0.1. Neglecting possible triplet repetition, each value in the weight triplet scales the impact on the final value of the fitness function. As a consequence, the number of triplets defines a new initial guess for the subsequent iteration in a sort of multi-start approach.

The second key input variable, which affects the number of solutions and therefore the computational time of the entire MDO routine, is the altitude parameter around which the optimization of the platform is performed. Its value is introduced as a discreet number in a nested for-cycle to investigate the range between 230km and 245km introduced in input with a step value of 5 km.

This approach was forced by the intrinsic relation between the atmospheric conditions (e.g., densities and temperature of the incoming flow) and operative

thruster parameters defined as optimization variables of the MDO process. In fact, according to the thruster performance relations introduced in Section 3.6.1.2, fixing either the thruster power consumption (P_{ramEP}) or the thruster acceleration voltage (ϕ_{ramEP}) an optimal altitude could be eventually found. Therefore, also introducing the altitude as an input parameter, the optimization process is constrained around its value. This approach was intentionally introduced to counterpose the technology-pushed approach, caused by the constrained introduction of the thruster design, with the mission-driven design, which is usually exploited for the mission analysis.

As a result of the weighted Pareto approach and the altitude constraint, a total of 134 solutions were obtained, all fulfilling the imposed constraints. The Pareto front obtained is shown in Figure 90 through a fit of the discrete points elaborated to highlight the value of the three objective functions introduced in the MDO process. Despite the possible local minimal, the spread of the data appears contained, allowing good representativeness of the fitting surface. As a consequence, the solution can be locally approximated fitted the data with a locally weighted smoothing quadratic method (see Figure 90).

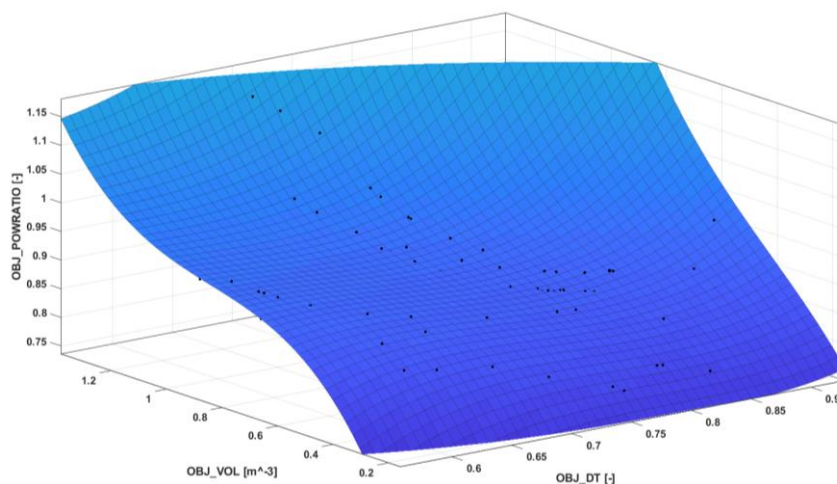


Figure 90: MDO Pareto front.

Once the Pareto front is defined from the MDO problem, the set of non-dominated solutions shall be further analysed to select either one or multiple results according to the stakeholders' preferences.

Even though complex a-priori and a-posteriori methods can be introduced, in the case of a ramEP platform design, targeted an IoD mission, could consider a set of the preferences offers to the user through the “result evaluation” module introduced as the last step of VLEO-MAGNETO. The identified selection criteria with the related rationale are:

- Maximum T/D value: this parameter was introduced to select the configuration with the higher operability in terms of orbital manoeuvres. The S/C configuration with the higher thrust-over-drag ratio can be operated in different

mission profiles, considering the orbit-raising phase. Moreover, this parameter evaluates the goodness of the S/C design about the generated drag.

- Maximum P_{ramEP} value: according to the thruster performance model provided by SITAEL, increasing the power allocated to the thruster, while the other model parameters are maintained constant, higher thrust value can be obtained with a moderate increase of the acceleration voltage. Therefore, this solution consists of the best thruster performance obtainable among the MDO solutions.
- Minimum FVAL value: the MDO process was introduced with the common approach of minimizing the value of the fitness function (see Eq. 3.3). As a consequence, the result presenting the minimum value of the fitness function can be considered the optimal solution over the entire feasible design space.

Therefore, considering the selection criteria here reported, three optimal solutions were identified on the Pareto front. Their main features are reported in Table 51.

Table 51: main output of the selected MDO results.

VARIABLES		U.M.	$\max T/D$	$\max P_{ramEP}$	$\min FVAL$
FVAL	Fitness function value	[–]	0,92	0,70	0,51
W_{PLT}	Platform total width [m]	[m]	1,77	2,16	2,03
WR_{B-W}	Body-Wing width ratio	[–]	0,52	0,52	0,53
$L_{ PLT}$	Platform length [m]	[m]	4,58	5,65	6,81
$L_{btm WING}$	Length of the lower wing side	[m]	6,95	4,61	3,97
$L_{top WING}$	Length of the top wing side	[m]	4,23	3,76	2,56
L_i	Length of the intake	[m]	1,20	1,27	1,00
L_c	Length of the collector	[m]	2,72	3,73	5,16
L_i/L_c	Intake-collector ratio	[m]	0,44	0,667	0,19
A_{INT}	Intake area	[m ²]	0,54	0,83	0,75
A_{SA}	Solar array area	[m ²]	7,85	10,30	9,84
$V_{av PLT}$	Bus available volume	[m ³]	0,79	0,40	0,35
Φ_{ramEP}	ramEP operating voltage	[V]	1807,2	1999,99	2000,1
T_{ramEP}	ramEP generated thrust	[N]	0,0057	0,007	0,0059
D	ramEP platform drag	[N]	0,0051	0,007	0,0069
T/D	Thrust over drag ratio	[–]	1,12	1	1
P_{ramEP}	ramEP power consumption	[W]	1328,8	1833,5	1739,4
P_{other}	Platform available power	[W]	300	300	300
$P_{ PLT}$	Total generated power	[W]	1686,5	2212,2	2114,2
PR	ramEP power consumption fraction	[–]	0,79	0,83	0,8227

As pointed out in Section 3.6.1.2, the MDO problem considers the high solar cycle as the worst condition for the derivation of the atmospheric parameters. The rationale behind this choice was based on the behaviour of the atmosphere during the high solar cycle. The high solar energy coming from the Sun results in an

expansion of the atmosphere. As a result, at a constant altitude, higher values of numeric density (and therefore the generated drag) are reached. In addition, the high solar cycle period presents and higher deviation from the average atmospheric trends as well as a higher variability over each Earth location of each parameter involved.

All three solutions belong to the output vector related to the nested loop at 230km of optimal altitude. This allows a direct comparison of the performance obtainable from the system for which the main characteristic mainly driven by the design features of the ramEP thruster. As a result of the MDO, all three ramEP thrusters have a number of intake duct equal to one avoiding the frontal structural surface necessary for the housing of the ducts, dividing the intake area into cells. The length of the ionization stage results comparable for all the three cases with an average value of 1.15 m constrained with respect to the ratio between the intake and collector lengths which cannot exceed 0,7, imposed as a non-linear constraint in the MDO routine. The rest of the length is intrinsically covered by the sizing of the collector stage, which reaches its maximum value of 5,16 m in the case of the configuration selected for min FVAL criteria. Despite the benefits brings by the higher compression ratio, which results in a higher flow density at the thruster interface, the longer collector stage, having a conical shape, reduced the available spacecraft volume, which in the min FVAL configuration, results in equal to 0,35 m³.

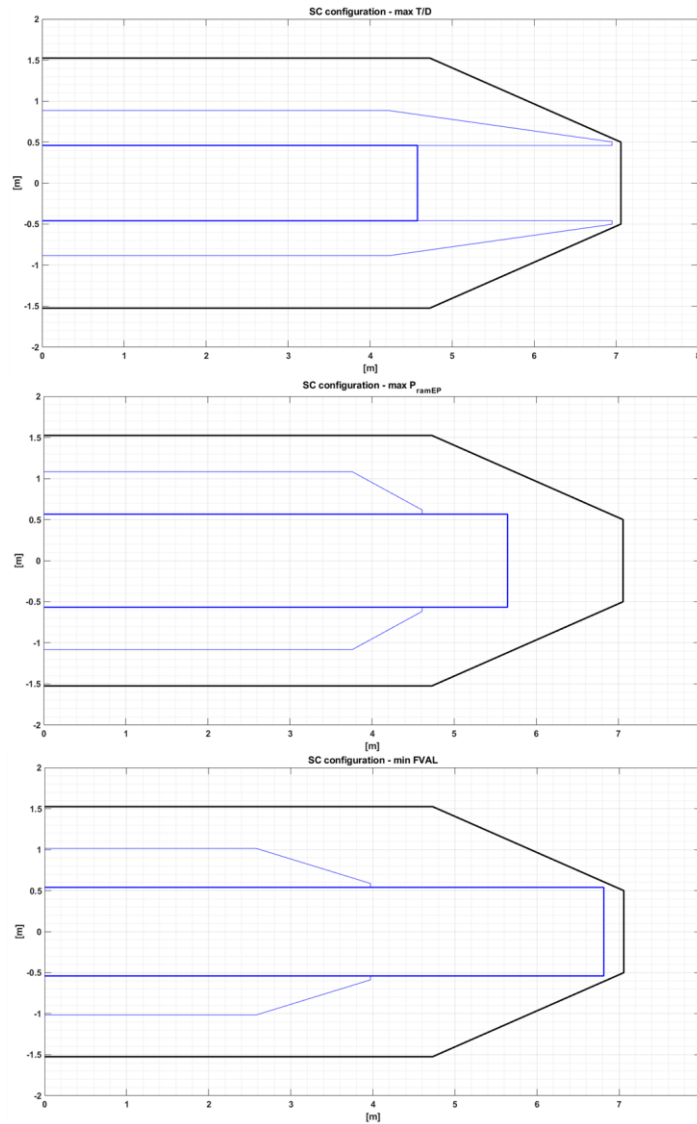


Figure 91: optimal configurations for the different criterion (i) min FVAL, (ii) max P_{ramEP} and (iii) max T/D.

The MDO solution shows a spacecraft power budget in a range between 1,5 kW and 2,2 kW over the entire Pareto front solution set. The consumption of the onboard subsystem necessary for operating the thruster itself and the rest of the spacecraft is always kept at 300W assumed independently as maximum consumption during all mission phases, following worst-case logics.

Some considerations on the thruster power consumption with respect to the solar array's configuration can be derived by analysing the spacecraft configurations shown in Figure 91. In particular, even if the max TD configuration has a comparable thruster power consumption with regard to the min FVAL configuration, around 2 kW, the spacecraft shapes present several differences. In fact, the min FVAL configuration presents a longer spacecraft body with two wings moved back with respect to it. On the contrary, the max T/D configuration presents a shorter body with thin and elongated wings which extend beyond the spacecraft body up to the maximum fairing allowable length. While the lateral area results

similar in both configurations, the elongation of the lateral wing and the shortest spacecraft body decrease the generated drag. Despite these considerations, this configuration could present some criticalities in term of attitude stability due to the centre of pressure moved forward by the wing's front elongation. The min FVAL presents, in turn, a wings layout that can be qualitatively evaluated beneficial from the stability point of view owing to the retrogression of the centre of pressure which enables a passive stabilization action of the spacecraft itself. Even though the correct assessment of the spacecraft stability might either pose a strong design choice or drive the selection of the final optimal results, the capability of numerically derived this impact is not yet included in the optimization process due to the preliminary phase of the spacecraft design.

After a qualitative assessment of the optimization solutions selected among the Pareto front set, the analysis of the three configurations proceeds with the evaluation of the spacecraft performance provided over the altitude range considered in the foreseen IoD mission scenario. This analysis is performed exploiting the atmospheric models derived from the averaging and a subsequent fitting of the different atmospheric variables for altitude values between 180 km and 250 km. A dedicated fitting atmospheric model is derived for each solar cycle period. In addition, the configurations were investigated according to both thruster Performance model (TPM) presented in Section 3.6.1.2 which relate the atmospheric condition to the thruster performance keeping constant either the thruster acceleration voltage (ϕ_a) or the thruster power consumption (P_{ramEP}). This allows highlighting two main aspects which characterized the selected configuration for their final selection.

The first evaluation is performed considering the trends of thrust-over-drag ratio and drag shown in Figure 92 and Figure 93, respectively.

With the increment of the altitude, the T/D ratio investigated for TPM at constant voltage presents a decreasing trend since the lower atmospheric density requires a higher acceleration voltage [176].

As previously anticipated, sustaining strong and quick power variations is a critical aspect to consider for the design of the power subsystem of the spacecraft. The preliminary analysis presented in this work does not fully describe the cross interactions caused by this possible approach for which a specific model should be developed.

On the contrary, the T/D trend results positive is the TPM adopted is that based on a constant P_{ramEP} since the acceleration voltage is regulated according to the incoming mass flow density variation. The trends derived from this TPM show a T/D value at a certain altitude value below 200 km equal to zero. Specifically, the limits for all the selected configurations are: (i) for High Solar Activity: $h < 196\text{km}$, (ii) for Medium Solar Activity: $h < 188\text{km}$ and (iii) for Low Solar Activity: $h < 185\text{km}$. According to the solar activity periods below these limits, the thruster is not able to sustain the discharge due to the excessive increment of the airflow mass

collected by the intake and provided to the thruster with a subsequent flameout. Therefore, the re-ignition of the thruster can be started only by increasing the spacecraft altitude beyond those limits with an additional propulsion system. Consequently, these altitudes shall be considered as lower boundaries for the operation of the ramEP system if the TPM is based on keeping the thruster power constant.

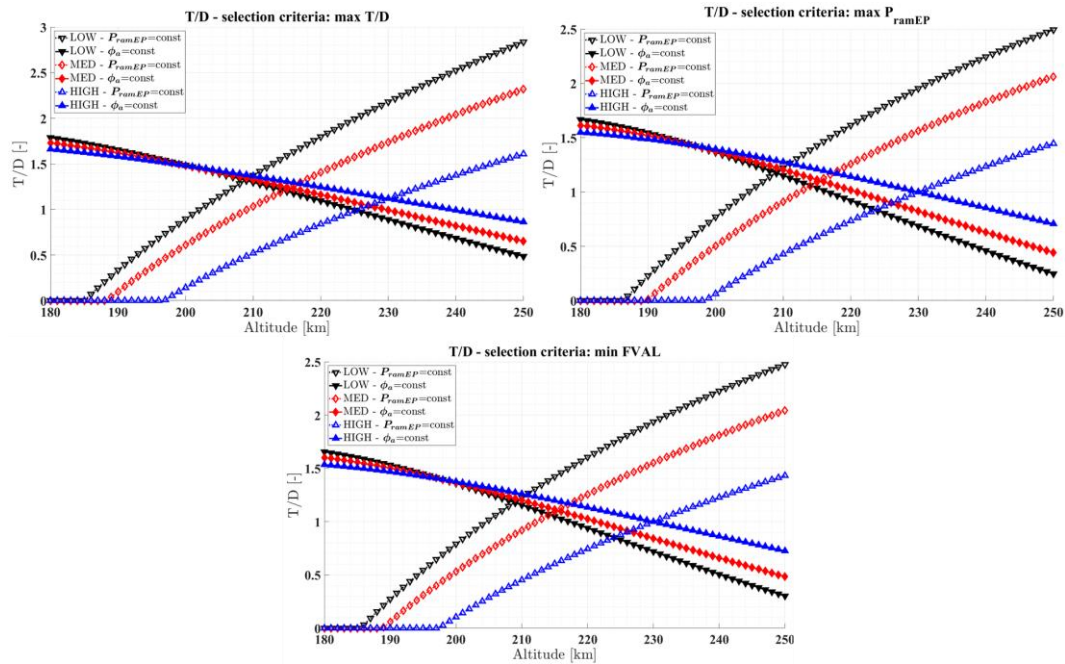


Figure 92: trends of the thrust-over-drag ratio for the selected configuration (top-left) max (T/D), (top-right) max (P_{ramEP}) and (bottom) min($FVAL$).

Despite the limitations on both TPM previously mentioned, the optimal thinkable solutions could be based on a mixed TPM for which at lower altitudes, the constant voltage law is used while for its increment, the PPU would change the control law in that keeping the thruster power constant. However, the system complexity could significantly increase, jeopardizing the technological feasibility of this solution. In particular, the most impacted component is the PPU for which its design shall strongly deviate with respect to the common approach based on a limited step of operative points at fixed voltage levels.

In Figure 93, the trends of the drag value generated by all the selected configuration relative to the different solar periods are shown.

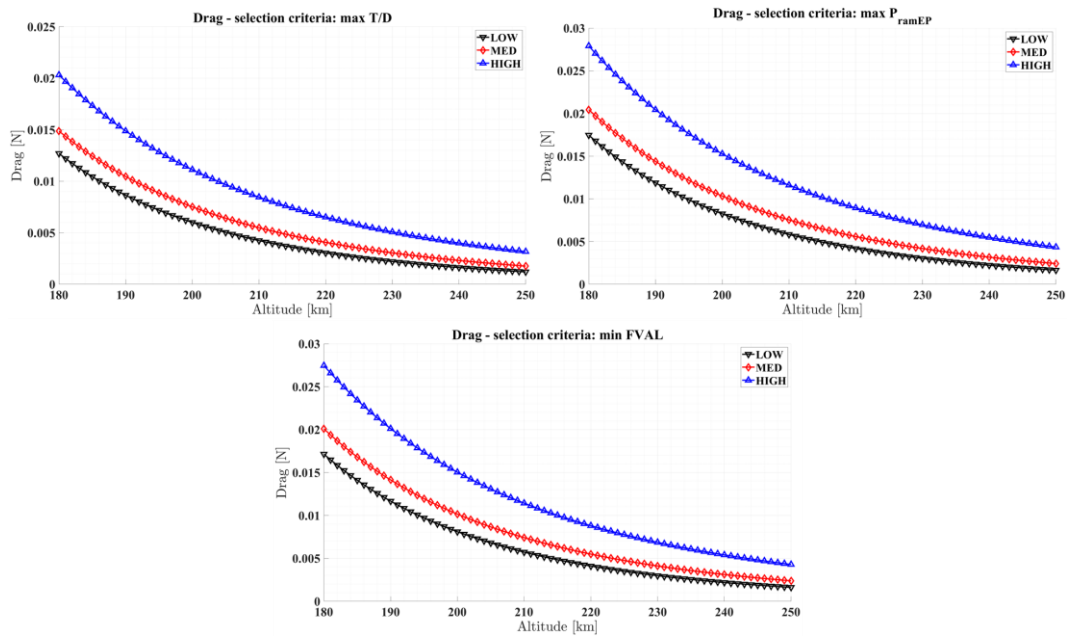


Figure 93 trends of the generated spacecraft drag for the selected configuration (top-left) $\max(T/D)$, (top-right) $\max(P_{ramEP})$ and (bottom) $\min(FVAL)$.

As expected, for a constant altitude, the higher drag value is obtained for the high solar activity period, usually greater than 40% with respect to the drag value for the medium solar activity period.

The technological limitations foreseen in the adoption of different TPM persist also selecting the constant power law for which a limitation on the acceleration voltage effectively reachable by the PPU shall be considered. In addition, according to the ramEP thruster design performed by SITAEL based on a double stage Hall thruster architecture, the acceleration voltage would not be increased excessively in order to avoid discharge instability and the consequent associated effects such as performance degradation as well as possible thruster flameout.

In Figure 94, the thrust trends for all the configurations are shown with the identification of the altitude for which the acceleration voltage is below 3000s.

The practicable thrust-over-drag points, respecting the same voltage limitation, are instead shown in Figure 95. From this second figure, the altitude range in which the ramEP operates, maintaining the orbital altitude constant along the trajectory, can be identified. In Table 52, the ranges where the obtained T/D ratio is greater than one respecting the limitation on the discharge voltage are shown.

Table 52: optimal operative altitude ranges for the selected configuration.

Configuration	Solar Activity Period	Lower altitude [km]	Higher altitude [km]
max T/D	HIGH	226	243
	MED	210	226
	LOW	203	218
max P_{ramEP}	HIGH	230	240
	MED	213	224
	LOW	204	216
min FVAL	HIGH	230	240
	MED	213	224
	LOW	204	216

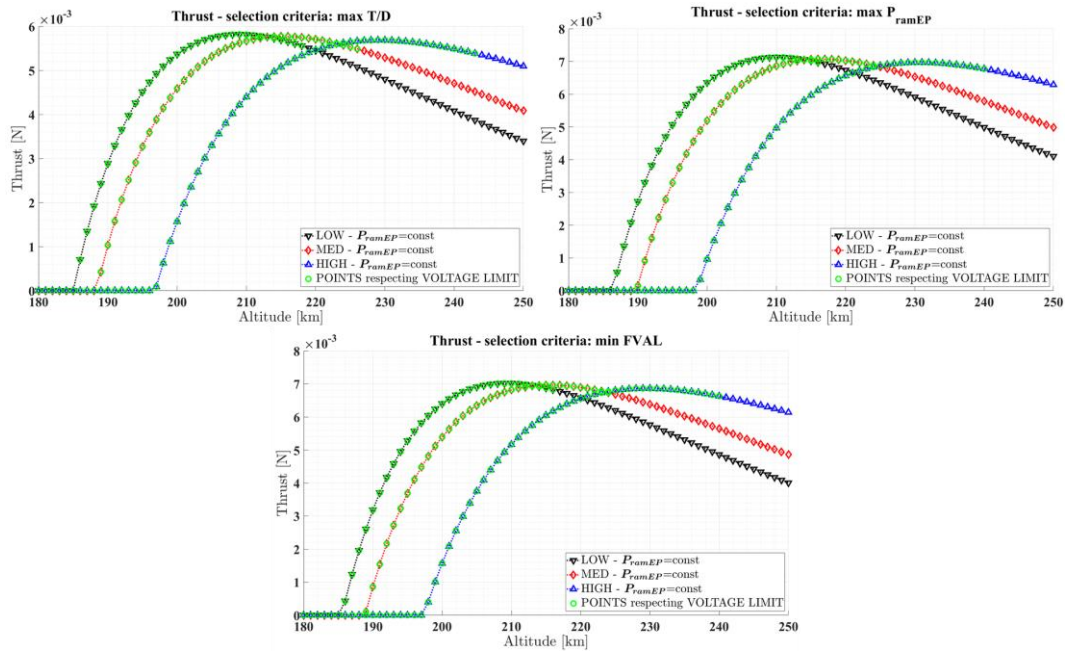


Figure 94: trends of the generated ramEP thrust for the selected configuration (top-left) max (T/D), (top-right) max (P_{ramEP}) and (bottom) min($FVAL$). The points on the trends fulfilling the acceleration voltage constraint are highlighted in green.

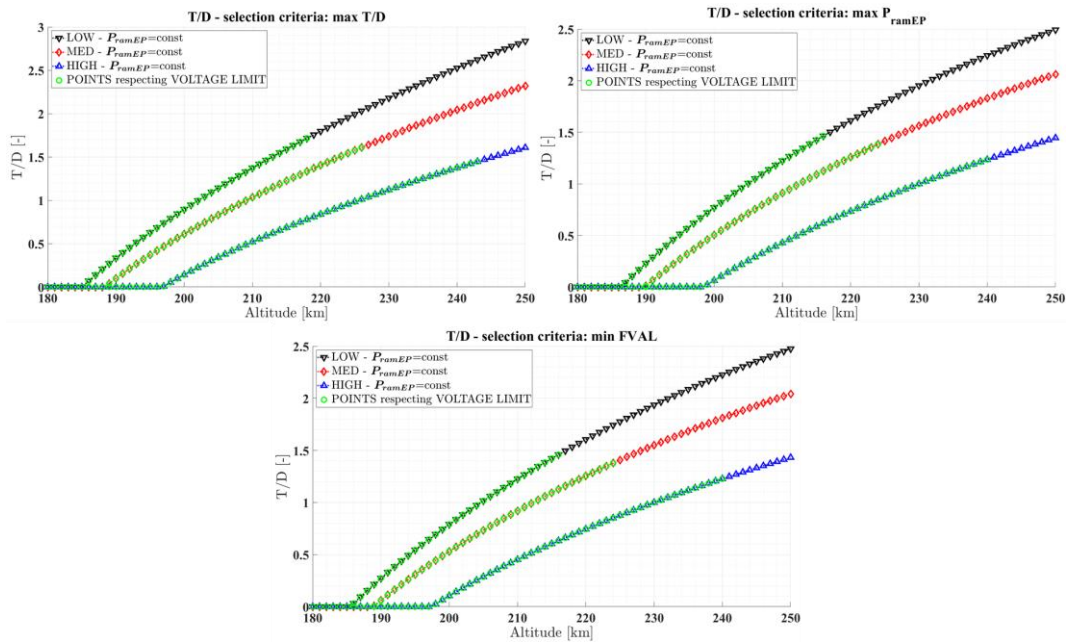


Figure 95: trends of the thrust-over-drag ratio for the selected configuration (top-left) max (T/D), (top-right) max (P_{ramEP}) and (bottom) min ($FVAL$). The points on the trends fulfilling the acceleration voltage constraint are highlighted in green.

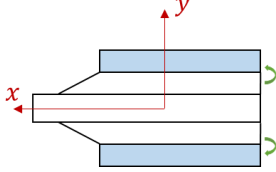
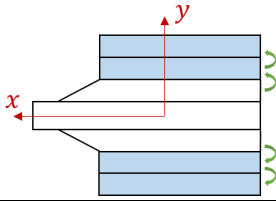
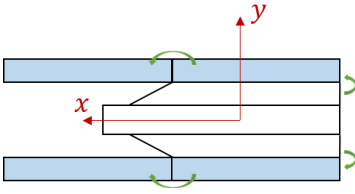
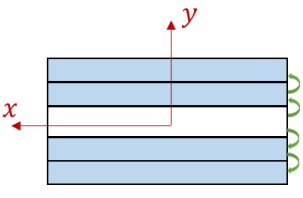
Alternative architecture configurations

An additional capability introduced in the design process of VLEO-MAGNETO consists of further investigating the alternative architectures of the solar arrays. As previously introduced, in the MDO process, the solar cells are assumed to cover one side of the spacecraft body and the lateral wing, sized accordingly to the MDO constraints. As explained in Section 3.6, these wings are fixed as a part of the structural layout of the spacecraft in a sort of GOCE-like configuration [198].

However, even with an increment of the system complexity, the possibility to deploy solar panels results in extreme interest- These are envisioned either always deployed or occasionally deployed to deal with contingency or particular high-power loads demanding.

A total of 4 additional cases were introduced investigated considering mechanism placed on the lateral wings for the deployable surfaces with an area comparable to the wing itself. In specific:

Table 53: alternative spacecraft wing configurations.

<p><i>SA-MOD-1</i>: A single solar panel for each side deployed around the x-axis</p>	
<p><i>SA-MOD-2</i>: Panels deployed around x-axis toward (+/-) y-direction</p>	
<p><i>SA-MOD-3</i>: Panels deployed around y-axis toward (+) x-direction.</p>	
<p><i>SA-MOD-4</i>: Defined clean configuration, the height of the deployable panels is comparable with one side of the octagonal section of the spacecraft body to ensure a minimum stowed envelope</p>	

The alternative solar array configurations reported in Table 53 were characterized by different solar array surfaces ($A_{SA|add}$) and an additional frontal area ($A_{f|add}$) which, in this case, is increased by the equivalent area necessary to accommodate the deployment mechanism. These parameters are reported in Table 54.

Table 54: additional available surfaces for the alternative wing configurations.

		MDO selected cases		
		$\max P_{ramEP}$	$\max T/D$	$\min FVAL$
SA-MOD-1	$A_{SA add} [m^2]$	3.59	3.90	2.44
	$A_{f add} [m^2]$	0,042	0,052	0,048
SA-MOD-2	$A_{SA add} [m^2]$	7,19	7,80	4,88
	$A_{f add} [m^2]$	0,085	0,104	0,095
SA-MOD-3	$A_{SA add} [m^2]$	7,19	7,80	4,88
	$A_{f add} [m^2]$	0,042	0,052	0,048
SA-MOD-4	$A_{SA add} [m^2]$	2,98 (*)	3,23 (*)	2,11 (*)
	$A_{f add} [m^2]$	0,035 (*)	0,043 (*)	0,041 (*)

(*) The surfaces related to the deployed solar panels here reported are considered replacing of the wing surface of the baseline MDO configuration.

For each MDO selected case, the alternative configurations of the solar arrays were analysed over the altitude range to assess the main trends and the spacecraft operability altitude region.

Figure 96 shows the thrust-over-drag ratio for the MDO solution selected for the maximum value of the P_{ramEP} . For SA-MOD-1, SA-MOD-2 and SA-MOD-3 configurations, the resulted T/D trends is higher than that obtained with the configuration without additional solar panels. In particular, the maximum value is obtained by SA-MOD-3 between 180km and 197.5 km, by the SA-MOD-2 between 197.5k and 228 km and, lastly, by the SA-MOD-3 beyond 228km. Similar trends can be identified for the max T/D and min FVAL configuration, shown in Figure 97 and Figure 98, respectively.

For all configurations, the minimal thruster operational altitude, below which the thruster cannot sustain the discharge due to the higher flow density, is strongly reduced allowing an extension of the effective range in which the spacecraft can operate. On the contrary, the constraint imposed on the maximum allowable acceleration voltage, which the PPU can provide, is fulfilled only by SA-MOD-1 and SA-MOD-2 for altitude ranges having a thrust-over-drag ratio greater than 1. This is caused by the shifting of the trends toward lower altitude and, in association with the flattening caused by the higher generated drag, caused the reduction of the viable points that can be considered for constant altitude operation.

The cases of particular interest for the comparison of the generated drag between frontal and lateral surfaces are the trends of SA-MOD-1 compared with SA-MOD-3. As a matter of fact, both configurations present an equal frontal area while the lateral area of the additional deployed wings is doubled in the case of SA-MOD-3. As a consequence, while at lower altitude values, the additional power coming from the deployed arrays can be exploited to reach a higher thrust value, with the increment of the altitude, the lower thrust level required can be directly translated into a lower thrust power demanding. In this condition, the additional solar arrays result not fully exploited, assuming that all the power coming from the deployed arrays is allocated to the thruster. On the contrary, at higher altitudes, if the power allocated to the thruster is maintained constant, the supplementary power could be exploited by other onboard subsystems, such as the payload. Despite the increase of the system complexities, the capability of deploying additional surfaces could represent an interesting solution to deal with either power consumption peaks or contingency situation in particular at lower altitudes.

Different considerations could be derived for the SA-MOD-4 configuration, which results in a spacecraft characterized by a lower T/D ratio trend. This is mainly caused by the reduction of the available platform power due to the lower solar array surface of the deployed wing. Considering the configuration resulted from the MDO process, the height of the lateral wings is commonly greater than the length of one side of the spacecraft body section. As a result, even considering the same length of the spacecraft, the deployed surface is lower with, instead, higher frontal surfaces caused by the deployed mechanism.

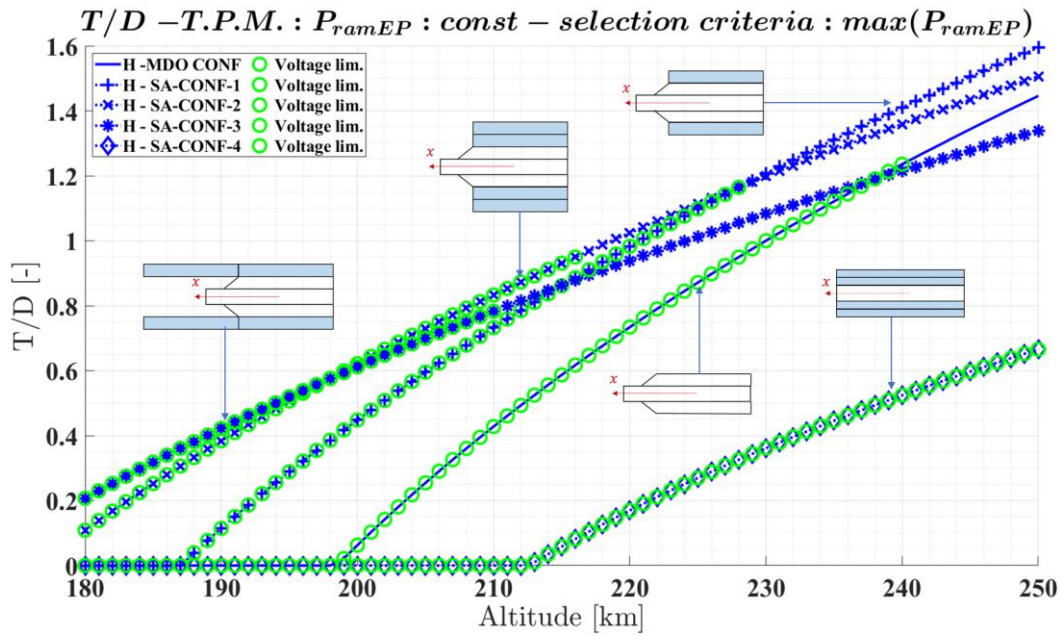


Figure 96: trends of the thrust-over-drag ratios considering alternative deployed wing configurations investigated for $\max(P_{ramEP})$ solution.

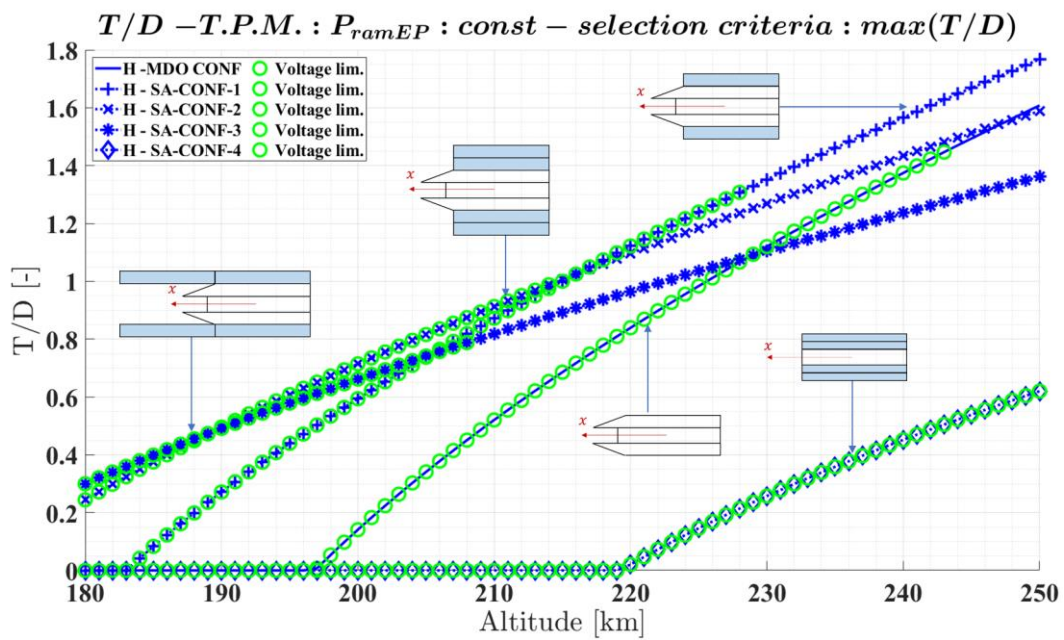


Figure 97 trends of the thrust-over-drag ratios considering alternative deployed wing configurations investigated for $\max(T/D)$ solution.

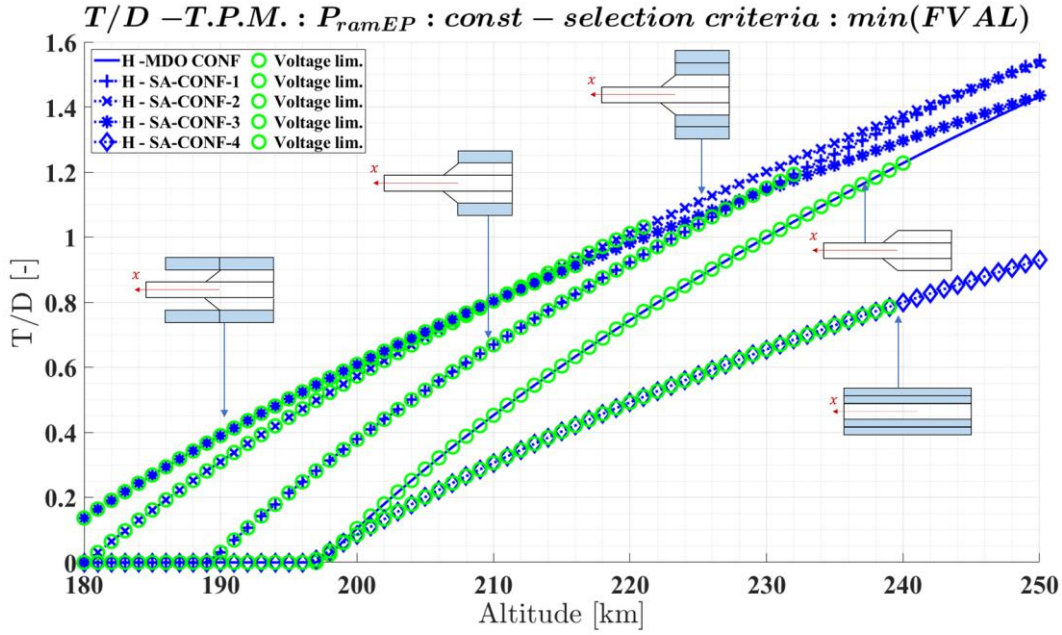


Figure 98 trends of the thrust-over-drag ratios considering alternative deployed wing configurations investigated for $\min(FVAL)$ solution.

The last module of VLEO-MAGNETO allows the simulation of the spacecraft operations according to the mission scenarios defined in the input files. As introduced in Section 3.6.1, this module called “Scenario Propagation” is based on a trajectory propagation module to simulate the orbital behaviour of the spacecraft and evaluate the operation of the ramEP thruster taking into consideration the thruster control logic defined in Section 3.6.1.3.

Coherently with the considerations reported in the previous paragraphs, the MDO solution selected as the reference case study for demonstrating the capability of this VLEO-MAGNETO module is the solution identified with $\max P_{ramEP}$ with the possibility to deploy supplementary solar arrays.

A total of three scenarios, each referred to a specific solar activity period (e.g., High, Medium, Low periods), were investigated. The propagation period was selected during periods of constant sunlight, which characterized the Dawn Dusk SSO @6 a.m. In specific, the scenarios were set to assess the minimal target altitude where the spacecraft can operate, maintaining a nearly constant altitude without a descending attitude. The propagation times were set equal to one week with a time step of 300s to limit the computational time below one hour. However, the simulation period and the time step adopted for each integration cycle can be modified by the user in the input file. For longer simulation, VLEO-MAGNETO offers the possibility to portion the overall output structure in sub-structures, avoiding an overallocation of the PC local memory.

The key results show for each integration step are (i) the different altitude values identified for each averaging process, (ii) the thruster acceleration voltage (ϕ_a), (iii) the activated thruster control modes and the (iv) the thrust-over-drag ratio values. These variables are shown for the High Solar Activity period in Figure 99, for the medium Solar Activity period in Figure 100 and the Low Solar Activity period in

Figure 101. All the propagations show the capability of the spacecraft to chase the set target altitude, even experiencing atmospheric variation according to the propagation time.

As expected, the minimum operative altitude grows with the increase of the solar activity for which: the altitude for the Low Solar Activity period is 206km, 216km is obtained for the Medium Solar Activity period, while 235km results for the High Solar Activity period. The target altitude is approached and maintained through the thruster operation after a period of free-fall trajectory used to collect a sufficient number of points to set up the altitude averaging process. In order to allow this calibration process, the initial altitude was set above the target altitude in all three scenarios. This assumption is sustained considering all commissioning operation that a platform shall perform after its release for the launch vehicle.

The ranges of T/D ratios and acceleration voltages are summarized in Table 55. According to the thruster control law, the limitation imposed on the maximum allowable acceleration voltages could command thruster switch off along the trajectory propagation considering the local trajectory atmospheric conditions. However, this condition was triggered only during the propagation for the High Solar Activity period where the switch-off modes D6.2 and D14.2 were activated around T0+40h, in a range between T0+77h and T0+96h, T0+125h, T0+152h and T0+167h (see Figure 99-(c)).

Table 55: T/D ranges and acceleration voltage ranges reported for each solar activity period.

	Starting date	T/D range		Acceleration Voltage range [V]	
		Min	Max	Min	Max
High Solar activity period	15 April 2014	0.79	1.25	1531	3079
Medium Solar activity period	15 February 2011	0.62	1.22	1158	2683
Low Solar activity period	15 December 2011	0.52	1.37	1110	2934

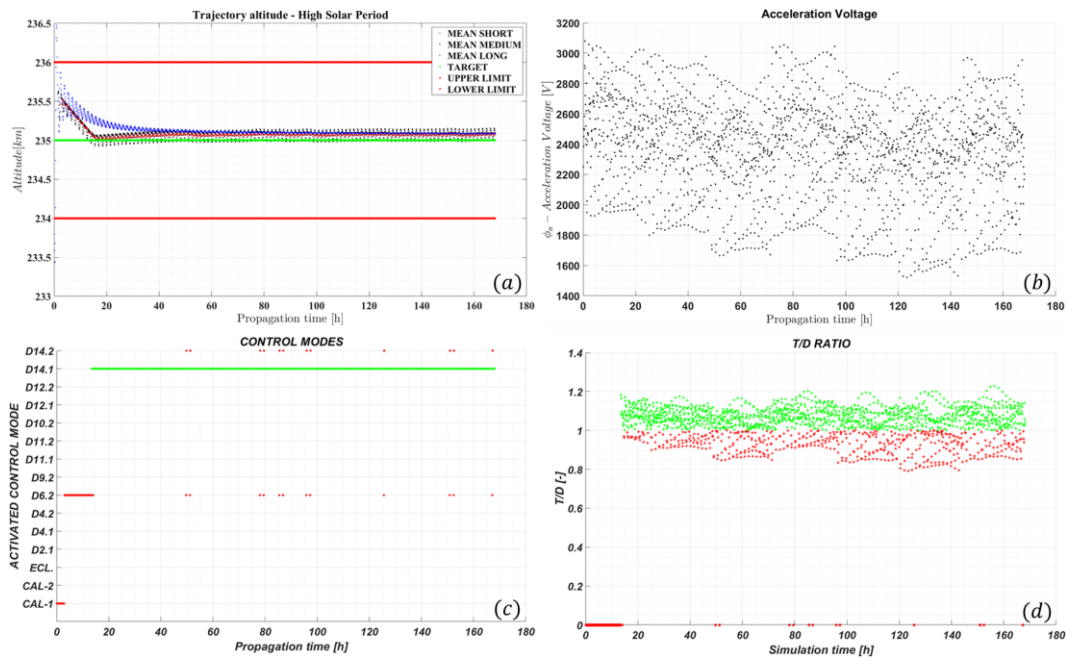


Figure 99: High Solar Activity propagation. (a) Altitude w.r.t. long, medium and short step averaging process, (b) thruster acceleration voltage, (c) activated thruster control modes, (d) T/D values.

As reported in Table 55 and shown in Figure 99-(d), Figure 100-(d), Figure 101-(d), the T/D values are characterized by strong variation along the trajectory. This is mainly caused by the variation of the real altitude used as input of the atmospheric model, which is affected by the Earth gravitational perturbation. However, despite the several points that resulted in a T/D value < 1 , the trajectory shows an intrinsically stable behaviour around the target value. This statement is further sustained by the activated control modes, in which thruster switch off modes are not triggered.

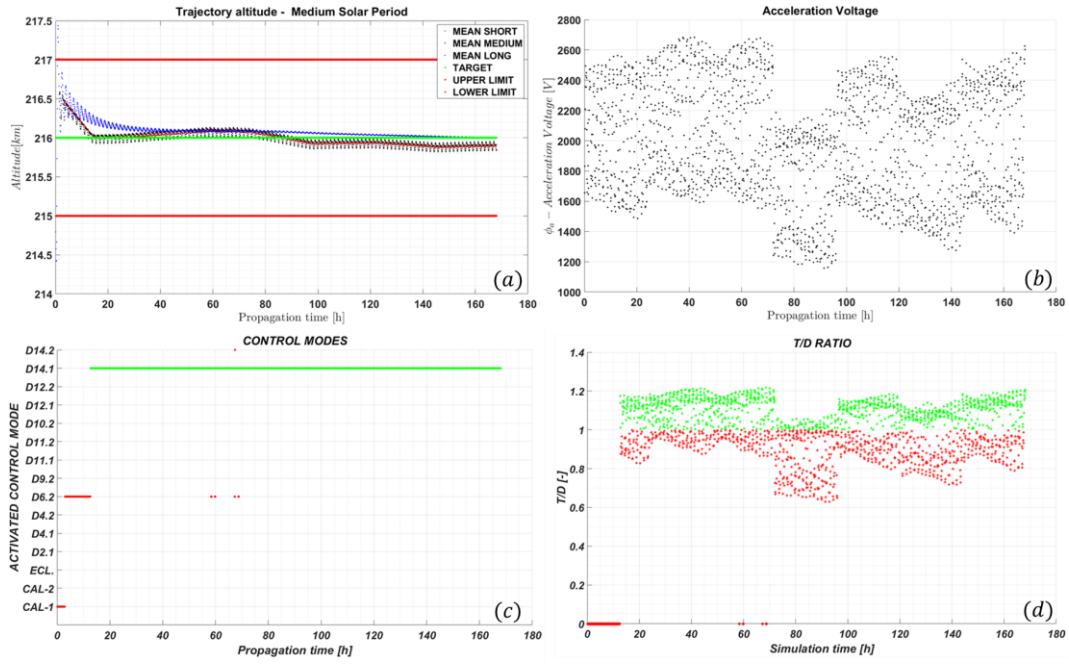


Figure 100: Medium Solar Activity propagation. (a) Altitude w.r.t. long, medium and short step averaging process, (b) thruster acceleration voltage, (c) activated thruster control modes, (d) T/D values.

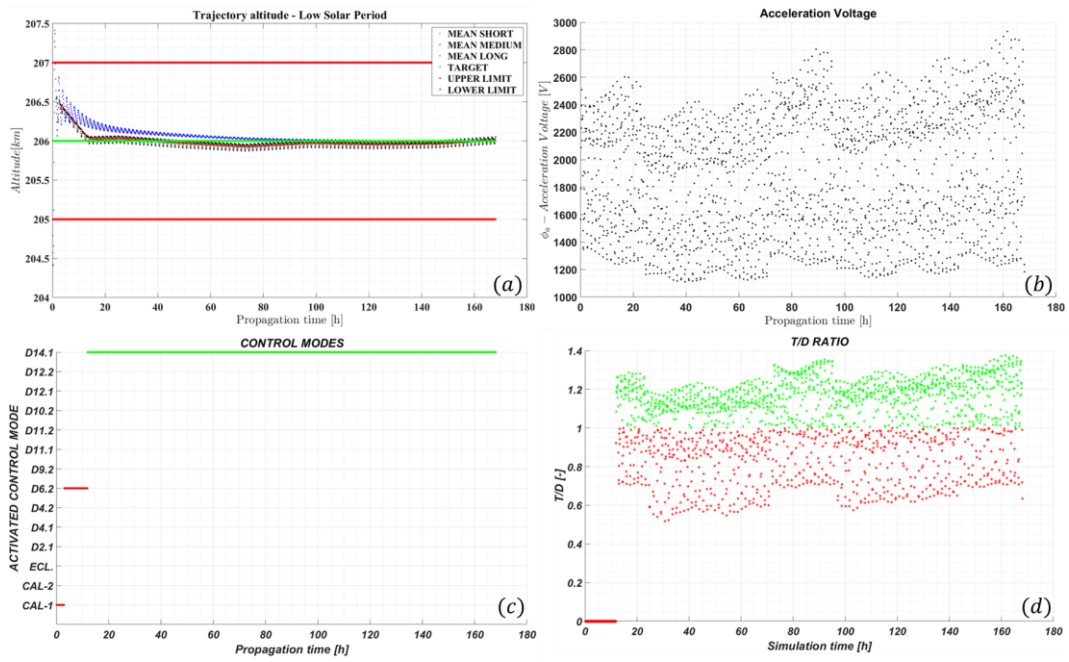


Figure 101: Low Solar Activity propagation. (a) Altitude w.r.t. long, medium and short step averaging process, (b) thruster acceleration voltage, (c) activated thruster control modes, (d) T/D values.

Chapter 4

Engine Health Monitoring applied to Hall Thrusters

4.1 Engine Health Monitoring concept

Through the decades, space systems have gained several advancements and additional functionalities thanks to introducing new technologies and innovative design methodologies.

The implementation of newly developed hardware caused an increased level of sophistication and complexity. This trend also involved software-based functionalities nowadays used in the substitution of physical components.

These aspects were further stressed by the introduction and the following widespread of an augmented onboard automatic control authority to maximise the fulfilment of mission objectives by optimising the spacecraft and payload operations.

Among the functionalities necessary to properly operate both onboard subsystems and payload, the capability to ensure safe and reliable operation is still a key driver to avoid a potentially critical situation that might jeopardize the nominal satellite status. Therefore, since the preliminary design phases, the evaluation of potential faults and dangerous situation is carefully performed. The analysis shall rely on different techniques, such as Failure Mode and Effect Analysis (FMEA), Failure Mode and Effect Criticality Analysis (FMECA), Fault Tree Analysis and Hazard Analysis.

These are methodologies commonly exploited since the early design steps for identifying potential failure modes and assessing their impacts usually through a ranking process based on the definition of failure severity and the likelihood of occurrence [179]. Consequently, possible corrective actions could be foreseen and implemented to mitigate or avoid any identified hazard.

During in-space operations, the reliability level ensured by the fault/failure tolerance approaches on the components (and architecture) implemented during the design phase shall be combined with a dedicated health monitoring system able to perform all Failure Detection Isolation and Recovery (FDIR) functions. As stated in [199,200], the FDIR aims "*to detect off-nominal conditions, isolate the problem to a specific subsystem/component, and recover of vehicle systems and capabilities*". Even considering the first function in the FDIR process, hence perform the detection of a possible failure, the complexity of the system and the

involved technologies represents a critical challenge. The currently adopted approaches rely on monitoring housekeeping telemetries consisting of specific system/component health parameters checked to compare the detected values with set limits (boundaries) exploited in model or rule-based decision methods [201]. This approach is usually followed also for the detection of the malfunctioning of electric propulsion subsystems. The Power Processing Unit has the function to collect all the housekeeping telemetries coming from the different propulsion subsystem components, particularly those under direct command authority, hence: the thruster, the cathode and the flow control unit. However, while simple telemetries might be processed by the onboard computer exploiting one of the methods mentioned above, eventually to trigger the safe mode of the spacecraft, to deal with most of the failure, the telemetries shall be transmitted to a ground station for remote processing. The distinction between these two types of operations could be identified in the number of parameters to be measured to provide a complete characterization of the system's health status. This represents a crucial point for the electric propulsion subsystem, where, depending on the thruster typology, the modes of failure can be identified by several operatives and detected parameters. However, notwithstanding the extensive adoption of electric propulsion-based systems presented in the previous chapter, the formal identification of their failure modes is still vague and mainly focused on the failures of single components included in the system.

In specific, one of the components still considered critical for the EP system is the thruster. According to Polk [202], the potential processes involved in the limitations of the Hall thruster lifetime are the following: (i) erosion of the anode poles, (ii) cathode emitter erosion, (iii) electromagnets failure/cracking due to thermal cycling, (iv) ceramic discharge channel cracking, (v) cathode keeper and orifice erosion and (vi) keeper-cathode loss of insulation and short circuits. From this list, all possible failures/fault that can be avoided through verification the thruster during the acceptance phase before the flight. Although this may be true for avoiding early failures, the pre-flight procedure cannot avoid possible failure related to either the ageing of the components throughout the mission lifetime or single damaging events. For these aspects, the standard industrial approach consists of demonstrating the life qualification performing lengthy and costly test campaign in which the mission profile is replicated on-ground considering additional safety margins.

In [202,203], a mixed approach consisting of modelling the failure causes and events and test activities focused on the thruster unit is suggested to increase this component's overall reliability, mitigating the current highly demanding practice. However, the lack of knowledge in the physical phenomena driving the failure mode often reduces the validity of the analytic approach, except for some specific wear out effects. This is the case of the erosion of the ceramic thruster channel on which a lot of effort put by the research community resulted in the development of several modelling outcomes.

Despite these advancements, the poor understanding of the failure processes does not allow the overall assessment of all different failure modes of the thruster, limiting the implementation of an autonomous health monitoring system.

Alternative failure detection methodologies not already exploited in the space field were developed and extensively used in other propulsion fields, such as aeronautic and maritime.

Specifically, techniques developed in the gas turbine field, such as Trend Analysis, Gas Path Analysis (GPA) and Engine Health Monitoring (EHM), may offer an alternative approach to the health monitoring of electric propulsion devices.

These methods have been developed with the primary objective to optimize the scheduling of maintenance activity, targeting a reduction of both cost and maintenance time while increasing the system availability. Consequently, for gas turbine maintenance strategies, the traditional failure maintenance techniques (so-called "first generation") have been replaced by preventing actions performed to avoid the failures and by condition-based monitoring and detection strategies, respectively second and third generations maintenance strategies [204]. The evolution of the maintenance strategies has represented a significant benefit for manufacturers and airline companies with the generation of more significant profits owing to the augmented revenue derived by the efficient and high-quality management of the aircraft fleet [205]. These economic reasons justified the adoption of the engine-health monitoring strategies based on the "gas path" approach since their first introduction in 1969, thanks to Urban [206].

As detailed in the next section, these methods consist of understanding the component characteristic deviation from the evaluation of the gas path parameter variations.

Under those circumstances, these processes allow the evaluation of the component degradation over time and, eventually, both detection and identification of the specific cause responsible for the degradation. However, the evident differences between Hall Thrusters and Gas Turbine do not allow the direct application of these approaches. Nonetheless, the primary approach and the main diagnostics principle can be adequately adapted and exploited to monitor electric thrusters.

As briefly introduced, one of the main diagnostic approaches is to monitor the health status of the thruster through the comparison of a set of measurable parameters compared to pre-established limits introduced to highlight possible fault or failures. This statement is supported by the fact that a failure that changes the component characteristics and performance causes variations on the observable parameters (i.e., parameters that can be measured). In this sense, the latter type of parameters is considered dependent variables while the unmeasurable characteristics are defined as independent variables. The relationship between these two categories of variables can be established in different ways. In this work, the followed approach has been based on the construction of the called "Influence Coefficient Matrix" (ICM), whose coefficients represent the relations between the changes of thruster characteristics and the variations of the measured parameters.

The ICM coefficients could be derived exploiting different approaches: (i) a complex theoretical model in which the phenomenological behaviour of the thruster is described or (ii) a data-driven method in which experimental measurements are processed.

While the first suggested approach suffers from the introduction of assumptions and empirical-based relations, the evaluation of the ICM coefficient through a numerical procedure has the fundamental advantage to avoid strong assumptions and, if adequately developed, it can handle peculiar thruster behaviour driven by non-linear phenomena.

Exploiting the information derived from the ICM, the diagnostic is performed by inverting the ICM, thus using the deviation of the measured parameters to deduce the unknown component characteristics. In this case, the inverted ICM is called Failure Coefficient Matrix (FCM).

The GPA approach adapted to Hall thrusters is shown in Figure 102, following the scheme introduced by Urban in [207].

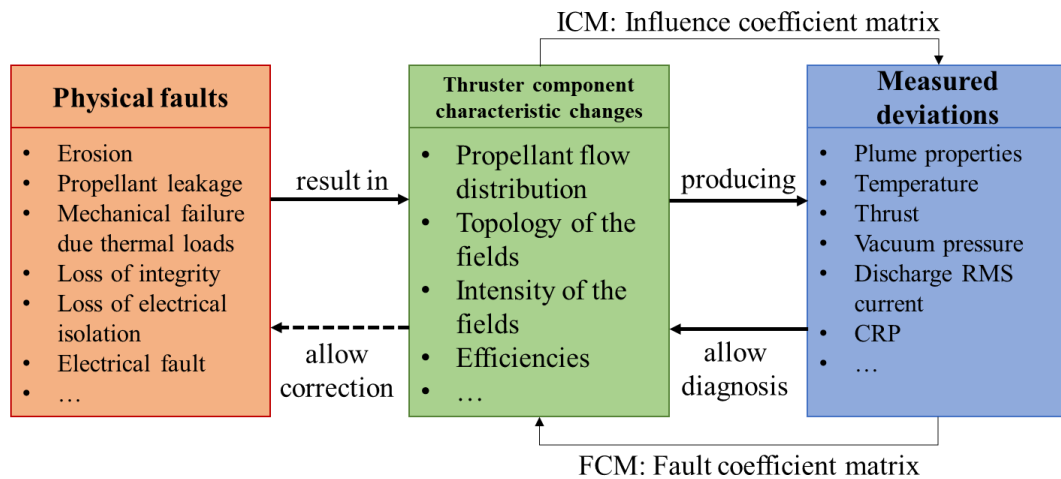


Figure 102:: Relation between physical degradation effects, component condition changes, and observable thruster performance parameters.

4.2 GPA/EHM state of the Art

During the past years, several methods have been developed to monitor aeronautical engine health status that could be envisaged for future applications in the space field, particularly for monitoring the propulsion system. These methods are usually classified for the type of information used to model the thruster's behaviour. First, the model-based (MB) rely on a phenomenological model of the thruster. Either physical or functional relations shall be introduced through specific mathematical equations. These types of models are commonly exploited when both single or multiple failures can be clearly described and linked to the physical and performance characteristics of the components. Qualitative and quantitative assessment can be performed with cost-effective procedures as well as relatively low computational demands. Nonetheless, their accuracy relies on the adopted mathematical model, which can cause a large margin of uncertainty. Moreover, many measurements are usually required. Among the MB methods, there are: (i) Linear Gas Path (LGPA), (ii) Non-linear Gas Path (NLGPA) and (iii) Kalman filter. Second, AI-based methods have recently gained fundamental importance in performing fault detection functions. These methods are adopted to overcome the drawbacks of the MB methods. They can deal with nonlinear behaviours of the components, learning in time with an evolutionary approach capable of generalizing the developed model according to the provided input data.

However, these methods usually required a large number of data coming from a direct experimental campaign or eventually derived through proper analytic models with an adequate level of representativeness. The implementation of these models requires the development of specific diagnostic methods validated through a sufficient number of operational data for which quality and type shall be ensured to embrace all behavioural aspects of the various components. Few steps are defined in the development phase of an AI-based diagnostic: after the acquisition and pre-processing of the data. They are provided to a dedicated training algorithm used to process them. The outputs provided by the trained algorithm are then evaluated until the pre-establish evaluation criteria are met.

A general subdivision of the AI-based methods is between (i) Neural Network, (ii) Bayesian Network, (iii) Expert System and (iv) fuzzy logic methods. An overall survey is presented in the following paragraphs.

- **Linear GPA (LGPA)**

In 1973, Urban [207] introduced the LGPA method based on linear relations between independent and dependent variables. This approach considers a steady-state process, assuming that measurements are not subject to uncertainties, there are no load variations, and the process is independent of the ambient conditions. The linear relations between the variations of dependent and independent variables are obtained from the equations introduced to model the system behaviour by

considering the first-order terms of Taylor expansion. The resulting mathematical expression can be expressed as follow:

$$\Delta Y = [ICM]\Delta X \quad (4.1)$$

where:

ΔY is the vector in which the changes of the measured parameters (dependent) are collected. The number of measured parameters involved is m .

ΔX is the vector in which the changes of the performance parameters (independent) are collected. The number of parameters involved is n .

ICM is a $m \times n$ matrix called Influence Coefficient Matrix (ICM).

The Fault Coefficient Matrix (FCM) can be obtained by inverting the ICM:

$$\Delta X = [ICM]^{-1}\Delta Y = [FCM]\Delta Y \quad (4.2)$$

The capability of deriving the FCM is given by the number of parameters in both vectors:

- $m > n$, the number of independent parameters (measurement) is greater than the number of dependent parameters (performance). The ICM is not square. Therefore, the FCM could be derived with a pseudo-inverse approach [208].
- $m = n$, the system is square, and the derived ICM can be inverted.
- $m < n$, the number of independent parameters (measurement) is lower than the number of dependent parameters (performance). The system is underdetermined, and a specific approach shall be exploited to obtain a solution, i.e. Volponi [147]

The approach of LGPA is often applied to relative variations of the measured and performance parameters. For example, if we consider a system described by the set of p performance parameters, which are related to q measured parameters through the functional relations $p = f(q)$, we can introduce the relative perturbations $dP = \Delta p/p$, and $dQ = \Delta q/q$. The linearize relations consider these new variables. This corresponds to the evaluation of the system model equations in terms of logarithmic variables, $P = \log(p)$. These variables are helpful in particular to identify trends in terms of simple power laws between the model parameters. In the case of functional relations as:

$$p_i = \prod_{j=0}^m q_j^{a_{ij}}, \quad (4.3)$$

where a_{ij} are generic exponential coefficients, the use of relative perturbations implies to rewrite the model as

$$(4.4)$$

$$\log p_i = \sum_{j=0}^m a_{ij} \log q_j,$$

which can be linearized as

$$dP_i = \sum_{j=0}^m a_{ij} dQ_j, \quad (4.5)$$

Comparing Eq. (4.5) with Eq. (4.1), we see that the exponential coefficients a_{ij} are the coefficients of the ICM for the relative perturbations.

The LGPA approach has been extensively used in the aeronautical field even though the linearization of the behavioural relations put substantial limitations on the representativeness over a wide operative range, in particular for a point far away from the design point.

- **Non-linear GPA (NL-GPA)**

When the assumption of linear behaviour of the thruster puts excessive limitations on the model representativeness, the NL-GPA can be introduced. The general mathematical relationship between dependent and independent parameters can be expressed as:

$$x + \delta x = \mathcal{H}(y + \delta y) = \mathcal{H}(y) + \delta x. \quad (4.6)$$

Considering the expansion of the central term and neglecting the higher-order terms, we obtain:

$$\mathcal{H}(y + \delta y) \cong \mathcal{H}(y) + J\delta y \quad (4.7)$$

which can be related to the Eq. (4.1) reported for LGPA. The NL-GPA method aims at determining the variation δy that satisfies the non-linear equation 4.3 through successive iterations of the LGPA, which corresponds to the application of the Newton-Raphson method.

With this approach, the ICM elements correspond to the percentage change of each performance parameters with respect to a determined measurement parameter. Considering an infinitesimal change of the involved parameters, the ICM consists of a Jacobian matrix as follow:

$$ICM = J = \begin{bmatrix} \frac{\partial Y_1}{\partial X_1} & \dots & \frac{\partial Y_1}{\partial X_N} \\ \vdots & \ddots & \vdots \\ \frac{\partial Y_M}{\partial X_1} & \dots & \frac{\partial Y_M}{\partial X_N} \end{bmatrix} \quad (4.8)$$

The representation of this method is shown in Figure 103.

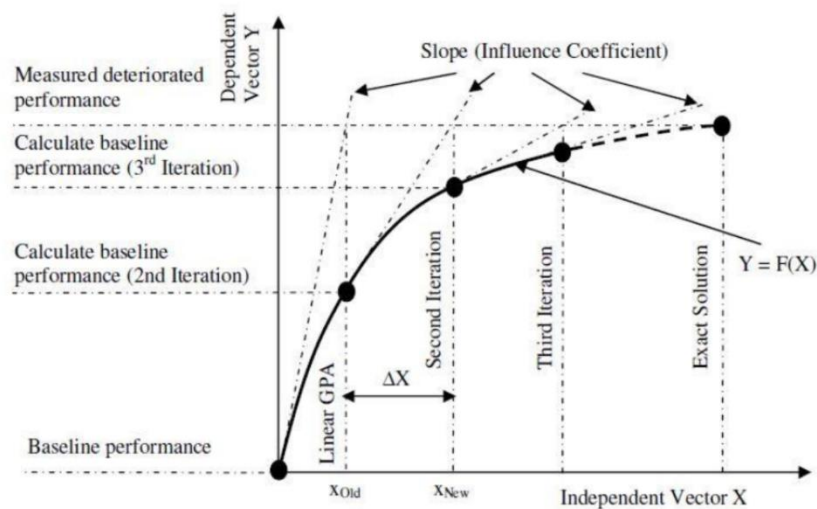


Figure 103: Non-Linear Gas Path representation [209].

The solution is evaluated considering the difference between the predicted and actual independent parameters obtained, varying the terms of the ICM and inverting the matrix to get the correspondent FCM. It is then applied to the deteriorated independent parameters (predicted values) to find the dependent parameters from which a new ICM is derived. Consequently, the new FCM is calculated until the solution converges. To consider possible variations of the exploited dataset, the iterations could be terminated by evaluating the RMS of the delta value between two consecutive steps.

Even though the NLGPA have been widely used in the aeronautical field, the capability to reach a final result with a high level of accuracy, as well as the possibility to deal with multiple faults of both the component under investigation and the associated diagnostics, is affected by the uncertainties related to sensors noise.

In order to handle these uncertainties, a possible model-based approach to the GPA is represented by the adoption of a Kalman Filter. Introduced by Rudolf Kalman in 1960 [210], this method foresaw a predictor-corrector two-step approach. The state vector at the first step determines the state vector at consecutive step through a weighted average approach between them.

- **Artificial Neural Network (ANN)**

An empirical method classified in the AI-based category is the approach to the GPA through Artificial Neural Network (ANN). This method has been widely used in different fields for its intrinsic capability to emulate a biological neural network capable of recognising a determined pattern in datasets when trained with a set of known input data. The ANN method is characterized by a high computational

speed, which is fundamental for some GPA applications. The capability to generalize the recognized pattern is another crucial characteristic of ANNs.

This allows the train of the implemented network to have a set of known output and a small number of input data. If a different input pattern is given in the input, the algorithm can interpret and correlate different patterns to optimise the correctness of the provided outputs.

The method capability is limited by the need of training complex ANNs necessary for a realistic representation of the behaviour of the component under study. This programming phase is also characterized by the quality of the known input pattern used. Consequently, the tolerance that characterized the input set is then directly linked with the goodness of the estimated results obtained by the algorithm. In order to deal with these criticalities, different approaches have been used, also based on an optimized input dataset.

- **Bayesian Belief Network (BBN)**

Another possibility to understand the relationship between dependent and independent parameters is adopting the Bayesian Belief Network (BBN) approach. Included in the category of AI-based method, this method consists of a graphical representation through which the causes are linked with the final effects, identifying the cause factors as well as possible faults and symptoms [211]. The probabilistic dependencies among these factors are represented by graphs in which the nodes are the involved variables (both dependent and independent), and the arc connecting them are the probabilistic dependencies. The nodes can contain specific states of the system (component) under analysis, possible faults and additional parameters obtained from external observers.

The probabilistic relations between the nodes are mathematically expressed as:

$$P(x/y) = \frac{P(y/x)P(x)}{P(y)} \quad (4.9)$$

where $P(x/y)$ is the probability of x with input y , while $P(y/x)$ is the probability of y with input x . The terms $P(x)$ and $P(y)$ are respectively the probability related to the independent and dependent parameters.

The BBN adoption has several benefits. This method allows the merging of different types of data, both qualitative and quantitative. Single and specific faults can be detected and isolated in their effects on the other parameters. This method implemented without the need of specializing the detection process to a single fault case, but it allows to observe multiple fault causes. However, the implementation of a BBN is not trivial. Good knowledge of the system under analysis is necessary to build the network. Moreover, the overall management could be complex, and network maintenance requires some practice and time.

Considering the advantages offered by this method, it has been largely used in the aeronautic field for the diagnostic of gas turbines [212–216]

- **Expert Systems**

An expert system is a software-based tool aimed to either solve or advise possible fault solutions about a certain problem by collecting human knowledge that is translated and structured into relationship rules. The so-called "Expert System shell" is the core of this method. It consists of two segments: the Inference Engine (IE) and the Knowledge base module. The end-user interacts with the method through an interface to the inference engine introduced to translate user input to input exploited by the knowledge base module to find the correct solution or to provide advice.

This method is usually adopted when the diagnostic problem can be well understood and extended human expert knowledge is available. It has a relatively low-demanding implementation and easy operability through the user interface. Moreover, expert logic is usually set up considering multiple knowledge-based contributions from the experts. With this approach, possible individual errors are eliminated. The main drawbacks are represented by uncertainties in the input/output data and a potential lack in the completeness of the knowledge base module.

- **Fuzzy-logic methods**

The Fuzzy-logic method is another method introduced to represent the human attitude to deal with uncertainty reasoning. It relies on the development of a non-linear mapping from the input value vector with the output vector. The scheme of a fuzzy method is usually based on four main blocks: (i) a block where fuzzy IF-THEN rules are defined, (ii) a fuzzifier, where the input values are processed into a fuzzy set characterized by linguistic variables and membership functions, (iii) an inference engine, exploited to establish the relationship among the fuzzy sets and (iv) a de-fuzzifier that allows the formalization of the outputs. Also, this method has been widely used in the aeronautic field, as detailed in [217–221].

4.4 EHM application process

As already mentioned in Section 4.1, the EHM applied to Hall thrusters has been developed following two parallel approaches. First, a phenomenological performance model has been derived for identifying the functional correlations between the variables involved in the operation of the thruster. From this model, it was thus possible to derive a theoretical ICM. The second approach instead relied on experimental data, from which the terms of the ICM were directly derived through a numerical procedure. Specifically, in this phase, we calibrated the ICM over the real thruster operating envelope. We then exploited the result for the diagnostic process through the calculation of the FCM.

The first model-based approach has been introduced to support the definition of both the dependent and the independent variables. As previously introduced, performance parameters or parameters considered representative of the thruster health status can be identified as dependent variables. The independent variables are usually the available thruster measurements, which can be directly derived from the adopted diagnostics or indirect methods when the diagnostic is either unavailable or not present. Under those circumstances, the determination of the dependent parameter set cannot be considered as a univocal process.

Once the sets of dependent and independent variables are established, the selected model shall include an adequate number of equations that allow describing the thruster behaviour in its operational range. When this is guaranteed, additional parameters of interest can be derived, including supplementary relations.

The classical mathematical formulation of the performance system is presented as follow:

$$z_i = P_i(x_j) = 0. \quad (4.10)$$

The introduced linear assumption can be considered valid if the changes of the involved variable are relatively small. Any variation which exceeds the linear trend might introduce a significant error that, depending on the utilization of the model, could be either corrected with a specific procedure or detected and interpreted as a possible failure. Considering a thruster operative point identified as a reference point, the equation of the performance system can be linearized around this point using a common linearization technique.

At this point, through the linearization approach considered in this work, the delta of a generic parameter p can be expressed in terms of relative changes between the value p_k of the k experimental points and the value of the selected baseline point as follows:

$$dP = \frac{\Delta p}{p_{ref}} = \frac{p_k - p_{baseline}}{p_{baseline}}. \quad \forall k \in 1, \dots, (s - 1) \quad (4.11)$$

Hence, the system can be expressed as (recalling Eq.4.2):

$$\Delta Z = [ICM]\Delta X \quad (4.12)$$

Calling " a_{ij} " the coefficient of the ICM relating the " i " dependent variable ΔZ ($i \in [1, \dots, m]$) and the " j " independent variable ΔX ($j \in [1, \dots, n]$), the ICM can be directly derived through the linearization of the performance model, and the coefficients are derived as follow:

$$a_{ij} = \frac{\partial P_i}{\partial X_j}. \quad (4.13)$$

Therefore, the ICM is represented by the Jacobian of the system:

$$[a_{ij}] = \begin{bmatrix} a_{11} & \cdots & a_{1j} \\ \vdots & \ddots & \vdots \\ a_{i1} & \cdots & a_{ij} \end{bmatrix} = \begin{bmatrix} \frac{\partial P_1(X)}{\partial x_1} & \cdots & \frac{\partial P_1(X)}{\partial x_n} \\ \vdots & \ddots & \vdots \\ \frac{\partial P_m(X)}{\partial x_1} & \cdots & \frac{\partial P_m(X)}{\partial x_n} \end{bmatrix} \quad (4.14)$$

As previously introduced, the second approach performs the derivation of the ICM through the processing of experimental data. The advantages of this procedure are mainly related to the performance model's incapability to fully describe the real operative behaviour of an HT. Both model approximations (or assumptions) and all secondary effects are taken into account without the needs of introducing complex relations between the independent and dependent parameters. Nevertheless, the variables considered in these two vectors shall be carefully evaluated to guarantee the representativeness of the system.

Once the variables are correctly identified, the empirical correspondence between deviations of measured variables and deviations of the performance variables is exploited to derive the ICM. Both deviations are calculated with respect to a reference point selected among the available experimental set, which is considered as a baseline for the proper operation of the thruster.

Considering a set of experimental data composed of many operative points equal to " s ", the vector of performance parameters (independent) can be expressed as:

$$\Delta X_i = [dX_{i1}, dX_{i2}, \dots, dX_{is}], \quad \text{with } i = 1, 2, \dots, m \quad (4.15)$$

while the vector of the measured parameters (dependent) is:

$$\Delta Z_j = [dZ_{1j}, dZ_{2j}, \dots, dZ_{sj}]. \quad \text{with } j = 1, 2, \dots, n \quad (4.16)$$

Hence, considering Eq. (4.15) and Eq. (4.16), the system in Eq. (4.12) can be further elaborated:

$$(4.17)$$

$$\begin{bmatrix} dZ_{1k} \\ \vdots \\ dZ_{nk} \end{bmatrix} - \begin{bmatrix} a_{11} & \cdots & a_{1m} \\ \vdots & \ddots & \vdots \\ a_{n1} & \cdots & a_{nm} \end{bmatrix} \begin{bmatrix} dX_{1k} \\ \vdots \\ dX_{mk} \end{bmatrix} = 0, \quad \forall k \in 1, \dots, s-1$$

In particular, the j^{th} row of the matrix can be expressed as

$$\begin{aligned} [dZ_{j1} \cdots dZ_{j(s-1)}] - [a_{j1} \cdots a_{jm}] \underbrace{\begin{bmatrix} dX_{11} & \cdots & dX_{1(s-1)} \\ \vdots & \ddots & \vdots \\ dX_{m1} & \cdots & dX_{m(s-1)} \end{bmatrix}}_{dX_{ik}} & \quad (4.18) \\ = 0, \quad \forall k \in 1, \dots, s-1 & \end{aligned}$$

where dZ and dX are the discrete delta column vector of the operative point selected as the baseline. The capability to solve the system in Eq. (4.18) depends on the possibility to invert the dX_{ik} matrix. If the number of experimental points is equal to the number of independent variables, the matrix is square ($m=s-1$), and the capability to derive the inverse matrix is determined by having a not null determinant. On the contrary, if the number of variables is different ($m \neq s-1$), specific methods shall be implemented in order to derive the so-called generalized inverse. One of the common methods is to use the Moore-Penrose inverse for which, for a given matrix A , its generalize inverse shall satisfy [208]:

$$AA^\dagger = (AA^\dagger)^T \quad A^\dagger A = (A^\dagger A)^T \quad AA^\dagger A = A \quad A^\dagger AA^\dagger = A^\dagger \quad (4.19)$$

Hence to find the j^{th} row of the ICM matrix, the system in Eq. (4.18), can be expressed as:

$$\begin{bmatrix} a_{j1} \\ \vdots \\ a_{jm} \end{bmatrix} = \begin{bmatrix} dX_{11} & \cdots & dX_{m1} \\ \vdots & \ddots & \vdots \\ dX_{1(s-1)} & \cdots & dX_{m(s-1)} \end{bmatrix}^\dagger \begin{bmatrix} dZ_{j1} \\ \vdots \\ dZ_{j(s-1)} \end{bmatrix}, \quad \forall j \in 1, \dots, n \quad (4.20)$$

If this procedure is repeated, taking at each iteration a different reference point, a number of ICM matrices equal to s is derived. Considering the non-linear behaviour of the thruster, the ICM coefficient has been averaged, adopting a weighted averaging process. As a consequence, each term of the k^{th} ICM contributes to the average with a weight proportional to the relative deltas between the reference point, the matrix built, and the other k points of the experimental data set. This process results in:

$$\overline{[ICM_{i,j}]} = \frac{1}{s} \sum_{k=1}^s \lambda_k [ICM_{i,j}]_k \quad \forall i, j \quad (4.21)$$

with:

$$\lambda_k = \frac{1}{dp_k} \quad (4.22)$$

Finally, recalling Eq. (4.1), the FCM is directly derived inverting the ICM:

$$\begin{aligned} \Delta Z = [ICM](\Delta X) &\rightarrow \Delta X = [ICM]^{-1}(\Delta Z) \\ &\rightarrow \Delta X = [FCM](\Delta Z) \end{aligned} \quad (4.23)$$

4.5 HT Performance Model

In this section, the performance model exploited in this study is presented. As previously introduced, the identification of the parameters considered representative for the health status of the thruster under analysis is fundamental to derive the system equations. As will be detailed in the following section, the selection process of both dependent and independent parameters has been performed considering the available laboratory measurements.

In Table 56 and Table 57, the selected independent and dependent variable lists are reported.

Table 56: Independent variable list.

Index j	Symbol ΔX_i	Quantity
1	V_d	Discharge voltage
2	$AMFR$	Anode Mass Flow Rate
3	$KMFR$	Cathode Mass Flow Rate
4	B	Magnetic Field Peak

Table 57: Dependent variable list

Index i	Symbol ΔZ_i	Quantity
1	T	Thrust
2	I_d	Discharge current
3	$\frac{\tilde{I}_d}{\bar{I}_d}$	RMS ratio
4	$I_{M i}$	Magnetic coil current
5	V_{CRP}	Cathode Reference Potential

Therefore, the introduced phenomenological model has been derived as a function of the independent parameter reported in the ΔX vector. In addition, the process introduced in Section 5.4 allows avoiding complex model formulation. The main

assumption made for the derivation of the model is to consider singly-charged ion, as presented in [222].

Based on both physical and empirical relations, several performance models of Hall thrusters have been developed in the past years, considering either partially or fully ionized propellant, including the effects of multiply-charged ions[223–230].

Discharge current, discharge current and thrust

The discharge current is considered in Hall Thrusters as the sum of the ion beam current coming from the discharge and the electron current coming from the cathode. The latter is responsible for the propellant ionization. Assuming that each electron-neutral collision generates an ion with the associated electron, the discharge current can therefore be expressed as:

$$I_d = I_b + I_e. \quad (4.24)$$

The current utilization efficiency is defined as the ratio between the beam current and the discharge current. This efficiency allows determining how efficiently the electrons coming from the cathode are used to generate ions from the neutral propellant.

$$\eta_b = \frac{I_b}{I_d} \quad (4.25)$$

while the electron current fraction is expressed as:

$$\varepsilon = \frac{I_e}{I_d} \quad (4.26)$$

Hence:

$$\eta_b = 1 - \varepsilon \quad (4.27)$$

The beam acceleration voltage V_b , which is the voltage at which the ions are accelerated, is related to the discharge voltage, imposed by the power supply, and loss voltages (V_L):

$$V_d = V_b - V_L \quad (4.28)$$

Hence, the voltage utilization is defined as the fraction of the discharge voltage that is used to accelerate the propellant [231]:

$$\eta_v = \frac{V_b}{V_d} = 1 - \frac{V_L}{V_d} \quad (4.29)$$

The so-called "Energy efficiency", η_v takes into account different factors for the definition of the involved voltage losses. First, the ionization of the propellant

occurs in other axial locations of the discharge chamber. Therefore, the effective acceleration potential can be lower than the imposed discharge potential at the anode, resulting in a differential acceleration of the ions, which will have different ejection velocity.

The second class of factors included in the definition of the voltage efficiency concerns the loss of voltage due to: cost of ion generation, wall losses, ion charge state and beam divergence [222]. Last, the plasma potential downstream to the thruster exit is not equal to the cathode potential because of the cathode coupling voltage. If we consider the ground testing configuration, the plasma in the thruster beam reaches a positive potential with respect to the reference facility ground. The cathode instead adjusts its potential with respect to ground depending on the specific grounding scheme that is adopted. When the cathode is insulated with respect to ground (or when it is connected through a resistance sufficiently high), the cathode reference potential (CRP) is typically negative.

$$V_{CRP} = |V_{CG}| + V_p \quad (4.30)$$

In Figure 104, a schematic of the potential distribution along the discharge chamber of a Hall thruster is shown. A typical V_{CRP} value during thruster operation is between -10V and -20V [222,231].

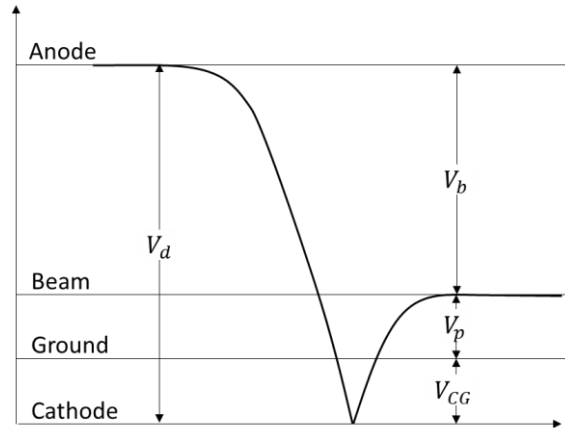


Figure 104: representative schematic of the voltage distribution in a Hall thruster discharge chamber.

The voltage efficiency can be defined for the single ionized particles contributions as [227,230,232,233]:

$$\eta_v = \alpha - c_i \phi_i \eta_i \left(\frac{1}{V_d} \right) \quad (4.31)$$

The term α is proportional to both wall and anode losses while the terms c_i and ϕ_i are the ionization potential in eV (for xenon equal to 12.13 eV) and ionization cost accounting for the excitation collisions, respectively.

As mentioned before, the ions are electrostatically accelerated along with the discharge chamber at a velocity depending on the local beam potential.

As a consequence, the average ion velocity is:

$$\bar{v}_{ej} = \sqrt{\frac{2q}{M_i} \bar{V}_b} \quad (4.32)$$

where q is the ion charge and M_i is the ion mass.

The ion flow rate that is accelerated through the potential drop represents a fraction of the propellant elaborated in the thruster. The total propellant fed is defined as the sum of the propellant injected from the anode (\dot{m}_a) and from the cathode (\dot{m}_c). Considering low values of the cathode flow fraction ($CFF = \dot{m}_c/\dot{m}_a$), the mass utilization efficiency can be defined as:

$$\eta_m = \frac{\dot{m}_b}{\dot{m}_p} \approx \frac{\dot{m}_b}{\dot{m}_a}. \quad (4.33)$$

The ion mass flow rate can be expressed as the beam current multiplied by the charge-to-mass ratio of the ions:

$$\dot{m}_b = \eta_m \dot{m}_a = \frac{M_i}{q} I_b \quad (4.34)$$

Neglecting the presence of multi-charged ions, for which specific corrective factors shall be added, the thrust generated can be related to the ion mass flow rate (\dot{m}_i) and its ejection speed (v_{ej}):

$$T = \dot{m}_i \bar{v}_{ej} \quad (4.35)$$

Finally, merging Eq. (4.20), (4.26) and (4.27), the thrust equation (4.30) becomes:

$$T = \eta_b I_a \sqrt{\frac{2M_i}{q}} \sqrt{\eta_v V_d} \quad (4.36)$$

Eq. (4.36) is valid for singly charged ions, and it shows a dependency on the discharge voltage, discharge current (i.e., mass flow rate) and the magnetic field peak.

Magnetic field peak vs magnet current

The magnetic field imposed in the discharge chamber has a fundamental role in determining the thruster performance. The magnetic field is generated through a magnetic circuit usually consisting of coil winding wrapped around a ferromagnetic core. Permanent magnets might also be used. The design of this circuit allows confining the magnetic flux and provides a specific shape to the topology of the field itself. The magnetic peak is usually located near the discharge channel exit,

while the magnetic field intensity tends to zero toward the anode. The ionization zone is usually identified in the region upstream of the magnetic field peak where a higher electron temperature is reached and consequently, the ionization events (i.e., ionization rate) are more probable. The blocking effect of the magnetic field on the electron motion toward the anode, caused by the azimuthal $E \times B$ drift of the electrons, shapes the axial electric field generated between the anode and the cathode and allows the establishment of a potential gradient through which the ions are then accelerated.

The complex design of a thruster magnetic circuit can be simplified, as shown in Figure 105.

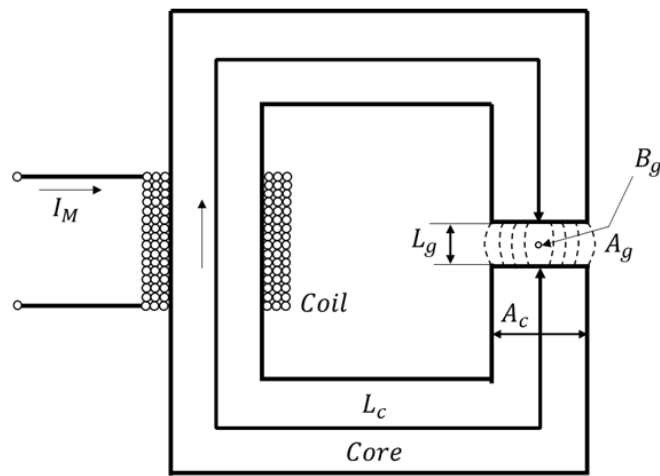


Figure 105: schematic of a simplified Hall thruster magnetic circuit [222].

The main features of the circuit are the following:

- A magnetic flux Φ_m is generated by a current I_M provided to a coil consisting of a certain number of turns (N_c).
- The ferromagnetic core has a mean length of L_c and cross-section area equal to A_c which is considered constant. The related permeability is assumed constant μ_c .
- The vacuum gap in which the magnetic flux is driven has a distance equal to L_g and a cross-sectional area of A_g .

Considering the magnetic flux constant also in the magnetic gap (i.e. neglecting any flux leaks), according to Hofer [222], the relation between the magnetic peak in the gap and the current fed into the coil can be expressed as

$$I_M = k_m B_g \quad (4.37)$$

with

$$(4.38)$$

$$k_m = \frac{(L_g + \frac{A_g \mu_0}{A_c \mu_c} L_c)}{\mu_0 N_c},$$

where μ_0 is the magnetic vacuum permeability.

The design of the magnetic circuit and the current fed into the coils determine the maximum values of magnetic field intensity along the discharge channel before the occurrence of any magnetic saturation in the circuit.

The magnetic circuit of a Hall thruster is more complex with respect to the simplified model (so-called “C-core”) shown in Figure 105. In the past years, several research works were published in which different magnetic models have been proposed to maximize the thruster performance through proper optimization of the magnetic topology.

Discharge current RMS

One of the crucial parameters for the evaluation of the thruster performance is the discharge current I_d .

The Hall thrusters are usually fed with electric power provided by external power supplies at fixed discharge voltage in the so-called “voltage regulated” mode.

The discharge itself then determines the discharge current and it mainly depends on propellant flowrate fed into the discharge chamber through the anode and the magnetic field generated by the magnetic circuit.

To investigate the time evolution of the discharge current profile, it is typically recorded with a pre-defined time step. The discharge current can be written as:

$$I_d(t) = \bar{I}_d + I_{dAC}(t) \quad (4.39)$$

where \bar{I}_d is the mean discharge current:

$$\bar{I}_d = \langle I_d(t) \rangle \quad (4.40)$$

The identification of the discharge current is derived considering the root mean square (RMS) of the AC component of the current historical data. This parameter reflects the oscillatory behaviour of the thruster. Therefore, low RMS values are preferred to guarantee the stability of the plasma discharge. It can be expressed as:

$$\tilde{I}_d(t) = \sqrt{\langle I_d(t) - \bar{I}_d \rangle^2} = \sqrt{\langle I_{dAC}(t) \rangle^2} \quad (4.41)$$

According to Sekerak et al. [234], the amplitude of the discharge current is evaluated through the ratio between the rms of the current data and the current average value (i.e. $\tilde{I}_d(t)/\bar{I}_d$). This latter ratio, along with the mean current and the current oscillation, are used to characterize the transition between the different

oscillation behaviours of the plasma [235,236]. It is influenced by different parameters, some related to the combination of operative thruster parameters, such as discharge voltage, propellant mass, CFF and magnetic field topology, some concerning the design of the thruster (e.g. channel walls properties and geometry, cathode location) and the testing condition (e.g. surrounding neutral environment) [237].

Even though this work is not specifically focused on the investigation of the different thruster operating mode, relations that link the dependent parameter to the evolution of the current based parameters could be used.

As reported by Sekerak [234], the mode transition can be related to operating parameters as:

$$B_g^* = C V_d^{*\beta} \dot{m}_a^{*\gamma} \quad (4.42)$$

wherewith “*” identifies the ratio between the current parameter value and the selected reference value, C is a linear constant and β and γ are the exponential coefficient. In his work, Sekerak exploited an inverse process based on a Moore-Penrose pseudoinverse matrix to determine the coefficient values from experimental data. In particular, for lower transition (i.e., between global and local oscillation modes), the following set has been estimated on a dataset provided through a specific test campaign performed on the H6 thruster:

$$[C, \beta, \gamma] = [0.593, 0.4, 0.5] \quad (4.43)$$

According to different authors [237], the discharge current can be related to the magnetic field with an exponential relation for which, considering Eq (4.43) and (4.43), $\tilde{I}_d(t)/\bar{I}_d$ can be expressed as:

$$I_d \propto B_g^\alpha \quad \Rightarrow \quad \tilde{I}_d(t)/\bar{I}_d = C V_d^\beta \dot{m}_a^\gamma B_g^\alpha \quad (4.44)$$

where α is the exponential coefficient that gives the dependence of the discharge current on the magnetic field, this coefficient can vary depending on the operative mode of the thruster. While in the global oscillation region, Sekerak reports a value of $\alpha=-2$, the relation became nearly linear in the local region.

The system has been linearised following the procedure detailed in Section 5.4. The logarithmic normalization has been exploited in which the derivative of the logarithms of both terms are taken according to Eq. (4.13), as reported in Table 58:

Table 58: ICM coefficient derivation.

#	Performance equations	Normalized relations
1	$T = \eta_b I_d \sqrt{\frac{2M_i}{q}} \sqrt{\eta_v V_d}$	$\delta T = \frac{1}{2} \delta V_d + \delta \dot{m}_a$
3	$\dot{m}_b = \eta_m \dot{m}_a = \frac{M_i}{q} \eta_b I_d$	$\delta I_b = \delta \dot{m}_a$
4	$\Rightarrow \quad \tilde{I}_d(t)/\bar{I}_d = C V_d^\beta \dot{m}_a^\gamma B_g^\alpha$	$\delta \left(\frac{\tilde{I}_d(t)}{\bar{I}_d} \right) = \beta \delta V_d + \gamma \delta \dot{m}_a + \alpha \delta B_g$
5	$I_M = k_m B_g$	$\delta I_M = \delta B_g$
6	$V_{CRP} = K_{CRP} \dot{m}_c$	$\delta V_{CRP} = \delta \dot{m}_c$

Consequently, the derived model-based ICM is the following:

	V_d	\dot{m}_a	\dot{m}_c	B_g
T	1/2	1	0	0
I_d	0	1	0	0
$\tilde{I}_d(t)/\bar{I}_d$	β	γ	0	α
I_M	0	0	0	1
V_{CRP}	0	0	1	0

(4.45)

Considering the value of α , β and γ defined by Sekerak [234], the ICM became:

$$ICM = \begin{bmatrix} 0.5 & 1 & 0 & 0 \\ 0 & 1 & 0 & 0 \\ 0.4 & 0.5 & 0 & 1 \\ 0 & 0 & 0 & 1 \\ 0 & 0 & 1 & 0 \end{bmatrix} \quad (4.46)$$

This matrix has been compared with the ICM derived from the experimental data following the procedure reported in Section 4.4.

4.6 Overview of the experimental apparatus

During the entire development of the HT20k (detailed in Section 4.7), experimental activities have been performed in SITAEL's facilities in Ospedaletto (Pisa-IT). In this section, a general overview of the vacuum facilities and the diagnostic apparatuses used during the tests of the HT20k DM2-S are reported.

4.6.1. IV10 Vacuum facility

All test campaigns of the HT20k DM2-S were conducted in the IV10 Vacuum facility at the Ospedaletto plant of SITAEL. IV10 is the largest vacuum chamber currently available in Europe for electric propulsion system testing. Figure 106 shows the rendering and pictures of IV10.



Figure 106: (Top picture) IV10 vacuum facility rendering; (Bottom-Left) IV10 laboratory and (Bottom-Right) movable cap equipped with conical Grafoil targets (credits: SITAEL).

The main characteristics of the IV10 vacuum facility are reported in Table 59.

Table 59: main technical characteristics of IV10 vacuum facility.

Characteristic	Value
Inner diameter	5740 mm
Inner free diameter	5400 mm
Length of the cylindrical section	6000 mm
Vacuum vessel length	9400 mm
Internal free volume	$> 160 \text{ m}^3$
Total leak rate	$< 10^{-5} \text{ Pa} \cdot \text{m}^3 \cdot \text{s}^{-1}$
Pump downtime	48 hours

The stainless-steel vacuum vessel allows an internal volume of over 160 m^3 . The initial design of the chamber relied on five cryo-panels and cold heads in order to pump out the propellant processed by the thruster. In 2019, their number was increased to eight (with the related Xe pumping copper panels, copper extension and Helium compressors), allowing an extended testing capability of up to 1,500,000 l/s on xenon. This upgrade targeted a pressure level below $3\text{e-}5$ mbar suitable for thruster operations up to 50 mg/s. As a consequent result, with the lower background pressure, longer continuous firing periods before forced maintenance activities are enabled. The 500 hours estimated for continuous operation of the HT20k outperform the firing period usually required during a characterization campaign, qualifying the IV10 vacuum chamber for testing activities with more powerful thrusters (higher mass flow rate elaborate by the thruster). The chamber flexibility was further extended with the installation of an Auxiliary Chamber (AC), which allows maintaining the vacuum pressure level in the main chamber while providing easy accessibility to the thruster. On the contrary, when the main vacuum chamber shall undergo maintenance operations, the AC can be used to maintain the thruster in a vacuum condition.

The AC was also designed to implement a motorized trolley mechanism to facilitate the handling of the thruster further.

4.6.2 Laboratory power supply

The power feeding and the control of the thruster were ensured by laboratory power suppliers. In specific, the following list of equipment was used during the HT20k DM2-S testing:

- 1 laboratory PSU to provide power to the thruster discharge.
- 1 laboratory PSU to provide power to the cathode heater.
- 1 laboratory PSU to provide power to the cathode keeper.
- 1 laboratory PSU to provide power to the inner electromagnet.
- 1 laboratory PSU to provide power to the outer electromagnet.

- 1 laboratory PSU to provide power to the auxiliary electromagnet.

The discharge line is also equipped with a filter unit to avoid dangerous oscillations on the PSU. A detailed schematic of the power supply used during all test campaigns is shown in [238].

4.6.3 Xenon Feeding System

A laboratory gas feeding system will provide xenon propellant (99.998% purity or better) to the HC60 cathode and the HT20k mock-up thruster.

The system is composed of a high-pressure feed line, coming from the Xe bottle to the primary pressure regulator stage, and of two low-pressure gas panels dedicated to the anode and the cathode feeding lines. Each panel is equipped with a secondary pressure regulator, a pneumatic shut-off valve, a mass flow controller, and a bypass line.

The specifications of the employed mass flow controllers are provided in Table 60, while the schematic of the system is shown in Figure 107

Table 60: Main characteristics of the Xenon feeding system.

Characteristics	Thruster Xe MFC	Cathode Xe FMC
Model	F-201CV-500-AAD-88V	F-201C-FAC 88-V
Xe MFR	0-800 s.l.m.	0-1000 s.l.m.
Accuracy	$\pm 0.5\%$ RD $\pm 0.1\%$ fs	$\pm 0.5\%$ RD $\pm 0.1\%$ fs
Inlet pressure	3.5 bar	3.5 bar
Leakage rate	1e-9 mbar/l.s GHe	1e-9 mbar/l.s GHe

The IV10 Xe feed system used during the test is shown in Figure 107.

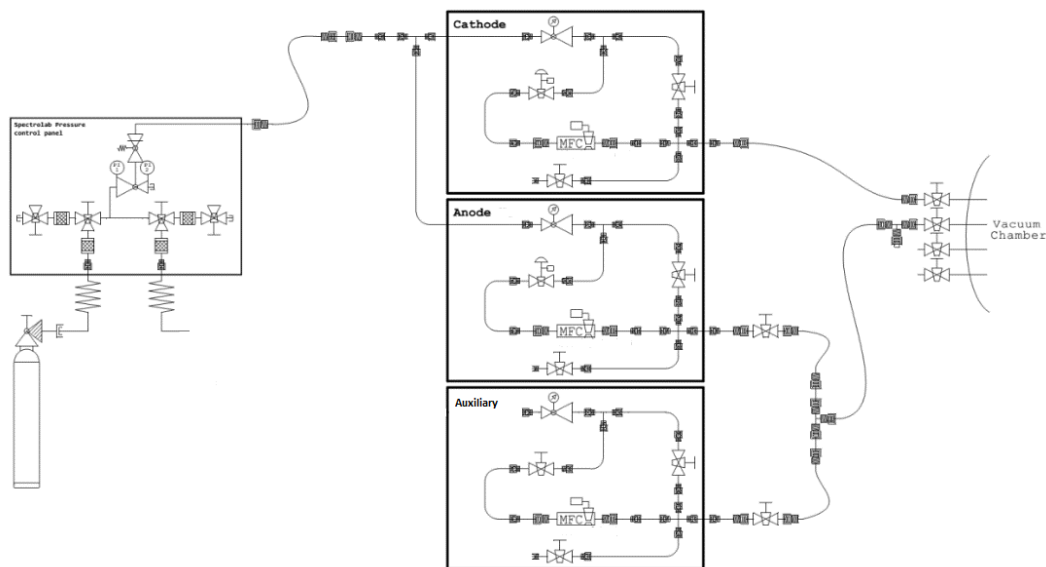


Figure 107: Schematic of the IV10 propellant feeding system.

4.6.4 Diagnostics

- **Thrust Balance**

For the thrust measurement, a single axis thrust balance having a double pendulum configuration is used. This configuration allows sustaining the thruster weight, ensuring a degree of freedom along the firing direction on which the thrust is measured. The detection of the thrust is enabled by high-precision load cells through which the strain on flexural elements is sensed. Before its operation, the thrust stand shall be calibrated to match the required accuracy. This phase considers different steps. An actuated tilting platform on which the thrust stand is mounted guarantees a proper level of the entire stand. The temperature is controlled by a high-accuracy thermoregulation system (in the order of 2 ‰) [238]. Furthermore, in order to provide a reference strain to be used during the calibration phase, an electromagnetic calibrator is used. The main specifications of the thrust balance are reported in Table 61.

Table 61: Thrust balance specifications.

Characteristic	Value
Maximum thruster weight allowable	75 kg
Thruster interface diameter	460 mm (max)
Max sensed thrust	3 N
Min sensed thrust	30 mN
Resolution	2 mN
F.s. accuracy	1%

- **Oscilloscope**

During all HT20k development test campaigns, the discharge current transient and steady-state signals were acquired employing a laboratory oscilloscope. Some specifications of the employed oscilloscope (Tektronics DPO 4104) are provided in Table 62.

Table 62: main characteristics of the employed oscilloscope.

Characteristic	Value
Analog channel	4
Bandwidth	1 GHz
Rise Time	350 ps
Sample rate	5 GS/s
Record length	20 Mbyte
Duration of the highest sample rate	2ms

4.7 HT20k Test points

In this section, the experimental test points exploited for the derivation of the EHM are reported. These points are related to two different test campaigns performed on the second HT20k development model (i.e., the HT20k DM2). After the successful conclusion of the experimental activities on the former HT20k model, the DM1, in June 2017 under an ESA/TRP development programme, the research on this thruster power-class continued with the design and development of a second demonstration model in the framework of three different programmes: the EU's H2020 Consortium for Hall Effect Orbital Propulsion System (CHEOPS), an ESA funded GSTP project and an ESA pre-development programme.

The complementarity of these programmes allows the investigation of alternative technological and design solutions as well as the assessment of the cross-effects that the adoption of such a high-power thruster might have at both system and mission level. In particular, these programmes targeted thruster performance optimization, the increasing of thruster reliability during an extended operative lifetime, and a robust mechanical and thermal design.

In the ESA pre-development programme framework, the main modifications to the design of the HT20k DM2 were also implemented thanks to the fruitful parallel development activities performed on the lower power-class thruster, the HT5k LL (Long Life). The re-design of the thruster targeted a maximum thrust level of 1.3 N with over 60% of efficiency and with a total impulse reachable of 100MN and an operative thruster voltage range from 220V up to 440V.

The main characteristics introduced in the new model was the magnetically shielded configuration. Moreover, a flexible magnetic circuit allowed testing different chamber geometries. This design solution allowed to determine the variation of the performance of a magnetically shielded thruster and to improve the thruster scaling model for the following development phases.

The alternative geometric configurations consisted of three variations of the ceramic channel width, simply called Small (S), Medium (M) and Large (L). Minor

modifications were also implemented on the magnetic pole to guarantee a similar magnetic field topology.

During the last months of 2018, each configuration of the DM2 was tested to evaluate their stability domain and characterize the thruster performance, taking into account the effect of the magnetic shielding. The DM2 presented a configuration with the cathode integrated in the central position. The mass flow rate of the cathode was maintained around an average value of 7% of the anode mass flow rate. Fixed values of the anode mass flow rate were maintained throughout the entire characterization campaign, while the discharge voltage was varied from 250V up to 500V.

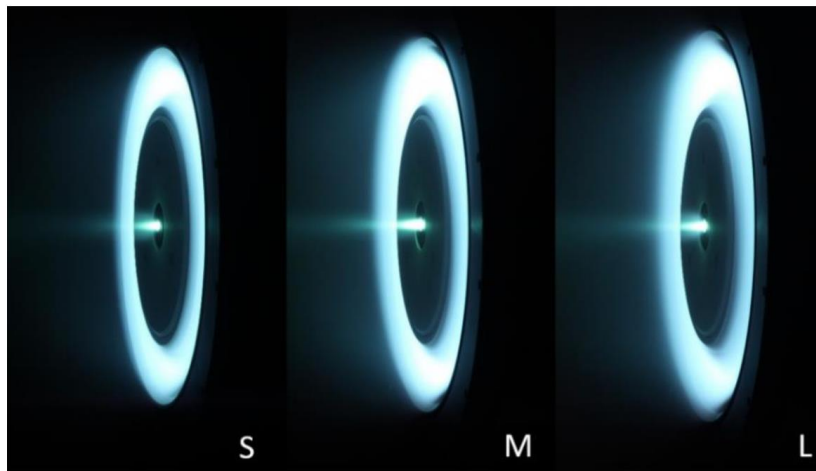


Figure 108: the three HT20k DM2 configurations (S,M and L) operated at 25mg/s @300V [43] .

A second experimental campaign was instead performed with the three configurations to find the optimal magnetic field configuration.

The magnetic field peak value was varied between 65% and 150% of the design value B_0 for the operative point reported in the characterization matrix (Table 63). These points were repeated for each DM2 configuration.

Table 63: HT20k DM2 characterization matrix.

\dot{m}_a	250 V	300	375	400	500
20 mg/s		X	X		
25 mg/s	X	X	X	X	X
30 mg/s	X	X	X	X	X
35 mg/s	X	X	X	X	X
40 mg/s		X		X	

After the conclusion of the HT20k DM2 test campaign, SITAEL started the design of an Engineering Model (EM) of the thruster. This new model benefitted from the outcome of the previous development phases. Minor modifications were also implemented to minimize the possible risks associated with thermal and structural

loads as well as to further reduce the erosion of critical components, such as the poles' covers.

With the end of the integration phase, which took place during the first quarter of 2019, the HT20k EM was tested in a first characterization campaign in SITAEL's IV10 Vacuum facility, after the facility upgrade implemented at the beginning of 2019. As reported in Section 4.6.1, these upgrades consisted of the improvement of the reachable vacuum condition and in the setup of the auxiliary chamber. However, the initial tests were performed with comparable condition with respect to the test performed before the chamber upgrades, i.e. operating only five cold panels. However, since the first points tested, the performance obtained did not reach those expected. Reductions from 5% up to 10% were obtained on thrust and discharge current with respects to the same operative point at 300V tested with the HT20k-M configuration. Due to the upgrades implemented to the vacuum chamber a few months before, a first possible explanation was identified in an accidental failure of the propellant and power feeding systems or of the adopted diagnostic equipment. As a consequence, before proceeding with an expensive and complex troubleshooting procedure directly on the thruster, the first solution was the exploitation of a well-known thruster already tested to provide a comparable set of data. Thus, this first attempt's objective was to identify a possible failure cause related to the chamber equipment, comparing this newly collected data with the previous data obtained in "normal" condition.

In order to reduce the time necessary to perform this investigation, the HT20k DM2 S was used, since it was the last thruster tested during the previous development activities.

Due to these time restrictions, due to the busy IV10 utilization schedule, only a few operative points were characterized. In specific the thruster was operated according to the points reported the Table 64, for which the magnetic peak value was varied with a factor of 1.25, 1.35 and 1.5 of the reference design value B_0 . Moreover, for those points exploited in this study, the IV10 background pressure was maintained in the order of $6.5 \cdot 10^{-5} \text{ mbar } (N_2)$, operating the facility with only five cold plates.

Table 64: HT20k DM2 characterization matrix used during failure investigation.

\dot{m}_a	250	300	350	400	500
20 mg/s					
25 mg/s	X*				
30 mg/s	X*	X*	X	X*	X*
35 mg/s		X*	X	X*	X*
(*) This point also tested during the first characterization campaign of the HT20k DM2-S					

Among the operative points reported in Table 64, only 10 points were directly comparable with those already tested during the characterization campaign of the HT20k DM2-S. In addition, other limitations were introduced considering the reduced chamber diagnostics available during the failure investigation campaign.

In particular, the oscilloscope was used only to record the average anode discharge current, while its channel for recording the entire current profile was not available. Similarly, during this test phase, the cathode reference potential was not recorded. The data available limited the applicability of the EHM to a restricted number of variables, as will be further detailed in the following section. Despite these limitations, the hypothesis related to a possible propellant leak was judged plausible through a wise analysis of the resulting data. Therefore, the investigation team decided to proceed with a visual inspection of the xenon feeding system.

Consequently, the failure occurred during the HT20k EM test campaign, and therefore investigated through using the DM-2, was finally detected on the pipework of the thrust stand. In particular, the inspection revealed the ungluing of the Teflon straps on the anodic pipeline, which caused the leak of propellant. The rapid recovery from this failure allowed the continuation of the test on the engineering model (HT20k EM) of the thruster.

4.8 Results

In this paragraph, the main results obtained for the application of the presented EHM model applied to HT are presented. In particular, the application of this methodology has been developed in three different steps. First, the performance model presented in Section 5.5 has been normalized to derive the functional ICM matrix (see Eq. 4.15). Despite the limitations introduced by the linearization process, the theoretical approach provides a clear understanding of the relations existing among the involved thruster parameters and the directions of relative variation. In addition, this step supports the process through which the variables are subdivided between dependent and independent parameters.

The second step concern the derivation of the ICM matrix from experimental data. This phase represents a fundamental step to calibrate the model for the real behavioural trends of the thruster over its operative range. Moreover, relying on an ICM derived from experimental data allows to include those phenomena neglected in the theoretical model by introducing both assumptions and simplifications. As previously mentioned, this phase considers the processing of experimental data collected during the extensive test campaign on the HT20k DM2-S during its development phase. A specific software module has been developed to process the raw experimental data to facilitate the following steps.

It is important to highlight that the derivation of the ICM is allowed for a specific thruster operative point, the so-called “reference point”. Therefore, the delta vectors of both dependent and independent parameters are determined for each point of the test matrix (see Table 63), resulting in a single ICM. As reported in Section 4.5, a weighted average process has been considered for obtaining the final set of ICM coefficients. Finally, the FCM is computed following a numerical procedure based on the Moore-Penrose pseudoinverse.

In order to demonstrate the application and the effectiveness of the proposed methodology on a real case, a degraded experimental dataset collected using the same thruster model (HT20k DM2-S) has been introduced. In Section 4.7, a general description of the failure that occurred on the propellant fluidic of the thrust balance stand has been described. The processing of the raw experimental data followed an analogous process already introduced for the “healthy” data of the thruster.

As clearly specified in Section 4.7, the diagnostic process based on the use of FCM allows estimating the deviation of the unmeasurable parameters from their healthy values. Consequently, a selection process is introduced to derive the operative points with the same setting values in both healthy and degraded datasets. Thus, applying Eq. (4.11), the deviation from the nominal thruster envelope is derived with a new set of deltas. The final step for the identification of the failure is the exploitation of the FCM derived from the data collected during nominal operation to find out the derivation (delta) of the unmeasured parameters.

In this analysis, the software-based process is concluded with the graphical representation of the ICM derived from the different dataset and the deltas derived from the use of the FCM. The entire process is represented in Figure 109.

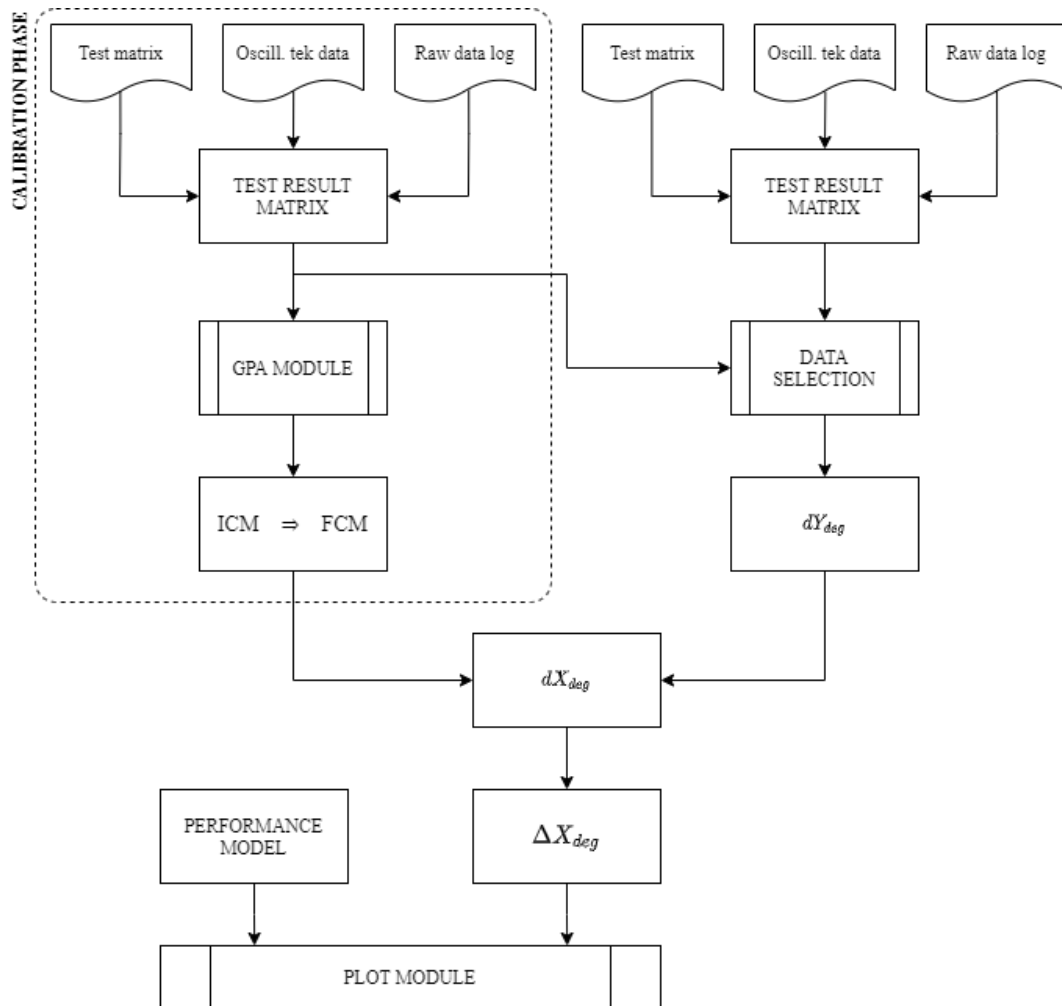


Figure 109:EHM based on GPA approach HT application process.

Following the analysis process summarized in Figure 109, an ICM for each of the operative points considered in the test matrix is obtained. The single ICM coefficient values are graphically represented in Figure 110 for comparison with the theoretical performance model (black points) and averaged ICM values (blue points). As shown in the figure, the dispersion of the ICM coefficients for both theoretical and average value is evident. This might be caused by two main factors: (i) the limited number of operative points tested during the experimental campaign of the thruster and (ii) the possible influence of the assumptions and simplification caused by the linearization process, which might cause differences between model and experimental-base results.

For a better understanding of ICM coefficient dispersion, each coefficient vector has been fitted with an equivalent Gaussian distribution, as shown in Figure 111.

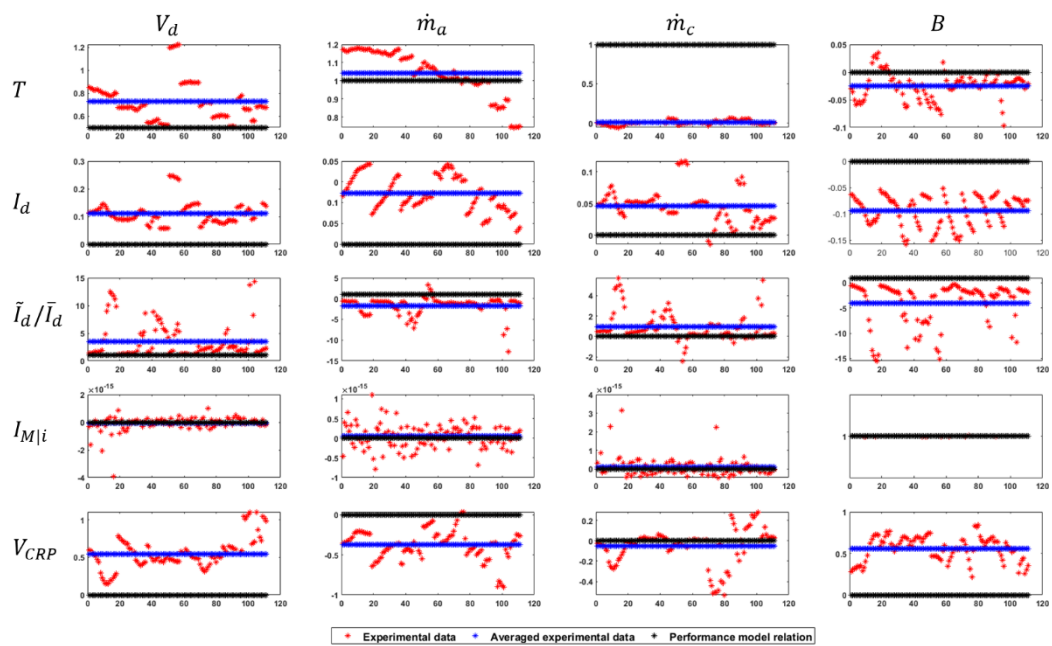


Figure 110: ICM coefficient values.

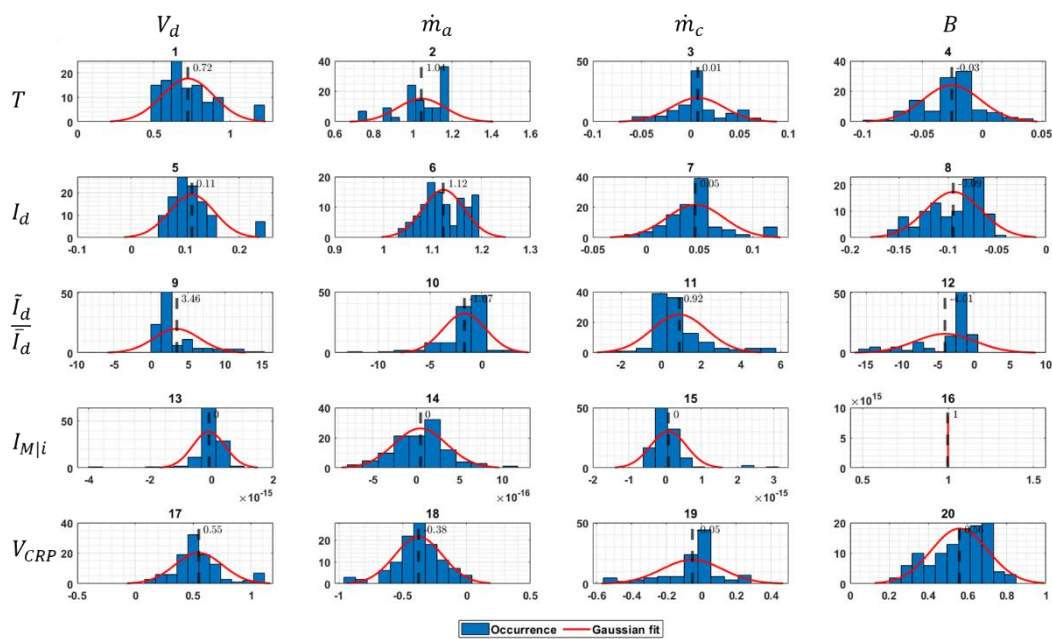


Figure 111: ICM coefficient distributions.

The obtained ICM values are the following:

Table 65: derived ICM matrix values.

		ΔX			
		V_d	\dot{m}_a	\dot{m}_c	B
ΔZ	T	0,72	1,04	0,01	-0,03
	I_d	0,11	1,12	0,05	-0,09
	\tilde{I}_d/\bar{I}_d	3,46	-1,67	0,92	-4,01
	$I_{M i}$	0,00	0,00	0,00	1,00
	V_{CRP}	0,55	-0,38	-0,05	0,56

As reported in Section 4.7, the experimental campaign of the HT20k DM2-S was performed to characterize the thruster on its operative envelope with a reduced number of tested operative points. In particular, the objective of the test was the magnetic peak optimization to minimize the discharge current. Consequently, to improve the representativeness of the effective distribution, a more significant number of operative points should be collected through a dedicated test campaign. Despite this limitation, Figure 111 shows the equivalent Gaussian distribution and the resulting data occurrence to highlight their dispersion.

For what concerns the coefficient related to the thrust, the values report in Table 32 shows a substantial proportionality to the AMFR according to the theoretical relation introduced in the performance model. The resulted coefficient of 0,72 slightly deviates compared to the common proportionality of the thrust to the square of the discharge voltage, as shown in Eq. (4.36). This difference could be explained by the higher mass utilization efficiency that reached increasing the discharge voltage at which the thruster is operated.

The thrust seems not dependent on the propellant mass flow into the cathode (KMFR), as expected by the theoretical model. The same consideration might be done with respect to the magnet field value, whose variation does not significantly affect the thrust value.

The second dependent parameter considered in the ICM is the discharge current (I_d). The main dependency of this parameter on the AMFR is consistent with Eq. (4.37). In fact, in this type of thruster, a large majority of the neutral particles injected from the anode are ionized to produce the necessary discharge current. With a value of 1,12, the discharge current results almost linearly proportional to the AMFR. The non-perfect linear behaviour could be related to an increment of the current efficiency. In fact, the fraction of electron current that flows from the cathode to the anode is increased, on one side, if a higher neutral density is provided, owing to the augmented electron-neutral collisional events in the discharge chamber, which facilitates the electronic transport toward the anode. On the other side, with a higher neutral density, the ionization efficiency is increased, which leads to a higher discharge current.

As it is possible to appreciate from Table 65, the discharge current is weakly dependent on the variation of the discharge voltage. This behaviour is different from what is expected by the theoretical performance model in which the two parameters result not dependent. Nonetheless, a possible explanation of this discrepancy could be found by investigating the assumption introduced in the performance model concerning the singly charged particles. In fact, increasing the discharge voltage, the electron temperature grows, more energetic collisions occur, generating multiply-charged ions [229] and improving the current.

The dependency of the discharge current on the KMFR could be neglected due to an equivalent ICM value of 0,05. On the contrary, even though the dependency on the magnetic field results weak, considering the small value of the related ICM coefficient, it is significant compared to the thrust-magnetic field ones, in particular owing to the associated coefficient sign. According to the negative sign, if the magnetic field is increased, the current from the cathode to the anode (the so-called “trigger” current) is lower. This behaviour is consequent to the strongest interaction of the magnetic field with the electrons, which prevents their motion toward the anode.

The fourth row of the derived ICM matrix is related to the RMS of the discharge current normalized for the mean value of the discharge current itself.

In Table 65, the resulting values strongly diverge from those presented by Sekerak in [234].

Moreover, as shown in Figure 111, the occurrence of the data shows an asymmetric distribution more similar to a Maxwell Boltzmann distribution rather than a symmetrical Gaussian distribution.

The differences from the Sekerak study on H6 thruster can be justified considering two main aspects. First, the test campaign performed on the H6 was specifically planned to highlight the transition between the operation modes of the thruster. In fact, the thruster was operated over a wide range of magnetic field values while all other operating parameters were kept constant. Second, the equation introduced by the author relates the variation of the magnetic field with respect to discharge voltage and AMFR, considering the transition between the global and the local operative mode. Instead of limiting the analysis to this specific set of data, the overall dataset has been employed in this study. The last and perhaps most important consideration on the discrepancies among the values concerns the different thruster technology. As a matter of fact, the H6 presents a “classical” magnetic field topology without a magnetically shielded configuration.

As well experienced and according to Eq. (4.37), the current supplied to the magnetic coils results linearly proportional to the magnetic field. In the derived ICM, even though the HT20k DM2-S presents a design based on three coils, independently controlled, the values are shown with respect to the equivalent coil current value.

The last row of the matrix reports the dependency of the cathode potential (CRP) on the independent parameters. Considering the value of 0,55, the CRP shows a

fundamental dependence on the discharge potential, while a very weak dependency results for those parameters which define the operative condition of the cathode itself. In particular, the coefficient related to the AMFR is equal to -0,38 which means a lower CRP value can be obtained if a higher current is required from the cathode. In fact, the CRP is related to the potential and temperature of the plasma in the plume. As a consequence, if the discharge voltage is increased, the electronic temperature is proportionally increased, leading to a higher voltage drop, with a consequent lower value of the CRP. In this condition, with a lower CRP, the cathode operates in a better condition due to the lower KMFR.

The last notable result obtained from the ICM is the dependency of the CRP on the magnetic field, which present a proportionality close to a square root, with a value of the coefficient equal to 0,56. In the HT20k DM2-S, the cathode is centrally mounted and, consequently, it is completely immersed in the magnetic field generated by the thruster coils. This specific relation shall be further investigated with a dedicated test campaign.

After the derivation of the matrix values, the FCM is derived and reported below:

$$FCM = \begin{bmatrix} 0.60 & -0.23 & 0.05 & -0.23 & 0.76 \\ 0.31 & 0.46 & -0.04 & 0.04 & -0.25 \\ -2.24 & 2.39 & 0.83 & 5.04 & -2.77 \\ -0.12 & 0.15 & 0 & 0.94 & 0.13 \end{bmatrix} \quad (4.47)$$

As previously reported, after the selection of the comparable operative points of the degraded dataset, the relative variations of the dependent parameters have been calculated. Finally, the variations of the independent parameters have been obtained through the FCM.

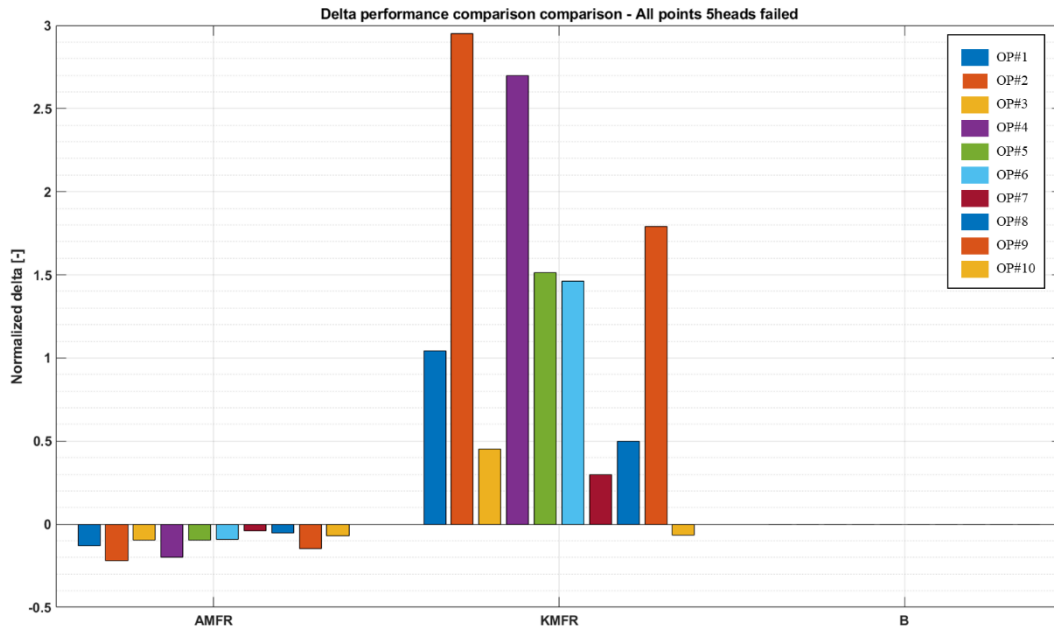


Figure 112: normalized delta of faulty operative points with respect to the nominal operative points.

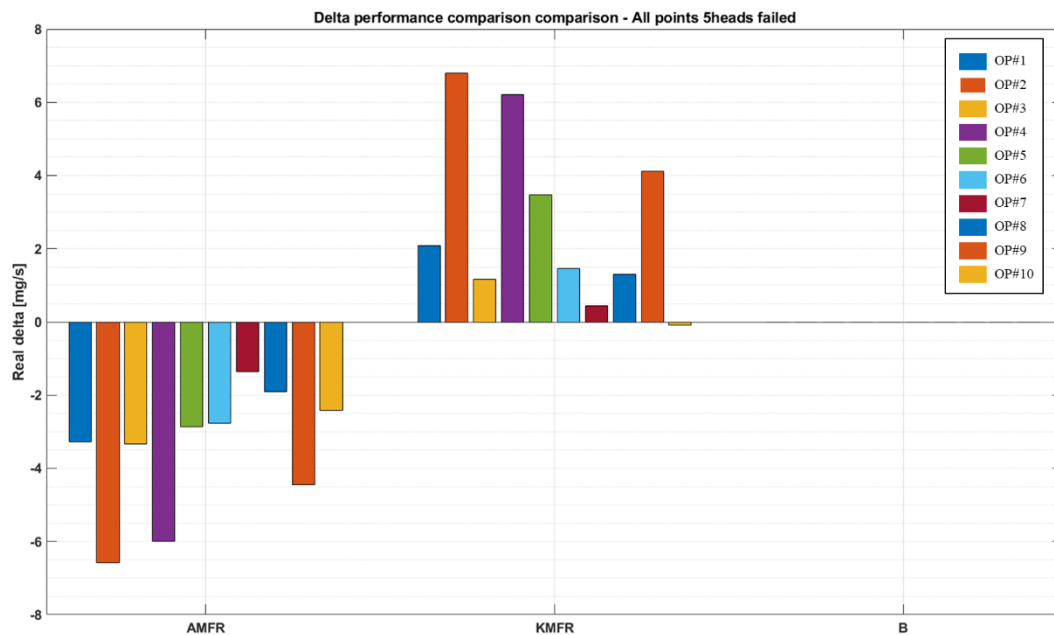


Figure 113: delta flow rate of the faulty points with respect to the nominal operative points.

The relative variation is shown in Figure 112, where the maximum deviation from the nominal operative point result for the point at 250 V and 30 mg/s operated with a magnetic field of 27 mT where the relative value reached a value equal to -0,21. Multiplied for the reference nominal point, the reduction of the AMFR feeds into the discharge chamber through the anode caused by the failure mentioned above is equal to -6.5 mg/s. The propellant leaks through the hole found on the anodic feeding line results proportional to the AMFR set through the control panel of the feeding system upstream of the failure. However, no particular relations have been identified on the difference among the occurred leak flow rate. The limited number

of operative points comparable to those tested in nominal condition does not allow further considerations. In order to improve the analysis, a full investigation of the nominal thruster operation with the collection of multiple data might lead to the derivation of nearly continuous trends, which may allow for a reliable evaluation of the deviation of the off-nominal points.

Chapter 6

Conclusion and way forward

In the next future, new space utilization opportunities will be available thanks to the development of innovative technological concepts.

International organizations such as space agencies and non-governative entities constantly review the roadmaps for future space objectives to embrace all possibilities.

Meanwhile, the establishment of the technological development steps of critical concepts, components and systems is considered a fundamental task to identify the essential building blocks.

Electric propulsion plays a fundamental role in opening new mission scenarios and making feasible mission concepts unfeasible up to now.

In particular, the Hall thrusters have reached a considerable level of maturity nowadays, with tens of missions already embarking and operating them for different purposes such as orbit transferring and station keeping manoeuvres.

These electric propulsion devices provide optimal performance in terms of thrust, specific impulse and thrust-over-power ratio compared to the other thrusters. The consistent widespread of their utilization is also due to the relatively high reliability and the relatively easy scalability properties of the thrusters. Furthermore, the current development status of the thruster technologies allows focusing the development toward the optimization of the electric propulsion subsystem architecture and its related components. It targets either to enhance the spacecraft performance through the improvement of the current platform design and also the possibility to exploit innovative platform concepts to strengthen further the benefits coming from the adoption of this technology.

In this thesis, the possibility offered by high power electric propulsion is investigated considering the reference study case of an innovative transportation system, the space tug. The main features of this system are its reusability for which, in association with the adoption of electric thruster, could make feasible and economically sustainable a mission scenario where the space tug is operated to provide On-Orbit Servicing (OOS). In particular, the two investigated mission scenarios consist of a main mission phase where the telecommunication satellite transfer from its launcher release orbit up to its GEO operational position. In addition, the second scenario also includes the possibility to relocate a second telecommunication satellite from a first longitude GEO position into a second GEO position. In this way, the telecom satellite can continue its operational life targeting a different geographical area where the same market application is not provided.

Therefore, the critical function of transferring payload (intended as the satellite that shall be serviced) shall be provided to an adequate design of the propulsion subsystem based in this case on high power electric thrusters.

The two reference thrusters considered in the study are the HT5k and the HT20k developed by SITAEL. These thrusters were considered in different subsystem architectures compared to more traditional architectures commonly used in the electric propulsion field. In specific, they are (i) cluster architecture based on multiple low powerful thrusters compared with the monolithic architecture of a single thruster, (ii) the Direct-Drive architecture in which the power source (e.g. solar arrays) directly feeds the generated power to the thruster compared with the typically used Power Processing Unit (PPU), and (iii) the krypton used as an alternative with respect to the commonly used xenon. A dedicated MAGNETO tool has been realised to preliminary designing the space tug based on the alternative architectural option mentioned before, including mission requirements and constraints defining through the performed standard mission analysis. This multi-input/output software provides a flexible and modular simulation environment through which the peculiarities of the propulsion subsystem based on electric propulsion are evaluated, highlighting their impacts on the other onboard subsystems in order to provide a preliminary estimation of mission and spacecraft budgets.

As mentioned, the investigation performed consisted of two analysis branches. First, the MS.1 consisting of the transferred OOS provided a direct comparison between the introduced EPS alternatives through a dedicated trade-off performed evaluating a set of representative figures of merit (FoM) defined to highlight the alternatives' advantages and disadvantages. Thus, they are (i) dry and wet spacecraft mass budget, (ii) power budget, (iii) transfer durations, (iv) propellant costs, (v) EPS reliability, (vi) EPS complexity and (vii) system TRL. When not directly available, the numerical value of the FoMs has been calculated through a dedicated model added in a modular subroutine in the evaluation block of MAGNETO.

In this case, the EPS design was based on two thruster operative points that characterized the possible operative options allowed by the Hall thruster while emphasizing the architecture operational features. The results show that the spacecraft design in which the krypton is exploited in substitution of the xenon represents the best design option, mainly justified by the strong costs reductions due to the low krypton price.

The second branch of analysis consisted of investigating the MS.2 for cluster architecture with a set based on 25 thruster operative points selected considering the target design performance of both thrusters (HT5k and HT20k). The comparison between the architectures based on the two thrusters resulted in 9 operative points directly evaluated considering a cluster architecture from one up to four HT20k and four up to 16 HT5k (considering cluster blocks of 4 thrusters).

The results have been presented highlighting the main differences in terms of dry and wet mass, delta-V and mission durations reported for each of the nine phases of the MS.2. As presented, the main advantages identified in the adoption of the

most powerful monolithic architecture is the lower complexity of the system that, in addition to the slightly higher performance reached by the HT20k, allows to consider this architecture the preferable design choice if compared with the cluster architectures based on HT5k.

To further extend the application enabled by innovative electric propulsion concepts and expand the analysis capabilities of MAGNETO, the second part of the thesis is dedicated to prove the feasibility of a mission specifically design for Very low Earth Orbits.

Ranging between 160km and 250 km, the operations in this region are nowadays limited by a high drag force which a propulsion system shall constantly counteract.

The current electric propulsion devices could be guaranteed for medium periods benefitting by higher specific impulse values than chemical-based. On the other hand, adopting the thruster based on air-breathing concepts allows to entirely avoid the limitation imposed by the need to carry onboard propellant.

The feasibility analysis presented in this thesis started with the preliminary design of the VLEO spacecraft adopting the so-called ramEP thruster designed through an MDO process.

Additional design modules were introduced in the MAGNETO design blocks to enable the different analyses necessary to include the cross-effects of the peculiar surrounding environment in the design of the platform itself.

Moreover, a dedicated propagation routine based on the thruster performance model, and exploiting a developed thruster control law routine, was introduced.

The optimal MDO results were selected among the possible solutions laying on a Pareto front generated through a weighted method applied on the following optimization objectives: (i) maximization of the thrust-over-drag ratio, (ii) maximization of the internal volume, (iii) minimization of the power allocated to the thruster. Including a multi-start algorithm for different target operative altitudes, the optimization resulted in over 400 investigated configurations.

The three optimal solutions have been selected according to (i) the maximum thrust-over-drag ratio, (ii) maximum thruster power, (iii) the maximum volume of the spacecraft.

The operational feasibility investigation of the selected optimal configuration was subdivided into two phases. First, the ramEP spacecraft configurations were analysed over the VLEO altitude range to highlight the altitudes where a thrust-over-drag ratio was greater than one. Then, the performance trends obtained for each configuration were limited according to additional constraints mainly related to the upper limit imposed on the maximum acceleration voltage that the PPU would sustain. The results have shown that the configuration selected considering the highest power allocated to the ramEP thruster is characterized by the most extended operative altitude range having T/D greater or equal to one and fulfilling the acceleration voltage limitation of 3000V.

To further extend the impact of the higher power budget allocated to the thruster, alternative spacecraft architecture based on the deployable wing were introduced.

They were considered as additional surfaces to the solar array area derived from the MDO process. The trends of the thrust-over-drag ratio on the VLEO altitude range showed the different effects of the drag value increment (due to the additional solar array) regarding the obtained thrust value. For lower altitudes, the configuration based on two solar arrays surfaces for each spacecraft wing deployed along with x and y-direction results in having the highest T/D ratio due to the high thrust generated by the additional power generated. On the contrary, at higher altitude, the configuration with the highest T/D value is that having a single solar array for each wing deployed along the y-direction.

The second part of the feasibility analysis was dedicated to propagating the spacecraft trajectory in different solar cycle periods to prove the maintenance of the target operative altitude throughout the solar activity variation. The configuration exploited for the propagation resulted from the MDO without the alternative solar array options.

For the mission period centred during the low, medium and high solar period, the propagated trajectories show the possibility to sustain the operation at 206km, 216km and 235km, respectively. It is important to highlight that in the three periods in which the trajectory has been propagated for a mission duration of one week, the spacecraft behaviour shows intrinsic stability following the daily atmospheric variations and dealing with the losses of altitude with following recovers.

The last part of the work tackles another building block considered fundamental to support electric propulsion devices' future development and exploitation.

Considering the current increment trend of the EP systems complexity and their components, the monitor of the performance and health status is of primary interest to ensure safe and reliable operations. Consequently, dedicated Engine Health Monitoring (EHM) methods shall be developed and integrated in the Failure Detection, Identification and Recovery (FDIR) functions of the future space systems. Moreover, these methods can be exploited during the development phase to provide fundamental information for the correct assessment of the component reliability and the evolution in time of the component performance.

In this work, the so-called "Gas Path Analysis" (GPA) has been adopted on EP system with the objective of providing a novel methodology for failure detection performed on propulsion system based on Hall thrusters. This method was extensively used in the aeronautic field to optimise the maintenance schedule of the gas turbine, proving an adequate level of reliability in identifying degradation impacting the nominal operation of the internal component.

The GPA is based on identifying the deviations from the nominal values of a set of unmeasured parameters, representing the health status of the components. This is accomplished by investigating the variations of measured parameters set from their nominal values (such as temperature and pressure in the case of a gas turbine) and correlate them to parameters indicating the health status of the component under analysis.

The relations among the two sets of parameters are established thanks to the Influence Coefficient Matrix (ICM).

This methodological approach has been employed in this thesis, subdividing its adoption into two main steps. First, a phenomenological thruster model was introduced and exploited for the identification of the functional relations between two sets of parameters and the definition of the ICM. The second phase of the analysis instead consisted of the calculation of the ICM through experimental data collected during the development phase of the SITAEL's HT20k. This process allowed the calibration of the ICM for the real thruster behaviour avoiding possible neglects introduced in the theoretical model. The results show a good agreement between the theoretical ICM and that derived from the experimental data. In particular, the main trends, well-reported in literature, were fully intercepted. As detailed in the chapter, the only exception was represented by the cathode potential reference (CRP). In the case of the HT20k, the peculiar position of the cathode could have a strong influence on its behaviour, in particular for what concerns the interaction between the cathode plume and the surrounding magnetic field generated by the magnetic circuit of the thruster.

In order to prove the capability of this newly developed Hall thruster EHM method in identifying possible failures, it was used on an experimental dataset of HT20k, collected during a test where a failure occurred on the feeding system. As shown in the results, the loss of propellant mass was clearly detected. However, even with the proven detection capabilities, the selected health parameter did not allow to distinguish the loss of propellant either on the cathode or anode line. As a consequence, after the detection of the failure, its identification shall be completed with the contribution of the external expert knowledge.

The future works concern mainly three directions. First, the MAGNETO shall be updated to simplify the modular software structure and generalize the input/output module of the different subroutines. Moreover, an improved version of the design block will be implemented to detail the different subsystems' design and refine mission and spacecraft budgets.

Second, the design of the VLEO spacecraft will be further improved, particularly for what concerns the MDO set-up process.

Furthermore, a new thruster performance model provided by SITAEL will be implemented to decouple the acceleration voltage and discharge current derivation with a consequent reduction of the number of interactions that the MDO algorithm shall process.

In addition, the propagation module will also be improved with a reduced atmospheric model always to decrease the computational time necessary at each integration step along the trajectory.

MAGNETO will also be upgraded thanks to the introduction of the developed EHM. This upgrade will allow the evaluation of the possible impacts of either a single failure or degradation of the propulsion system performance at both system and mission level.

Lastly, the EHM itself will be further extended with additional parameters concerning the thruster's geometrical definition to further generalize the failure detection capability toward other power-class thrusters. A possible future improvement will also be included by exploiting this model during the qualification campaign of a 5kW-class thruster. Moreover, a specific test will be performed with the centrally mounted cathode to fully depicted its performance behaviour in this peculiar configuration.

References

- [1] ISECG, The Global Exploration Roadmap, 2018. www.globalspaceexploration.org. (accessed August 27, 2018).
- [2] I. International Space Exploration Coordination Group, Global Exploration Roadmap - Supplement August 2020, 2020. https://www.globalspaceexploration.org/wp-content/uploads/2020/08/GER_2020_supplement.pdf (accessed June 5, 2021).
- [3] NASA, 2020 NASA Technology Taxonomy, 2020. https://www.nasa.gov/sites/default/files/atoms/files/2020_nasa_technology_taxonomy_lowres.pdf (accessed June 5, 2021).
- [4] A. Long, M. Richards, D.E. Hastings, On-Orbit Servicing: A New Value Proposition for Satellite Design and Operation, *J. Spacecr. Rockets*. 44 (2007) 964–976. <https://doi.org/10.2514/1.27117>.
- [5] J.R. Wertz, D.F. Everett, J.J. Puschell, *Space Mission Engineering: The New SMAD*, Space Technology Li..., 2011.
- [6] J.R. Wertz, W. Larson, *Space Mission Analysis and Design*, Microcosm Press, 1999. http://www.amazon.ca/Space-Mission-Analysis-Design-James/dp/0792359011/ref=sr_1_1?s=books&ie=UTF8&qid=1430653992&sr=1-1&keywords=9780792359012.
- [7] J.R. Wertz, *Orbit & Constellation Design & Management*, 1994. <https://doi.org/10.1002/cmr.1820060106>.
- [8] K. Ho, K. Gerhard, A.K. Nicholas, A.J. Buck, J. Hoffman, On-orbit depot architectures using contingency propellant, *Acta Astronaut*. 96 (2014) 217–226. <https://doi.org/10.1016/j.actaastro.2013.11.023>.
- [9] D. Smitherman, G. Woodcock, Space Transportation Infrastructure Supported By Propellant Depots, in: *AIAA Sp. 2011 Conf. Expo.*, 2011.
- [10] D. Arney, A. Wilhite, Orbital Propellant Depots Enabling Lunar Architectures Without Heavy-Lift Launch Vehicles, *J. Spacecr. Rockets*. 47 (2010). <https://doi.org/10.2514/1.44532>.
- [11] J. Ahn, O.L. De Weck, Mars Surface Exploration Caching from an Orbiting Logistics Depot, *J. Spacecr. Rocket*. 47 (2010). <https://doi.org/10.2514/1.37694>.
- [12] M. Baine, G. Grush, E. Hurlbert, An Open Exploration Architecture Using an L-1 Space Propellant Depot, in: *SpaceOps 2010 Conf.*, Huntsville, Alabama, 2010. <https://doi.org/10.2514/6.2010-2158>.
- [13] F. Zegler, B. Kutter, Evolving to a Depot-Based Space Transportation Architecture, in: *AIAA Sp. 2010 Conf. Expo.*, Anaheim, California, 2010. <https://doi.org/10.2514/6.2010-8638>.
- [14] J. Goff, J.A. Goff, B.F. Kutter, F. Zegler, D. Bienhoff, F. Chandler, J. Marchetta, Realistic Near-Term Propellant Depots: Implementation of a Critical Spacefaring Capability , in: *AIAA Sp. 2009 Conf. Expo.*, AIAA, 2009. <https://doi.org/10.2514/6.2009-6756>.
- [15] J.T. Howell, J.C. Mankins, J.C. Fikes, In-Space Cryogenic Propellant Depot stepping stone, *Acta Astronaut*. 59 (2006) 230–235. <https://doi.org/10.1016/j.actaastro.2006.02.019>.

- [16] W. Notardonato, Active control of cryogenic propellants in space, *Cryogenics* (Guildf). 52 (2012) 236–242. <https://doi.org/10.1016/j.cryogenics.2012.01.003>.
- [17] M.W. Liggett, Space-based LH2 propellant storage system: subscale ground testing results, *Cryogenics* (Guildf). 33 (1993) 438–442. [https://doi.org/10.1016/0011-2275\(93\)90174-M](https://doi.org/10.1016/0011-2275(93)90174-M).
- [18] G.R. Woodcock, Logistics support of lunar bases, *Acta Astronaut.* 17 (1988) 717–738. [https://doi.org/10.1016/0094-5765\(88\)90186-5](https://doi.org/10.1016/0094-5765(88)90186-5).
- [19] A. David Street Advisor Alan Wilhite, D. Street, A. Wilhite, A Scalable Orbital Propellant Depot Design AE8900 MS Special Problems Report Space Systems Design Lab (SSDL A Scalable Orbital Propellant Depot Design, 2006.
- [20] SpaceX, SpaceX - Starship Users Guide Revision 1.0, 2020.
- [21] Review of U.S. Human Spaceflight Plans Committee, Seeking a Human Spaceflight Program - Worthy of a Great Nation, 2009.
- [22] NASA, Emerging Space - The Evolving Landscape of 21st Century American Spaceflight, n.d.
- [23] Satellite Database | Union of Concerned Scientists, (n.d.). <https://www.ucsusa.org/resources/satellite-database> (accessed April 22, 2021).
- [24] NASA, Robotic Refueling Mission - Factsheet, 2013. https://nexus.gsfc.nasa.gov/images/RRM_Factsheet.pdf (accessed May 2, 2021).
- [25] J. McGuire, NASA’s Robotic Refueling Mission , in: 2nd Annu. ISS Res. Dev. Conf., 2013.
- [26] E. Ackerman, How NASA Will Grapple and Refuel a Satellite in Low Earth Orbit - IEEE Spectrum, (2019). <https://spectrum.ieee.org/tech-talk/aerospace/satellites/how-nasa-will-grapple-and-refuel-a-satellite-in-low-earth-orbit> (accessed May 2, 2021).
- [27] ArianeSpace, VEGA User’s Manual Issue 4 Revision 0 , 2014. https://www.arianespace.com/wp-content/uploads/2018/05/Vega-Users-Manual_Issue-04_April-2014.pdf (accessed March 31, 2021).
- [28] ArianeSpace, VEGA C USER’S MANUAL, 2018.
- [29] Ariane 5 User’s Manual Issue 5 Revision 2 Issued and approved by Arianespace Roland LAGIER Senior Vice president Chief technical officer, n.d. www.arianespace.com (accessed April 29, 2021).
- [30] P. Bravais, P. Bravais, R. Salome, R. Salome, C. Gelas, C. Gelas, Improved xenon loading equipment with loading capacity up to 1200 kg for alphabus, in: 28th Int. Electr. Propuls. Conf., Toulouse, France, 2003.
- [31] E.C. for S. Standardization, Space engineSpace Engineering Technology readiness Level (TRL guidelines, Noordwijk, The Netherlands, 2017.
- [32] NASA, TRL - Technology Readiness Level, (n.d.). <https://esto.nasa.gov/trl/>.
- [33] S. ESA-ESTEC SRE-PA & D-TEC, Margin philosophy for science assessment studies, 2012.
- [34] ECSS, ECSS-E-TM-10-25A 2010 Engineering design model data exchange CDF, (2010) 31.
- [35] U.S. of CommerceDepartment, NIST - National Institute of Standard and Technology, (n.d.). <https://webbook.nist.gov/cgi/inchi?ID=C7440633&Mask=200>.
- [36] Y. Zhao, L. Sun, X. Yu, W. Sun, Supercritical Xe as Propellant in Satellite

- Electric Propulsion System: Experimental Study on Thermal Physical Properties, *IOP Conf. Ser. Mater. Sci. Eng.* 562 (2019). <https://doi.org/10.1088/1757-899X/562/1/012086>.
- [37] P. Fortescue, G. Swinerd, J. Stark, *Spacecraft Systems Engineering*, 4th Edition | Wiley, 4th Edition, 2011.
- [38] D. Milligan, D. Milligan, D. Gestal, D. Gestal, O. Camino, O. Camino, P. Pardo-Voss, P. Pardo-Voss, D. Estublier, D. Estublier, C. Koppel, C. Koppel, SMART-1 Electric Propulsion Operational Experience, *Proc. Int. Electr. Propuls. Conf. 2005.* (2005) 1–13.
- [39] C.A. Paissoni, *Electric Propulsion for cislunar Space tug: preliminary sizing and investigation on mutual influences*, Politecnico di Torino, 2017.
- [40] V. Giannetti, E. Ferrato, A. Piragino, M. Reza, F. Faraji, M. Andrenucci, T. Andreussi, HT5k Thruster Unit Development History, Status and Way Forward, in: *36th Int. Electr. Propuls. Conf.*, Vienna, Austria, 2019: pp. 1–19.
- [41] V. Giannetti, T. Andreussi, A. Leporini, D. Estublier, M. Andrenucci, LONG-LIFE LOW EROSION HALL EFFECT THRUSTER: MODEL AND SIMULATIONS, in: *Sp. Propuls. 2016*, MARRIOTT PARK HOTEL, Rome, Italy, 2016. http://www.sitael.com/wp-content/uploads/2016/05/3125199_LONG-LIFE_LOW_EROSION_HET_MODEL_SIMULATIONS_Giannetti.pdf (accessed September 3, 2018).
- [42] A. Piragino, A. Leporini, V. Giannetti, D. Pedrini, A. Rossodivita, T. Andreussi, M. Andrenucci, D. Estublier, Characterization of a 20 kW-class Hall Effect Thruster, in: *35th Int. Electr. Propuls. Conf.*, Atlanta, Georgia, USA, 2017. https://iepc2017.org/sites/default/files/speaker-papers/iepc-2017-381_characterization_of_a_20kw_class_hall_effect_thruster_0.pdf.
- [43] T. Andreussi, A. Piragino, M. Reza, V. Giannetti, F. Faraji, E. Ferrato, D. Pedrini, A. Kitaeva, A. Rossodivita, M. Andrenucci, S. SpA, I. Christopher Andrea Paissoni, G. Becatti, Development status and way forward of SITAEL's 20kW class Hall thruster, the HT20k, n.d.
- [44] D. Pedrini, F. Cannelli, C. Ducci, T. Misuri, F. Paganucci, M. Andrenucci, Hollow Cathodes Development At Sitael, in: *Sp. Propuls. 2016*, Rome, Italy, 2016. http://www.sitael.com/wp-content/uploads/2016/05/3124925_HOLLOW_CATHODES_DEVELOPMENT_AT_SITAEI_pedrini.pdf.
- [45] B.E. Beal, *Clustering of Hall Effect Thrusters for High-Power Electric Propulsion Applications*, University of Michigan, 2004.
- [46] Y. Chen, Q. Yang, Reliability of two-stage weighted-k-out-of-n systems with components in common, *IEEE Trans. Reliab.* 54 (2005) 431–440. <https://doi.org/10.1109/TR.2005.853274>.
- [47] P.J. Boland, F. Proschan, The Reliability of K Out of N Systems, *Ann. Probab.* 11 (2007) 760–764. <https://doi.org/10.1214/aop/1176993520>.
- [48] P. Boddu, L. Xing, Reliability evaluation and optimization of series-parallel systems with k-out-of-n: G subsystems and mixed redundancy types, *Proc. Inst. Mech. Eng. Part O J. Risk Reliab.* 227 (2013) 187–198. <https://doi.org/10.1177/1748006X12473569>.
- [49] J.S. Snyder, J.R. Brophy, R.R. Hofer, D.M. Goebel, I. Katz, Experimental investigation of a direct-drive Hall thruster and solar array system at power levels up to 10 kW, *48th AIAA/ASME/SAE/ASEE Jt. Propuls. Conf. Exhib.*

2012. (2012) 1–22. <https://doi.org/10.2514/6.2012-4068>.
- [50] J.S. Snyder, J.R. Brophy, R.R. Hofer, D.M. Goebel, I. Katz, Experimental investigation of a direct-drive Hall thruster and solar array system, *J. Spacecr. Rockets*. 51 (2014) 360–373. <https://doi.org/10.2514/1.A32479>.
- [51] F. Faraji, M. Reza, U. Cesari, N. Giusti, G. Morreale, T. Andreussi, L. Benetti, M. Andrenucci, Experimental Investigation of a Direct-Drive Hall Thruster, in: *Sp. Propuls.* 2018, Seville, Spain, 2018.
- [52] K.J. Metcalf, Power Management and Distribution (PMAD) Model Development Final Report, Cleveland, Ohio, 2011.
- [53] K.J. Metcalf, Power Management and Distribution (PMAD) Model Development Final Report, Nasa Sti. (2011).
- [54] S. White, E. Al., Next Generation UltraFlex solar array for NASA’s New Millennium Program Space Technology 8, in: *IEEE Aerosp. Conf.*, 2005: pp. 824–836. <https://doi.org/10.1109/AERO.2005.1559374>.
- [55] C.R. Mercer, T.W. Kerslake, R.J. Scheidegger, A.A. Woodworth, J.-M. Laustein, Solar Electric Propulsion Technology Development for Electric Propulsion, in: *33rd Sp. Power Work.*, Huntington Beach, CA, 2015.
- [56] C.R. Mercer, M.L. McGuire, S.R. Oleson, M.J. Barrett, Solar Electric Propulsion Concepts for Human Space Exploration, in: *AIAA Sp. 2015 Conf. Expo.*, Pasadena, California, 2015. <http://www.sti.nasa.gov> (accessed August 27, 2018).
- [57] G. Zubi, R. Dufo-López, M. Carvalho, G. Pasaoglu, The lithium-ion battery: State of the art and future perspectives, *Renew. Sustain. Energy Rev.* 89 (2018) 292–308. <https://doi.org/10.1016/j.rser.2018.03.002>.
- [58] J.R. Brophy, R. Gershman, N. Strange, D. Landau, R.G. Merril, T. Kerslake, 300-kW Solar Electric Propulsion System Configuration for Human Exploration of Near-Earth Asteroids, in: *47th AIAA/ASME/SAE/ASEE Jt. Propuls. Conf. Exhib.*, San Diego, California, n.d. https://doi.org/10.2458/azu_uapress_9780816532131-ch043.
- [59] R.R. Hofer, T.M. Randolph, Mass and Cost Model for Selecting Thruster Size in Electric Propulsion Systems, *J. Propuls. Power*. 29 (2013) 166–176. <https://doi.org/10.2514/1.B34525>.
- [60] E.S.E.-E. Requirements & Standards Division, ECSS-EST-35-01C__Liquid and electric propulsion for spacecraft, 2009.
- [61] E.S.E.-E. Requirements & Standards Division, ECSS-E-ST-35C_R1__Propulsion general requirements, 2009.
- [62] D.A. Herman, K.G. Unfried, XENON ACQUISITION STRATEGIES FOR HIGH-POWER ELECTRIC PROPULSION NASA MISSIONS, 2015.
- [63] F. Malet, V. Leconte, Y. Borthomieu, D. Division, OVERVIEW AND IN-ORBIT BEHAVIOUR OF THE FIRST LITHIUM-ION BATTERIES USED ONBOARD EUTELSAT 7A AND EUTELSAT HOT BIRD 13B GEO TELECOMMUNICATIONS SATELLITE, in: *10th Eur. Sp. Power Conf.*, Noordwijkerhout, The Netherland, 2014.
- [64] D.G. Gilmore, *Spacecraft Thermal Control Handbook Volume I: Fundamental Technologies*, The Aerospace Press, 2002.
- [65] B.N. Tomboulia, *Lightweight, High-Temperature Radiator for In-Space Nuclear- Electric Power and Propulsion*, University of Massachusetts Amherst Follow, 2014.
- [66] C. Rampersad, Preliminary design of a Very-Low-Thrust Geostationary Transfer Orbit to Sun-Synchronous Orbit Small Satellite Transfer, 2004.

- [67] D.A. Vallado, *Fundamentals of astrodynamics and applications*, 1997.
- [68] C.A. Paissoni, J. Rimani, N. Viola, T. Andreussi, GEO telecommunication satellite: New opportunities enabled by a 20kW class Hall thruster, in: *Proc. Int. Astronaut. Congr. IAC*, 2019.
- [69] R.H. Battin, *An Introduction to the Mathematics and Methods of Astrodynamics*, Revised edition, 1999.
- [70] G. Narducci, *Analysis of phasing maneuver performed by a solar electric platform*, Politecnico di Torino, 2020.
- [71] T. Bahill, A.M. Madni, *Tradeoff Decisions in System Design*, 2017. <https://doi.org/10.1007/978-3-319-43712-5>.
- [72] E.S.E.-E. Requirements & Standards Division, *ECSS-E-AS-11C_ISO_16290_Space_System_TRL*, 2014.
- [73] M. Mammarella, *A Comprehensive Modeling Framework for Integrated Mission Analysis and Design of a Reusable Electric Space Tug*, Politecnico di Torino, 2018.
- [74] C.A. Paissoni, N. Viola, T. Andreussi, A. Kitaeva, M. Andrenucci, The selection of an electric propulsion subsystem architecture for high-power space missions, in: *Proc. Int. Astronaut. Congr. IAC*, 2019.
- [75] M. Mammarella, C.A. Paissoni, R. Fusaro, N. Viola, T. Andreussi, A. Rossodivita, A 20kW-class Hall Effect Thruster to Enhance Present and Future Space Missions, in: *69 Th Int. Astronaut. Congr.*, 2018.
- [76] J. Virgili-Llop, P.C.E. Roberts, Z. Hao, Very Low Earth Orbit mission concepts for Earth Observation. Benefits and challenges DISCOVERER-VLEO satellites for EO View project Flexible Atmospheric Entry Heat Shield Deployed by Centrifugal Force View project, 2014. <https://www.researchgate.net/publication/271499606> (accessed March 31, 2021).
- [77] J.F. Gutiérrez Baena, *Study of the Business Model of three Earth Observation (EO) companies already present in the Very Low Earth Orbit market (VLEO)*, Master's Degree Thesis Aerosp. Eng. (2020).
- [78] ILS International Launch Services, *Experience ILS Achieve your mission - Angara*, 2017. www.ilslaunch.com (accessed March 31, 2021).
- [79] PSLV - ISRO, (n.d.). <https://www.isro.gov.in/launchers/pslv> (accessed March 31, 2021).
- [80] China Academy of Launch Vehicle Technology, *Long March 2C (LM-2C) Users Manual*, 199AD.
- [81] China Great Wall Industry Corporation, *LM-2D --- Launch Vehicle --- CGWIC*, (n.d.). <http://www.cgwic.com/launchservices/launchvehicle/LM2D.html> (accessed March 31, 2021).
- [82] China Great Wall Industry Corporation, *LM-4 --- Launch Vehicle --- CGWIC*, (n.d.). <http://www.cgwic.com/launchservices/launchvehicle/LM4.html> (accessed March 31, 2021).
- [83] ChangZheng 6 (Long March 6) Launch Vehicle - SinoDefence.com, (n.d.). <https://web.archive.org/web/20090302005031/http://www.sinodefence.com/space/launcher/changzheng6.asp> (accessed March 31, 2021).
- [84] Orbital Sciences Corporation, *Minotaur IV User's Guide*, 2006.
- [85] Orbital Sciences Corporation, *Taurus-Launch System Payload User's Guide*, 1993.

- [86] JAXA, User's Manual Epsilon Launch Vehicle, 2018.
- [87] M.L. Services, Cyclone-4M SLS ABBREVIATED USER'S GUIDE Cyclone-4M SLS User's Guide, 2019.
- [88] Arianespace, Soyuz User's Manual Issue 2-Revision 0, 2012. www.arianespace.com (accessed April 22, 2021).
- [89] Northrop Grumman, ANTARES Medium-class space launch vehicle, n.d.
- [90] Demetriades, S. T, A NOVEL SYSTEM FOR SPACE FLIGHT USING A PROPULSIVE FLUID ACCUMULATOR, *J. Brit. Interplanet. Soc. Vol: 17* (1959).
- [91] F. Berner, M. Camac, Air scooping vehicle, *Planet. Space Sci.* 4 (1961) 159–183. [https://doi.org/10.1016/0032-0633\(61\)90130-1](https://doi.org/10.1016/0032-0633(61)90130-1).
- [92] R.H. Reichel, T.L. Smith, D.R. Handford, Potentialities of Air-Scooping Electrical Space Propulsion Systems, in: *Electr. Propuls. Dev.*, American Institute of Aeronautics and Astronautics, 1963: pp. 711–743. <https://doi.org/10.2514/5.9781600864865.0711.0743>.
- [93] R.H. Reichel, Reichel, R. H., The Air-Scooping Nuclear-Electric Propulsion Concept for Advanced Orbital Space Transportation Missions, *JBIS.* 31 (1978) 62. <https://ui.adsabs.harvard.edu/abs/1978JBIS...31...62R/abstract> (accessed April 22, 2021).
- [94] A. Dolgich, Soviet Studies on low-thrust orbital Propellant-Scooping System, *Foreign Sci. Bull.* . 5 (1969).
- [95] L.A. Singh, M.L.R. Walker, A review of research in low earth orbit propellant collection, *Prog. Aerosp. Sci.* 75 (2015) 15–25. <https://doi.org/10.1016/j.paerosci.2015.03.001>.
- [96] M.A. Minovich, SELF-REFUELING ROCKET PROPULSION FOR FUTURE SPACE TRAVEL., in: *AIAA Pap.*, AIAA, 1985. <https://doi.org/10.2514/6.1985-1370>.
- [97] Y. Hisamoto, K. Nishiyama, H. Kuninaka, Development Statue of Atomic Oxygen Simulator for Air Breathing Ion Engine, *Int. Electr. Propuls. Conf.* (2011) 1–7. http://erps.spacegrant.org/uploads/images/images/iepc_articledownload_1988-2007/2011index/IEPC-2011-294.pdf.
- [98] K. Fujita, Air-intake performance estimation of air-breathing ion engines, *Nihon Kikai Gakkai Ronbunshu, B Hen/Transactions Japan Soc. Mech. Eng. Part B.* 70 (2004) 3038–3044. <https://doi.org/10.1299/kikaib.70.3038>.
- [99] K. Fujita, Air Intake Performance of Air Breathing Ion Engines, *J. Japan Soc. Aeronaut. Sp. Sci. JAPAN Soc. Aeronaut. Sp. Sci.* 52 (2004) 514–521. <https://doi.org/10.2322/jjsass.52.514>.
- [100] D. Di Cara, J. Gonzalez del Amo, A. Santovicenzo, B. Carnicero Dominguez, M. Arcioni, A. Caldwell, I. Roma, RAM Electric Propulsion for Low Earth Orbit Operation : an ESA study, *30th Int. Electr. Propuls. Conf.* (2007) IEPC-2007-162.
- [101] K. Hohman, V. Hruby, B. Pote, L. Olson, J. Szabo, P. Rostler, Atmospheric Breathing Electric Thruster for Planetary Exploration , *NIAC Spring Symp.* (2012).
- [102] K. Hohman, Atmospheric breathing electric thruster for planetary exploration, 2012.
- [103] F. Ceccanti, S. Marcuccio, Earth observation from elliptical orbits with very low altitude perigee, *4th IAA Symp. Small Satell. Earth Obs.* . (2003) 1–4. <https://www.researchgate.net/publication/254337349>.

- [104] A. Shabshelowitz, Study of RF Plasma Technology Applied to Air-Breathing Electric Propulsion, University of Michigan, 2013.
- [105] C. Explorer, GOCE: Gravity field and steady-state ocean circulation explorer, Eur. Sp. Agency ESA BR. (2003) 2–3.
- [106] C. Steiger, R. Floberghagen, M. Fehringer, J. Pineiro, P.P. Emanuelli, Flight Operations for Goce , Esa ' S Gravity Mission, ESA Living Planet Symp. (2010).
- [107] GOCE - eoPortal Directory - Satellite Missions.pdf, (n.d.).
- [108] C. Steiger, M. Romanazzo, P.P. Emanuelli, R. Floberghagen, M. Fehringer, The deorbiting of ESA's gravity mission GOCE - Spacecraft operations in extreme drag conditions, 13th Int. Conf. Sp. Oper. SpaceOps 2014. (2014). <https://doi.org/10.2514/6.2014-1934>.
- [109] H. Nagano, K. Kajiwara, Y. Hayakawa, T. Ozaki, Y. Kasai, Optimization of the Operating Parameters for a 20 mN Class Ion Thruster, in: 32nd Int. Electr. Propuls. Conf., Wiesbaden, Germany, 2011.
- [110] A. Noda, M. Homma, M. Utashima, The Study of a Super Low Altitude Satellite, A Feasibility Study Auton. Orbit Control SLATS. 7 (2009).
- [111] T. Fujita, M. Yamamoto, M. Utashima, H. Nagano, A feasibility study of autonomous orbit control for SLATS, 2009. <https://pdfs.semanticscholar.org/d5eb/f3a0dfd01da92475f31073b425a6e09eaaf2.pdf> (accessed May 14, 2021).
- [112] H. Nagano, K. Kajiwara, H. Osuga, T. Ozaki, T. Nakagawa, K. Shuto, Development Status of a New Power Processing Unit of Ion Engine System for the Super Low Altitude Test Satellite, in: 31st Int. Electr. Propuls. Conf., Ann Arbor, Michigan • USA, 2009.
- [113] G. Cifali, T. Misuri, P. Rossetti, M. Andrenucci, D. Valentian, D. Feili, B. Lotz, Experimental characterization of HET and RIT with atmospheric propellants, 32nd Int. Electr. Propuls. Conf. (2011) IEPC-2011-224.
- [114] G.O. Semenko, A. V., & Chislov, Study of anode layer thruster operation with gas mixtures, in: 24th Int. Electr. Propuls. Conf., 1995: pp. 95–78.
- [115] Busek Hall Effect Thrusters, (n.d.). http://www.busek.com/technologies__hall.htm (accessed April 25, 2021).
- [116] A. Gurciullo, A.L. Fabris, M.A. Cappelli, Ion plume investigation of a Hall effect thruster operating with Xe/N₂ and Xe/air mixtures, J. Phys. D. Appl. Phys. 52 (2019) 464003. <https://doi.org/10.1088/1361-6463/ab36c5>.
- [117] Francesco Romano, Stefanos Fasoulas, Schönherr Tony, et al-, Performance Evaluation of a Novel Inductive Atmosphere-Breathing EP System, in: 35th Int. Electr. Propuls. Conf., Georgia, USA, 2017. https://www.researchgate.net/publication/321619304_Performance_Evaluation_of_a_Novel_Inductive_Atmosphere-Breathing_EP_System (accessed April 25, 2021).
- [118] H. Kamhawi, W. Huang, T. Haag, R. Shastry, G. Soulas, T. Smith, I. Mikellides, R. Hofer, Performance and Thermal Characterization of the NASA-300MS 20 kW Hall Effect Thruster, in: 33rd Int. Electr. Propuls. Conf., Washington D.C. USA, 2013. <https://ntrs.nasa.gov/search.jsp?R=20140017775> (accessed August 2, 2018).
- [119] D.E. Clemens, Performance Evaluation of the Microwave Electrothermal Thruster Using Nitrogen, Simulated Hydrazine, and Ammonia, 2008.
- [120] A.I. Erofeev, A.P. Nikiforov, G.A. Popov, M.O. Suvorov, S.A. Syrin, S.A. Khartov, Air-Breathing Ramjet Electric Propulsion for Controlling Low-

- Orbit Spacecraft Motion to Compensate for Aerodynamic Drag, *Sol. Syst. Res.* 51 (2017) 639–645. <https://doi.org/10.1134/S0038094617070048>.
- [121] C. Charles, R.W. Boswell, R. Laine, P. MacLellan, An experimental investigation of alternative propellants for the helicon double layer thruster, *J. Phys. D. Appl. Phys.* 41 (2008) 175213. <https://doi.org/10.1088/0022-3727/41/17/175213>.
- [122] DISCOVERER - Project website, (n.d.). <https://discoverer.space/> (accessed April 25, 2021).
- [123] DISCOVERER – DISruptive teChnOlogies for VERY low Earth oRbit platforms | DISCOVERER Project | H2020 | CORDIS | European Commission, (n.d.). <https://cordis.europa.eu/project/id/737183/it> (accessed April 25, 2021).
- [124] N.H. Crisp, P.C.E. Roberts, S. Livadiotti, A. Macario Rojas, V.T.A. Oiko, S. Edmondson, S.J. Haigh, B.E.A. Holmes, L.A. Sinpetru, K.L. Smith, J. Becedas, R.M. Domínguez, V. Sullioti-Linner, S. Christensen, J. Nielsen, M. Bisgaard, Y.A. Chan, S. Fasoulas, G.H. Herdrich, F. Romano, C. Traub, D. García-Almiñana, S. Rodríguez-Donaire, M. Sureda, D. Kataria, B. Belkouchi, A. Conte, S. Seminari, R. Villain, In-orbit aerodynamic coefficient measurements using SOAR (Satellite for Orbital Aerodynamics Research), *Acta Astronaut.* 180 (2021) 85–99. <https://doi.org/10.1016/j.actaastro.2020.12.024>.
- [125] H.C. Nicholas, C.E.R. Peter, S. Edmondson, et al., SOAR - A Satellite for Orbital Aerodynamics Research, in: *Int. Astronaut. Congr.*, Bremen, Germany, 2018. https://www.researchgate.net/publication/327987918_SOAR_-_A_Satellite_for_Orbital_Aerodynamics_Research (accessed April 25, 2021).
- [126] D. González, V. Cañas, J. Becedas, R.M. Domínguez, P.C.E. Roberts, N.H. Crisp, V.T.A. Oiko, S. Edmondson, S.D. Worrall, S. Haigh, K. Smith, R.E. Lyons, S. Livadiotti, C. Huyton, L.A. Sinpetru, A. Striker, S. Rodriguez-Donaire, D. Garcia-Almiñana, M. Sureda, D. Kataria, G.H. Herdrich, F. Romano, Y. Chan, A. Boxberger, S. Fasoulas, C. Traub, R. Outlaw, V. Hanessian, A. Mølgaard, J. Nielsen, M. Bisgaard, R. Villain, J.S. Perez, A. Conte, B. Belkouchi, A. Schwalber, B. HeiBerer, Scilab and Xcos for VLEO satellites modelling, n.d. www.esi-group.com (accessed April 25, 2021).
- [127] F. Romano, Y.-A. Chan, G. Herdrich, P.C.E. Roberts, C. Traub, S. Fasoulas, N. Crisp, S. Edmondson, S. Haigh, B.A. Holmes, S. Livadiotti, A. Macario-Rojas, V.T. Abrao Oiko, K. Smith, L. Sinpetru, J. Becedas, R.M. Dominguez, S. Christensen, T.K. Jensen, J. Nielsen, M. Bisgaard, D. Garcia-Almiñana, S. Rodriguez-Donaire, M. Sureda, M. Garcia-Berenguer, D. Kataria, R. Villain, S. Seminari, A. Conte, B. Belkouchi, RF Helicon-based Plasma Thruster (IPT): Design, Set-up, and First Ignition, 2020.
- [128] F. Romano, Y.A. Chan, G. Herdrich, C. Traub, S. Fasoulas, P.C.E. Roberts, K. Smith, S. Edmondson, S. Haigh, N.H. Crisp, V.T.A. Oiko, S.D. Worrall, S. Livadiotti, C. Huyton, L.A. Sinpetru, A. Straker, J. Becedas, R.M. Domínguez, D. González, V. Cañas, V. Sullioti-Linner, V. Hanessian, A. Mølgaard, J. Nielsen, M. Bisgaard, D. Garcia-Almiñana, S. Rodriguez-Donaire, M. Sureda, D. Kataria, R. Outlaw, R. Villain, J.S. Perez, A. Conte, B. Belkouchi, A. Schwalber, B. HeiBerer, RF Helicon-based Inductive Plasma Thruster (IPT) Design for an Atmosphere-Breathing Electric

- Propulsion system (ABEP), *Acta Astronaut.* 176 (2020) 476–483. <https://doi.org/10.1016/j.actaastro.2020.07.008>.
- [129] F. Romano, G. Herdrich, P.C.E. Roberts, Inductive Plasma Thruster (IPT) for an Atmosphere- Breathing Electric Propulsion System: Design and Set in Operation, in: 36th Int. Electr. Propuls. Conf., Vienna, Austria, 2019. https://www.researchgate.net/publication/335985019_Inductive_Plasma_Thrustert_IPT_for_an_Atmosphere-Breathing_Electric_Propulsion_System_Design_and_Set_in_Operation/stats (accessed April 25, 2021).
- [130] S. Masillo, F. Romano, R. Ruggero, Analysis of electrodeless plasma source enhancement by an externally applied magnetic field for an inductive plasma thruster (IPT), in: 7th Russ. Conf. Electr. Propuls., Germany, 2018. https://www.researchgate.net/publication/331479205_Analysis_of_electrodeless_plasma_source_enhancement_by_an_externally_applied_magnetic_field_for_an_inductive_plasma_thruster_IPT (accessed April 25, 2021).
- [131] F. Romano, B. Massuti-Ballester, T. Binder, G. Herdrich, S. Fasoulas, T. Schönherr, System analysis and test-bed for an atmosphere-breathing electric propulsion system using an inductive plasma thruster, *Acta Astronaut.* 147 (2018) 114–126. <https://doi.org/10.1016/j.actaastro.2018.03.031>.
- [132] T. Andreussi, G. Cifali, V. Giannetti, A. Piragino, E. Ferrato, A. Rossodivita, M. Andrenucci, J. Longo, L. Walpot, Development and Experimental Validation of a Hall Effect Thruster RAM-EP Concept, 35th Int. Electr. Propuls. Conf. (2017) IEPC-2017-377. https://iepc2017.org/sites/default/files/speaker-papers/iepc-2017-377_ram_final.pdf.
- [133] AETHER Project | Demonstrating Air-Breathing Electric Space Propulsion, (n.d.). <https://aether-h2020.eu/> (accessed April 25, 2021).
- [134] Air-breathing Electric THrustER | AETHER Project | H2020 | CORDIS | European Commission, (n.d.). <https://cordis.europa.eu/project/id/870436/it> (accessed April 25, 2021).
- [135] T. Andreussi, C.A. Paisonni, E. Ferrato, V. Giannetti, M. Reza, F. Faraji, A. Piragino, A. Kitaeva, A. Rossodivita, M. Andrenucci, SITAEL’s activities on the development of air breathing technology, *Proc. Int. Astronaut. Congr. IAC. 2020-Octob* (2020) 12–14.
- [136] CLOSE TO THE EARTH, (n.d.). <https://www.dtascarl.org/en/progettidta/close-to-the-earth/> (accessed April 25, 2021).
- [137] PWC, *Main Trends & Challenges in the Space Sector 2 nd Edition*, 2020.
- [138] K.W. Crane, E. Linck, B. Lal, R.Y. Wei, *Measuring the Space Economy: Estimating the Value of Economic Activities in and for Space*, 2020.
- [139] S. Fishman, *EARTH OBSERVATION: STATE OF PLAY AND FUTURE PROSPECTS*, in: *Advis. Comm. Commer. Remote Sens. Meet.*, 2018.
- [140] *Satellite Value Chain Report - Key Trends and Indicators on Supply and Demand*, (n.d.). <https://www.globenewswire.com/news-release/2019/05/01/1813961/0/en/Satellite-Value-Chain-Report-Key-Trends-and-Indicators-on-Supply-and-Demand.html> (accessed April 22, 2021).

- [141] Euroconsult, SATELLITES TO BE BUILT & LAUNCHED BY 2028, 2019. https://www.euroconsult-ec.com/research/WS319_free_extract_2019.pdf (accessed April 22, 2021).
- [142] Bryce - Reports, (n.d.). <https://brycetech.com/reports> (accessed April 22, 2021).
- [143] Space Foundation, Space Foundation Annual Report 2019, 2019.
- [144] CATAPULT, Routes to Market Report Satellite Technologies for 24-Persistent Surveillance, n.d.
- [145] S. Voigt, F. Giulio-Tonolo, J. Lyons, J. Kučera, B. Jones, T. Schneiderhan, G. Platzcek, K. Kaku, M.K. Hazarika, L. Czarán, S. Li, W. Pedersen, G.K. James, C. Proy, D.M. Muthike, J. Bequignon, D. Guha-Sapir, Global trends in satellite-based emergency mapping, *Science* (80-.). 353 (2016) 247–252. <https://doi.org/10.1126/science.aad8728>.
- [146] I. Cozmuta, New Space Opportunities in the US, n.d.
- [147] A.J. Volponi, Gas turbine engine health management: Past, present, and future trends, *J. Eng. Gas Turbines Power.* 136 (2014). <https://doi.org/10.1115/1.4026126>.
- [148] European Commission, COPERNICUS MArker Report, 2019. <https://doi.org/10.2873/011961>.
- [149] I. Coppa, P. Woodgate, Global Outlook 2018: Spatial Information Industry, *CRC Spat. Inf.* (n.d.). https://www.researchgate.net/publication/324691018_Global_Outlook_2018_Spatial_Information_Industry (accessed April 22, 2021).
- [150] Digital Globe, Remote Sensing Technology Trends and Agriculture, n.d. www.digitalglobe.com/Corporate (accessed April 22, 2021).
- [151] P. Besha, A. Macdonald, Economic Development OF LOW EARTH ORBIT, n.d.
- [152] J. Greason, J.C. Bennett, THE ECONOMICS OF SPACE: AN INDUSTRY READY TO LAUNCH, 2019.
- [153] Esre, ESRE Whitepaper Selected Trends and Space Technologies Expected to Shape the Next Decade, 2017.
- [154] Innovation Finance Advisory, European Investment Advisory Hub, The future of the European space sector How to leverage Europe’s technological leadership and boost investments for space ventures, n.d.
- [155] L. Bryce Space and Technology, Global Space Industry Dynamics, 2019.
- [156] ICEYE, Persistent agriculture land monitoring with daily radar satellite data, 2019.
- [157] ICEYE, Preventing illegal fishing with actionable radar satellite data, 2019.
- [158] ICEYE, Problem solving in the insurance industry with SAR data, 2019.
- [159] O. De Weck, R. De Neufville, M. Chaize, Staged deployment of communications satellite constellations in low earth orbit, *J. Aerosp. Comput. Inf. Commun.* (2004) 119–136. <https://doi.org/10.2514/1.6346>.
- [160] A. Space, LEO Commercialization Concept, 2018.
- [161] B. Lal, A. Balakrishnan, A. Picard, B. Corbin, J. Behrens, E. Green, R. Myers, B. Zuckerman, M. Yarymovych, I. Boyd, M. Macdonald, Trends in Small Satellite Technology and the Role of the NASA Small Spacecraft Technology Program Final Update to the NASA Advisory Committee Technology, Innovation and Engineering Committee, 2017.
- [162] WMO OSCAR | List of all Satellites, (n.d.). <https://www.wmo-sat.info/oscar/satellites> (accessed April 22, 2021).

- [163] Satellite Missions Directory - Earth Observation Missions - eoPortal, (n.d.). <https://directory.eoportal.org/web/eoportal/satellite-missions> (accessed April 22, 2021).
- [164] CelesTrak: Search Satellite Catalog, (n.d.). <https://celestrak.com/satcat/search.php> (accessed April 23, 2021).
- [165] NASA, NASA Space Science Data Coordinated Archive, (n.d.). <https://nssdc.gsfc.nasa.gov/nmc/>.
- [166] Grand View Research, Satellite Communication Market Size Report, 2020-2027, 2020. <https://www.grandviewresearch.com/industry-analysis/satellite-communication-market> (accessed April 23, 2021).
- [167] C. Henry, GEO satellite orders are up, but full rebound remains to be seen - SpaceNews, SpaceNews. (n.d.). <https://spacenews.com/geo-satellite-orders-are-up-but-full-rebound-remains-to-be-seen/> (accessed April 23, 2021).
- [168] Caleb Henry, Geostationary satellite orders bouncing back - SpaceNews, SpaceNews. (2020). <https://spacenews.com/geostationary-satellite-orders-bouncing-back/> (accessed April 23, 2021).
- [169] G. Curzi, D. Modenini, P. Tortora, Large constellations of small satellites: A survey of near future challenges and missions, *Aerospace*. 7 (2020). <https://doi.org/10.3390/AEROSPACE7090133>.
- [170] W.J. Pang, Bo B., X. Meng, X.Z. Yu, J. Guo, J. Zhou, BOOM OF THE CUBESAT: A STATISTIC SURVEY OF CUBSATS LAUNCH IN 2003-2015, in: 67th Int. Astronaut. Congr., 2016. https://www.researchgate.net/publication/311279467_BOOM_OF_THE_CUBESAT_A_STATISTIC_SURVEY_OF_CUBSATS_LAUNCH_IN_2003-2015 (accessed April 23, 2021).
- [171] SmallGEO - eoPortal Directory - Satellite Missions, (n.d.). <https://earth.esa.int/web/eoportal/satellite-missions/s/smallgeo> (accessed April 23, 2021).
- [172] H. Luebberstedt, J.C. Bastante, M. Lau, S. Beekmans, M. De Tata, A. Schneider, P. Rathsman, Electra - Full Electric Propulsion Satellite Platform for GEO Missions, 2017. <https://www.ohb-system.de/electra-358.html>.
- [173] J. Gonzalez del Amo, European Space Agency (ESA) Electric Propulsion Activities, in: 34th Int. Electr. Propuls. Conf., Dresden, 2017.
- [174] Next Generation Platform (NEOSAT) Overview | ESA's ARTES Programmes, (n.d.). <https://artes.esa.int/neosat/overview> (accessed April 23, 2021).
- [175] Earth Observation | Euroconsult, (n.d.). <https://www.euroconsult-ec.com/earthobservation> (accessed April 23, 2021).
- [176] E. Ferrato, V. Giannetti, A. Piragino, M. Andrenucci, T. Andreussi, C.A. Paissoni, Development Roadmap of SITAEL 's RAM-EP System, 36th Int. Electr. Propuls. Conf. (2019) 1–18.
- [177] E. Ferrato, NUMERICAL MODELING OF AN AIR BREATHING HALL EFFECT THRUSTER Dipartimento di Ingegneria Civile e Industriale, University of Pisa, 2017.
- [178] D. Di Cara, J. Gonzalez Del Amo, A. Santovincenzo, B. Carnicero Dominguez, M. Arcioni, A. Caldwell, I. Roma, RAM Electric Propulsion for Low Earth Orbit Operation: an ESA study, n.d.
- [179] NASA, NASA Systems Engineering Handbook, *Syst. Eng.* 6105 (2007) 360. [https://doi.org/10.1016/0016-0032\(66\)90450-9](https://doi.org/10.1016/0016-0032(66)90450-9).
- [180] G. Chiandussi, M. Codegone, S. Ferrero, F.E. Varesio, Comparison of multi-

- objective optimization methodologies for engineering applications, *Comput. Math. with Appl.* 63 (2012) 912–942. <https://doi.org/10.1016/j.camwa.2011.11.057>.
- [181] B. Wie, C.M. Roithmayr, Attitude and Orbit Control of a Very Large Geostationary Solar Power Satellite, *J. Guid. Control. Dyn.* 28 (n.d.). <https://doi.org/10.2514/1.6813>.
- [182] J.M. Picone, A.E. Hedin, D.P. Drob, A.C. Aikin, NRLMSISE-00 empirical model of the atmosphere: Statistical comparisons and scientific issues, *J. Geophys. Res. Sp. Phys.* 107 (2002) 1–16. <https://doi.org/10.1029/2002JA009430>.
- [183] E.S.E.-E. Requirements & Standards Division, ECSS-E-ST-10-04C_Space environment, 2008.
- [184] N.S. and I.S.N.C. for E.I. US Department of Commerce, NOAA National Centers for Environmental Information (NCEI), (n.d.).
- [185] J.N. Moss, K.A. Boyles, F.A. Greene, Orion Aerodynamics for Hypersonic Free Molecular to Continuum Conditions, n.d. <https://ntrs.nasa.gov/search.jsp?R=20060056443> (accessed April 3, 2021).
- [186] M.M. Moe, S.D. Wallace, K. Moe, Refinements in determining satellite drag coefficients - Method for resolving density discrepancies, *J. Guid. Control. Dyn.* 16 (1993) 441–445. <https://doi.org/10.2514/3.21029>.
- [187] P.A. Chambre, S.A. Schaaf, *Flow of Rarefied Gases* | Princeton University Press, Princeton Legacy Li..., 1969. <https://press.princeton.edu/books/hardcover/9780691654904/flow-of-rarefied-gases> (accessed April 23, 2021).
- [188] S. Varma, *Control of Satellites Using Environmental Forces : Aerodynamic Drag / Solar Radiation Pressure*, 2011.
- [189] C. Pardini, W.K. Tobiska, L. Anselmo, Analysis of the orbital decay of spherical satellites using different solar flux proxies and atmospheric density models, in: *Adv. Sp. Res.*, Elsevier Ltd, 2006: pp. 392–400. <https://doi.org/10.1016/j.asr.2004.10.009>.
- [190] X. Jia, M. Xu, X. Pan, X. Mao, Eclipse Prediction Algorithms for Low-Earth-Orbiting Satellites, *IEEE Trans. Aerosp. Electron. Syst.* 53 (2017) 2963–2975. <https://doi.org/10.1109/TAES.2017.2722518>.
- [191] W. Torge, *Geodesy*, Walter de Gruyter, Berlin-New York, 1991. [http://fgg-web.fgg.uni-lj.si/~mkuhar/Zalozba/Torge-Geodesy\(2001\).pdf](http://fgg-web.fgg.uni-lj.si/~mkuhar/Zalozba/Torge-Geodesy(2001).pdf) (accessed April 23, 2021).
- [192] F.G. Lemoine, S.C. Kenyo, J.K. Factor, R.G. Trimmer, N.K. Pavlis, D.S. Chinn, C.M. Cox, S.M. Klosko, S.B. Luthcke, M.H. Torrence, Y.M. Wang, R.G. Williamson, E.C. Pavlis, R.H. Rapp, T.R. Olson, *The Development of the NASA GSFC and NIMA Joint Geopotential Model*, NASA-Goddard Spac..., Greenbelt, Maryland , 1998. https://doi.org/10.1007/978-3-662-03482-8_62.
- [193] N.K. Pavlis, S.A. Holmes, S.C. Kenyon, J.K. Factor, The development and evaluation of the Earth Gravitational Model 2008 (EGM2008), *J. Geophys. Res. Solid Earth.* 117 (2012) 4406. <https://doi.org/10.1029/2011JB008916>.
- [194] H. Yildiz, Quantifying the individual contributions of GOCE gradients for regional quasi-geoid modeling in a relatively rough topography, *J. Appl. Geophys.* 187 (2021) 104289. <https://doi.org/10.1016/j.jappgeo.2021.104289>.
- [195] E. Sinem Ince, F. Barthelmes, S. Reißland, K. Elger, C. Förste, F. Flechtner,

- H. Schuh, ICGEM – 15 years of successful collection and distribution of global gravitational models, associated services, and future plans, *Earth Syst. Sci. Data*. 11 (2019) 647–674. <https://doi.org/10.5194/essd-11-647-2019>.
- [196] ESA - GOCE first global gravity model, (n.d.). https://www.esa.int/ESA_Multimedia/Images/2010/06/GOCE_first_global_gravity_model (accessed May 19, 2021).
- [197] GOCE flight control team (HSO-OEG), GO-RP-ESC-FS-6268: GOCE End-of-mission operations report, (2014) 1–193.
- [198] Alenia Spazio, E. Astrium, A. Space, Onera, GOCE (System Critical Design Review (CDR) Executive Summary), 2005.
- [199] E.S.E.-E. Requirements & Standards Division, ECSS-S-ST-00-01C_Glossary of terms, 2012.
- [200] Glossary - NASA Crew Exploration Vehicle, SOL NNT05AA01J, Attachment J-6, (n.d.). <http://www.spaceref.com/news/viewsr.html?pid=15201> (accessed April 13, 2021).
- [201] S. Singh, A DATA-DRIVEN APPROACH TO CUBESAT HEALTH MONITORING, Polytechnic State University, 2017.
- [202] J.E. Polk, J.R. Brophy, Life Qualification of Hall Thrusters By Analysis and Test, in: *Sp. Propuls.* 2018, Seville, Spain, 2018.
- [203] J.W. Dankanich, J.R. Brophy, J.E. Polk, Lifetime Qualification Standard for Electric Thrusters, in: 45th AIAA/ASME/SAE/ASEE Jt. Propuls. Conf. Exhib., Denver, Colorado, 2009. <https://doi.org/10.2514/6.2009-5095>.
- [204] L. Marinai, GAS-PATH DIAGNOSTICS AND PROGNOSTICS FOR AERO-ENGINES USING FUZZY LOGIC AND TIME SERIES ANALYSIS School of Engineering PhD THESIS, Cranfield University, 2004.
- [205] L. Marinai, D. Probert, R. Singh, Prospects for aero gas-turbine diagnostics: a review, *Appl. Energy*. 79 (2004) 109–126. <https://doi.org/10.1016/j.apenergy.2003.10.005>.
- [206] L.A. Urban, Gas turbine engine parameter interrelationships, 1969.
- [207] L.A. Urban, Gas Path Analysis Applied to Turbine Engine Condition Monitoring, *J. Aircr.* 10 (n.d.). <https://doi.org/10.2514/3.60240>.
- [208] R. Macausland, Moore-Penrose Inverse, 2014.
- [209] A.M. Sajeev, Gas Turbine Diagnostics Based on Gas Path Analysis. (MSc. Thesis), Delft University of Technology, 2015.
- [210] R.E. Kalman, A new approach to linear filtering and prediction problems, *J. Fluids Eng. Trans. ASME*. 82 (1960) 35–45. <https://doi.org/10.1115/1.3662552>.
- [211] S. Sampath, Fault diagnostics for advanced cycle marine gas turbine using genetic algorithm, Cranfield University, 2003. <http://dspace.lib.cranfield.ac.uk/handle/1826/10204> (accessed April 10, 2021).
- [212] J.S. Breese, E.J. Horvitz, M.A. Peot, R. Gay, G.H. Quentin, Automated decision-analytic diagnosis of thermal performance in gas turbines, in: *ASME 1992 Int. Gas Turbine Aeroengine Congr. Expo. GT 1992*, American Society of Mechanical Engineers, 1992. <https://doi.org/10.1115/92-GT-399>.
- [213] C.A. Palmer, Combining Bayesian belief networks with gas path analysis for test cell diagnostics and overhaul, in: *Proc. ASME Turbo Expo*, American Society of Mechanical Engineers (ASME), 1998. [261](https://doi.org/10.1115/98-</p>
</div>
<div data-bbox=)

GT-168.

- [214] C. Romessis, K. Mathioudakis, A. Stamatis, Setting up a Belief Network for Turbofan Diagnosis With the Aid of an Engine Performance Model, Undefined. (2001).
- [215] K. Mathioudakis, P. Kamboukos, A. Stamatis, Turbofan performance deterioration tracking using nonlinear models and optimization techniques, *J. Turbomach.* 124 (2002) 580–587. <https://doi.org/10.1115/1.1512678>.
- [216] C. Romessis, K. Mathioudakis, Bayesian network approach for gas path fault diagnosis, *J. Eng. Gas Turbines Power.* 128 (2006) 64–72. <https://doi.org/10.1115/1.1924536>.
- [217] and P.F. Karvounis, George, Automated Detection of Engine Health Using a Hybrid Model-Based and Fuzzy-Logic Approach, in: 16th Int. Symp. Air-Breathing Engines, Cleveland, OH, 2003.
- [218] P.C. Chang, C.H. Liu, R.K. Lai, A fuzzy case-based reasoning model for sales forecasting in print circuit board industries, *Expert Syst. Appl.* 34 (2008) 2049–2058. <https://doi.org/10.1016/j.eswa.2007.02.011>.
- [219] M.; Yang, Shen, Reinforcing fuzzy rule-based diagnosis of turbomachines with case-based reasoning, *Int. J. Knowledge-Based Intell. Eng. Syst.* 12 (n.d.) 173–181. <https://doi.org/10.3233/KES-2008-12208>.
- [220] W.C. Larson, D.L. Brown, W.A. Hargus, Thrust Efficiency, Energy Efficiency, and the Role of VDF in Hall Thruster Performance Analysis (Preprint) Performance Measurement of a Rotating Detonation Rocket Engine View project, in: 43rd AIAA/ASME/SAE/ASEE Jt. Propuls. Conf. Exhib., Cincinnati, OH, 2007. <https://doi.org/10.2514/6.2007-5270>.
- [221] R. Ganguli, Data rectification and detection of trend shifts in jet engine path measurements using median filters and fuzzy logic, *J. Eng. Gas Turbines Power.* 124 (2002) 809–816. <https://doi.org/10.1115/1.1470482>.
- [222] R.R. Hofer, Development and Characterization of High-Efficiency, High-Specific Impulse Xenon Hall Thrusters, University of Michigan, 2004.
- [223] B. Pote, V. Hrubby, J. Monheiser, Performance of an 8 kW Hall Thruster, n.d.
- [224] C.H. McLean, J.B. McVey, T. Schappell, Testing of a U.S.-built HET system for orbit transfer applications, in: 35th Jt. Propuls. Conf. Exhib., American Institute of Aeronautics and Astronautics Inc, AIAA, 1999. <https://doi.org/10.2514/6.1999-2574>.
- [225] V. Hrubby, B. Pote, M. Gamero-Castaño, G. Kolencik, L. Byrne, R. Tedrake, M. Delichatsios, Hall Thrusters Operating in Pulsed Mode, 2001.
- [226] A.I. Bugrova, A.S. Lipatov, A.I. Morozov, D. V. Churbanov, On a similarity criterion for plasma accelerators of the stationary plasma thruster type, *Tech. Phys. Lett.* 28 (2002) 821–823. <https://doi.org/10.1134/1.1519018>.
- [227] M. Andrenucci, I. Engine, H.E. Thruster, Performance Mapping of Electrostatic Propulsion Devices Space Propulsion 2018, 2018 (2018).
- [228] F. Battista, E.A. De Marco, T. Misuri, M. Andrenucci, A Review of the Hall Thruster Scaling Methodology, in: 30th Int. Electr. Propuls. Conf., Florence, Italy, 2007. <https://doi.org/10.1109/TPS.2014.2315851>.
- [229] D.Y. Oh, R.R. Hofer, I. Katz, J.A. Sims, N.Z. Warner, T.M. Randolph, R.T. Reeve, R.C. Moeller, Benefits of Using Hall Thrusters for a Mars Sample Return Mission, in: 31st Int. Electr. Propuls. Conf., Ann Arbor, Michigan, 2009.
- [230] R.R. Hofer, R.S. Jankovsky, A hall thruster performance model incorporating the effects of a multiply-charged plasma, in: 37th Jt. Propuls.

- Conf. Exhib., American Institute of Aeronautics and Astronautics Inc., 2001. <https://doi.org/10.2514/6.2001-3322>.
- [231] D.M.D.M. Goebel, I. Katz, K. I. Atz, *Fundamentals of Electric Propulsion: Ion and Hall Thrusters*, JPL SPACE, JPL SPACE SCIENCE AND TECHNOLOGY SERIES, 2008.
- [232] V. Kim, Main Physical Features and Processes Determining the Performance of Stationary Plasma Thrusters, *J. Propuls. Power.* 14 (1998) 736–743.
- [233] M. Andrenucci, L. Biagioni, S. Marcuccio, F. Paganucci, *Fundamental Scaling Laws for Electric Propulsion Concepts-Part 1: Hall Effect Thrusters*, 2003.
<http://scholar.google.com/scholar?hl=en&btnG=Search&q=intitle:Fundamental+scaling+laws+for+electric+propulsion+concepts+-+Part+1+:+Hall+Effect+Thrusters#1>.
- [234] M.J. Sekerak, A.D. Gallimore, A. Arbor, Mode Transitions in Hall-Effect Thrusters Induced by Variable Magnetic Field Strength, (n.d.) 1–15. <https://doi.org/10.2514/1.B35709>.
- [235] J.P. Boeuf, Tutorial: Physics and modeling of Hall thrusters, *J. Appl. Phys.* 121 (2017). <https://doi.org/10.1063/1.4972269>.
- [236] J.P. Boeuf, L. Garrigues, Low frequency oscillations in a stationary plasma thruster, *J. Appl. Phys.* 84 (1998).
- [237] K. Hara, M.J. Sekerak, I.D. Boyd, A.D. Gallimore, Mode transition of a Hall thruster discharge plasma, *J. Appl. Phys.* 115 (2014). <https://doi.org/10.1063/1.4879896>.
- [238] A. Piragino, F. Faraji, M. Reza, E. Ferrato, A. Piraino, T. Andreussi, Background Pressure Effects on the Performance of a 20 kW Magnetically Shielded Hall Thruster Operating in Various Configurations, *Aerospace*. 8 (2021) 69. <https://doi.org/10.3390/aerospace8030069>.

Appendix A - Functional Analysis and Function/Product Matrices for space tug OOS mission

The functional analysis and Function/Product matrices derived for the space tug OOS mission are presented in this appendix. In particular, the functional analysis allows identifying the functions that shall be provided at the component level. The function/Product matrices are then used to allocate each function to a specific component. For a better reporting of the matrices, they were already subdivided for each subsystem of the space tug.

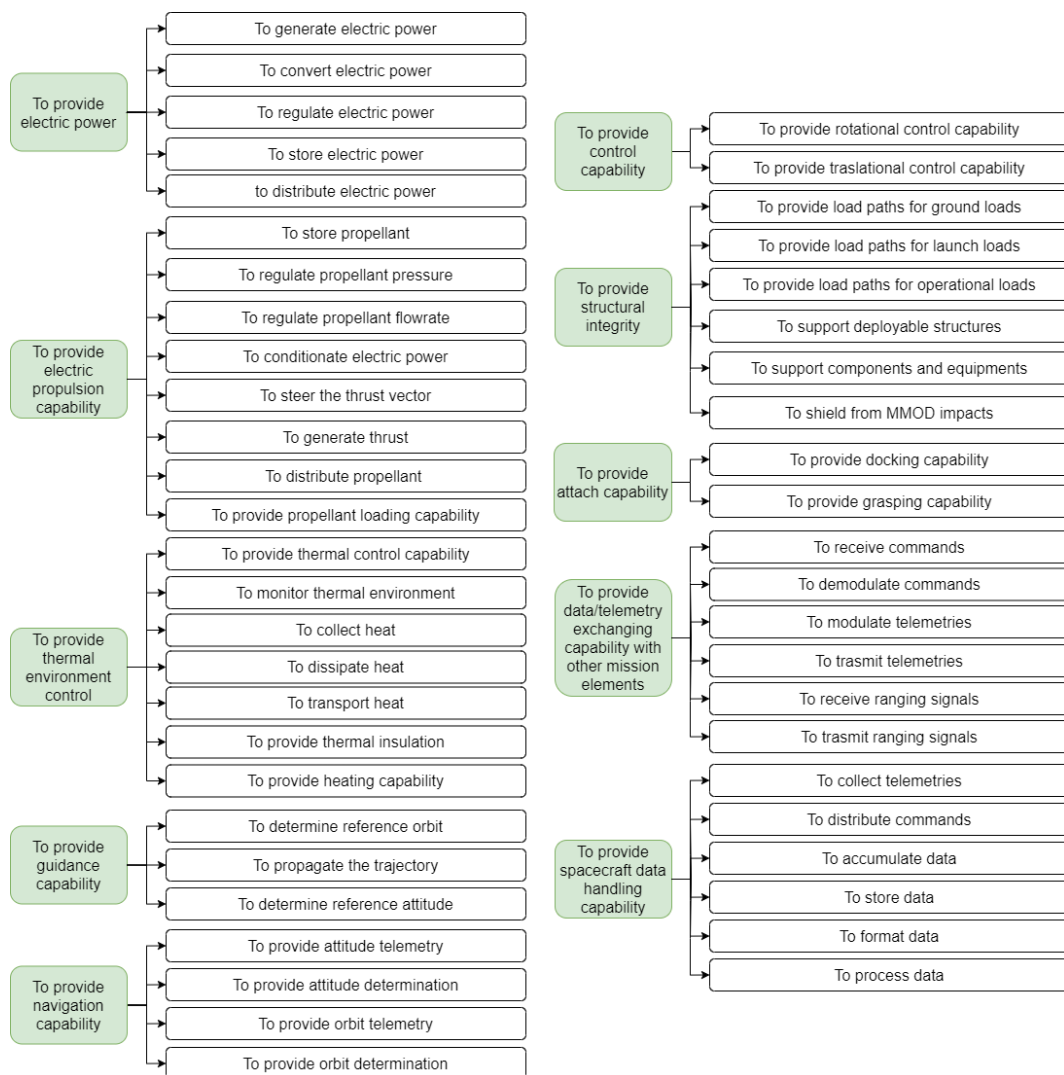


Figure 114-ANNEX-A: Functional tree at subsystem/component level of a space tug operated in the OOS scenario.

Table 66-ANNEX-A: Function/Product matrix for POW subsystem.

	Solar Array	PCDU	Battery	Power Bus	SADM
To generate electric power	X				
To convert electric power		X			
To regulate electric power		X			
To provide electric power distribution		X			
To recharge the batteries		X			
To store electric power			X		
To distribute electric power to the other system components				X	
To provide Sun alignment					X

Table 67-ANNEX-A: Function/Product matrix for EPS subsystem.

	Tank	PMA	FCU	PPU	TPM	TU	Piping	Fill-in
To store propellant	X							
To regulate propellant pressure		X						
To regulate propellant flowrate			X					
To conditionate electric power				X				
To provide commands for the propellant pressure regulation				X				
To provide commands for the propellant flowrate regulation				X				
To steer the thrust vector					X			
To generate thrust						X		
To distribute propellant							X	
To provide propellant loading capability								X

Table 68-ANNEX-A: Function/Product matrix for TCS subsystem.

	TCS Controller	TCS sensors	Radiators	Heat Pipes	MLI blankets	Heaters
To provide thermal control capability	X					
To measure the temperature		X				
To dissipate heat			X			
To transport heat				X		

To provide thermal insulation					X	
To provide heating capability						X

Table 69-ANNEX-A: Function/Product matrix for POW subsystem.

	AOCS Controller	AOCS Sensors - Sun Sensors	AOCS Sensors - Star Trackers	AOCS Sensors - IMU	AOCS - Attitude actuators	AOCS Thrusters
To provide orbit determination	X					
To provide attitude determination	X					
To provide orbit propagation	X					
To provide reference trajectory determination	X					
To provide reference attitude determination	X					
To measure the relative direction of the Sun for orbit determination		X				
To measure the relative direction of the stars for orbit determination			X			
To measure linear acceleration				X		
To measure the relative direction of the Sun for attitude determination		X				
To measure the relative direction of the stars for attitude determination			X			
To measure the spacecraft spin rate				X		
To provide translational control						X
To provide rotational control					X	

Table 70-ANNEX-A: Function/Product matrix for STRUCT subsystem.

	Primary Structure	Secondary Structure/Mechanisms	MMOD Shields	Docking Interface	Gasping Interface
To provide load paths for ground loads	X				

To provide load paths for launch loads	X				
To provide load paths for operational loads	X				
To support deployable structures		X			
To support components and equipment		X			
To shield from MMOD impacts			X		
To provide docking capability				X	
To provide the grasping capability					X

Table 71-ANNEX-A: Function/Product matrix for COMM subsystem.

	Antenna	Receiver	Transmitter	Communication	Tracking Equipment
To receive ranging signals					X
To transmit ranging signal					X
To provide pointing capability					X
To receive data	X				
To transmit data	X				
To demodulate received data		X			
To modulate data to be transmitted			X		
To provide data interface of the COMM				X	

Table 72-ANNEX-A: Function/Product matrix for CDH subsystem.

	Storage Unit	Data Bus	CDMU
To collect data			X
To process data			X
To store data	X		
To format data			X
To process on-board data			X
To collect telemetries			X
To process telemtries			X
To validate command			X
To process command			X
To provide data connection among the components	X		

Appendix B – Results of Space Tug architecture analysis

The results of the analysis performed on the cluster vs monolithic architectures based on both HT5k and HT20k are presented. The scenario exploited for these simulations is the MS.2 in which the space tug services a telecommunication satellite for its initial transferring in GEO and successively is operated for a relocation manoeuvre of a second telecommunication satellite.

The following results show the main mission budgets in terms of (i) Mission total duration, (ii) space tug dry mass, (iii) space tug wet mass, and (iv) space tug wet mass with telecommunication satellite mass.

Table 73 - APPENDIX-B: Mission total duration, HT20k configurations.

# Thr	First Phasing Angle [°]	Second Phasing Angle [°]	Miss Total Duration [Days]
1	30	30	845,3
2	30	30	582,5
3	30	30	490,5
4	30	30	446,4
1	30	60	847,4
2	30	60	584,0
3	30	60	493,6
4	30	60	443,3
1	30	90	847,1
2	30	90	582,8
3	30	90	492,1
4	30	90	443,4
1	30	120	847,1
2	30	120	586,5
3	30	120	490,0
4	30	120	444,5
1	30	150	845,8
2	30	150	582,5
3	30	150	494,6
4	30	150	445,2
1	30	180	844,2
2	30	180	582,6
3	30	180	490,1

4	30	180	443,2
---	----	-----	-------

Table 74 - APPENDIX-B: Mission total duration, HT5k configurations.

# Thr	First Phasing Angle [°]	Second Phasing Angle [°]	Miss Total Duration [Days]
4	30	30	799,6
8	30	30	552,5
12	30	30	465,7
16	30	30	426,0
4	30	60	803,0
8	30	60	549,2
12	30	60	464,3
16	30	60	426,5
4	30	90	801,6
8	30	90	548,8
12	30	90	463,6
16	30	90	427,2
4	30	120	800,1
8	30	120	552,2
12	30	120	463,4
16	30	120	424,7
4	30	150	802,1
8	30	150	548,0
12	30	150	462,2
16	30	150	427,3
4	30	180	802,4
8	30	180	553,2
12	30	180	465,4
16	30	180	424,8

Table 75 - APPENDIX-B: Mass dry HT20k configurations.

# Thr	First Phasing Angle [°]	Second Phasing Angle [°]	Mass Dry [Kg]
1	30	30	2159,5
2	30	30	4023,1
3	30	30	5872,8
4	30	30	7724,2
1	30	60	2160,0
2	30	60	4023,2
3	30	60	5873,3

4	30	60	7723,7
1	30	90	2160,0
2	30	90	4022,8
3	30	90	5873,3
4	30	90	7723,3
1	30	120	2159,8
2	30	120	4023,3
3	30	120	5873,0
4	30	120	7724,3
1	30	150	2159,6
2	30	150	4022,7
3	30	150	5872,7
4	30	150	7723,5
1	30	180	2159,6
2	30	180	4022,7
3	30	180	5872,8
4	30	180	7723,5

Table 76 - APPENDIX-B: Mass dry HT5k configurations.

# Thr	First Phasing Angle [°]	Second Phasing Angle [°]	Mass Dry [Kg]
4	30	30	2098,4
8	30	30	3920,3
12	30	30	5738,2
16	30	30	7707,0
4	30	60	2098,5
8	30	60	3920,3
12	30	60	5737,3
16	30	60	7707,2
4	30	90	2098,6
8	30	90	3920,1
12	30	90	5737,7
16	30	90	7707,0
4	30	120	2098,4
8	30	120	3920,1
12	30	120	5737,6
16	30	120	7706,4
4	30	150	2098,2
8	30	150	3919,9
12	30	150	5737,1
16	30	150	7706,2

4	30	180	2098,3
8	30	180	3920,2
12	30	180	5737,9
16	30	180	7706,6

Table 77 - APPENDIX-B: Mass wet HT20k configurations.

# Thr	First Phasing Angle [°]	Second Phasing Angle [°]	Mass Wet [Kg]
1	30	30	5373,9
2	30	30	8509,1
3	30	30	11535,6
4	30	30	14584,8
1	30	60	5380,0
2	30	60	8510,3
3	30	60	11542,2
4	30	60	14578,4
1	30	90	5379,1
2	30	90	8505,9
3	30	90	11542,2
4	30	90	14573,7
1	30	120	5377,2
2	30	120	8511,2
3	30	120	11539,0
4	30	120	14586,1
1	30	150	5374,7
2	30	150	8504,8
3	30	150	11535,1
4	30	150	14576,0
1	30	180	5375,0
2	30	180	8504,1
3	30	180	11536,5
4	30	180	14576,2

Table 78 - APPENDIX-B: Mass wet HT5k configurations.

# Thr	First Phasing Angle [°]	Second Phasing Angle [°]	Mass Wet [Kg]
4	30	30	5014,7
8	30	30	7953,8
12	30	30	10840,9
16	30	30	13979,5
4	30	60	5016,9

8	30	60	7953,5
12	30	60	10829,9
16	30	60	13982,1
4	30	90	5017,5
8	30	90	7951,0
12	30	90	10835,0
16	30	90	13980,0
4	30	120	5015,5
8	30	120	7950,8
12	30	120	10833,5
16	30	120	13971,9
4	30	150	5012,6
8	30	150	7947,9
12	30	150	10826,8
16	30	150	13970,0
4	30	180	5013,7
8	30	180	7951,7
12	30	180	10836,7
16	30	180	13975,3

Table 79 - APPENDIX-B: Mass wet + mass serviced satellite, HT20k configurations.

# Thr	First Phasing Angle [°]	Second Phasing Angle [°]	Mass Wet With Payload [Kg]
1	30	30	8015,0
2	30	30	10954,7
3	30	30	13840,7
4	30	30	16980,9
1	30	60	8018,8
2	30	60	10953,3
3	30	60	13827,7
4	30	60	16980,9
1	30	90	8018,7
2	30	90	10951,8
3	30	90	13834,2
4	30	90	16981,8
1	30	120	8015,7
2	30	120	10951,5
3	30	120	13834,0
4	30	120	16974,1
1	30	150	8014,0

2	30	150	10949,3
3	30	150	13826,5
4	30	150	16969,0
1	30	180	8015,2
2	30	180	10952,8
3	30	180	13834,4
4	30	180	16973,0

Table 80 - APPENDIX-B: Mass wet + mass serviced satellite, HT5k configurations.

# Thr	First Phasing Angle [°]	Second Phasing Angle [°]	Mass Wet With Payload [Kg]
4	30	30	8015,0
8	30	30	10954,7
12	30	30	13840,7
16	30	30	16980,9
4	30	60	8018,8
8	30	60	10953,3
12	30	60	13827,8
16	30	60	16980,9
4	30	90	8018,7
8	30	90	10951,8
12	30	90	13834,2
16	30	90	16981,8
4	30	120	8015,7
8	30	120	10951,5
12	30	120	13834,0
16	30	120	16974,1
4	30	150	8014,0
8	30	150	10949,3
12	30	150	13826,5
16	30	150	16969,0
4	30	180	8015,2
8	30	180	10952,8
12	30	180	13834,4
16	30	180	16973,0